University of Reading

Modelling Enceladus' ocean stratification, circulation, and impacts upon potential observables

Flynn Ames

Department of Meteorology

University of Reading

A thesis submitted for the degree of

Doctor of Philosophy

September 2025

Declaration

I confirm that this is my own work and the use of all material from other sources has been properly and fully acknowledged

Flynn Ames

Acknowledgements

Firstly I'd like to thank my supervisors: To David, for the unwavering support and guidance throughout this project, for having patience with me and believing in my work even when I did not myself. To Arnaud and Adam, for suggestions and feedback which really helped shape the direction of this thesis. I have very much enjoyed working with you all.

I'd also like to thank others who provided help at various stages in the project. To Mikhail Kruglyakov, for impressively prompt guidance with GEMMIE, without which the final work chapter would not have materialised. To Jean-Michel Campin and many others on MITgcm community forum, for answering my many queries in this regard. To Wanying Kang for helping when I got stuck with my freezing rate computation. To Robin Smith and Jonathan Gregory who formed my monitoring committee and whose guidance helped me stay on track.

I'd finally like to thank friends and family, whose checking in, company and encouragement has kept me going, particularly during the PhD's final hour.

Abstract

Enceladus - an ice-covered moon of Saturn - harbours a global subsurface ocean, a prime target in the search for life. Material lofted into space via plumes erupting from fissures in its south polar ice shell is believed sourced from the ocean, and has been used to infer the ocean composition. This thesis highlights the role of ocean stratification and circulation in modulating the representability of plume material of the bulk ocean, and the sensitivity of these to ocean salinity effects.

A general circulation model (GCM) is adapted from terrestrial applications for the study of Enceladus. Leveraging this, it is shown that the ocean beneath Enceladus' south polar ocean should be stratified if steady state is assumed for its overlying ice shell. Stratification arises owing to ocean salinity effects via two mechanisms: the reversal in the thermal expansion coefficient (α_T) at low salinity, and ice melting. Stratification extent is modulated by mean salinity, ice melting rate, as well as uncertain mixing induced by eddies (κ_{GM}) and tidal- and librational- energy dissipation (κ_z). Stratification is shown to delay transit of hydrothermally- derived particulates to the plumes by 1000s to 100,000s of years. It is therefore argued that robust modelling of ocean bottom-to-top transport within Enceladus should account for ice shell freshwater fluxes, and a non-linear equation of state that permits α_T to vary within the ocean.

Assuming a steady state ice shell, constraints are then obtained upon the relative freshening of Enceladus' south polar ocean. Relative freshening is found stronger for larger melting rate, weaker κ_z and larger bulk ocean salinity. The work suggests that salt concentrations within plume material may represent an underestimate of the salinity of the bulk ocean.

Enceladus' 3D time-mean ocean circulation is demonstrated to produce a motionally induced magnetic field. This magnetic signature is found to differ at differing ocean salinity, but is likely too weak to detect using modern fluxgate magnetometers. Results obtained here inform future efforts to obtain alternative constraints upon Enceladus' ocean salinity via its magnetic signature.

Contents

List of Tables

List of Figures

Notation

The tables below list the major notation used in this thesis.

Coordinates

Symbol	Description
λ	Longitude
ϕ	Latitude
r	Radial (distance from centre of sphere)
z	Height referenced to sea level
Θ	Colatitude

Physical parameters

Symbol	Description
u	Zonal (positive eastwards) velocity
v	Meridional (positive northwards) velocity
w	Vertical (positive upwards) velocity
S	Ocean salinity
P	Pressure
T	Ocean potential temperature
T_f	Water freezing temperature
T_{crit}	Critical temperature
ρ	Ocean in-situ density
ρ_0	Constant reference density
α_T	Thermal expansion coefficient
q	Ice freezing rate
η_{melt}	Ice melting viscosity
κ_z	Effective vertical diffusivity
κ_{GM}	GM (a.k.a. thickness) diffusivity
$\vec{J}$	Electric current density
$\vec{B}$	Magnetic field
R_E	Enceladus radii

Acronyms

The table below lists the major acronyms used in this thesis.

Acronym	Description
GCM	General circulation model
DNS	Direct numerical simulation
MITgcm	Massachusetts Institute of Technology general circulation model
HPEs	Hydrostatic primitive equations
GEMMIE	Global EM Modeling code based on Integral Equation (IE) approach
OIEF	Ocean induced electric field
OIMF	Ocean induced magnetic field

Chapter 1

Thesis overview

1.1 Motivation and aims

Planetary oceanography is a burgeoning field. Only at the turn of the century was a stable reservoir of liquid water discovered elsewhere in the solar system (Khurana et al. 1998). More have since been identified (Iess et al. 2014; Saur et al. 2015; Lainey et al. 2024; Cochrane et al. 2025). More are suspected (Cochrane et al. 2021). In contrast to Earth, these oceans exist in the subsurface, within globally ice-covered moons orbiting Jupiter and Saturn. Shielded from cosmic radiation (Paranicas et al. 2009), 'icy moon' oceans could be abodes for life if co-located with an energy source and suitable chemical elements (Hand et al. 2020). This is the primary motivation for their exploration and study (Hendrix et al. 2019).

Before the funding of this project, the circulation of icy moon oceans had been seldom investigated. Existing simulations lacked consideration of ocean salinity, or an explicit representation of ice-ocean interaction (Goodman and Lenferink 2012; Soderlund et al. 2014; Soderlund 2019), known to be tightly coupled with ocean transport in ice-covered waters at Earth (Losch 2008; Roquet et al. 2022). Given the exceptional challenge of drilling through kilometres of ice in the outer solar system (Dachwald et al. 2014; Konstantinidis et al. 2015), environments at the depths of icy moon oceans can currently only be inferred via data acquired at or above the ice surface. Such inferences often rely upon assumptions regarding transport in the underlying ocean (e.g., Hsu et al. 2015) which, in turn, controls the convergence (or lack thereof) of heat, salt, particulates and putative biosignatures (signs of life) from depth to the overlying ice that we can probe. This motivates the study of icy moon ocean circulation.

This thesis attempts to bridge terrestrial and planetary oceanography by applying theory and models developed for Earth oceans to that of an ice-covered moon. To keep the scope manageable, the work presented hereafter focuses upon Enceladus - moon of Saturn. Enceladus is chosen because its ocean is believed to have been indirectly sampled via material vented into space through fissures in its south polar ice shell (dubbed 'the plumes'; Porco et al. 2006; Waite et al. 2009; Postberg et al. 2009). In doing so, this work is relevant for existing attempts to constrain Enceladus' habitability via plume material observations.

The overarching aims of this thesis are as follows:

- To clarify and quantify Enceladus' ocean stratification and circulation and the role of ocean salinity effects.
- Determine implications of these for efforts to constrain Enceladus' ocean composition and environments at depth via plume material.
- Determine if ocean stratification and circulation could be detectable via signatures at or above the ice shell.

1.2 Structure

Chapter 2 introduces the framework for numerical modelling of Enceladus' ocean used in this thesis. A general circulation model (GCM), originally developed to study Earth's oceans, is configured from scratch for the study of Enceladus. Its components are described and rationalised. A 2D reference solution is illustrated. Sensitivity tests are performed to identify the most significant model components.

Chapter 3 investigates the effect of ocean salinity and uncertain mixing parameters upon the stratification of Enceladus' ocean, along with implications for the transport of hydrothermally-derived particulates therein. The fundamental control of stratification upon the transport timescale, and its sensitivity to uncertain mixing parameters is highlighted. Discrepancies with existing interpretation of plume material are identified.

Chapter 4 attempts to constrain the freshening of Enceladus' south polar ocean - the source of Enceladus' plumes - relative to the bulk ocean assuming steady state of its ice shell. In doing so, the effects of ocean upper boundary height upon stratification are also investigated. Here it is argued that relative freshening could result in plume material significantly diluted relative to the bulk ocean, again dependent upon uncertain mixing parameters.

Chapter 5 rounds off the work chapters, investigating whether Enceladus' time-mean ocean circulation could, itself, leave a magnetic signature detectable above the ice surface, to provide an alternative constraint upon ocean salinity and transport. To this end, fully global 3D GCM simulations of Enceladus' ocean are conducted, along with 3D electromagnetic simulations investigating the interaction of simulated ocean flows with Saturn's magnetic field. While the magnetic signature of the time-mean circulation is concluded too weak to detect at present, the work provides a foundation for future efforts to constrain the ocean induced signature owing to ocean tides, as well as at other ice-covered worlds.

Chapter 6 concludes the thesis by summarising the main findings and providing recommendations for future work.

Chapter 2

Open source icy moon oceanography with the MITgcm

2.1 Introduction

Global, subsurface oceans are known to reside within numerous ice-covered moons orbiting Jupiter and Saturn (Khurana et al. 1998; Saur et al. 2015; Thomas et al. 2016; Lainey et al. 2024), and could plausibly exist beneath the surface of other icy bodies in our solar system (Cochrane et al. 2021; Hussmann, Sohl and Spohn 2006). As stable reservoirs of liquid water, they satisfy a fundamental condition for life, representing potentially habitable environments within reach of existing spacecraft instrumentation (Hand et al. 2020). Evidence implying the existence of icy ocean worlds was first gathered by the Galileo probe orbiting Jupiter from 1997-2003 (Pappalardo et al. 1999; Khurana et al. 1998; Kivelson et al. 2000), and Cassini probe orbiting Saturn from 2004-2017 (Porco et al. 2006; Postberg et al. 2009; Spencer et al. 2006; Iess et al. 2014; Thomas et al. 2016; Béghin et al. 2012; Iess et al. 2012). In the 2030s, two missions - ESA's JUICE and NASA's Europa Clipper - will arrive at the Jupiter system, dedicated to constraining the geophysical properties of Ganymede, Europa and Callisto (Grasset et al. 2013; Howell and Pappalardo 2020). Beyond that, both NASA and ESA have prioritised a dedicated future mission to Enceladus - moon of Saturn - with objectives that include searching for evidence of extant life (MacKenzie et al. 2021; Martins et al. 2024). Icy ocean worlds are therefore expected to remain a prime target for scientific research in the coming decades as observational constraints improve significantly (Hendrix et al. 2019).

Given that drilling through kilometres of ice in the outer solar system is currently technologically prohibitive, it is expected that observational constraints upon the underlying ocean environments (at least in the foreseeable future) will necessarily be gained via data acquired at and above the ice surface. This has so far been achieved using surface composition (e.g., Zolotov and Shock 2001), magnetic signature (Vance et al. 2021), and in the case of Enceladus, ocean material that has been vented through the ice out into space (e.g., Waite et al. 2009; Postberg et al. 2009; Waite et al. 2017). Such means will be leveraged by future missions (Grasset et al. 2013; Howell and Pappalardo 2020; MacKenzie et al. 2021). However, the representability of these observations of the underlying ocean will be sensitive to the global ocean dynamics and stratification, which will control the transport of heat, salt, particulates, and chemical species vertically and laterally therein (Ashkenazy and Tziperman 2021; Šachl et al. 2024; Ames et al. 2025). An improved understanding of the physical oceanography of ice-covered moons is therefore necessary to provide context to existing and future observations, particularly where attempting to infer environments at depth (Soderlund et al. 2024).

Work to improve understanding of the physical oceanography of ice-covered moons has commenced. In contrast to Earth, where understanding of the ocean transport is gained via the combination of numerical modelling and observational data of ocean flow velocities, temperature, salinity and other passive 'tracers' (chemical species and particulates transported by the ocean that do not affect the dynamics or stratification; Fox-Kemper et al. 2019), understanding of icy moon ocean transport currently relies solely on modelling. So far, two approaches have emerged: Direct numerical simulations (DNS) adapted from core convection applications (Soderlund 2019; Lemasquerier, Bierson and Soderlund 2023; Šachl et al. 2024; Bouffard et al. 2025), and the use of general circulation models (GCM) adapted from terrestrial oceanography applications (Zeng and Jansen 2021; Ashkenazy and Tziperman 2021; Bire et al. 2022; Zhang, Kang and Marshall 2024; Ames et al. 2025). Both approaches have strengths and weaknesses. Namely, DNS resolves all scales of fluid motion down to the Kolmogorov scale, therefore avoiding the need to rely upon parameterisation schemes whose applicability for icy moon oceans has not yet been verified. However, unlike GCMs, they have not yet been configured to account for the effects of salinity anomalies, arising from ice melting and freezing, nor non-linearities in the equation of state for water density that can control the stratification of icy moon oceans and ice-ocean interaction (e.g., see Ames et al. 2025).

As far as these authors are aware, the existing literature lacks a documented, open-source configuration for simulating icy moon ocean dynamics and stratification. We argue such a manuscript and configuration would be useful for the following reasons:

- Firstly, a signposted, open-source configuration would provide a better foundation for other planetary scientists to set up their own simulations of ice-covered oceans, by providing the base configuration, describing and rationalising each component, and clarifying which are the most essential.

- Secondly, it could promote a peer-reviewed discussion regarding best practice for conducting robust icy-moon-ocean simulations, outputs from which are of significant consequence for potential observables, but currently cannot themselves be verified by observational data.

- Thirdly, areas requiring further development can be flagged, and the configuration tested and built upon, to promote development of improved tools for modelling the

physical oceanography of ice-covered oceans, accessible to all.

Here we choose to follow the GCM approach of modelling ice-covered oceans, and present an open source configuration of the Massachusetts Institute of Technology General Circulation Model (MITgcm; Marshall et al. 1997b) configured for the study of Enceladus. The MITgcm is chosen owing to its customisability as well as flexibility in being both a solver of the full-non-hydrostatic set of momentum equations, while including essential physics regarding the effects of ocean composition. The importance of these are discussed in section 2.4. We choose to apply the model here to Enceladus because its ocean boundary conditions and geometry are perhaps the best constrained of all known ice-covered oceans, namely owing to constraints upon the shape of its overlying ice shell (Hemingway and Mittal 2019; Park et al. 2024). Furthermore, model solutions are likely to have implication for *existing* interpretation of ocean material vented into space via Enceladus' south polar plumes (in turn sampled by the Cassini probe Porco et al. 2006; Waite et al. 2009; Postberg et al. 2009; Postberg et al. 2011; Waite et al. 2017; Postberg et al. 2018; Postberg et al. 2023). The model configuration can be modified for the study other ice-covered moons, but requires care in doing so. This will be discussed in section 2.5.

In the following section, the approach taken to modelling Enceladus' (and differences to that of modelling Earth's) ocean is described and rationalised. We then demonstrate the model solution, followed by its sensitivity to individual model components, focusing upon those with the largest impact. These include the boundary forcings and lateral variation therein; representation of eddies and convection, and approximations to the equations of motion, and equation of state for water density. This is followed by concluding remarks. We stress that the following is not an exhaustive list of sensitivity tests. We do not conduct a thorough exploration of model numerics. Neither do we quantitatively compare model outputs with those from other authors or numerical models. This is left for future work.

2.2 A GCM approach to modelling Enceladus' ocean

At Earth, ocean circulation is initiated via forcing of momentum and buoyancy. Wind stress directly imparts momentum into the oceans, and is the primary driver of many time-mean flow features nearer the surface (e.g., Stommel 1948; Munk 1950; Olbers et al. 2004). Fluxes of heat are imparted non-uniformly at the ocean top, via solar radiative forcing, as well as sensible and latent heat exchange with overlying atmosphere (Large and Yeager 2009) and ice. Variations in ocean salinity arise due to evaporation, precipitation, riverine input and ice melting and freezing (Durack 2015). Resultant gradients in ocean density (and thus buoyancy) can indirectly drive ocean circulation - resultant stores of potential energy are then converted to kinetic energy via convecting or eddying motions that act to stratify the ocean and can contribute to the mean flow (Gill, Green and Simmons 1974; Griffies 1998; Marshall and Schott 1999). Internal waves, generated through the action of wind stress, as well as the flow of tides over topography, act to mix the ocean upon breaking. This permits fluxing of buoyant water downwards, moving potential energy stores into the ocean interior, energising a greater portion of the ocean (Wunsch and Ferrari 2004; Ferrari and Wunsch 2009).

Aside from winds, similar processes are expected to be at play on Enceladus (Soderlund et al. 2024). Ocean tides are expected to dissipate energy within its ocean (Rekier et al. 2019; Hay and Matsuyama 2019), although energy dissipation by ice shell libration (periodic movement of the ice shell over the ocean) may be orders of magnitude stronger (Rekier et al. 2019). Such mixing, combined with lateral buoyancy gradients imparted by the overlying ice shell, may drive ocean circulation (Kang 2023; Jansen et al. 2023). More generally, it is been suggested that tides could drive a significant time-mean flow in icy moon oceans (Hay, Hewitt and Katz 2024). Electromagnetic pumping of a salt-bearing ocean within a time-varying ambient magnetic field may also drive ocean circulation (Gissinger and Petitdemange 2019)

The model configuration outlined here primarily solves for the buoyancy-driven flow. The effects of tidally- and librationally-driven flows upon ocean mixing (i.e., via emission, transmission and breaking of internal waves) are parameterised via an effective vertical diffusivity κ_z. The approach is a good first order approximation to this pathway in Earth's oceans (Simmons et al. 2004). We expect the approach should be valid for stratified oceans within ice-covered moons. However, the appropriate value and distribution of κ_z is unknown as it, along with poorly constrained tidal and librational energy dissipation

(Zeng and Jansen 2021), is coupled with ocean stratification (Osborn 1980). Given that the effects of κ_z are explored elsewhere (Ames et al. 2025), it is not a focus here. κ_z is set constant and uniform at 10^{-3} m^2 s^{-1}. Electromagnetic effects are neglected, exploration of which is left for future work.

2.2.1 Equations of motion and associated approximations

Making the Boussinesq and anelastic approximations, the MITgcm configuration here solves the non-hydrostatic momentum equations on a finite volume grid, using spherical polar coordinates, along with height as a vertical coordinate (Marshall et al. 1997b):

$$\frac{\partial u}{\partial t} = -\mathbf{v}.\nabla u - (\underline{\frac{uw}{r}} - \frac{uv\tan\phi}{r}) - (-2\Omega v\sin\phi + \underline{2\Omega w\cos\phi}) + F_u - \frac{1}{\rho_0 r\cos\phi}\frac{\partial\delta P}{\partial\lambda} \quad (2.1)$$

$$\frac{\partial v}{\partial t} = -\mathbf{v}.\nabla v - (\underline{\frac{vw}{r}} - \frac{u^2\tan\phi}{r}) - (-2\Omega u\sin\phi) + F_v - \frac{1}{\rho_0 r}\frac{\partial\delta P}{\partial\phi} \quad (2.2)$$

$$\underline{\underline{\frac{\partial w}{\partial t}}} = \underline{\underline{-\mathbf{v}.\nabla w}} + (\underline{\frac{(u^2+v^2)}{r}}) + (\underline{2\Omega u\cos\phi}) - g\frac{\delta\rho}{\rho_0} + \underline{\underline{F_w}} - \frac{1}{\rho_0}\frac{\partial\delta P}{\partial r} \quad (2.3)$$

$$\nabla.\mathbf{v} = 0, \quad (2.4)$$

where u, v, and w are the zonal, meridional and vertical flow components of the velocity vector $\mathbf{v}$ (m s^{-1}), λ, ϕ, and r, the longitude, latitude, and radial coordinates, ρ_0 the reference (constant) value of ocean density (kg m^{-3}), $\delta\rho$ the difference between the in-situ ocean density ρ and ρ_0, δP the anomaly of in-situ pressure P (Pa) relative to that of a resting stratified ocean, and g gravity (m s^{-2}). The first, second, and third terms on the right hand side of each equation represent the advective (momentum tendencies arising from advection of momentum by the flow), metric (momentum tendencies arising from use of a spherical coordinate system), and Coriolis (momentum tendencies arising from momentum conservation of fluid moving on a rotating spherical body) terms respectively. The last two terms in each equation are the dissipation and pressure gradient terms. In the vertical momentum equation, $g\frac{\delta\rho}{\rho_0}$ is the buoyancy term. Eq. (2.4) is the continuity equation, mandating conservation of mass.

Note it is customary in Earth ocean modelling to simplify Eqs. (2.1)-(2.3) further and

make the hydrostatic, traditional, and thin shell approximations, yielding the hydrostatic primitive equations (HPEs; Fox-Kemper et al. 2019). The thin shell approximation assumes that variations in r are small relative to radius of the planet, neglecting effects of a varying radial distance to the centre of the body. The traditional approximation neglects Coriolis terms in the horizontal momentum equations involving the vertical velocity, and metric terms in these equations including a product of velocity terms (note the traditional and thin shell approximations must be made together to ensure a complete angular momentum principle; Marshall et al. 1997b). The hydrostatic approximation assumes that the pressure gradient and buoyancy terms balance in the vertical momentum equation (Vallis 2017). As in Marshall et al. (1997b), terms in the momentum equations neglected in the HPEs are underlined (either once or twice - the double underline represents terms neglected in the quasi-hydrostatic approximation to the momentum equations discussed in section 2.4.4).

In the reference configuration here, these terms are maintained. Their influence are explored in sections 2.3.3 and 2.4.4, where it is shown that the $2\Omega w \cos\phi$ is significant.

2.2.2 Ocean density: the equation of state

Ocean density ρ is computed as a function of the potential temperature (the temperature a water parcel would be if raised to a reference pressure level) T ($^\circ$ C), local salinity S (g kg^{-1}), and pressure P (dbars):

$$\rho = \rho(T, S, P) \tag{2.5}$$

Eq. (2.5) is known as the equation of state, which in combination with the momentum equations, governs the buoyancy-driven flow. A linear equation of state for the ocean can be derived from first principles (with coefficients derived numerically) and written as (Vallis 2017):

$$\rho = \rho_0(1 - \alpha_T(T - T_{ref}) + \beta_S(S - S_{ref})), \tag{2.6}$$

where α_T is thermal expansion coefficient (quantifying the expansion of water with increasing temperature) and β_S the haline contraction coefficient (quantifying the contraction of water with increasing ocean salinity). The linear equation of state is not typically employed in quantitative terrestrial oceanography because it neglects essential non-linearities

that can significantly influence ocean transport (Roquet et al. 2015b), namely the variation of α_T with ocean pressure, temperature, and salinity (Roquet et al. 2015b; Roquet et al. 2022). Instead, employed equations of state are typically long polynomial expressions that have been tuned to observations (e.g., Roquet et al. 2015a). The validity of these equations of state for oceans beyond Earth depends upon the composition and pressures therein. Within Enceladus' ocean, pressures are expected to be comparable to those on Earth owing to its weak surface gravity (0.113 m s^{-2}, $\sim$ 100 times lower than at Earth, meaning pressures at 60 km depth at Enceladus $\approx$ pressures at 0.6 km depth on Earth). Enceladus' ocean composition is less certain, although the composition of E-ring ice grains are suggestive of sodium chloride as the dominant salt, with concentrations at or below concentrations present at Earth (Postberg et al. 2009; Glein and Truong 2025).

Overall, we believe that equations of state, tuned to Earth's oceans, should be suitable for studies aiming to determine qualitative characteristics of Enceladus' ocean circulation and stratification. The non-linear equation of state of Jackett and Mcdougall (1995) is therefore employed in simulations here unless specified otherwise. In section 2.4.2, it is demonstrated that accounting for non-linearities in the equation of state become essential when assuming a mean ocean salinity lower than $\sim$ 20 g kg^{-1}. Otherwise, simulations presented hereafter assume an Earth-like mean ocean salinity of 35 g kg^{-1}.

2.2.3 Ocean density: dependent variables

Gravity g is allowed to vary as a function of height z (referenced to the model surface), using the formulation of Kang and Jansen (2022):

$$g(z) = \frac{4\pi G[\rho_{\text{core}}(r_{\text{s}} - H_{\text{i}} - H_{\text{o}})^3 + \rho_{\text{oi}}((r_{\text{s}} - z)^3 - H_{\text{i}} - H_{\text{o}})^3]}{3(r_{\text{s}} - z)^2}, \tag{2.7}$$

where $G = 6.67 \text{ x } 10^{-11}$ m^3 kg^{-1} s^{-2} is the gravitational constant, $\rho_{\text{core}} = 2370$ kg m^{-3} and $\rho_{\text{oi}} = 1000$ kg m^{-3} the approximated mean densities of the core and ocean-ice (combined) layers respectively, $r_{\text{s}} = 252$ km the mean radius at the ice shell (and model) surface, and $H_{\text{i}} = 20$ km and $H_{\text{o}} = 40$ km the assumed mean thickness of the ice and ocean layers respectively (Hemingway and Mittal 2019; note that default planetary parameters employed in this manuscript can also be found in table 2.1). The vertical profile of gravity within Enceladus is shown in fig. 2.1. Gravity is approximately 10% stronger at the ocean bottom relative to the ice surface.

The vertical profile of gravity is then used to compute the pressure P. In the momentum Eqs. (2.1)-(2.3), the in-situ non-hydrostatic pressure is obtained through inversion of a 3D elliptic equation (see Marshall et al. (1997a)). For computation of ocean density via Eq. (2.5), a horizontally and temporally constant pressure is instead assumed:

$$P = -g\rho_0 z \tag{2.8}$$

While the MITgcm permits use of in-situ non-hydrostatic pressure in Eq. (2.5), it has negligible effect upon solutions here, while significantly increasing computational cost. The simpler approach is therefore adopted.

Density is computed using the potential temperature and salinity. These are solved in the model as (Marshall et al. 1997b):

$$\frac{\partial T}{\partial t} = -\nabla.(\mathbf{v}T) + F_T \tag{2.9}$$

$$\frac{\partial S}{\partial t} = -\nabla.(\mathbf{v}S) + F_S, \tag{2.10}$$

where the latter term in both equations represents the sources and sinks of temperature and salinity respectively. In the configuration here, forcings include the restoring of temperature and salt at the upper boundary, and a heat flux applied at the bottom boundary. These are discussed in the next section.

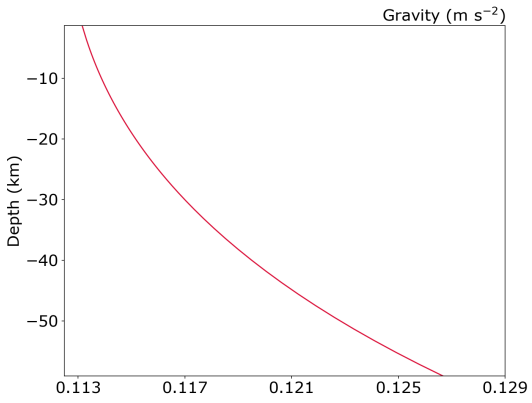

Figure 2.1: Vertical profile of gravity (m s^{-2}) assumed in the model, as a function of height z referenced to the model surface, taken as Enceladus' mean surface radius of 252 km.

Parameter	Value
Ice shell surface radius (r_s)	252 km
Core radius (r_c)	192 km
Mean ocean thickness (H_o)	40 km
Mean ice thickness (H_i)	20 km
Ice density (ρ_i)	925 kg m^{-3}
Ocean mean salinity (S_ref)	35 g kg^{-1}
Ocean reference pressure (P_ref)	$\rho_\mathrm{i} g H_i$
Ocean reference temperature (T_ref)	Freezing temp at P_ref and S_ref
Ocean reference density (ρ_0)	Density at T_ref, P_ref and S_ref
Core density (ρ_core)	2370 kg m^{-3}
Rotation rate (Ω)	5.307 x 10^{-5} s^{-1}
Core total heat output (F_tot)	20 GW
Specific heat capacity of water (c_p)	4000 J kg^{-1} K^{-1}
Eddy diffusivity (κ_GM)	0.1 m^2 s^{-1}
Vertical diffusivity (κ_z)	10^{-4} m^2 s^{-1}
Ice melting viscosity (η_melt)	10^{14} Pa s

Table 2.1: Key parameters used in default numerical simulations and in computation of boundary forcings in this chapter.

2.2.4 Boundary forcings

Upper boundary

Enceladus' ocean is overlain by a global ice shell whose thickness profile has been constrained using gravity, shape and libration data acquired via the Cassini mission. While estimates for the mean thickness vary, it is suggested to be at least 20 km (Hemingway and Mittal 2019; Park et al. 2024). There is a consensus that Enceladus' ice shell exhibits pronounced thinning at its south pole, < 5 km thick here, compared to the expected equatorial thickness of at least ~ 30 km (also corroborated by observed patterns of heat outflow - Spencer et al. 2006). Assuming the ice is floating on the ocean below, the majority of ice thickness variation must manifest below 'sea level'. This means the upper boundary height of Enceladus' ocean likely varies by tens of kilometres from equator-to-pole. While this far exceeds any magnitude of upper boundary height variations observed at Earth, the ocean beneath ice shelves can exhibit comparable *relative* height variations from outer edge to grounding line (Griggs and Bamber 2011), and so may be the closest terrestrial analogue.

In terrestrial ocean modelling, the interaction of ice shelves and underlying ocean are typically modelled using the flagship three equation formulation (Holland and Jenkins

1999; Losch 2008). These solve for the salt flux into the ocean arising from ice melting and freezing. They also solve for the heat flux out of the ocean - a function of the upwards conductive heat loss (in turn a function of ice thickness and temperatures at the ice top and bottom), ocean heat transport, and latent heat fluxes from ice melting and freezing. The three-equation formulation is incorporated into the MITgcm's shelfice package, which has been employed in existing simulation of icy moon oceanography (Ashkenazy and Tziperman 2021; Kang et al. 2022a; Zeng and Jansen 2024). A caveat of using this approach at Enceladus is that the thermodynamics of Enceladus' upper boundary remains uncertain. Namely, it is not clear whether tidal heating (arising from the contraction and expansion of Enceladus as it orbits eccentrically about Saturn) is significant in the ice shell, enough to balance the heat outflow observed at the south pole (Howett, Miles and Quick 2025) and that expected globally owing to conductive heat loss (Hemingway and Mittal 2019), to maintain the current ice thickness profile (i.e., steady state). Current tidal heating models are unable to impart enough heat in the ice shell to balance this heat loss (Souček et al. 2019), while models of ocean circulation have reached opposing conclusions about whether (alternatively) sufficient heat can be transported upwards from Enceladus' core to balance the heat budget of its south polar ice shell (Choblet et al. 2017; Kang et al. 2022b; Zeng and Jansen 2024; Bouffard et al. 2025).

Given existing uncertainties and to enable consistent solutions, the configuration here assumes steady state and adopts a simplified treatment of the upper boundary. In doing so, the configuration is modular, allowing components to be turned on and off to examine sensitivities (e.g., see section 2.4.1). These components will now be described.

The geometric effect of ice topography is accounted for by depressing the upper boundary height of the ocean to that expected given the prescribed ice thickness profile of (Čadek et al. 2019 - here truncated at degree 3), assuming Airy isostasy (i.e., that the ice shell is floating on the ocean). Pressure at the ice-ocean interface is then computed using the mass of water displaced beneath 'sea level'. Shaved grid cells are used to more precisely represent boundary height variation (Adcroft, Hill and Marshall 1997), by permitting ocean to occupy a fraction of the vertical extent of a grid cell, in increments of 20%. Given that the roughness of the ice shell base is not known, a simple linear drag coefficient of 10^{-4} m s^{-1} is applied at the ocean top to represent the frictional effect of (and thus dissipation of momentum owing to) the overlying ice. Adoption of a linear drag coefficient is preferred here vs a no-slip condition, to provide a tunable constraint upon the boundary stress.

Temperature is restored interactively at the upper boundary to the pressure- and salinity-dependent freezing temperature, computed using the formulation of Millero (1978):

$$T_f = 1.710523 \times 10^{-3} S^{\frac{3}{2}} - 2.154996 \times 10^{-4} S^2 - 0.0575 S - 7.53 \times 10^{-8} P, \qquad (2.11)$$

with a restoring timescale of 30 days. This is fast relative to the advective timescale and thus (in the absence of changing salinity and pressure) effectively acts as a fixed temperature boundary condition. As with the equation of state, we expect this freezing temperature formulation to be qualitatively robust for Enceladus' ocean given existing constraints upon its ocean composition (Postberg et al. 2009). The pressure dependence of freezing temperature enables a weak meridional gradient (~ 0.1 °C) of the upper boundary restoring temperature, somewhat analogous (but two orders of magnitude weaker and inverted relative) to Earth's equator-to-pole temperature gradient. In section 2.4.1 the importance of accounting for this lateral variation is demonstrated.

Following Kang et al. (2022a) the freshwater flux at the ocean top is prescribed given that required to balance the divergence of the computed ice flow (note that associated mass fluxes are not accounted for).

The ice flow rate is computed using the formulation of Kang and Flierl (2020) (assuming that Enceladus' ice shell is not undergoing solid state convection, which would be difficult to reconcile with the large variations in observed ice thickness; Hemingway and Mittal 2019):

$$M(\phi) = -\frac{2g\frac{\rho_\mathrm{i}}{\rho_0}(\rho_0 - \rho_\mathrm{i}) H_\mathrm{ilat}^3}{r_\mathrm{s}\eta_\mathrm{melt} ln^3\left(\frac{T_\mathrm{s}}{T_\mathrm{f}}\right)} \frac{\mathrm{d}H_\mathrm{ilat}}{\mathrm{d}\phi} \int_{T_\mathrm{s}}^{T(z)} \int_{T_\mathrm{s}}^{T_\mathrm{f}} exp\left[\frac{-E_\mathrm{a}}{R_\mathrm{g} T_\mathrm{f}}\left(\frac{T_\mathrm{f}}{T_\mathrm{i}} - 1\right)\right] ln\left(\frac{T_\mathrm{i}'}{T_\mathrm{f}}\right) \frac{dT_\mathrm{i}'}{T_\mathrm{i}'} \frac{dT_\mathrm{i}}{T_\mathrm{i}}, \qquad (2.12)$$

where g is surface gravity, $\rho_\mathrm{i} = 925$ kg m^{-3} and ρ_0 the ice and ocean reference densities respectively. H_ilat gives the thickness of the ice layer at a point latitude, r_s the mean radius of Enceladus, η_melt the ice melting viscosity (at the base of the ice shell), T_f and T_s the prescribed temperatures at the ice-ocean interface (freezing temperature) and surface respectively. T_i(z, ϕ) is the ice temperature (computed using Eq. (S7) from Kang and Flierl 2020). $E_\mathrm{a} = 59.4$ kJ mol^{-1} is the activation energy for diffusion creep, $R_\mathrm{g} = 8.31$ J K^{-1} is the gas constant and $T_\mathrm{i}' = T_\mathrm{i}(z)$ is an integral variable (prime symbol used to distinguish the outer vs inner integral). The surface temperature T_s is computed using a radiative

balance at the ice shell surface, given the solar constant at Saturn and assuming a surface bond albedo of 0.81 (Spencer et al. 2006), using the analytic approach of Ashkenazy (2019) (note the computed meridional variation of surface temperature has negligible effect upon the ice flow rate, but that the mean surface temperature is important).

The freezing rate is then computed using the ice flow divergence (Kang et al. 2022a):

$$q(\phi) = \frac{1}{r_{\mathrm{s}} \cos\phi} \frac{\partial}{\partial \phi}(M \cos\phi), \tag{2.13}$$

and converted to a salinity tendency in the uppermost layer in the model:

$$S_{tendency} = \frac{q S_{int} \rho_{fresh}}{\rho_0 \Delta z} \tag{2.14}$$

where S_{int} and Δz are the salinity (g kg^{-1}) and thickness (m) of the upper most ocean layer adjacent to the boundary, and ρ_{fresh} the reference density (kg m^{-3}) of freshwater.

The upper boundary height (km), and resultant restoring temperature (° C), ice flow rate (km^2 Myr^{-1}), and ice freezing rate (km Myr^{-1}) are shown in fig. 2.2. Ice flows from thicker ice regions nearer the equator to regions of thinner ice nearer the poles, consistent with previous work exploring the flow of icy moon ice shells (Ashkenazy, Sayag and Tziperman 2018; Čadek et al. 2019; Kang and Flierl 2020). Melting rates are largest nearer (but not adjacent to) regions of thinner ice nearer the poles. Freezing dominates nearer the equator. This corroborates profiles obtained by Kang et al. (2022a).

The approach to upper boundary forcings taken here has caveats that should be highlighted. Firstly, the use of a meridionally varying restoring temperature at the ice interface can permit a net heat flux from the ice shell *into* the ocean in regions where ice is thinner (owing to warmer interface temperatures here; see section 2.3.2). This is contrary to expected patterns of global conductive heat *loss* ($Q_{cond} = \frac{\kappa_{cond}}{H_{ilat}} \ln\left(\frac{T_f}{T_s}\right)$, where ice conductivity $\kappa_{cond} = 632$ W m^{-1}) of Enceladus' ocean to space, expected to be strongest where the ice is thinnest (see fig. 2.2, bottom left).

A plausible mechanism for this implied heat flux could be tidal heating of Enceladus' ice shell. Tidal heating scales inversely to ice thickness and given this (and that latent heat fluxes are unlikely to heat the south polar ocean at steady state - see below), may represent a mechanism capable of preferentially heating Enceladus ocean from above where ice is thin. However, it is important to note that existing modelling of tidal heating within

Enceladus' ice shell suggests that it is probably only significant near Enceladus' south polar region (e.g., Souček et al. 2019).

A second caveat is that the model does not explicitly account for latent heat fluxes arising from prescribed freezing and melting. Instead, it assumes that latent heat fluxes, along with heat transport from the ocean below, balance the conductive heat loss away from the ocean (and other implied sources of heat within the ice), to permit the required melting and freezing. In fig. 2.2, the upwards latent heat flux ($Q_{Latent} = \rho_i q L_f$, where $L_f = 333.55$ KJ kg^{-1} is the latent fusion energy of ice) at the ocean-ice interface expected from the prescribed freshwater flux is shown. Typical magnitudes (of order 10 mW m^{-2}) are comparable to the expected conductive heat loss to space, and would act to reinforce heat loss nearer the south pole (see fig. 2.16). Care must be taken using the approach here, ensuring that the latent heat flux of a prescribed freshwater forcing could be reasonably balanced by other heat fluxes (e.g., tidal heating) at the ice-ocean interface.

A third caveat is that the approach assumes no temporal variation in the freshwater flux. While quasi-equilibrium mandates a time-mean melting at the poles, it could still permit intermittent periods of freezing. Whether temporal variability of freezing rates is to be expected within Enceladus, and possible effects thereof upon ocean dynamics and stratification, is yet to be explored and is left for future work.

Finally, by not explicitly resolving mechanisms of freezing, the configuration misses physics that could plausibly influence ocean circulation and tracer transport. As water moves upwards into regions of lower pressure (and by extension, warmer freezing temperature) in Enceladus' ocean, it may become supercooled (i.e., cooler than the local freezing temperature), causing it to freeze - this mechanism is known as the 'ice pump' (Lewis and Perkin 1986). On Earth, ice pump can occur as water moves upwards along the ice interface of an ice shelf (directly refreezing onto the ice base; Lewis and Perkin 1986), but also where water is supercooled in the ocean interior. This latter results in the generation of frazil ice, that then buoyantly rises to the ice base where it then accumulates (Holland and Feltham 2005). The freezing of supercooled water in the ocean interior would release latent heat into the ocean, with implications for ocean buoyancy (dependent upon the thermal expansion coefficient). Frazil ice formation could play a role in vertical tracer transport, either indirectly through its effects upon ocean buoyancy, or directly through the capture of tracers within the frozen ice as it rises buoyantly to the ice interface. Such effects go beyond the scope of this manuscript, but should be investigated in future work.

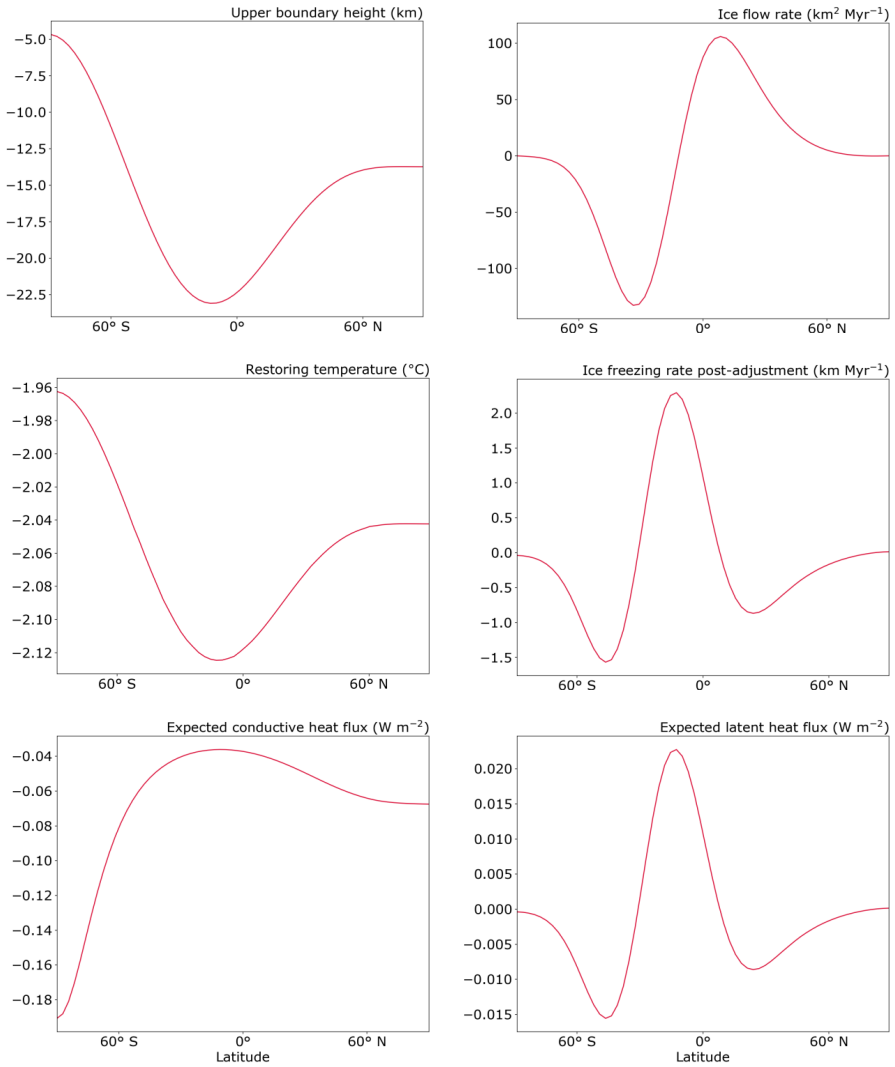

Figure 2.2: Top Left: Upper boundary height (km) in the model, defined as the thickness of ice below sea level, in turn taken as Enceladus' mean radius of 252 km. Middle left: Restoring temperature (°C) at the ocean top, corresponding to the freezing temperature as a function of pressure and salinity in the reference configuration, computed with the formulation of Millero (1978). Bottom left: Expected conductive heat flux (W m^{-2}) at the top of the ocean owing to heat loss to space. Note all values are negative, because the ocean is expected to lose heat globally to space. Also note the flux is not represented in the configuration presented in this manuscript, which solely uses a restoring temperature to represent heat fluxes from the overlying ice. Top right: Ice flow rate (km^2 Myr^{-1}) computed given the prescribed ice thickness profile. Middle right: Ice freezing rate (km Myr^{-1}) computed given the divergence of the ice shell flow rate. Bottom left: Expected latent heat flux (W m^{-2}) at the top of the ocean computed from the freezing rate shown in the middle right panel. Note this latent heat flux is not represented in the configuration presented in this manuscript, which assumes that heat fluxes at the ice interface balance (i.e., steady state). Note comparable orders of magnitudes to expected conductive heat fluxes shown in the bottom left panel.

Lower boundary

As on Earth (Pollack, Hurter and Johnson 1993), Enceladus may experience a heat flux at the bottom of its ocean. The total radiogenic heat flux (heat leftover from Enceladus' formation) emanating from Enceladus' core is expected to be no larger than 0.3 GW, limited by its small size (Travis and Schubert 2015). Tidal heating could increase the core heat output significantly. Thermal modelling of Enceladus' rocky core suggests 10-30 GW of heat could be generated via tidal dissipation in the core, so long as it is sufficiently porous (Roberts 2015; Choblet et al. 2017). In this case, the vertically integrated core heating exhibits a degree 2 like-pattern, strongest at the poles and weakest at the equatorial sub- and anti-Saturn points, manifesting at the core-ocean boundary as a complex 'web-like' pattern, with localised hotspots associated with upwellings of interstitial water convected upwards through the heated core below. The globally averaged heat flux leaving the core is ~ 50 mW m^{-2}, comparable to or slightly weaker than radiogenic heat fluxes observed on Earth (Pollack, Hurter and Johnson 1993).

At Earth, geothermal heating is often neglected in ocean simulations because associated heat fluxes are weak compared to those at the surface. Simulations accounting for geothermal heating find small (but non-negligible) influence upon ocean overturning (Adcroft, Scott and Marotzke 2001; Scott, Marotzke and Adcroft 2001; Hofmann and Morales Maqueda 2009). In contrast at Enceladus', bottom heat fluxes are expected to be comparable to the conductive heat loss through the ice shell aloft (Miles et al. 2025). Previous work has demonstrated that ocean circulation on ice-covered moons can be driven entirely via bottom heating (Bire et al. 2022; Jansen et al. 2023). In section 2.2.4, the importance of bottom heating in shaping ocean stratification in the presence of upper boundary forcings is additionally demonstrated. For this, the reference simulation adopts an idealised 2D profile (neglecting strong localised variation), borrowing the formulation of Zeng and Jansen (2021):

$$Q_{\text{core}}(\Theta) = \frac{F_{\text{tot}}[0.5Y_{20}(\Theta) + K]}{4\pi K r_c^2}, \tag{2.15}$$

where $r_c = 192$ km is the core radius (radius to the ocean bottom), $K \approx 0.904$ a constant and Y_{20} a degree 2, order 0 spherical harmonic function (as a function of co-latitude Θ). A total core heat output of $F_{\text{tot}} = 20$ GW is assumed. The resulting bottom heating pattern is polar amplified, with heating twice as large at the poles vs the equator, corresponding to patterns of previously-simulated, vertically integrated tidal heating within Enceladus' core (Choblet et al. 2017).

Note that the effects of strong, localised variation in bottom heating within Enceladus have been explored previously (Kang et al. 2022b; Bouffard et al. 2025; Zhang et al. 2025) and are therefore not a focus here. Kang et al. (2022b) and Zhang et al. (2025) concluded that localised bottom heating variations are likely homogenised within Enceladus' ocean by baroclinic eddies at depth, preventing this pattern of heating being translated upwards through the ocean to the ice shell (although c.f. Bouffard et al. (2025)), suggesting that an idealised bottom heating profile should be sufficient for simulation of tracer transport from ocean bottom-to-top.

Note also that the ocean bottom is assumed flat here given the current inability constrain icy moon ocean bathymetry (Hemingway and Mittal 2019). Exploration of bathymetry effects within ice-covered oceans is left for future work. Given the roughness of Enceladus' ocean bottom is also not known, a simple linear drag coefficient of 10^{-4} m s^{-1} is applied at the ocean bottom to represent the dissipation of momentum owing to frictional effects here.

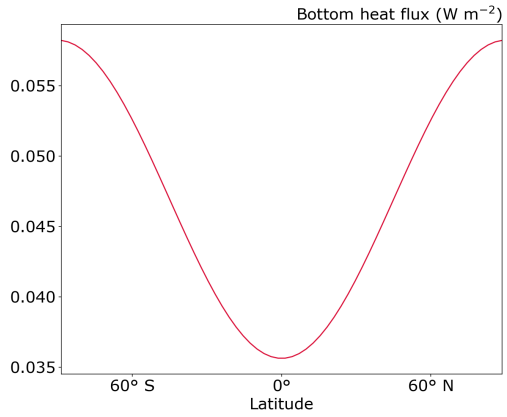

Figure 2.3: Heat flux (W m^{-2}) applied at the ocean bottom boundary in the configuration, computed using Eq. (2.15).

2.2.5 Parameterisation: convection and eddies

Enceladus is tidally-locked to Saturn, orbiting (and thus rotating) once every ~ 32.5 hours - comparable to Earth's rotation period (Beuthe 2016). Existing estimates suggest a bottom heat flux (Choblet et al. 2017) that is sufficiently weak for Enceladus' ocean dynamics to be contolled by rotation rather than buoyancy (Soderlund 2019; Bire et al. 2022). Convective motions are also expected where buoyant water directly underlays denser water (Marshall and Schott 1999). As noted by Zeng and Jansen (2021), an estimate for the minimum horizontal scale of convective plumes can be obtained via the rotational length scale (Jones and Marshall 1993)

$$l_r = B^{1/2} f^{-3/2}, \tag{2.16}$$

where f (s^{-1}) is the Coriolis parameter and B ($\mathrm{m}^2\ \mathrm{s}^{-3}$) is the buoyancy flux. Letting $f \approx 10^{-4}\ \mathrm{s}^{-1}$ and $B = \frac{F\alpha_T g}{c_p \rho_0}$ (where heat flux F is assumed 50 mW m^{-2}, thermal expansion coefficient α_T assumed $5\times\ 10^{-5}\ \mathrm{K}^{-1}$ and specific heat capacity c_p assumed 4000 J $\mathrm{kg}^{-1}\ \mathrm{K}^{-1}$), $\mathrm{l}_r \approx 0.25$ m. Such a small length scale is unlikely to be resolved globally by existing general circulation models, necessitating parameterisation of the mixing otherwise induced by convection.

As in previous work (Kang et al. 2022a; Zeng and Jansen 2024), a simple diffusive adjustment scheme is adopted here. κ_z is increased to 1 $\mathrm{m}^2\ \mathrm{s}^{-1}$ (obtained via scaling of Jones and Marshall (1993)) in regions of static instability to simulate the vertical mixing that unresolved convection may otherwise induce (Klinger, Marshall and Send 1996). It is important to note that the assumption that convection occurs solely in the radial (i.e., vertical) direction is unlikely to be valid for icy moon oceans (Zeng and Jansen 2025). As far as these authors are aware, work verifying a parameterisation scheme for icy moon ocean convective mixing does not yet exist. As a result, we fall back on a scheme tuned for terrestrial oceans and remain mindful of its limitations, exploring them in section 2.4.3.

An additional process requiring parameterisation in a rotating stratified fluid is mixing associated with ocean eddies. A lateral ocean density gradient can give rise to contours of constant density (isopycnals) that slope (because ocean density also increases in the vertical owing to compressibility effects). In the presence of sloped isopycnals, buoyant water can reside deeper in the ocean than denser water on the opposite side of the slope. This sets up a potential energy store that, in a rotating stratified fluid, energises baroclinic

eddies. At Earth, the characteristic length scale of eddies (and thus resolution required to resolve them) is the Rossby radius of deformation (Chelton et al. 1998), and this is expected to hold at Enceladus (Zhang, Kang and Marshall 2024). However, given that the Rossby radius is coupled to the magnitude of ocean stratification (in turn modulated by the eddies themselves), offline computation of the Rossby radius in ice-covered oceans is not trivial, and likely depends upon assumed mixing parameters and boundary forcings (Zhang, Kang and Marshall 2024). Furthermore, eddies cannot be resolved in 2D-latitude-depth configurations as employed in this chapter (see section 2.2.7), and so they must be parameterised.

Here we choose to parameterise baroclinic eddies via the combination of a Gent McWilliams (GM) and Redi schemes (Gent and Mcwilliams 1990; Redi 1982) - a flagship standard in terrestrial ocean modelling. The Gent-McWilliams (GM) component represents the adiabatic stirring effects of eddies (Gent and Mcwilliams 1990), using a bolus (i.e., eddy-induced) velocity (see Griffies 1998), parameterised as:

$$\boldsymbol{u^*} = \begin{pmatrix} u^* \\ v^* \\ w^* \end{pmatrix} = \begin{pmatrix} -\partial_z(\kappa_{\mathrm{GM}} S_x) \\ -\partial_z(\kappa_{\mathrm{GM}} S_y) \\ \partial_x(\kappa_{\mathrm{GM}} S_x) + \partial_y(\kappa_{\mathrm{GM}} S_y) \end{pmatrix}, \tag{2.17}$$

where S is the isoneutral slope (slope of locally referenced potential density - density of water after being moved to a reference pressure level) in the x or y directions (denoted by subscript), and κ_{GM} is the thickness diffusivity, also referred to as the GM or eddy diffusivity. After it is computed, the bolus velocity is then added back onto the Eulerian (resolved) velocity field, to account for GM transport.

Secondly, the Redi component parameterises along-isopycnal mixing induced by mesoscale eddies introducing a term in the tendency of a tracer field C:

$$\nabla.(\kappa_{\mathrm{Redi}} K_{\mathrm{Redi}} \nabla C), \tag{2.18}$$

where κ_{Redi} is known as the isopycnal or Redi diffusivity, and K_{Redi} a tensor and function of the isoneutral slope S (Redi 1982). In Earth ocean models, the small slope approximation is typically employed (i.e., $S << 1$). This yields the small slope Redi tensor (Griffies et al. 1998):

$$K_{\text{redi}} = \begin{Bmatrix} 1 & 0 & S_x \\ 0 & 1 & S_y \\ S_x & S_y & |S|^2 \end{Bmatrix}. \tag{2.19}$$

It is unclear whether the small-slope approximation is valid for icy moon oceanography. Therefore, we employ the full unapproximated Redi tensor (Redi 1982), defined as:

$$K_{\text{redi}} = \frac{1}{1+|S|^2} \begin{Bmatrix} 1+S_y^2 & -S_x S_y & S_x \\ -S_x S_y & 1+S_x^2 & S_y \\ S_x & S_y & |S|^2 \end{Bmatrix}. \tag{2.20}$$

A κ_{GM} of 1 m^2 s^{-1} is chosen (Zhang, Kang and Marshall 2024). For simplicity and given a lack of constraints, we set κ_{Redi}=κ_{GM} and assume both are uniform and time constant. Note sensitivities to the magnitude of κ_{GM} are explored elsewhere (chapters 3 and 4) and are not the focus of this chapter.

Due to the near infinite slopes that can develop in statically unstable regions, we apply a slope clipping scheme which limits the magnitude of the GM streamfunction, $\psi_y = \kappa_{\text{GM}} S_y$, above a slope of 2 to maintain numerical stability. While this introduces diabatic fluxes, it does so only in statically unstable regions, in contrast to an explicit horizontal diffusivity (used in many previous icy moon ocean simulations) which also introduces diabatic fluxes in stratified regions of ocean. In section 2.4.3 however, it will be shown that neglecting GMREDI in favour of an explicit horizontal diffusivity recovers a similar tracer field distribution and stratification nearer the ice shell.

Finally, where eddies are not resolved, their dissipation of momentum must also be parameterised. This is done by employing a turbulent viscosity as is common practice in Earth ocean modelling (Griffies et al. 2005). The appropriate values of viscosity within Enceladus are not known. Here they are chosen to fix the Prandtl number (ratio between tracer and momentum diffusivity) to 10 in the vertical, and 50 in the horizontal (to damp grid scale noise).

2.2.6 Numerics: time stepping and equilibration

Tracer and momentum variables are integrated forwards in time using a second-order Adams-Bashforth timestepping scheme. Stabilising weights are applied to prevent the growth of unstable modes which otherwise develop owing to the idealised nature of the configuration, which makes it more susceptible to the growth of numerical artifacts. Vertical diffusive fluxes of momentum and tracers are stepped forwards in time implicitly using a backwards method for stability. This is necessary given the diffusive adjustment convection parameterisation scheme employed here.

Equilibration of the reference solution takes approximately 10,000 years, limited by the slow diffusive adjustment of the freshwater lenses nearer the poles, controlled largely by κ_z (see 4). These equilibration timescales are longer than typically obtained in terrestrial ocean modelling (order 1000 years - Danabasoglu, McWilliams and Large (1996)) because the thickness of stratified regions of ocean simulated here can be many times the depth of Earth's ocean and the diffusive timescale is proportional to the square of a stratified layer thickness (Ames et al. 2025; note that simulations presented in this chapter use a κ_z two orders of magnitude larger than typically assumed for Earth. Equilibration timescales for simulations in chapter 4, using weaker κ_z, can exceed 750,000 years).

To make equilibration of stratified icy moon oceans computationally feasible at lower κ_z, asynchronous timestepping is employed to accelerate convergence. A typical synchronous timestepping approach steps tracer, free surface, and momentum fields forwards in time using the same timestep Δt. In the coarse-resolution configuration here, the momentum timestep is limited by the inertial timescale stability criterion, requiring that:

$$\Delta t < 0.5/f, \tag{2.21}$$

yielding a maximum momentum timestep of ~ 4500 seconds. Asynchronous timestepping removes this constraint. It does so by first stepping tracer and free surface fields forwards in time at a larger timestep (here 36 hours), and only then stepping momentum fields forwards in time at a much smaller timestep (here 1 hour). In doing so, asynchronous timestepping speeds up convergence of the reference solution by $\sim$ factor 30, and the reference 2D configuration simulates ~ 15000 model years per day using two parallelised CPUs. In section 2.4.5, the effects of asynchronous timestepping upon the reference solution are shown to be negligible.

2.2.7 Resolution and geometry

The reference configuration here is 2D latitude-depth, with one point in the zonal direction. A coarse resolution of 2.8125 degrees is employed in latitude. In section 2.4, a sensitivity test to higher resolution (1 degrees) is conducted and tracer solutions found to be nearly identical.

The omission of a zonal dimension is expected to have a minimal, quantitative impact upon tracer solutions near the ice shell and, by extension, the extent of ocean stratification and magnitude of south polar ocean freshening (explored in chapters 3 and 4 respectively). These are predominantly controlled by the boundary forcings imposed at the ice shell, as well as κ_z and eddy induced mixing within stratified regions of ocean (see chapters 3 and 4). While including a zonal dimension would allow eddies to be resolved (at sufficient resolution), their effects upon ocean mixing can be parameterised within stratified regions of ocean as described in section 2.2.5, and uncertainty explored by varying the eddy diffusivity κ_{GM}, as done in chapters 3 and 4. Zonal ice thickness variations are expected no larger than $\sim$ 5 km at Enceladus (diminishing nearer the poles), small compared to expected meridional variations (exceeding $\sim$ 25 km variation from equator-to-pole; Hemingway and Mittal 2019; Čadek et al. 2019). Hence, meridional profiles of temperature and salinity restoring nearer the ice shell are expected to vary little about the zonal mean where zonal variations are accounted for. Because of the above, it is argued that a 2D modelling approach is justified for the purpose of exploring tracer distributions and stratification near the ice shell. Note that in chapter 5, a 3D configuration is employed (and outlined), because 3D flow fields are necessary to reproduce the magnetic signature of the flow. A 2D configuration is leveraged in the remainder of the thesis (where it is justified) because its low computational cost permits exploration of a much broader parameter space (e.g., in ocean salinity and κ_Z,) than can be achieved via a 3D model, owing to long equilibration timescales (see previous section 2.2.6). This also affords exploration of sensitivities to individual model components, as performed in section 2.4.

The near 20 km variation in upper boundary height of Enceladus' ocean introduces computational challenges. If vertical resolution is too coarse, a 'geometric trapping' effect can arise, where neither the eddy parameterisation or advective flow can mix freshwater anomalies away from the staircase like-topography, and unrealistically large salinity anomalies ensue. To overcome this while balancing computational cost, the reference configuration includes thinner layers of 550 m in the ocean above the ice base (the deepest

point of ice in the ocean), coarsening to 2000 m thick via a hyperbolic tangent profile beneath this depth. This yields 60 vertical layers in total. Note that the vertical resolution at the ocean top is at least an order of magnitude coarser than typically used in Earth ocean models and boundary circulations at the ice interface are unlikely to be fully resolved. As far as these authors are aware, investigation into the boundary circulations of ice-covered moons are yet to be conducted in the presence of varying upper boundary height. Given that these would modulate heat and tracer transport nearer the ice shell, it is an important path for future research.

Finally, Enceladus' ocean is much thicker relative to its radius ($\sim 16\%$ than Earth's ($< 0.1\%$) and as consequence, the total area of its ocean shrinks with increasing depth owing to the effects of spherical geometry. Here, this effect is accounted for by employing the MITgcm's 'deep atmosphere mode' (where the name simply refers to the usual application of this capability to atmospheric modelling). For an Enceladus' ocean of uniform 60 km depth, the surface area of a 2.8125 x 2.8125 degree grid cell at the ocean bottom is approximately 60 % that at the ice surface (fig. 2.4).

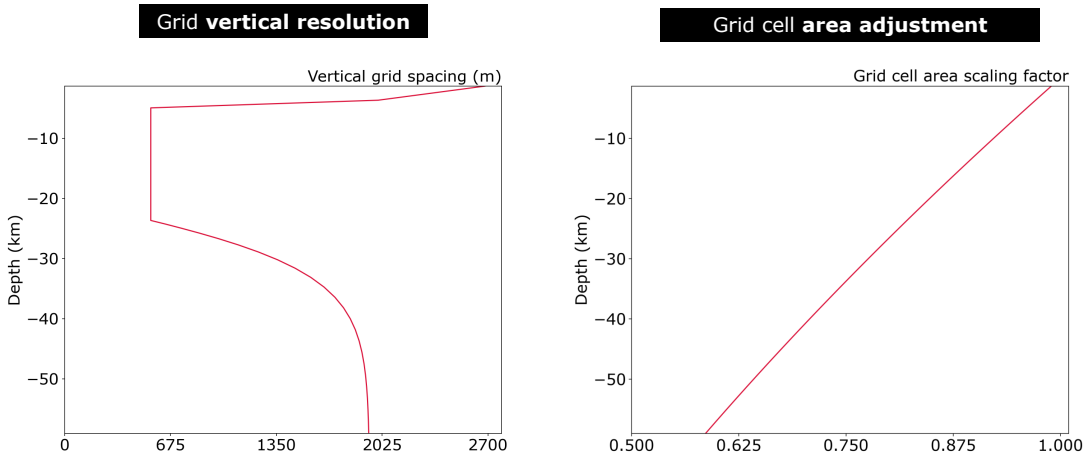

Figure 2.4: Left: Thickness of model grid layers (m) in the vertical. Note coarser layers are employed in 'dry' layers (i.e., where no ocean exists) because the resolution here has negligible effect upon the solution. Right: Scaling factor for the grid cell area as a function of depth relative to the ice surface. Grid cell areas shrink with increasing depth owing to the use of spherical geometry.

2.3 The 2D solution

In the following section, the reference solution of the model configuration is presented in detail. This solution provides the point of comparison for sensitivity tests presented in section 2.4.

2.3.1 Tracer fields

Illustrated in fig. 2.5 are fields of temperature (° C), salinity (g kg^{-1}) and potential density (kg m^{-3}) anomaly, referenced about the reference temperature (T_{ref}), salinity (S_{ref}) and density (ρ_0) respectively. Also shown is the Brunt-Vaisala frequency $N^2 = -\frac{g}{\rho_0}\frac{\partial \rho}{\partial z}$ (s^{-2}) - indicating ocean stratification (i.e., regions with no convection) - along with the tracer age (years). The latter defines the volume-weighted mean time elapsed since a water parcel lost contact with the ocean bottom (computed by restoring age to zero at the ocean bottom, and incrementing age across the whole domain with time), providing a lower bound transport timescale for particulates sourced at depth to a position in space.

Owing to the near-isothermal upper boundary forcing (see fig. 2.2), temperature anomalies are small, not exceeding ~ 0.1 °C. Warmest waters are found at the south polar ice-interface, far from regions of heating at the ocean bottom. Temperatures are warmer at the polar ice interface vs the equatorial interface owing to the pressure dependence of freezing temperature (the restoring temperature at the ocean top; see fig. 2.2), in turn a function of ice thickness. The warmer polar waters aloft are buoyant, permitting stable stratification (no convection) here. This stable stratification is reinforced by freshening given the prescribed ice melting profile. As with temperature, salinity anomalies are small, not exceeding 0.02 g kg^{-1}.

Nearer the equator, cooler, more saline (and thus denser) water sinks, filling the ocean depths. Isopycnal slopes are steep, and the GMREDI parameterisation scheme acts continuously to flatten them, resulting in a neutral (near-zero) stratification here. As a result, the ocean is well mixed here and at depth - indicated by the order of magnitude reduced age at the equatorial ice interface vs the poles, and much weaker horizontal gradients in temperature and salinity (see fig. 2.5).

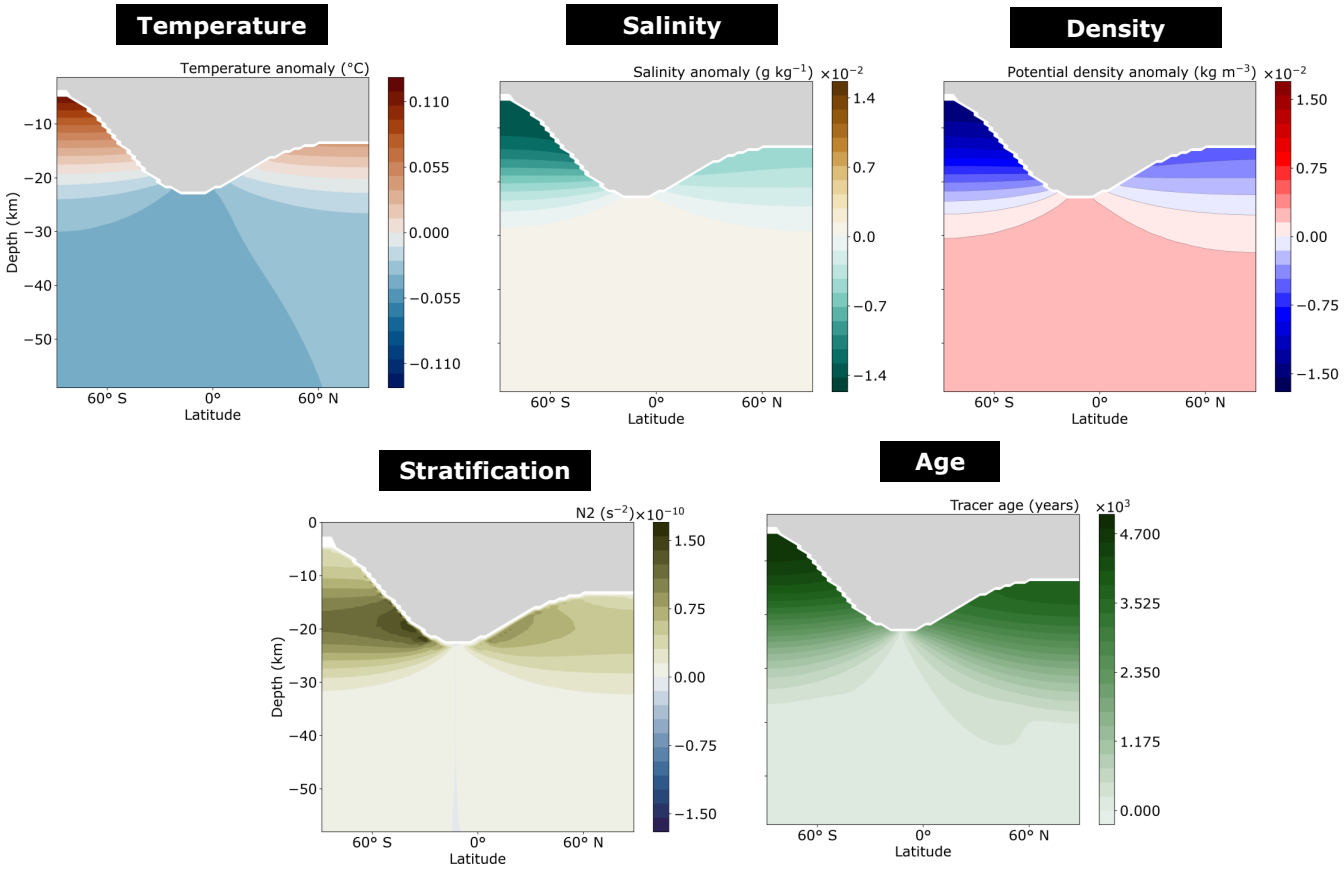

Figure 2.5: Top: Tracer fields for the reference solution showing temperature (left; °C), salinity (centre; g kg^{-1}), and potential density (right, kg m^{-3}) anomalies referenced about the reference temperature, salinity and density respectively (see table 2.1). Bottom: showing the Brunt-Vaisala frequency N^2 (s^{-2}) indicating ocean stratification, along with the tracer age (years), defining the lower bound time elapsed since a water parcel lost contact with the ocean bottom.

2.3.2 Heat and salt transport

The total vertically integrated meridional ocean heat transport and meridionally integrated vertical ocean heat transport (GW) solutions are shown in fig. 2.6. Note that these have been scaled up by factor 128 to obtain a global flux from the singular zonal strip configuration employed here.

Heat is converged meridionally to latitudes of thicker ice, as found previously (Kang, Bire and Marshall 2022). Beneath the ice shell base (deepest point of ice), the total vertical heat flux is a near-constant upwards 20 GW, equivalent to the prescribed globally integrated bottom heating (see fig. 2.3). Above the ice base, the vertical heat flux is no longer a constant 20 GW and reverses direction, becoming net downwards. This is

owing to heat fluxes associated with the restoring of temperature at the ice interface which, importantly, varies meridionally in both its temperature and height of application. Higher up near the poles - where temperatures are restored to warmer values owing to the pressure dependence of waters' freezing point - the restoring acts to flux heat into the ocean (fig. 2.7). The heat is then transported downwards to the cooler equatorial ice shell. Thus, it is meridional temperature gradients at the ice interface, rather than bottom heating, which dominates heat transport within the ice-ocean boundary region here.

As discussed in section 2.2.2, the 'implied' heat flux at the poles is taken here to be tidal heating in the ice shell. Note that magnitude of this 'implied' heat flux nearer the poles (order 0.01 W m^{-1}) is comparable to the prescribed bottom heat flux (see fig. 2.3). Also note that the significant tidal heating of the ice shell 'implied' at the north pole here contrasts existing modelling of ice shell tidal heating (Souček et al. 2019), as well as Cassini observations, from which heat loss rates there were inferred to be comparable to that expected from conductive heat loss alone (Miles et al. 2025). While the globally integrated restoring heat flux matches the integrated core heating to within 0.25% in simulations here (meaning the heat budget of the model is closed and suffices for the purpose of exploring a steady state Enceladus ocean here, largely controlled by salinity gradients), this caveat should be kept in mind when interpreting the north polar heat budget in the rest of this chapter.

Also shown in fig. 2.6 are equivalent solutions of salt transport (kg s^{-1}). The pattern of meridionally integrated salt transport almost perfectly matches the pattern of computed ice flow (see fig. 2.2). This is because in steady state, where ice flow converges freshwater to regions of thinner ice, ocean circulation must converge salt to compensate. The vertical salt transport peaks nearer the base of the ice shell, with an upwards transport of salt above this point. This occurs because freezing occurs deeper in the water column and again, at steady state, salt must be transported upwards to regions of melting to balance the salt budget.

Decomposing the meridional heat transport (fig. 2.8), one can observe that it is dominated by contributions from the GMREDI eddy parameterisation scheme. The advective transport is an order of magnitude weaker, and dominated by noise.

Decomposing the GMREDI transport, one can observe that GM and Redi contributions to meridional heat transport are of comparable order when vertically integrated yet, locally,

GM contributions dominate that of Redi. A notable feature is that the majority of GM heat transport is accomplished in one model layer adjacent to regions of heating at the ocean bottom. Here, GM converges heat to the latitude of maximum freezing. Above this layer, GM instead acts to diverge heat from this latitude.

As with meridional transport, GM and Redi contributions to vertical transport (fig. 2.9) are of comparable order when vertically integrated, with GM dominating locally. GM vertical heat transport appears to be concentrated at one point in latitude, corresponding to the latitude of maximum freezing. The severe concentration of vertical heat transport here is likely a numerical artifact, arising because GM transport is proportional to the isopycnal slope, which tends to infinity at this latitude. Yet given the meridional convergence of heat here by GM, a strong upwards transport in this region is nonetheless expected. The upwards transport by GM and Redi are partially offset by a downwards diffusion of heat via κ_z (which here includes the background prescribed diffusivity as well as transient spikes owing to the convective adjustment scheme; fig. 2.9).

Fig. 2.10 shows the proportion of model time that the convective parameterisation scheme is turned on, along with the proportion of model time that slope clipping of GM is applied (i.e., where isopycnals slopes exceed the prescribed maximum slope of 2). Overall, convective adjustment and slope clipping are predominantly limited to the latitude of maximum freezing. The use of slope clipping causes the GM streamfunction to saturate here and this can be seen in fig. 2.11. Otherwise, GM effectively acts to 'take over' from the convective adjustment scheme where the ocean is neutrally stratified, owing to the steep isopycnal slopes in these regions, permitting efficient vertical transport here (fig. 2.5) even where convective adjustment is not employed. It is unclear if this behaviour is realistic because it is, in turn, unclear how eddies interact with convection in an ocean quasi-permanently destabilised from above and below. In section 2.4.3 the sensitivity of the solution to the use of GM is explored.

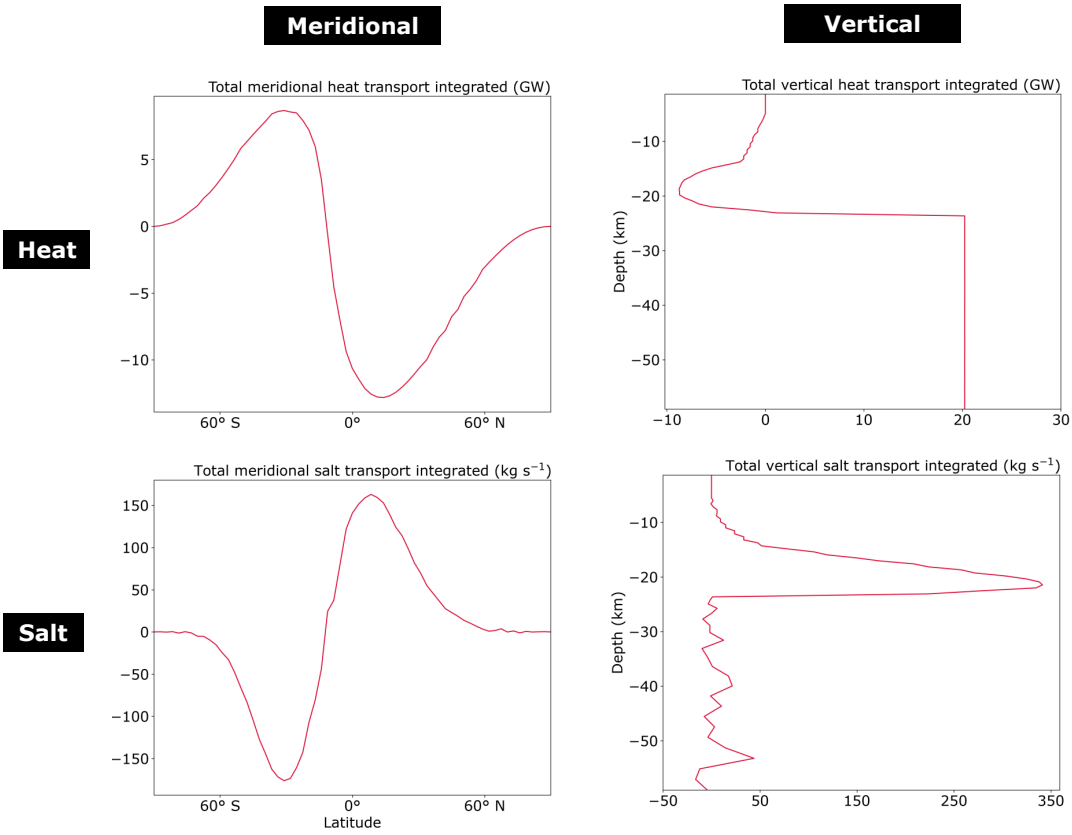

Figure 2.6: Top left: Vertically integrated meridional ocean heat transport (GW) within the ocean as a function of latitude. Top right: Meridionally integrated vertical ocean heat transport (GW) as a function of ocean depth. Bottom: Same as upper panels but instead showing transport of salt (kg s^{-1}). Note that heat and salt transports have been scaled up by factor 128 in all panels, given the singular zonal strip configuration employed here, to obtain a global heat transport.

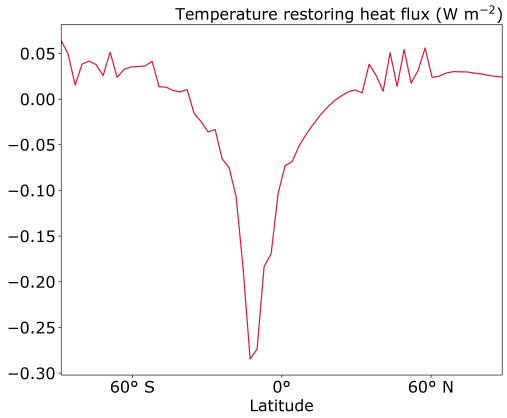

Figure 2.7: The heat flux entering the ocean from above (W m^{-2}) owing to the imposed temperature restoring (in turn shown in fig. 2.2.2, middle left panel). Note the positive heat flux into the ocean contrasts the expected heat loss owing to conduction and latent heating effects (see fig. 2.2), and requires an 'implied' source of heat within the ice shell, assumed here to be tidal heating.

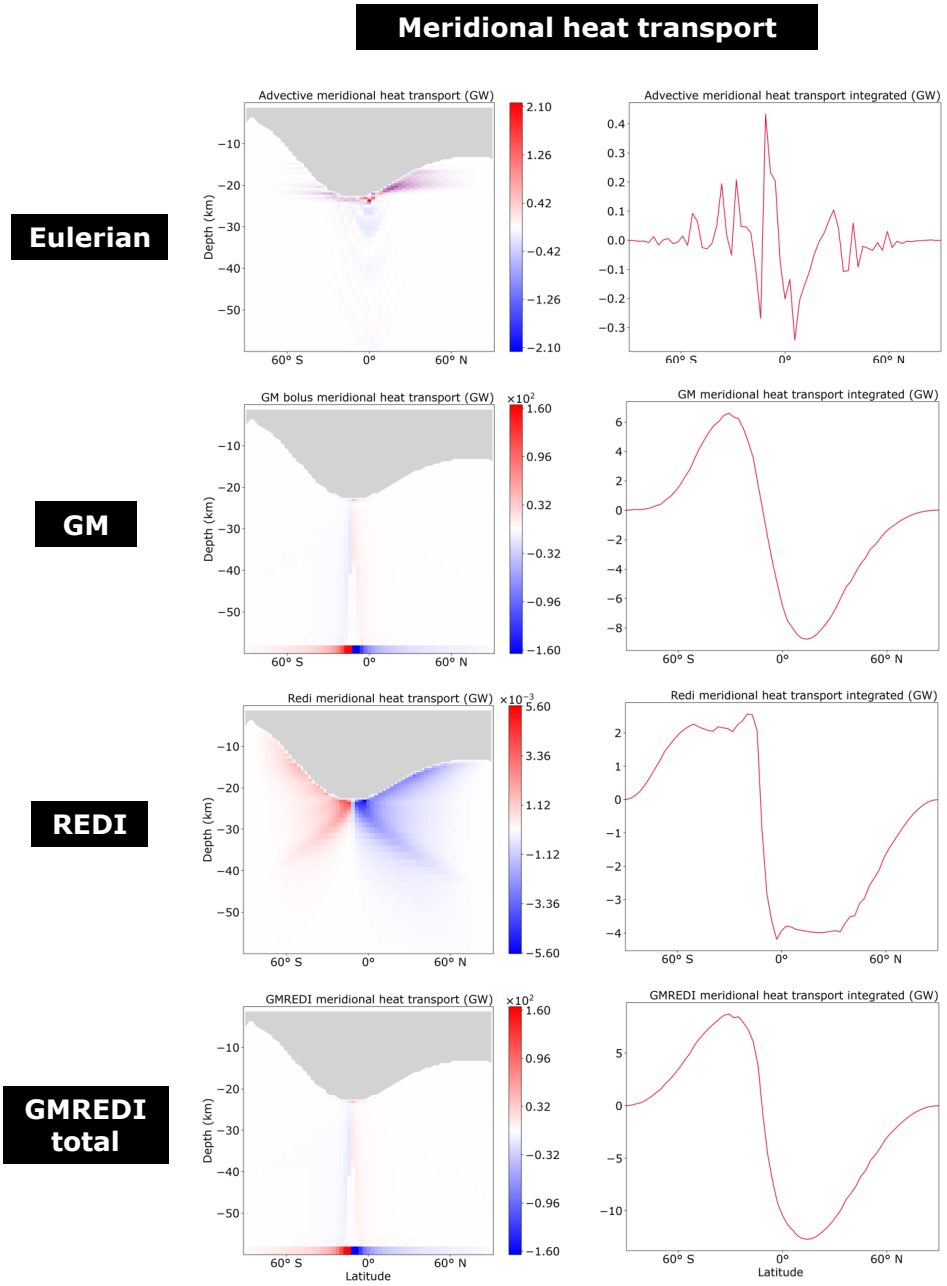

Figure 2.8: Meridional heat transport (GW), in-situ (left) and vertically integrated (right), showing contributions from different model components. Top shows contributions from the resolved Eulerian (advective) flow, the following rows then show contributions from the GM and Redi components of the GMREDI eddy parameterisation scheme, followed by their sum. Note that the reversal in sign of GM heat transport above the bottom boundary layer ensures that the magnitude of its vertical integral is comparable to that of the Redi component.

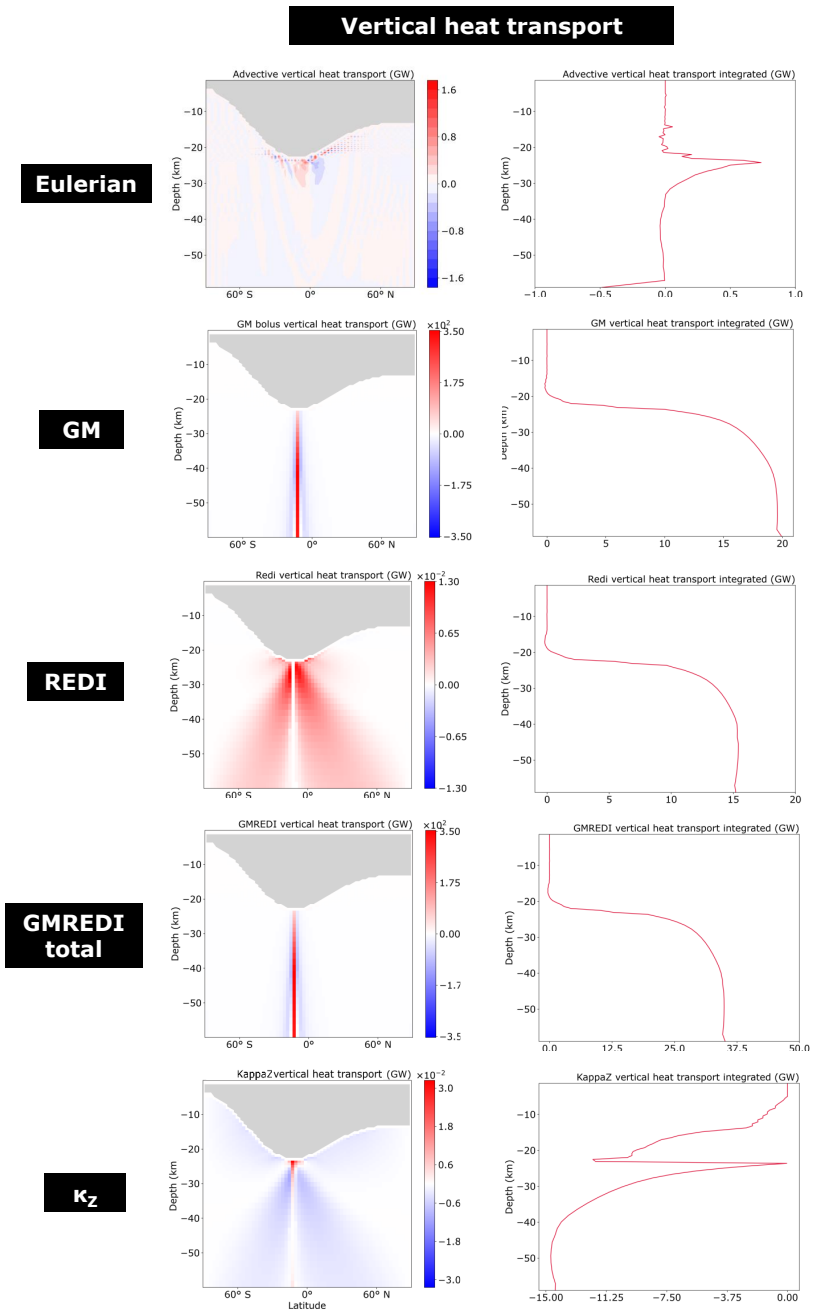

Figure 2.9: Vertical heat transport (GW), in-situ (left) and meridionally integrated (right), showing contributions from different model components. Top shows contributions from the resolved Eulerian (advective) flow, the following rows then show contributions from the GM and Redi components of the GMREDI eddy parameterisation scheme, followed by their sum, and finally contributions from the effective vertical diffusivity κ_z.

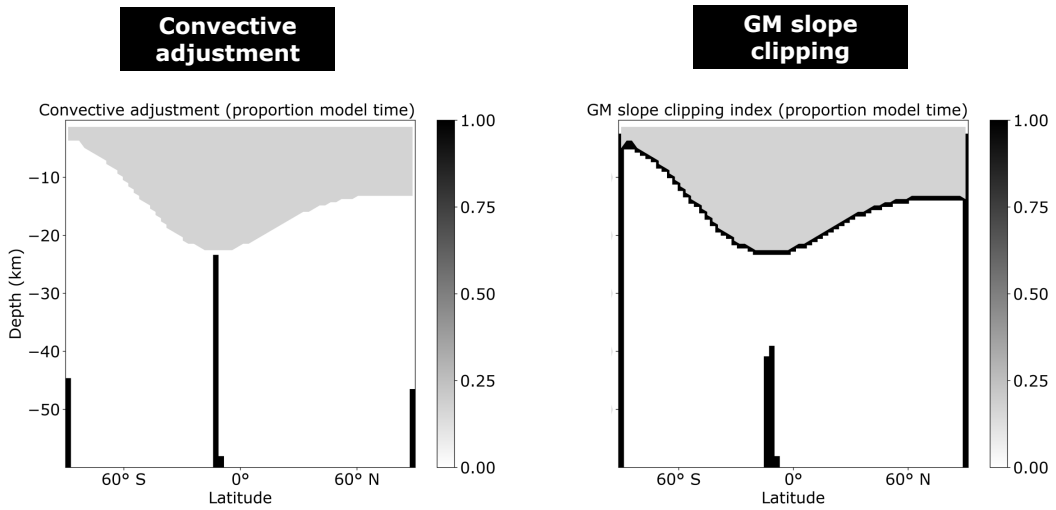

Figure 2.10: Left: Proportion of model time that the models' convective adjustment scheme is turned on. This happens where the ocean is unstratified. Right: Proportion of model time that slope clipping is applied to the GM component of the eddy parameterisation scheme. This arises where the isopycnal (density contour) slope exceeds the prescribed maximum slope clipping threshold of 2.

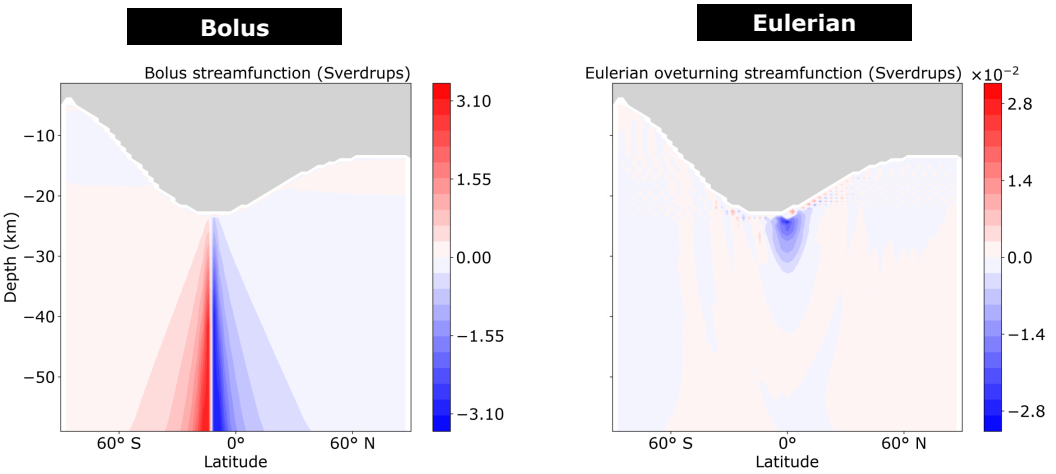

Figure 2.11: The meridional overturning streamfunction (Sverdrups) indicating mass transport in the reference solution, decomposed into contributions from the GM component of the eddy parameterisation scheme (left) along with contributions from the resolved advective flow (right). Note that all transports have been scaled up by factor 128 given the singular zonal strip configuration employed here, to obtain a global transport.

2.3.3 Ocean velocity solutions

Fig. 2.12 show the resolved meridional and vertical ocean velocities (m s^{-1}). Meridional velocities of magnitude 10^{-5} m s^{-1} are obtained. This is orders of magnitude weaker than observed near Earth's ocean surface, expected owing largely to the absence of winds, and thus reduced energy available to drive the flow. It is at least an order of magnitude weaker than that expected given energetic constraints (Jansen et al. 2023). Explanations may include the viscosity employed for numerical stability, as well as the zonal-average nature of the reference configuration.

To visualise patterns of ocean velocity away from the ocean upper boundary, fig. 2.12 also shows these with the colourbar saturated at the 95th percentile. In doing so, two features become apparent. Firstly, grid scale noise in ocean velocities manifests in stratified regions of ocean above the ice base (the source of this noise is explored further in section 2.4). Secondly, arc-like structures in the ocean velocity fields become apparent in neutrally stratified regions of ocean at depth. These arc-like features align with the axis of rotation (fig. 2.13) and are a manifestation of Taylor-Proudman theorem:

$$(\vec{\zeta}.\nabla)\mathbf{v} = 0 \tag{2.22}$$

where $\vec{\zeta} = 2\vec{\Omega}$ is the absolute vorticity vector and $\vec{\Omega} = \Omega(\cos(\phi)\,\mathbf{j} + \sin(\phi)\,\mathbf{k})$ the planetary vorticity vector.

Eq. (2.22) describes a regime where ocean velocity cannot vary parallel to the vorticity axis (which on rotating planetary bodies, is the axis of the bodys' rotation), resulting in column-like structures of 'stiffened' velocity parallel to the rotation axis, known as Taylor columns (Vallis 2017). Taylor-Proudman theorem is expected to hold in weakly (or unstably) stratified fluids, where the square root of the Brunt-Vaisala frequency N is much smaller than the rotation frequency (measured by the Coriolis parameter f). In simulations here, $f \approx 10^{-4}$ s^{-1}. $N \approx 10^{-5}$ s^{-1} in stratified regions nearer the interface, and tends to zero in neutrally stratified regions at depth. The requirements for Taylor Proudman theorem are better satisfied at depth than near the ice interface, which may partially explain the differences in flow alignment in these regions (see fig. 2.13).

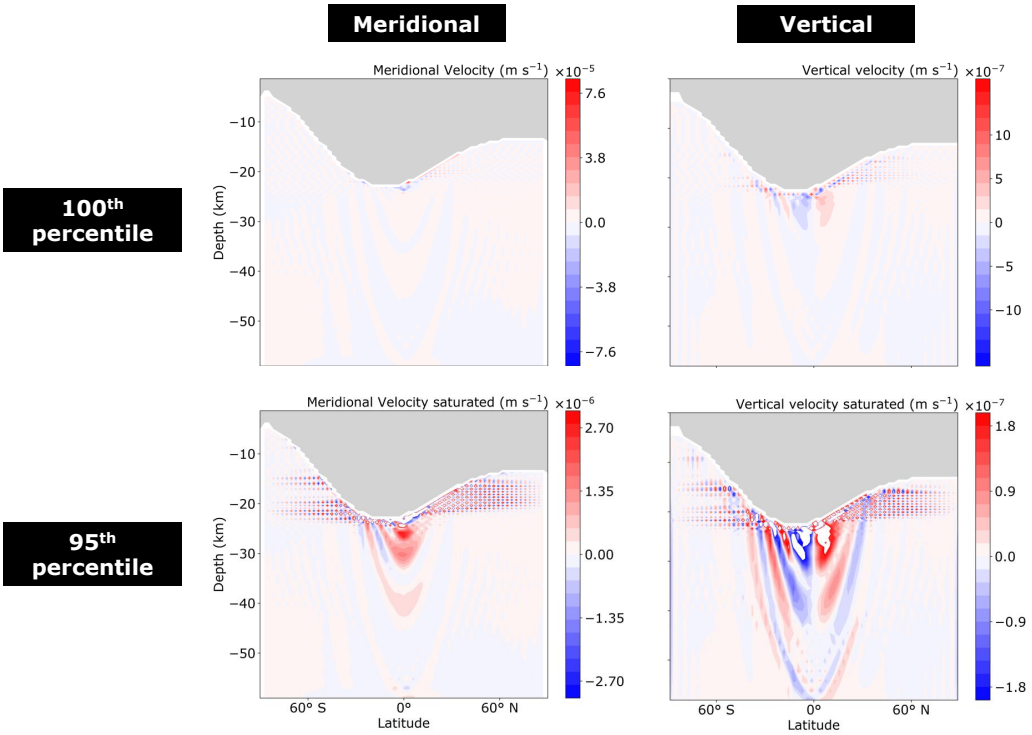

Figure 2.12: Meridional (left) vertical (right) ocean flow velocity (m s^{-1}) in the reference solution. Top and bottom rows show colourbars saturated at the 100th and 95th percentile respectively, the latter to visualise patterns of ocean flow features away from the upper boundary.

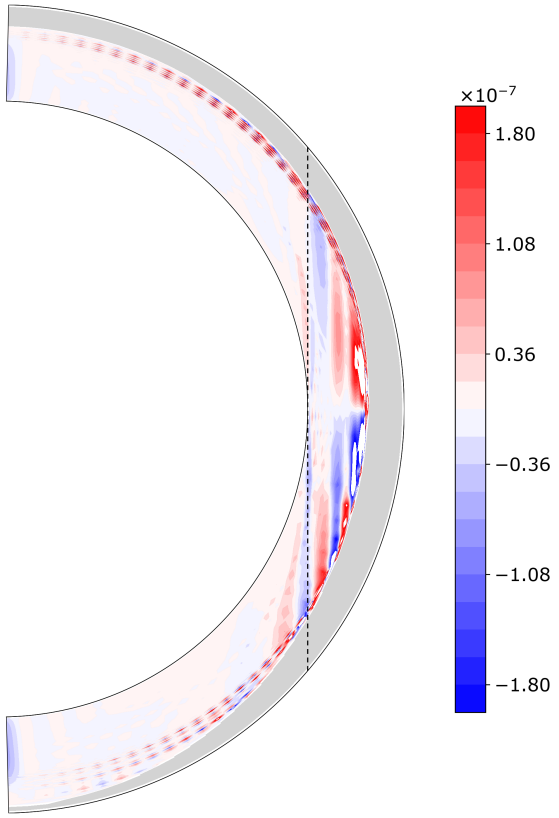

Figure 2.13: Vertical ocean velocity (m s^{-1}), with the colourbar saturated at the 95th percentile. Black dotted line denotes the tangent cylinder (a cylinder parallel to the axis of rotation, intersecting the ocean bottom at the equator).

Fig. 2.14 shows tendencies in the meridional ocean flow (m s^{-2}) arising from pressure gradient ($\frac{1}{\rho_0 r}\frac{\partial \delta P}{\partial \phi}$), Coriolis ($2\Omega u \sin\phi$), metric ($\frac{u^2 \tan\phi}{r} - \frac{vw}{r}$), and dissipation ($F_v$) terms in Eq. (2.2). Also shown is the tendency induced by the Adams-Bashforth time-stepping scheme.

Pressure gradient and Coriolis terms dominate the meridional momentum budget, suggestive of geostrophic balance (i.e., $\frac{1}{\rho_0 r}\frac{\partial \delta P}{\partial \phi} \approx -2\Omega u \sin\phi$). Contributions from dissipation terms are two orders of magnitude weaker. Weaker still are contributions from metric terms, suggesting these are of lesser importance in accurately resolving the dynamics, as well as tendencies arising from the use of stabilising weights in the Adams-Bashforth time stepping scheme, suggesting this numerical implementation does not significantly influence the flow field.

The zonal flows appear to follow from the meridional flow right at the upper boundary, which converges to the latitude of ice thickness maxima, slightly southwards of the equator

(fig. 2.12, top left). Overall, this ensures a predominantly equatorwards meridional flow here. Under the action of the Coriolis force, an equatorwards flow is deflected westwards to conserve angular momentum, in accordance with Eq. (2.1) ($\frac{\partial u}{\partial t} \sim 2\Omega v \sin\phi$). The meridional flow at the upper boundary is polewards only in the narrow band separating the ice thickness maxima and the equator. Under the action of the Coriolis force, this polewards flow is deflected eastwards.

The gradient of zonal flow with depth appears to follow thermal wind balance, which follows from geostrophic and hydrostatic balance (Bire et al. 2022; Zeng and Jansen 2024):

$$2\Omega \sin(\phi)\frac{\partial u}{\partial r} + \frac{2\Omega \cos(\phi)}{r}\frac{\partial u}{\partial \phi} = \frac{g}{\rho_0 r}\frac{\partial \rho}{\partial \phi} \tag{2.23}$$

Note the $\frac{2\Omega \cos(\phi)}{r}\frac{\partial u}{\partial \phi}$ term in Eq. (2.23) is not typically considered in Earth oceanography. This term is non-negligible in the reference solutions here, but of second order (fig. 2.15).

Density is largest at the latitude of maximum freezing near the equator. In the southern hemisphere this yields a predominantly positive $\frac{g}{\rho_0 r}\frac{\partial \rho}{\partial \phi}$ (RHS term in Eq. (2.23)). Where this is the case and assuming the $2\Omega \sin(\phi)\frac{\partial u}{\partial r}$ term dominates the left hand side of Eq. (2.23), an eastward tendency of the flow with depth (remembering r is positive upwards) ensues, strongest further equatorward. In the narrow region separating the equator and latitude of maximum ice thickness, the meridional density gradient reverses. Accordingly, the flow instead tends westward with depth in this region.

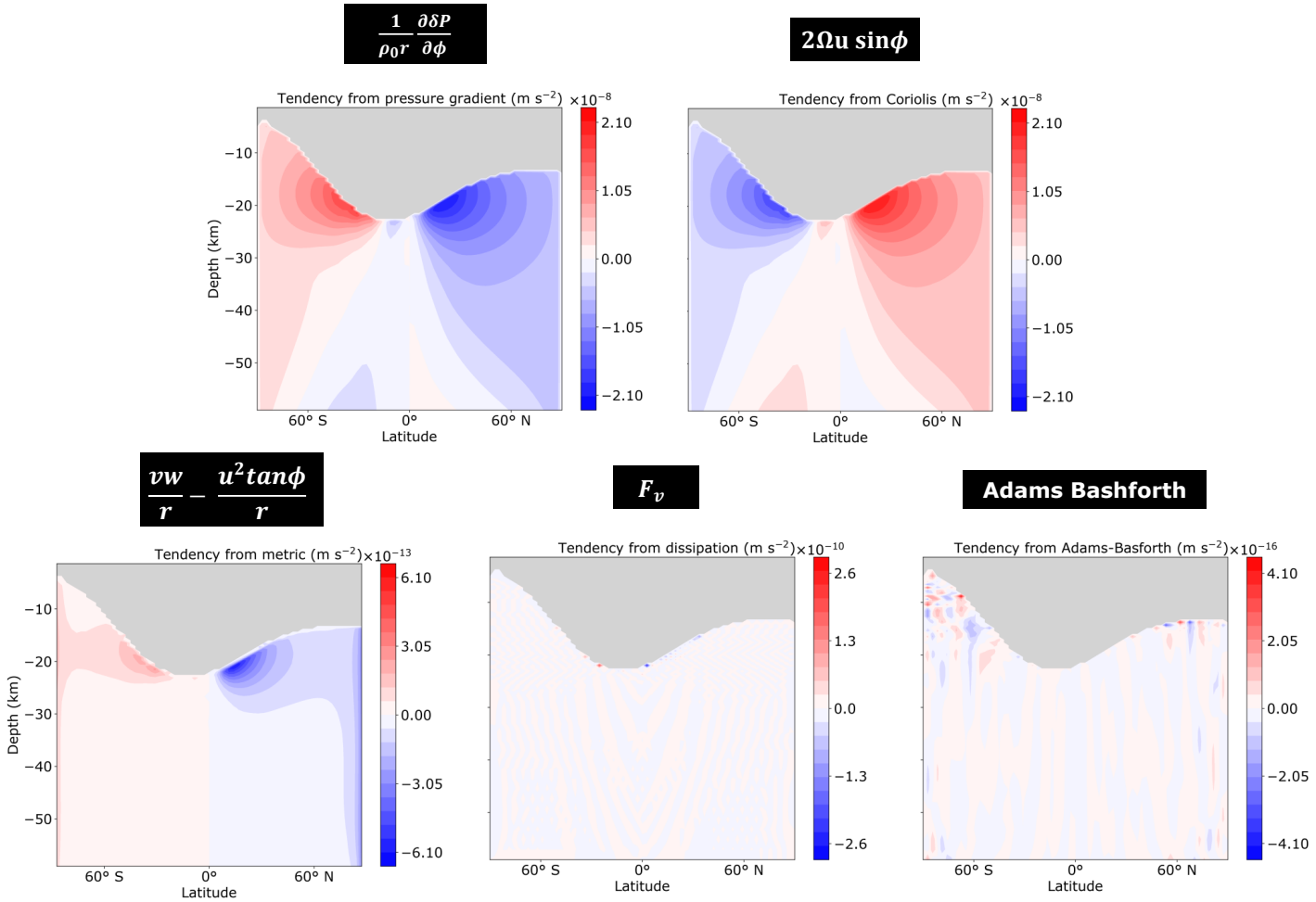

Figure 2.14: Tendencies in the meridional ocean velocity (m s^{-1}) s^{-1}) arising from the pressure gradient term (top left), Coriolis terms (top right), metric terms (bottom left), dissipation terms (bottom middle) and Adams-Bashforth time stepping scheme (bottom right). Note the colourbars are saturated and vary throughout. These terms, excluding the Adams Bashforth contribution, are presented in Eq. (2.2) in section 2.2.1.

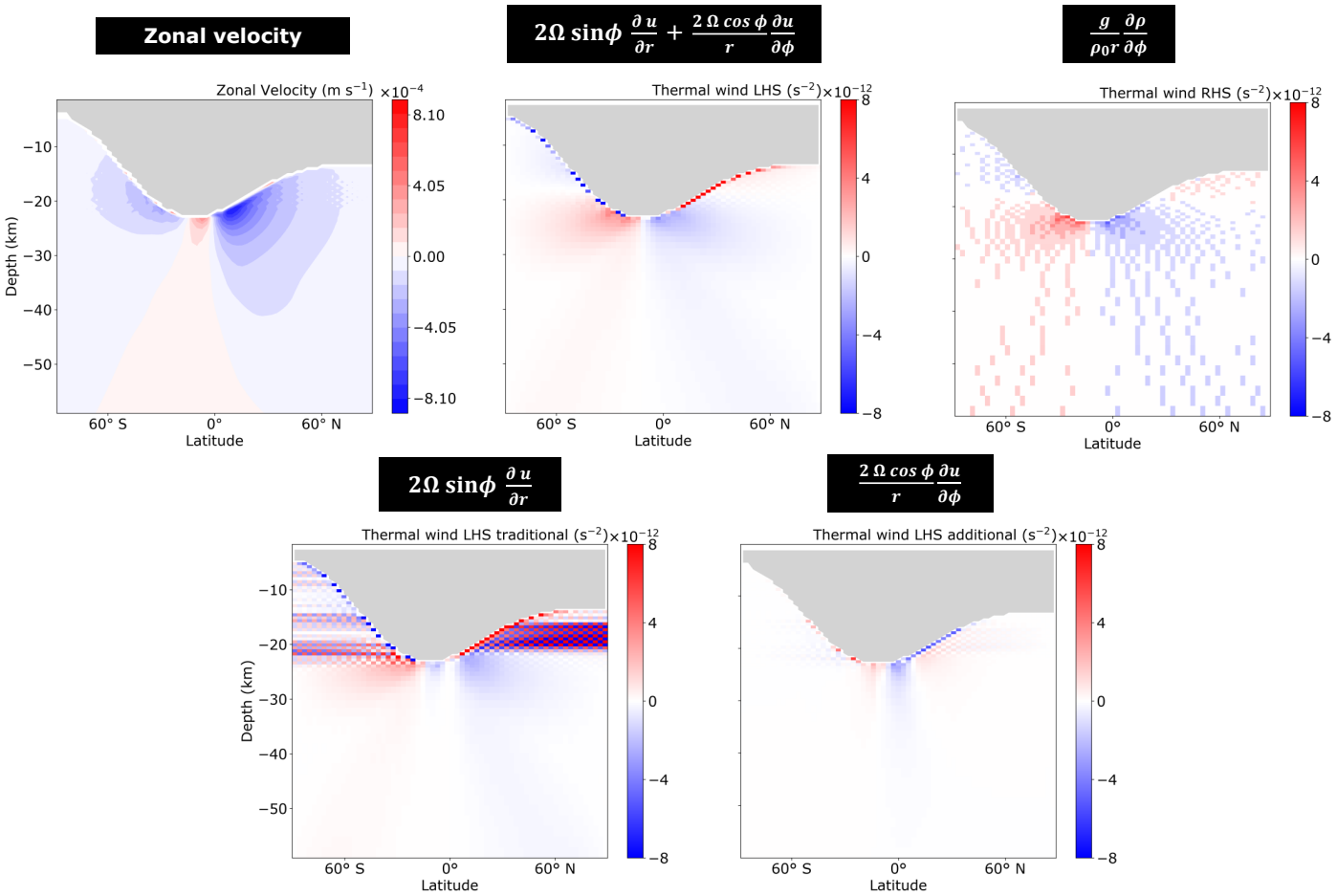

Figure 2.15: Showing the zonal velocity (m s^{-1}; top left), along with terms in the thermal wind balance equation (s^{-2}; Eq. (2.23)).

2.4 Sensitivity tests

In the following section, sensitivity tests are performed to clarify the impact of individual model components upon the solution. The tests are broadly categorised here into five groups: boundary forcings, the equation of state, parameterisation schemes, the equations of motion, and numerics. The test groups are ordered so that those with the largest impact upon the tracer solutions are presented first

2.4.1 Boundary forcings

Sensitivity to upper boundary forcings and its lateral variation

To clarify the influence of upper boundary forcings, fig. 2.16 compares the reference solution with simulations lacking a freshwater forcing (i.e., no melting and freezing and thus no salinity gradients in the solution), and a simulation additionally removing lateral variation in restoring temperature at the upper boundary. In the latter, temperature is restored uniformly at the ocean top to the reference temperature T_{ref} (table 2.1).

Where the ocean is cooled to a uniform temperature at the ocean top with no freshwater forcing, the ocean remains entirely unstratified (i.e., convecting). The tracer age distribution exhibits vertical columns, a product of the convective adjustment scheme that is quasi-permanently turned on across the whole ocean, fluxing tracers vertically. The transit time across the ocean owing to the diffusive adjustment convection parameterisation scheme can be estimated using the diffusive timescale $\tau = \frac{H^2}{2\kappa_z}$ where H is the assumed ocean depth (Ames et al. 2025). Letting $H = 40$ km and $\kappa_z = 1$ m^2 s^{-1} (section 2.2.5) yields $\tau \approx 10$ years. This is approximately twice as long as the numerical solution shown in fig. 2.16. The discrepancy may arise owing to the use of a full-slope Redi tensor (Eq. (2.20)). As isopycnal slopes tend to the vertical, Redi diffusion tends towards a vertical diffusivity, acting to reinforce κ_z in this case (see Eq 2.20). Given an eddy diffusivity 1 m^2 s^{-1} is employed here, Redi diffusion effectively acts to double the vertical diffusivity in unstratified regions of ocean and thus half the transit time.

Adding back lateral variation in the upper boundary restoring temperature changes the stratification and tracer regime (fig. 2.16, middle column). The ocean becomes stably stratified at both poles and neutrally (near-zero) stratified at depth and nearer the equator. This occurs despite the ocean still being cooled from above, for two reasons. Firstly, the

pressure dependence of freezing temperature (the temperature at the ocean top) means it co-varies with ice thickness, warmest where ice is thin, coolest where thick. At the ice interface, warmer, buoyant water is therefore always found above cooler water, acting to stratify the ocean above the ice base.

The second factor is that lateral variation in ocean temperature (which given the uniform ocean salinity in this test owing to a lack of freshwater forcing, controls density) can permit sloped isopycnals in the ocean interior so long as processes exist to flux surface waters here (i.e., non-zero κ_z as modelled here; Zhang, Kang and Marshall 2024). Sloped isopycnals result in activation of the GMREDI parameterisation scheme (mimicking the mixing effects of baroclinic eddies), which acts to flatten the isopycnals and stratify the ocean. This permits stable stratification beneath the ice base. Stably stratified waters are poorly mixed owing to the stifling of convection in these regions. A diffusive gradient in tracer age arises within. This is because vertical transport in this region is predominantly achieved via κ_z (Ames et al. 2025). The tracer age at the south polar ice-interface increases three orders of magnitude (relative to the uniform cooling case) to over 4000 years as a result.

Adding back ice shell freshwater fluxes increases the tracer age at the south polar ice-interface by only 300 years ($< 10\%$). This is despite the stratification magnitude increasing fivefold. The stratification magnitude is increased because the freshening of water higher up in the water column reinforces the stratifying effects of the restoring temperature. The stratification extent increases marginally as the freshwater anomalies are fluxed deeper into the ocean interior. The latter is the predominant factor explaining the larger tracer age. The vertical extent of stratification (rather than its magnitude), combined with the employed value κ_z, controls the bottom-to-top transit timescale therein, according to $\tau = \frac{H^2}{2\kappa_z}$.

Overall, the above tests highlight the importance of including expected lateral variation in upper boundary forcings for any attempt to resolve the transport of tracers (including heat, salt, and other particulates and chemical species) to the ice shell. In the steady-state model here, this also entails an accurate representation of the ice shell thickness and flow.

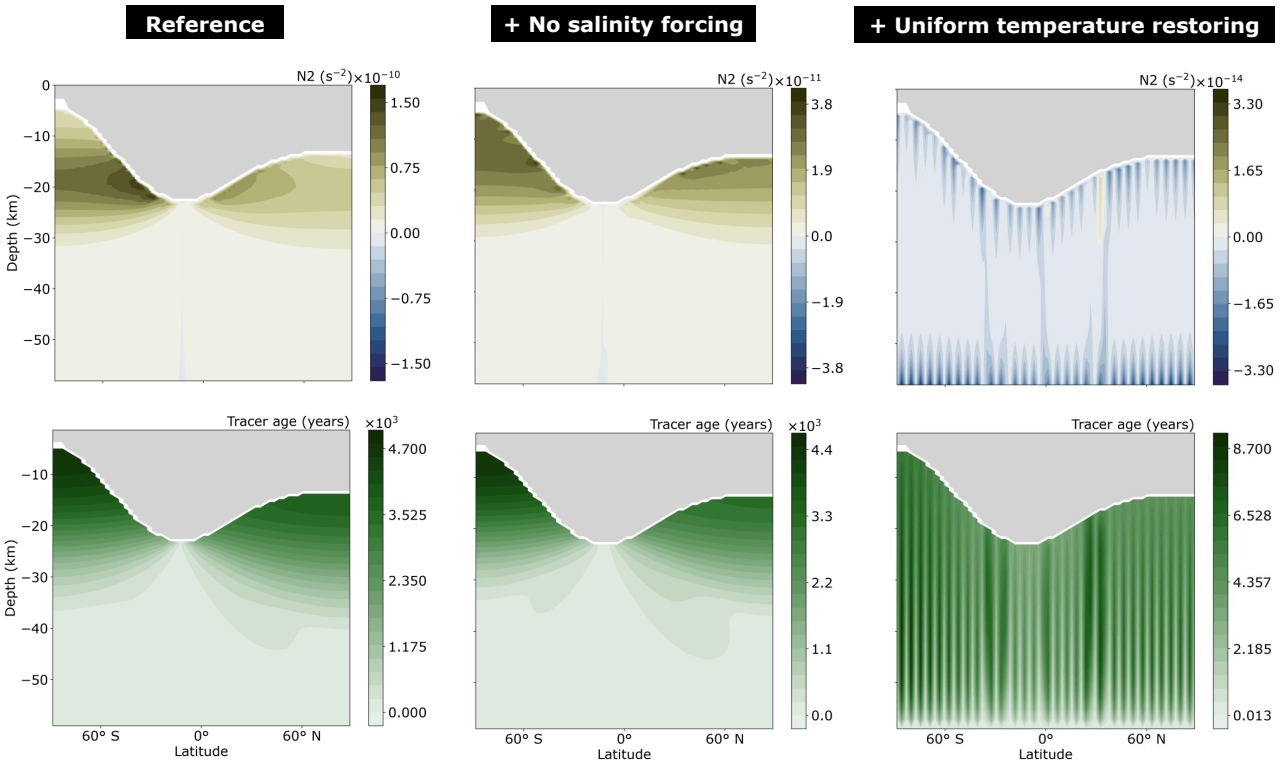

Figure 2.16: Top: The Brunt-Vaisala frequency N^2 (s^{-2}) indicating ocean stratification. Bottom: The tracer age (years) defined as the volume weighted time elapsed since water lost contact with the ocean bottom, providing a lower bound transit timescale from the ocean bottom to a position in space. Shown for the reference 2D solution (left), then with the upper boundary freshwater forcing omitted (centre), followed by a simulation additionally removing lateral variation in the restoring temperature applied at the upper boundary (right).

Sensitivity to bottom heating

Fig. 2.17 shows fields of temperature and salinity anomalies, stratification, and tracer age where heating at the ocean bottom is excluded. All other components of the configuration are maintained. Fig. 2.17 should be compared to fig. 2.5 which shows equivalent fields for the reference solution.

Near the ice shell, temperature and salinity anomalies are near identical to the reference solution. The warmest and freshest waters are found nearer the poles. Cooler temperatures are obtained at depth, albeit more homogeneous than the reference solution. Stable stratification dominates at the poles, weakening at depth as in the reference solution. However, the distribution and magnitude of tracer age is very different to the reference solution. Tracer age is poorly mixed across the domain, exhibiting a diffusive gradient from ocean bottom-to-top.

To explain this discrepancy, fig. 2.18 shows the potential density anomaly and isopycnal slopes beneath the base of the ice shell, for both the reference configuration and that excluding bottom heating.

In the solution with bottom heating excluded, isopycnals sourced from the ice interface do not intersect the ocean bottom at any latitude. While the ocean is destabilised from above via ice freezing, the parameterised eddies effectively redistribute equatorial salinity anomalies laterally (flattening the isopycnals) above $\sim$ 45 km depth. This contrasts the reference solution, where near-vertical isopycnals arise in regions of prescribed freezing, extending the full ocean depth. The disparity arises because bottom heating destabilises the ocean globally from below. Where an ocean is quasi-permanently destabilised from both above (e.g., ice freezing) and below, we find GM is unable to completely flatten the isopycnals (i.e., the ocean always quasi-permanently convects) and isopycnals tend towards being vertical where destabilisation of the water column is strongest (here occurring at the latitude of maximum freezing).

The disparity in tracer age arises because the parameterised eddies act to flux tracers *along* isopycnals in all solutions. This is achieved via the full-slope Redi tensor (tending to a vertical diffusion where the isopycnals are vertical). Where an isopycnal slope is steep, along-isopycnal transport is directed further upwards in the ocean (see Eq. (2.20)). Where isopycnals are flat at depth (the case with no bottom heating), along-isopycnal transport is not an efficient means to flux tracers vertically and vertical transport is dominated by κ_z, which in the modelled case is much less efficient in transporting tracers.

Overall, bottom heating shapes ocean stratification at depth by destabilising the ocean from below. Efforts to constrain Enceladus' stratification should therefore account for bottom heating effects.

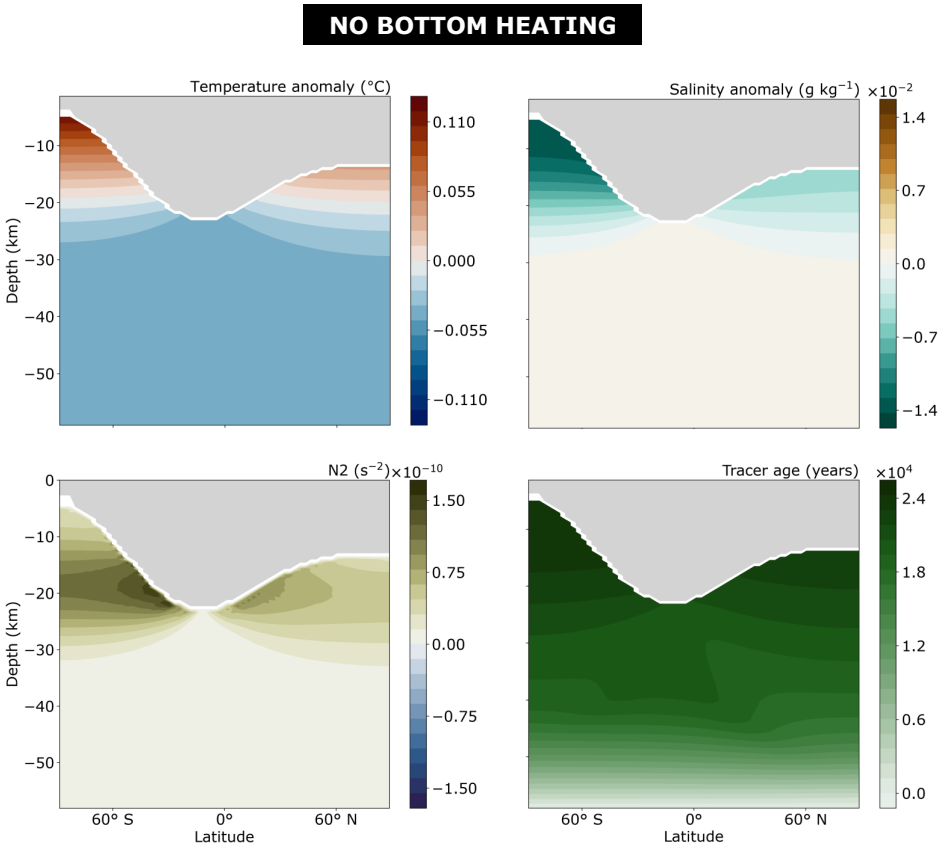

Figure 2.17: Solutions for a simulation excluding bottom heating, showing temperature (°C; top left) and salinity (g kg^{-1}; top right) anomalies about the reference temperature and salinity respectively. Bottom left shows the Brunt-Vaisala frequency N^2 (s^{-2}) indicating ocean stratification. Bottom right shows the tracer age (years) defined as the volume weighted time elapsed since water lost contact with the ocean bottom, providing a lower bound transit timescale from the ocean bottom to that position in space.

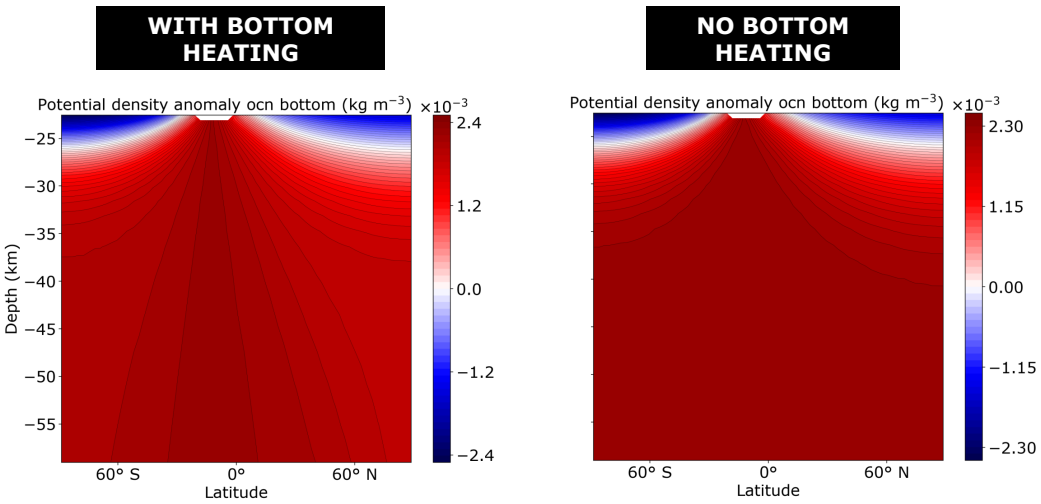

Figure 2.18: Potential density anomaly (kg m^{-3}) for the reference solution (left) and configuration with bottom heating removed (right), showing the ocean beneath the ice shell base (white region in upper middle of plot).

2.4.2 Non-linearity in the equation of state

To clarify the importance of accounting for non-linearities in the equation of state, tests are performed with a linear equation of state assuming a constant thermal expansion coefficient (α_T) of 3×10^{-5} K^{-1} and haline contraction coefficient (β_S) of 7.8×10^{-5} K^{-1} (Roquet et al. 2015b). Tests are performed at the default mean salinity of 35 g kg^{-1}, as well as a lower mean salinity of 20 g kg^{-1}. Fig. 2.19 shows solutions of tracer age (years).

When assuming mean salinity of 35 g kg^{-1}, employing a linear equation of state yields changes in tracer age no larger than 50 years ($\sim 1\%$) vs the reference solution. Given that the configuration here is not convection resolving, and that density is dominated by gradients in ocean salinity, accounting for the variation of α_T (approximately factor 2 in the reference simulation, with variation predominantly owing to pressure, indicated by flat contours; fig. 2.20), does not significantly affect the stratification extent. As a result, tracer age shows little change.

At 20 g kg^{-1} mean salinity however, the choice of equation of state is far more consequential. Employing a linear equation of state yields a tracer age regime similar to that at 35 g kg^{-1}, with larger age at the poles and lower ages nearer the equator. In contrast, a non-linear equation of state yields ages of order 3000 years across all latitudes above

$\sim$ 30 km depth, with an equatorial region no longer well-mixed near the ice interface.

The change arises because when using a non-linear equation of state, α_T changes sign at $\sim$ 30 km depth (fig. 2.20). In the presence of negative α_T, cooling from the overlying ice shell above, and warming from below, act to stably stratify the ocean nearer the ice interface at all latitudes. In chapter 3, it is shown that this behaviour is expected for an Enceladus ocean near freezing point with mean salinity lower than $\sim$ 20 g kg^{-1}. The phenomenon (referred to as inverse stratification), is explored in more detail there. Here, it is simply demonstrated that a linear equation of state is a poor approximation where the thermal expansion coefficient is expected to change sign in the ocean, with a large impact upon the tracer age. Otherwise, a linear equation of state is a reasonable approximation in the non-convection resolving configuration here, so long as an appropriate value of α_T is employed.

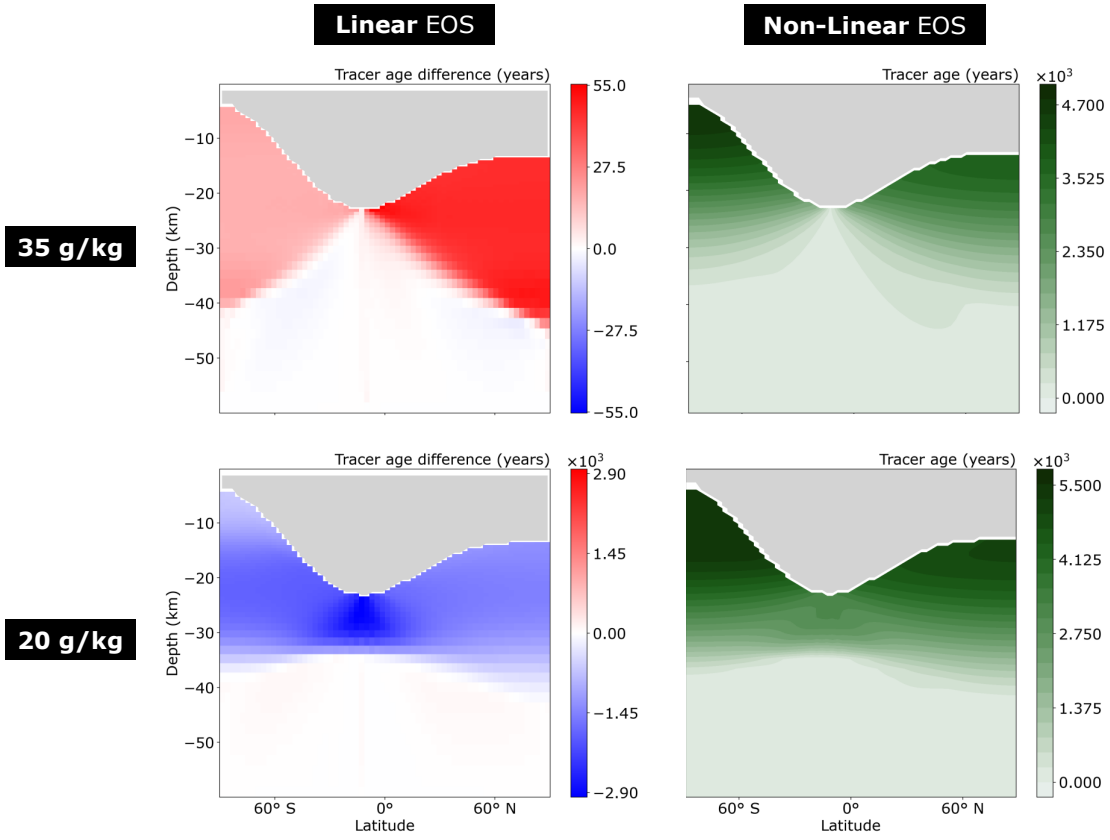

Figure 2.19: The tracer age (years; defined as the volume weighted time elapsed since water lost contact with the ocean bottom). Right: Solutions employing a non-linear equation of state at 35 g kg^{-1} (top; reference solution as illustrated in fig. 2.5) and 20 g kg^{-1} (bottom). Left: Solutions for simulations employing a linear equation of state (assuming a constant thermal expansion coefficient of 3×10^{-5} K^{-1}), showing the *difference* relative to solutions in the right hand panel. Note colourbars are saturated and vary throughout.

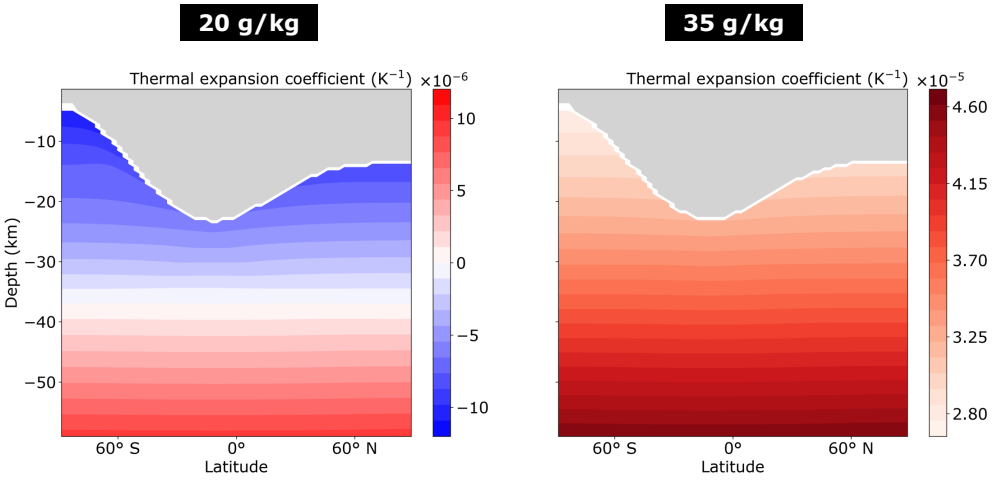

Figure 2.20: The thermal expansion coefficient ($°K^{-1}$ - quantifying the expansion of water with increasing temperature) shown for the reference solution at 35 g kg^{-1} (right) and a simulation performed at 20 g kg^{-1} (left) mean ocean salinity with a non-linear equation of state (Jackett and Mcdougall 1995). Note the colourbar scales are different between the plots.

2.4.3 Parameterisation schemes

Sensitivity to eddy parameterisation

An alternative approach to representing horizontal mixing by unresolved eddies is to employ an explicit horizontal diffusivity κ_h. The approach has been phased out of terrestrial ocean modelling because κ_h can flux tracers *across* isopycnals, violating a well-known property of ocean mesoscale eddies (Griffies 1998). Instead, a GMREDI combination is now standard, which fluxes tracers adiabatically along-isopycnals, except in regions where the isopycnal slope tends to infinity. Here the GM transport is either capped or tapered to zero, the ocean is allowed to become unstably stratified, and across-isopycnal fluxes are introduced as a result. Such regions of unstable or neutral stratification are transient and localised on Earth, but it is plausible that they are far more extensive in ice-covered oceans, which may be quasi-permanently destabilised from both top and bottom. It is, in turn, therefore plausible that assumptions underpinning GMREDI are violated over large regions of icy moon oceans. All previous GCM simulations have instead opted for κ_h as a crude approximation to horizontal mixing realised by eddies (e.g., Ashkenazy and Tziperman 2021; Zeng and Jansen 2024).

Fig. 2.21 shows temperature and salinity anomalies, along with the stratification, convective adjustment index, and tracer age solutions, for a configuration with GMREDI replaced by a κ_h of 1 m^2 s^{-1}.

Overall, using κ_h broadly recovers the tracer fields of the reference solution (fig. 2.5). The magnitude of temperature and salinity anomalies at the ice-interface, as well as their penetration into the ocean interior, show little change. Tracer fields differ at depth, where contours are vertically aligned, in contrast to the reference case where they are sloped. The horizontal diffusivity, fluxing across isopycnals, is less effective at restratifying the water column here, and wider unstable stratification (as opposed to neutral stratification) results. Because of this, the convective adjustment scheme is turned on permanently below $\sim$ 40 km depth, extending from ocean bottom-to-top in regions of freezing at the equator (fig. 2.21).

Tracer age is slightly weaker at the south polar ice interface using an explicit horizontal diffusivity. A possible explanation is that κ_h fluxes salt *horizontally* from regions of freezing (nearer the equator) into the meltwater lens, in contrast to GMREDI that fluxes along the isopycnal slope. This effectively reduces the thickness of stratified ocean that tracers must traverse through via κ_z to get to the ice interface.

Velocity fields are of comparable magnitude when employing an explicit horizontal diffusivity (fig. 2.22). Above the ice base, grid-scale noise remains, suggesting that GMREDI itself is not the cause. At depth, flow features exhibit slightly improved alignment with the axis of rotation vs the reference case, suggesting the use of a GMREDI scheme inhibits this tendency somewhat. It is unclear which is the realistic behavior here.

Fig. 2.23 shows the vertically integrated meridional heat transport and meridionally integrated vertical heat transport. As in the reference solution, heat transport is dominated by the employed parameterisation schemes. Meridional advective heat transport is dominated by noise and does not exhibit a significant trend with latitude. The explicit horizontal diffusivity converges heat to the latitude of maximum heating, with peaks in the magnitude of transport approximately twice that of GMREDI in the reference configuration. Unlike GMREDI, meridional heat transport is not concentrated at the lower boundary, rather achieved near-uniformally with depth. As in the reference case, vertical

upwards heat transport is concentrated in a narrow latitudinal band beneath the latitude of maximum freezing. This is despite the ocean convecting at all latitudes at depth (fig. 2.21).

Overall, employing an explicit horizontal diffusivity recovers the qualitative features of a solution employing GMREDI. Despite this, we prefer GMREDI because it is well tested and physically robust in stratified regions of oceans, expected to be present near the ice shell. Meanwhile, it is unclear if either κ_h or GMREDI are appropriate for unstably- or neutrally- stratified regions at depth.

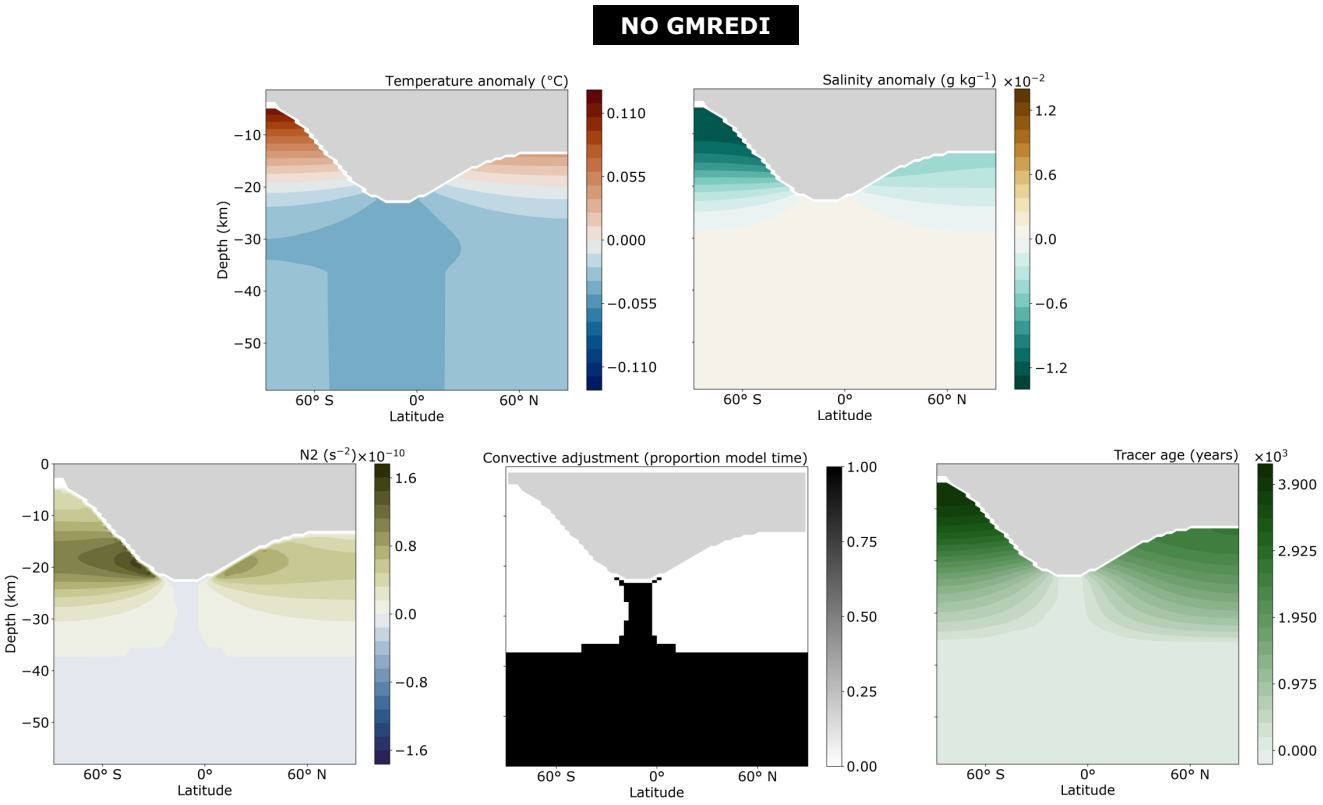

Figure 2.21: Solutions for a simulation employing an explicit horizontal diffusivity κ_h to parameterise mixing by eddies (rather than GMREDI, as used in the reference configuration), showing temperature (°C; top left) and salinity (g kg^{-1}; top middle) anomalies about the reference temperature and salinity respectively. Bottom left shows the Brunt-Vaisala frequency (s^{-2}) indicating stratification. Bottom middle shows the proportion of model time where the convective adjustment scheme is activated, occurring where the ocean is unstratified. Bottom right shows the tracer age (years) defined as the volume weighted time elapsed since water lost contact with the ocean bottom, providing a lower bound transit timescale from the ocean bottom to a position in space.

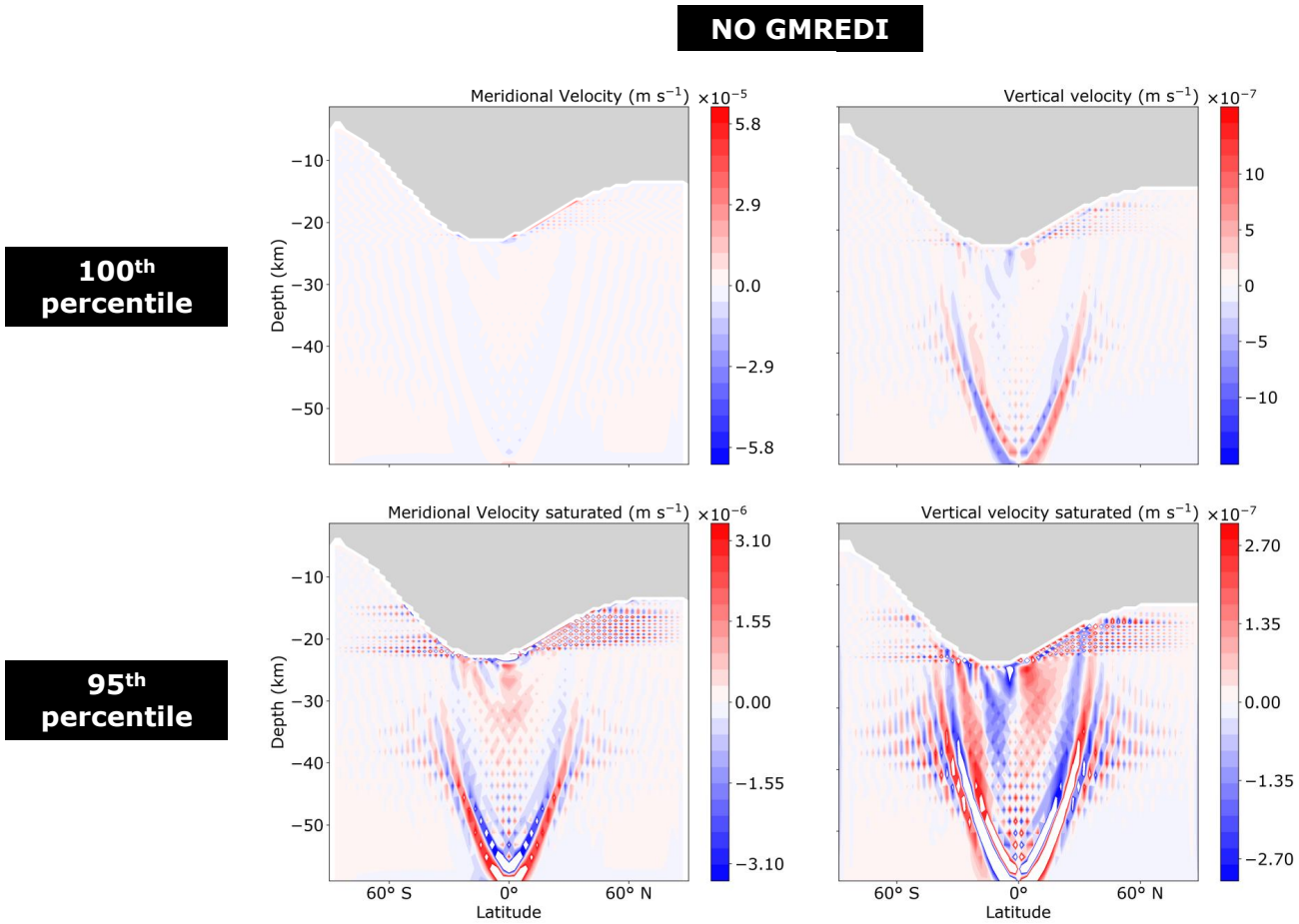

Figure 2.22: Meridional (left) and vertical (right) velocity (m s^{-1}) solutions for a simulation employing an explicit horizontal diffusivity κ_h to parameterise eddy mixing (rather than GMREDI, as used in the reference configuration). Bottom shows the same fields, but with the colourbar saturated at the 95th percentile (rather than the 100th percentile) to visualise weaker flow features away from the boundaries.

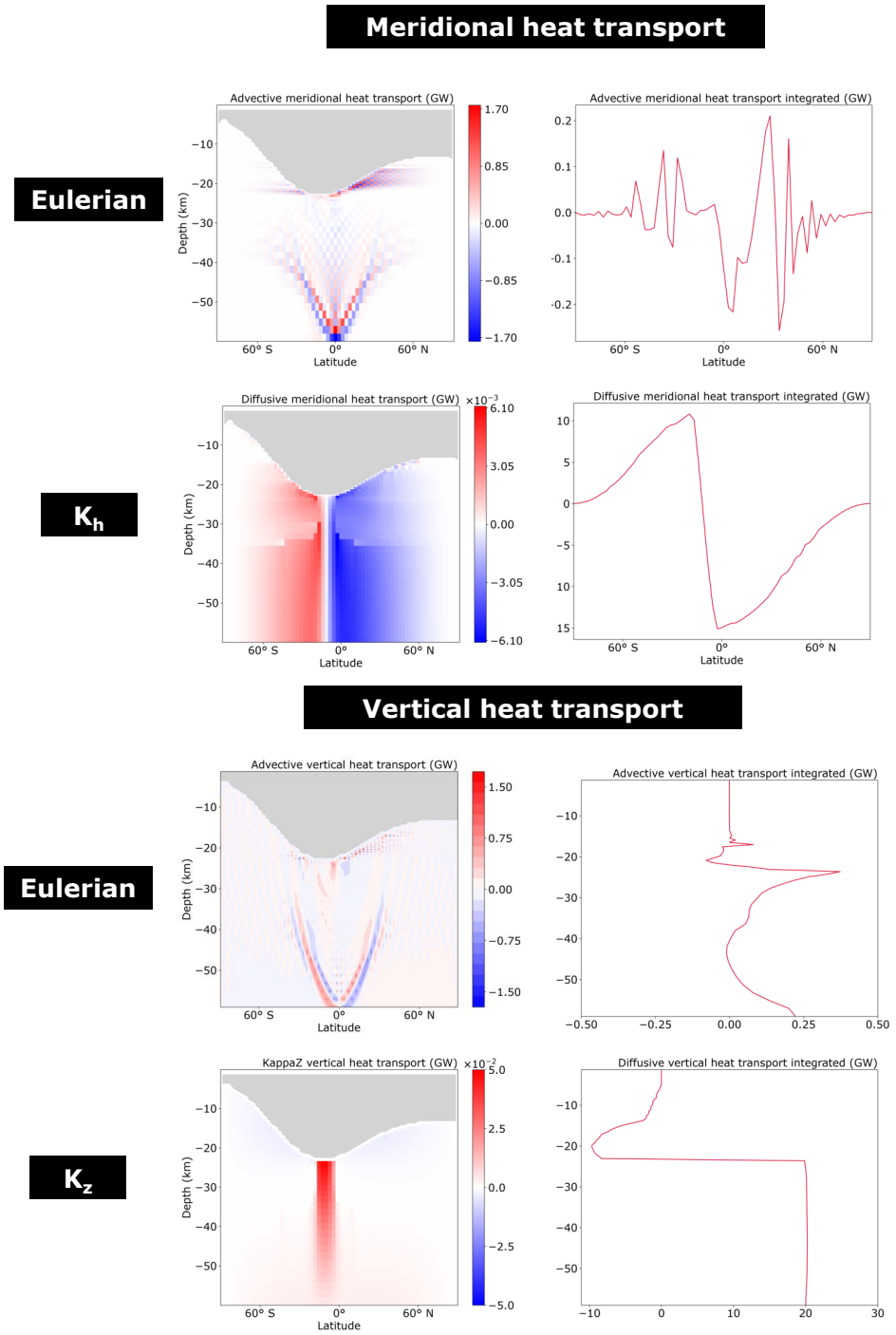

Figure 2.23: Heat transport (GW) for a simulation employing an explicit horizontal diffusivity κ_h to parameterise eddy mixing (rather than GMREDI as done in the reference configuration). Top quadrant shows meridional heat transport (left in-situ and right vertically integrated) achieved by advective flow (top) and the explicit horizontal diffusivity (bottom). Bottom quadrant shows vertical heat transport achieved by the advective flow (top) and κ_z (bottom). Note the latter includes contributions from the background κ_z as well as the convective adjustment scheme.

Sensitivity to convection parameterisation

Fig. 2.24 illustrates solutions of temperature and salinity anomalies, along with stratification and tracer age for a simulation excluding the convective adjustment parameterisation scheme. Note that an explicit horizontal diffusivity κ_h is employed in this sensitivity test, rather than GMREDI as used in the reference solution. As mentioned in section 2.3.1 a full slope GMREDI acts to 'take over' from the convective adjustment scheme in neutrally stratified regions of ocean and a near identical solution is obtained in this case when the convective adjustment scheme turned off. Solutions in this test should therefore be compared to solutions in figures 2.21, 2.22, and 2.23.

Omitting the convective adjustment scheme has little effect upon fields of temperature, salinity, and stratification near the polar ice interface, which are near identical to the reference solution. This highlights how, in stably stratified regions, it is the interplay of the parameterised eddies and κ_z that control transport within these lenses, and their vertical penetration into the ocean interior (Zhang, Kang and Marshall 2024).

The ocean is unstratified beneath $\sim$ 30 km, similar to solutions in fig. 2.21. Despite this, gradients of tracer age with height are similar to those in stratified regions above the ice base, suggesting the ocean is poorly-mixed. In the absence of a convection parameterisation scheme, vertical tracer transport can only be achieved through resolved (vertical) ocean flows and κ_z. Here, these appear to be less efficient transporting heat upwards than the parameterisation schemes employed in the reference configuration. It is important to note that the coarse resolution of the simulation means that convection is very unlikely fully resolved in this test. As consequence, heat and tracer transport are also unlikely being fully resolved.

Removing the convective adjustment scheme significantly changes the ocean flow field (fig. 2.25). The magnitude of zonal and meridional flows increases by one order, and vertical flows by two orders. Adherence to Taylor-Proudman theorem increases, especially outside of the tangent cylinder (defining a cylinder whose sides are tangential to the ocean bottom at the equator - denoted with black dotted line in fig. 2.25), where flows remain strongest. Here, Taylor columns form in the meridional and vertical velocity fields, thinner than those in the reference solution. Vertical velocities weaken at the equator beneath regions of ice freezing, possibly explaining why a stronger unstable stratification develops

beneath the equatorial ice base then elsewhere (fig. 2.25), lower left). The zonal velocity field also exhibits alignment with the axis of rotation, in contrast to the reference solution.

The stronger and more structured ocean flow enables a greater contribution to heat transport by the advective flow (fig. 2.26). In contrast to the reference solution, the advective flow appears to diverge heat away from the equator. This may arise because of the alignment of flow features with axis of rotation. As convection originating from the ocean bottom at the equator aligns with the axis of rotation, initially upwards heat transport will tend to the polewards direction, acting to flux heat and tracers polewards. Despite this effect, meridional heat transport is still dominated by the employed horizontal diffusivity, resulting in overall convergence of heat to the equatorial ice-interface.

Overall, omitting a convection parameterisation scheme likely leads to unrealistically weak mixing at depth yet characteristics of the advective flow, seemingly suppressed when using a scheme tuned for Earth, are allowed to emerge. Constraining the efficiency of convection in transporting heat upwards in Enceladus' ocean requires simulations that can resolve both convection and the eddies that convective plumes would interact with. In the absence of this, it is difficult to draw conclusions of the validity of parameterisation schemes tuned for Earth.

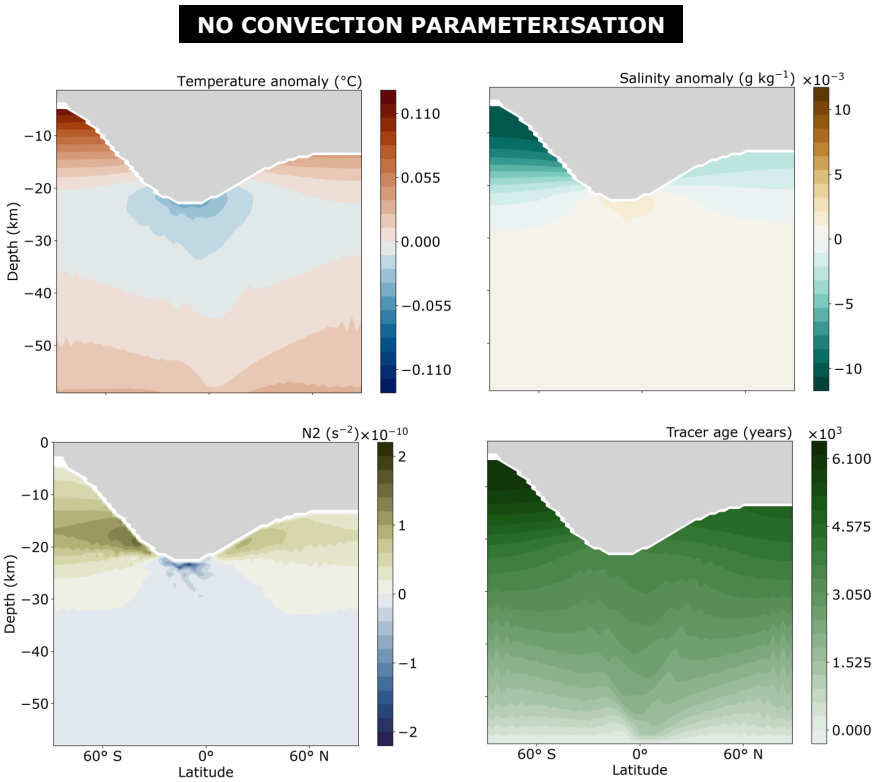

Figure 2.24: Solutions for a simulation with no parameterisation of convection, showing temperature (°C; top left) and salinity (g kg^{-1}; top right) anomalies about the reference temperature and salinity respectively. Bottom left shows the Brunt-Vaisala frequency (s^{-2}) indicating ocean stratification. Bottom right shows the tracer age (years) defined as the volume weighted time elapsed since water lost contact with the ocean bottom, providing a lower bound transit timescale from the ocean bottom to that position in space. Note that this configuration employs an explicit horizontal diffusivity to parameterise eddy mixing (rather than GMREDI as used in the reference configuration) and should therefore be compared to fig. 2.21.

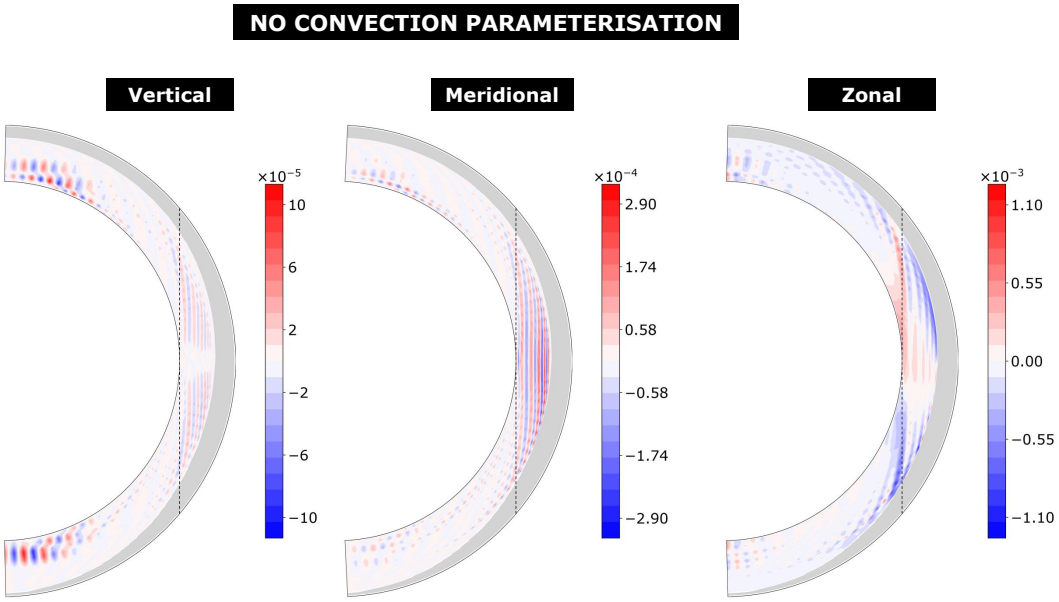

Figure 2.25: Solutions for a simulation with no parameterisation of convection, showing the resolved vertical (left), meridional (centre), and zonal (right) ocean velocity fields (m s^{-1}). Note that this configuration employs an explicit horizontal diffusivity to parameterise eddy mixing (rather than GMREDI as used in the reference configuration) and should therefore be compared to fig. 2.22.

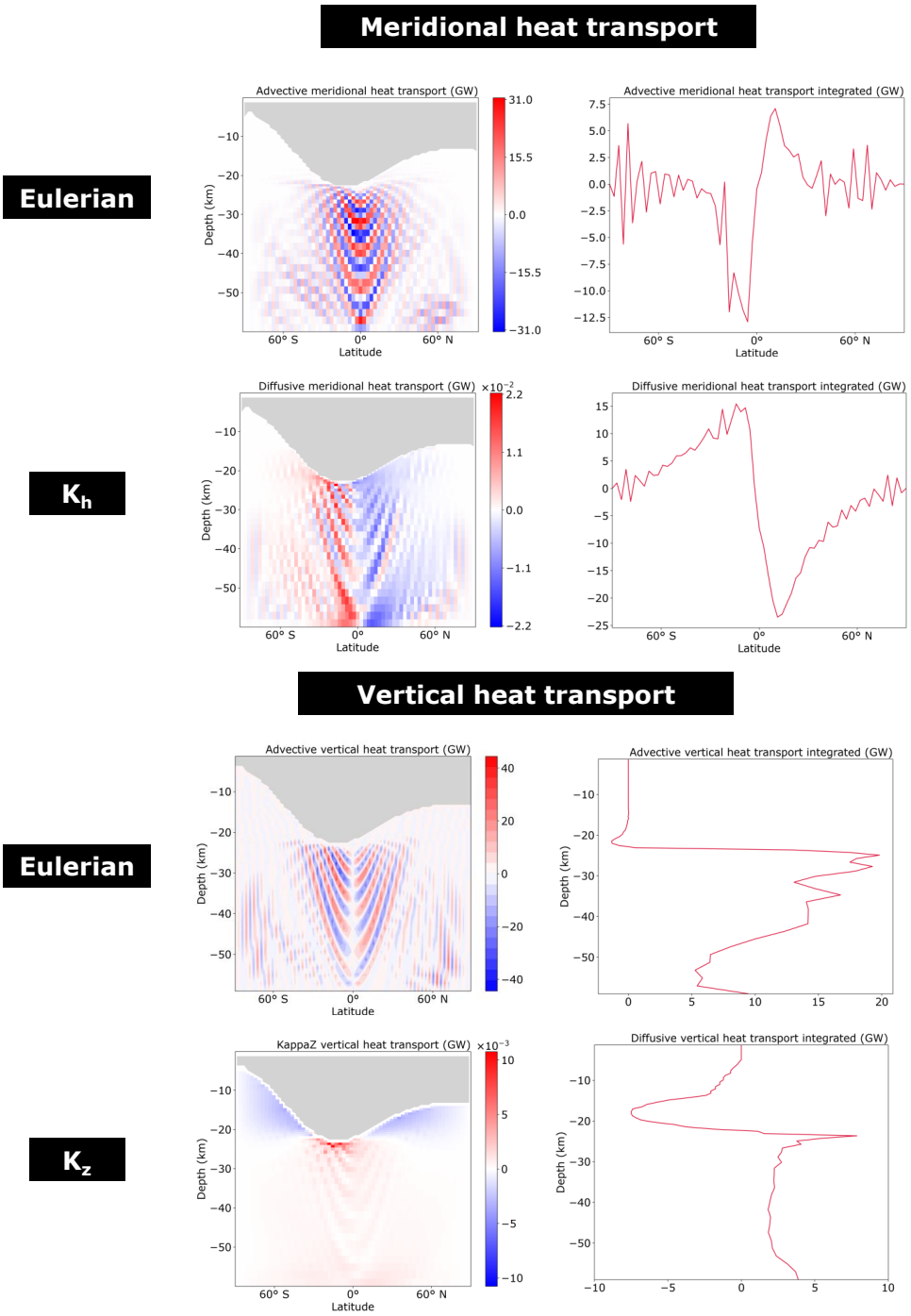

Figure 2.26: Solutions for a simulation with no parameterisation of convection, showing meridional and vertical heat transport (GW). Note that this configuration employs an explicit horizontal diffusivity (κ_h) to parameterise eddy mixing (rather than GMREDI as used in the reference configuration) and should therefore be compared to fig. 2.23. Top quadrant shows meridional heat transport (left in-situ and right vertically integrated) achieved by advective flow (top) and κ_h (bottom). Bottom quadrant shows vertical heat transport achieved by the advective flow (top) and the background vertical diffusivity κ_z (bottom).

2.4.4 Approximations in the equations of motion

As described in Marshall et al. (1997b), the MITgcm's quasi-hydrostatic mode simplifies the vertical momentum equation (Eq. (2.3)) by neglecting the vertical acceleration, advective, and dissipation terms therein. All other terms in the momentum equations are maintained, ensuring a full treatment of the Coriolis force, and complete angular momentum principle. The advantage of the MITgcm's quasi-hydrostatic (along with its hydrostatic) mode is that it allows sensitivities to these terms to be explored.

Fig. 2.27 illustrates three solutions: the full non-hydrostatic reference (as shown in figures 2.12 and 2.15), a simulation making a quasi-hydrostatic to the equations of motion (double underlined terms in Eqs. (2.1)-(2.3) neglected), and simulation employing the hydrostatic primitive equations (HPEs; all underlined terms in Eqs. (2.1)-(2.3) neglected). Note that colourbars in the meridional and vertical velocity fields are saturated at the 95th percentile to improve visibility of flow features away from the boundary.

Away from the ocean boundaries, employing the HPEs yields stronger flow features confined closer to the equator, while employing the quasi-hydrostatic approximation yields weaker flow features that tend to arc in the ocean interior, aligning with the axis of rotation. In both configurations, vertical velocity is not obtained prognostically via the momentum equations, but rather from the continuity equation (i.e., mass conservation), as a function of the zonal and meridional flow velocities (Eq. (2.4)). Therefore, it is the differences in zonal and meridional velocities (i.e., terms in Eqs. (2.1) and (2.2)) that must be associated with the discrepancies in the vertical ocean flows between these simulations. The negligible influence of metric terms (fig. 2.14) and use of a 2D model here, suggests that it is the inclusion the $2\Omega w\cos(\phi)$ term which permits arcing of flow features along the axis of rotation. This is perhaps because the inclusion of $2\Omega w\cos(\phi)$ enables a correct representation of the planetary vorticity vector, and where Taylor-Proudman theorem is expected to hold (Eq. (2.22)), features align with the axis of rotation rather than the radial direction, otherwise expected if this component of the planetary vorticity vector is omitted.

Moving from quasi-hydrostatic to full non-hydrostatic results in no significant change to the solution. This may be because the configuration here is not convection-resolving. Combined with the use of temporally constant boundary forcings, this results in vertical ocean flows that, at steady state, exhibit no significant change with time. It is plausible

that such terms could be significant in a convection-resolving model, although such a simulation is beyond the computational resources available for this work.

Overall, full treatment of the Coriolis force is found here to significantly influence the pattern of the Eulerian flow field, while solving prognostically for the vertical flow is found to be unnecessary in a steady state model with negligible time variation in the vertical flow. Given that making the quasi-hydrostatic approximation to the equations of motion yields a 2-3 times faster compute time, coarse-resolution models could use this as a means to save computational cost without sacrificing the integrity of the solution. Note that the changes in flow fields in fig. 2.27 do not result in significant changes to the tracer fields (not shown), because vertical transport is predominantly achieved via the eddy parameterisation scheme.

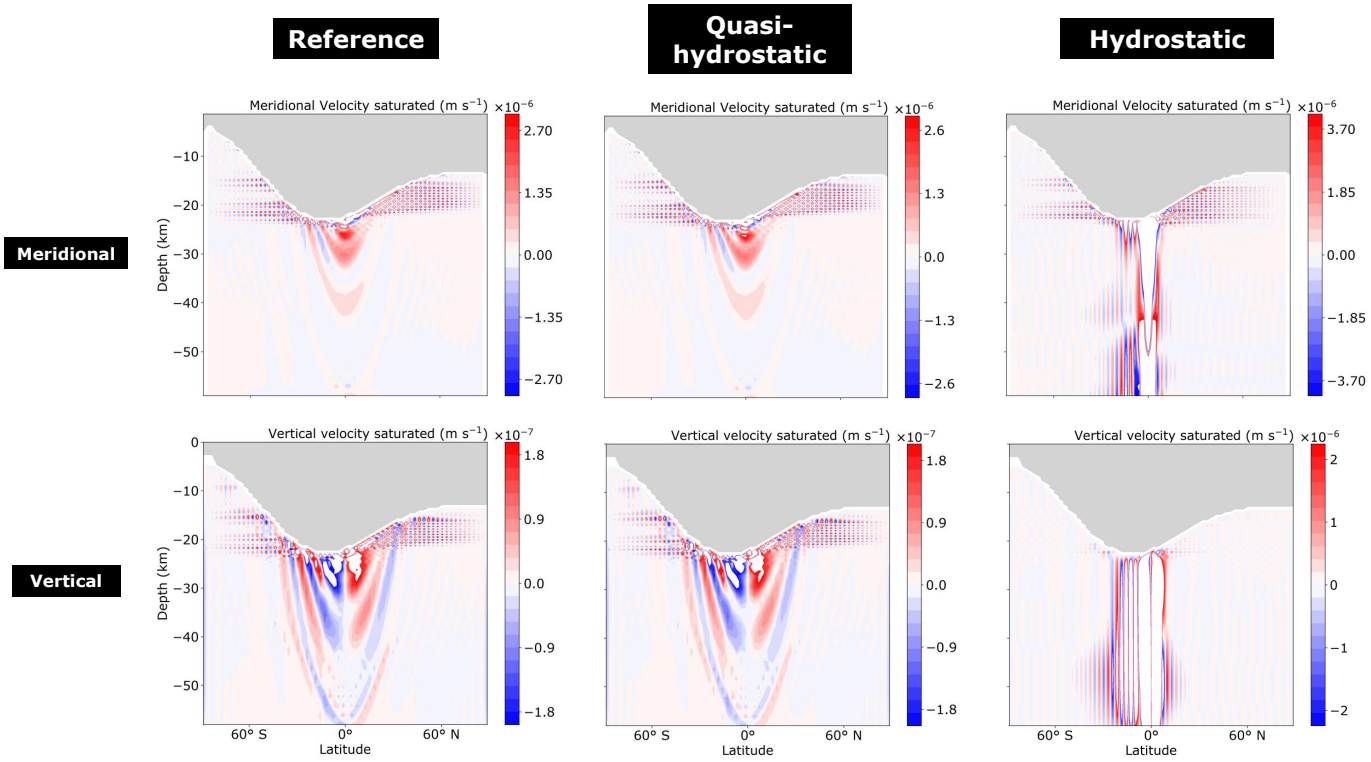

Figure 2.27: Meridional (top) and vertical (bottom), solutions for the reference simulation (left), and simulations employing a quasi-hydrostatic (centre) and hydrostatic (right) approximation to the equations of motion (Eqs. (2.1)-(2.3)). Note that colourbars are saturated at the 95th percentile, to improve visibility of weaker flow features away from the boundaries.

2.4.5 Numerics

Sensitivity to viscosity

A common approach to damping noise in numerical models is to employ a larger turbulent viscosity. Given the presence of noise near the ice interface in solutions here, tests are performed at vertical viscosities 10 and 5000 times larger than the reference case (yielding a vertical Prandtl number of 100 and 50000 respectively). The latter vertical viscosity is of comparable order of magnitude to that used in previous 2D simulations attempting to constrain advective heat transport in Enceladus' ocean (e.g., Kang et al. 2022a). Solutions of ocean velocity and Eulerian meridional overturning streamfunction are shown in fig. 2.28.

Little change in the solution arises when increasing vertical viscosity by factor 100. Grid-scale noise is maintained in the velocity field and the magnitude of the Eulerian streamfunction is near identical.

Increasing vertical viscosity by factor 5000 causes significant change in the solution. Grid scale noise in stratified regions begin to coalesce to form circulation cells, that converge towards the equator at the ice interface. Here, two overturning cells straddle the equator, rather than the singular cell as in the reference solution (fig. 2.28, bottom). The Eulerian overturning streamfunction is an order of magnitude larger here than in the reference case. At the ocean top, a boundary circulation develops in a direction opposing these circulation cells. This may arise because the Ekman layer depth ($H_{Ek} \approx \frac{2\nu}{|f|} \approx 1000$ m) becomes large enough to be resolved by the model.

It is unclear whether the viscosity-driven cells in tests here are realistic. The viscosity driven cells increase the advective contribution to meridional heat transport by approximately an order of magnitude (fig. 2.29), 'taking over' some heat transport from GMREDI. Given that viscosity exerts a non-negligible control upon ocean heat transport to the ice shell, studies aiming to constrain this should choose values of ocean viscosity with care.

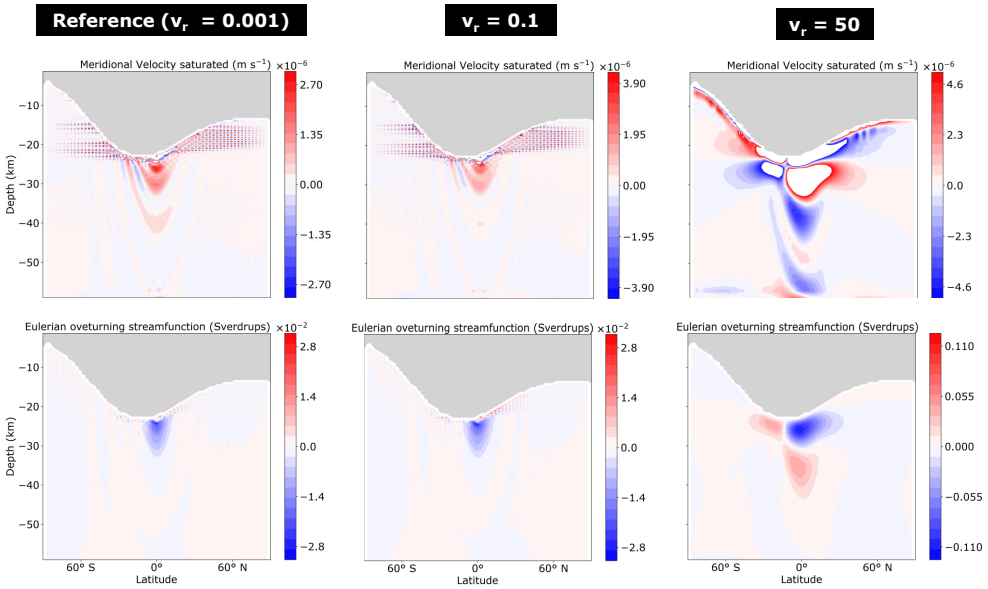

Figure 2.28: Meridional ocean velocity (m s^{-1}; top) and Eulerian overturning streamfunction (Sverdrups; bottom) for solutions at three vertical viscosities of 0.01 (as used in the reference simulation), 0.1, and 50 m^2 s^{-1}. Note the meridional velocity solutions have been saturated at the 95th percentile to improve visibility of weaker flow features away from the upper boundary.

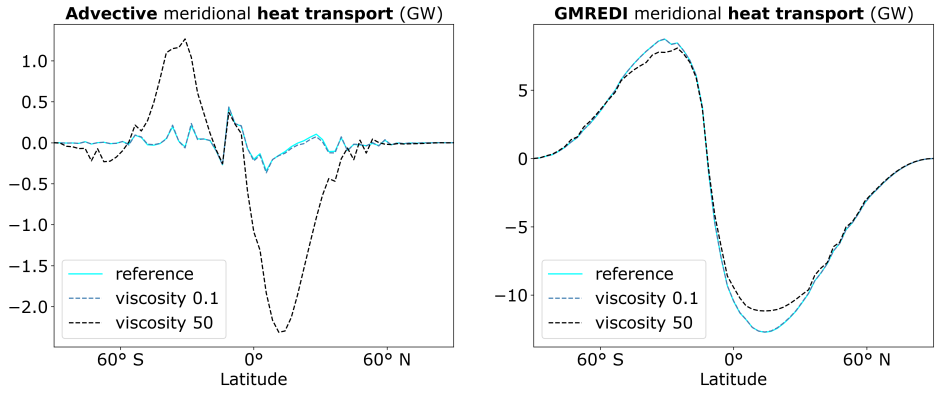

Figure 2.29: Vertically integrated meridional heat transport (GW) as a function of latitude, split into contributions from the advective flow (left) and GMREDI eddy parameterisation scheme (right). Here the effects of increasing viscosity relative to the reference value of 0.01 m^2 $^{-1}$ is tested, with differing vertical viscosity indicated by different colour lines. Note heat transport has been scaled up by factor 128 to obtain a global heat transport from the singular zonal strip model employed here.

Sensitivity to asynchronous time stepping

Fig. 2.30 shows solutions obtained using synchronous time-stepping, rather than asynchronous as done in the reference simulation (see section 2.2.6). To achieve this, the simulation is initialised using the equilibrated asynchronous solution, and then allowed to re-equilibrate. Shown are differences relative to the reference solution. Differences are typically at least ~ 3 orders of magnitude smaller than gradients obtained within the reference solution (see fig. 2.5 for comparison), suggesting the use of asynchronous timestepping has negligible influence upon the solution here. This is likely because the key assumption of the asynchronous approach - that temperature and salinity gradients control the ocean flows (Danabasoglu, McWilliams and Large 1996) - is well satisfied.

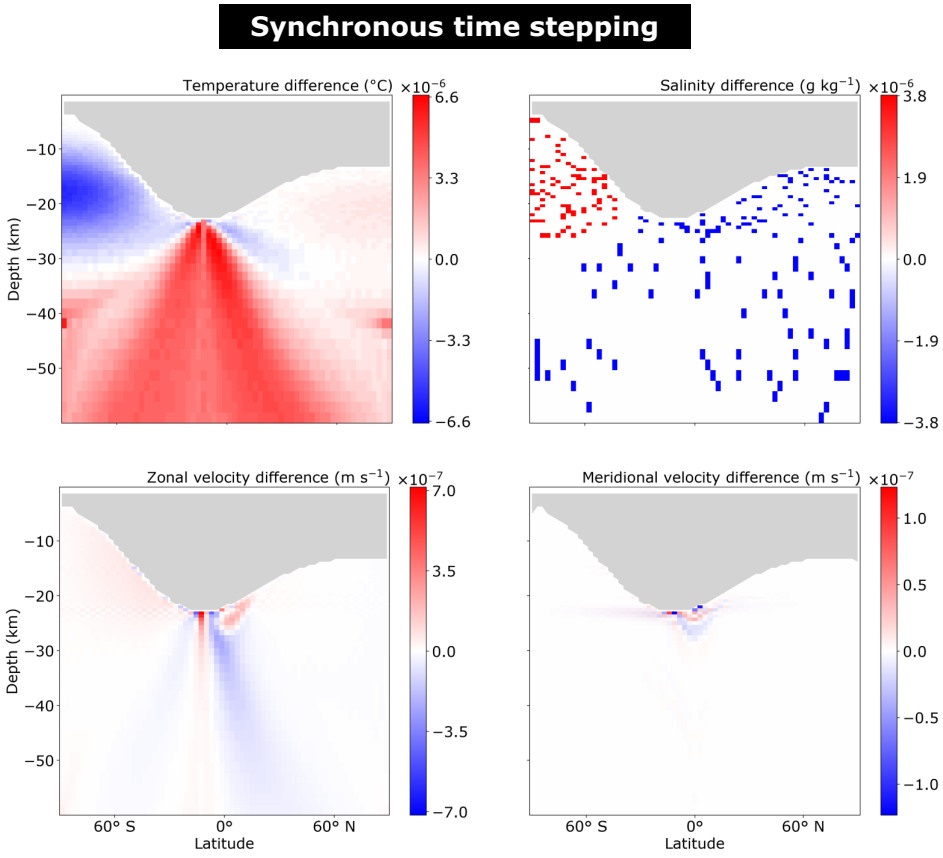

Figure 2.30: Showing anomaly of a simulation timestepped synchronously (i.e., with identical timesteps employed for momentum and tracer fields) relative to the reference solution which employs asynchronous timestepping (where tracer fields are stepped out first at a much larger timestep than momentum fields). Shown are anomalies of temperature (° C; top left) and salinity (g kg^{-1}; top right), along with zonal and meridional velocity fields (m s^{-1}; bottom left and right respectively)

Sensitivity to resolution

Fig. 2.31 shows tracer fields for a simulation with $\sim$ three times finer meridional resolution than the reference simulation. Tracer fields are nearly identical while grid scale noise in velocity solutions is reduced in stratified regions, enabling a more structured advective contribution to tracer transport (not shown). Yet, the continued dominance of GMREDI and κ_z in controlling tracer and heat transport means this has negligible effects upon the tracer solutions.

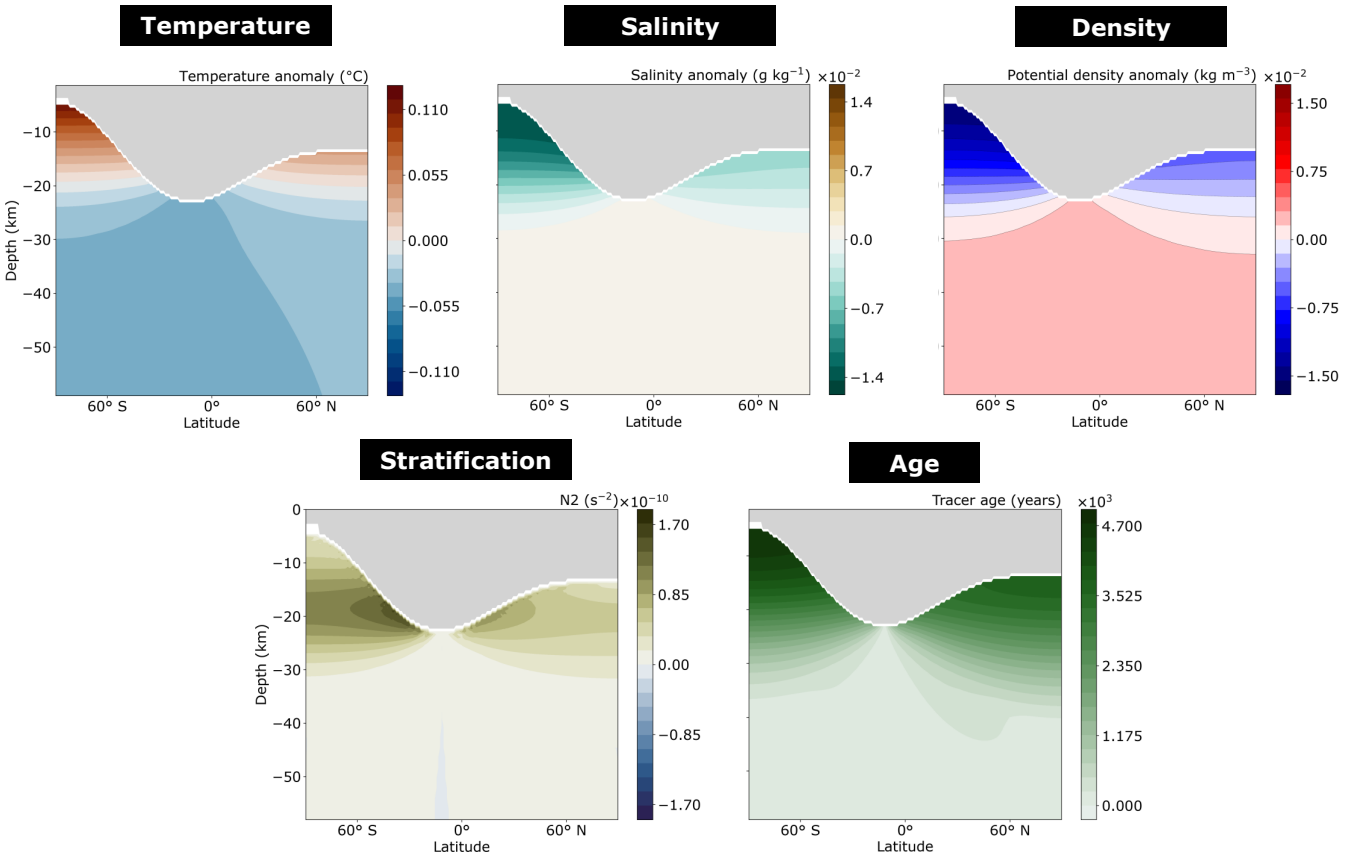

Figure 2.31: As in fig. 2.5, but for a simulation with $\sim$ 3 times finer meridional resolution of 1 degree. Top shows temperature (left; °C), salinity (centre; g kg^{-1}), and potential density (right, kg m^{-3}) anomalies referenced about the reference temperature, salinity and density respectively (see table 2.1). Bottom shows the Brunt-Vaisala frequency N^2 (s^{-2}) indicating ocean stratification, along with the tracer age (years), defining the lower bound time elapsed since a water parcel lost contact with the ocean bottom.

2.5 Setting up the configuration for other ice-covered moons

The configuration presented in this chapter can be adapted for the study of ocean circulation within other ice-covered moons. If the assumptions made here about Enceladus can be applied to the 'moon of choice', the only modifications required are the changing of planetary parameters illustrated in table 2.1 (e.g., ocean mean salinity, radius, surface gravity, rotation rate), along with the assumed bottom heating pattern and ice thickness profile.

Note however that a lack of observational constraints at ice-covered moons means these parameters are often uncertain or unknown. Until observational constraints are obtained (e.g., via the JUICE and Europa Clipper missions in the 2030's), modelling efforts should take care to account for associated uncertainty. In particular, it is demonstrated in section 2.4.1 that lateral variation in upper boundary forcings dictates ocean stratification and by extension tracer transport to the ice shell. Currently, it is only at Enceladus where observational constraints upon the ice thickness profile has been obtained. Larger ice-covered moons are expected to have flatter ice shells (larger gravity improves the efficiency of ice flow, and is expected to improve oceanic heat convergence to regions of thicker ice; Kang and Jansen 2022). But even small ice-thickness gradients can force significant meridional temperature gradients at the ocean top (particularly at larger gravity, which would strengthen the depth-dependence of waters' freezing temperature), that can drive ocean flow (Zhang, Kang and Marshall 2024). Investigating the implications of small ice thickness variations at large ice-covered moons (under the assumption of steady state) can be conducted using the configuration presented in this manuscript.

For moons such as Ganymede and Titan, ocean compositions may be very different to Earth and pressures large enough to permit higher pressure ice phases at depth (Vance et al. 2018). The applicability of an Earth-like equation of state to these moons is therefore less clear and requires investigation. However, such investigations could be performed with the configuration here if a user can code the desired alternative equation of state into the MITgcm.

2.6 Conclusions

In this manuscript, a general circulation model (GCM) configuration for simulating the stratification and circulation of ice-covered oceans is presented and rationalised. The model assumes a steady state overlying ice shell, and is necessarily idealised. Sensitivity tests are conducted to identify components with the largest impact upon the solution. The central findings of these tests are as follows:

- Stratification and, by extension, ocean circulation and tracer transport, is controlled by baroclinic eddies, energised in the presence of a laterally varying buoyancy forcing at the upper boundary, expected for an ocean overlain with ice of non-uniform thickness.

- Bottom heating, sourced from tidal dissipation in the underlying core, can act to destabilise the stratification of an ice-covered ocean beneath the ice base, improving vertical transport from the ocean bottom to the ice shell.

- Weakly stratified regions of ocean can permit Taylor-Proudman theorem to take hold, with velocity features tilting in the direction of the rotation axis. This requires a full treatment of the Coriolis force to be represented, and influences tracer transport achieved by convection where it is resolved.

- Representing non-linearity in the equation of state for water density is required to accurately model ocean stratification where the thermal expansion coefficient is predicted to change sign in the ocean.

Given these findings, we firstly conclude that robust estimates for oceanic heat (and other tracer) convergence to icy moon ice shells must account for any expected bottom heating, along with expected lateral variation of temperature and salinity forcings at the ocean top. This presents a challenge for the modelling of most known icy ocean worlds, where ice shell shape is currently poorly constrained. Until improved constraints are acquired (e.g., via JUICE or Europa Clipper at the Galilean moons), it may be premature to draw precise, quantitative, conclusions regarding the ocean circulation patterns of these moons. Instead, work up until this point should aim to consider and explore uncertain parameter space, identifying implications upon potential observables.

Our second conclusion is that a 'hierarchy of models' (as employed in terrestrial oceanography) will be necessary to advance understanding of icy moon oceanography. The need

for models of varying resolution and scale is compounded by our current inability to verify numerical solutions via observations, as is done for Earth. Given that the fundamental equations of fluid dynamics are expected to hold for ice-covered oceans (as they do in the atmospheres of other planets), convection- and eddy- resolving simulations of ice-covered oceans may, at present, be the most reliable means to gain insight into the dynamics therein. However, the computational expense of such simulations makes them less accessible and as a result, precludes the exploration of the broad uncertain parameter space of ice-covered oceans that shape their stratification (and by extension, circulation and tracer transport), at least at global scale.

A broader exploration of parameter space can instead be achieved using simplified models at coarser resolution (e.g., Ames et al. 2025). However, these models must parameterise the mixing induced by unresolved processes, namely eddies, convection, and processes encapsulated by κ_z (all found here to dominate the heat and tracer transport). The suitability of existing eddy and convection parameterisation schemes has not yet been verified for ice-covered oceans. Future work should therefore focus on addressing this issue. We expect that modifications to existing schemes may be required in quasi-unstably stratified regions of ocean, which are not present at Earth, but may be present in permanently ice-covered oceans.

Finally, note that the configuration here solves only the buoyancy driven flow. The role of ocean tides and ice shell libration is parameterised via an effective vertical diffusivity κ_z, assumed constant. In ice-covered oceans, κ_z will very likely be coupled to the model stratification. Numerical models coupling tidally- and librationally- mixing with the stratification profile of a buoyancy-driven model could provide a means to develop an improved parameterisation of tidally- and librationally- induced mixing, reducing the breadth of uncertain parameter space yet to be explored in the simulation of ice-covered oceans.

Chapter 3

Ocean stratification impedes particulate transport to the plumes of Enceladus

The following chapter has been published in the Nature-Springer journal *Communications: Earth and Environment*, with the following reference:

Ames, F., Ferreira, D., Czaja, A., Masters, A., 2025. Ocean stratification impedes particulate transport to the plumes of Enceladus. *Communications Earth and Environment*. 6, 63. https://doi.org/10.1038/s43247-025-02036-3

3.1 Introduction

Global oceans of liquid water underlay the surface of several icy satellites in our solar system and among them Enceladus - a $\sim$ 500 km wide moon of Saturn - is a leading astrobiological target (Khurana et al. 1998; Iess et al. 2012; Saur et al. 2015; Thomas et al. 2016; Lainey et al. 2024). Unique to Enceladus are the geyser-like plumes containing water vapour and ice grains that erupt continuously from fissures in its south polar ice shell (Porco et al. 2006). These plumes, sustained by tidal stresses imparted by Enceladus' eccentric orbit about Saturn (Hedman et al. 2013; Kite and Rubin 2016), eject ocean material into space, providing an opportunity to probe its composition.

Existing interpretations of plume vapour and particulates, sampled via the Cassini spacecraft, hint at an ocean conducive for life (Choblet et al. 2021), with possible submarine hydrothermal activity at the ocean bottom (Hsu et al. 2015; Waite et al. 2017), perhaps fueled by tidal heating in Enceladus' rocky core (Choblet et al. 2017). Combined with detected CHNOP bio-essential elements (Waite et al. 2009; Postberg et al. 2023), and low ocean pressures (owing to Enceladus' weak gravity), this implies physico-chemical environments at depth comparable to those around submarine hydrothermal vent fields on Earth, which provide the redox agents necessary for chemosynthetic life (Kotelnikova 2002; Kelley et al. 2005; Crane, Hecker and Golubev 1991).

Given the recent prioritisation of a mission returning to Enceladus, dedicated to probing plume material as a means to constrain Enceladus' biogeochemistry and search for evidence of extant life (MacKenzie et al. 2021), it is necessary to estimate the extent to which plume material (sourced from a localised region near Enceladus' south polar ocean-ice interface) can be assumed representative of the ocean bottom, where hydrothermal systems capable of supporting life may exist. Previous work highlighted fractionation processes within the geyser conduit as a means to create compositional differences between the plume and ocean (e.g., Fifer, Catling and Toner 2022). Here we highlight the role of ocean stratification (measuring the strength of density layering within the ocean), which if present, could isolate the ocean-ice interface from the ocean bottom and yield plume material that misses components present at depth.

Stable stratification inhibits convection - an efficient mechanism for vertical transport of particulates and dissolved substances (Schoenfeld et al. 2023). In Earth's predominantly stably stratified ocean (Li et al. 2020) this permits the marine snow phenomena, where

organic matter, unable to maintain neutral buoyancy, undergoes 'detrainment', settling down to the ocean bottom (Iversen and Lampitt 2020; Waite et al. 1997; Turner 2015). Meanwhile, the slow ascent of hydrothermally-derived, dissolved substances provides time for scavenging processes and usage by life, resulting in surface concentrations far lower than those present nearer source regions at depth (Nishioka, Obata and Tsumune 2013; Measures et al. 2015; Saito et al. 2013; Resing et al. 2015; Roshan et al. 2020).

In contrast, Enceladus' ocean has been assumed in much previous work to be convecting from top to bottom (thus entirely unstratified - Fig. 3.1, upper left), able to efficiently transport hydrothermally-derived substances to the plumes (Hsu et al. 2015; Choblet et al. 2017; Schoenfeld et al. 2023). The assumption is made on the basis that Enceladus' ocean is cooled from above and heated from below, by an ice shell (via conductive or convective heat loss) and tidally-heated rocky core, respectively. However, such boundary forcings can only induce convection where the thermal expansion coefficient (α_T - quantifying the expansion of water with increasing temperature) is positive, so that colder water is denser and thus sinks. For water of salinity $\lesssim$ 20 g kg^{-1} (Enceladus' ocean salinity as implied by Cassini ice grain observations - (Postberg et al. 2009), α_T is in fact negative near its freezing point (which is necessarily approached at the ocean-ice interface) (Fig. 3.1, upper right). This means that cooling from above, rather than inducing convection, should act to increase water buoyancy and promote the development of a stratified layer underlaying the ice shell (Zeng and Jansen 2021). The same mechanism for stratification occurs in freshwater lakes on Earth during winter and is commonly referred to as inverse stratification (Forel 1892; Woolway et al. 2022), terminology that will be used here.

An inverse stratification was previously suggested for Europa by (Melosh et al. 2004) but as pointed out by (Zeng and Jansen 2021), is more likely for Enceladus due to its lower pressures (compared to Europa), which could permit negative α_T (and thus inverse stratification) to extend the full ocean depth (Roquet et al. 2022). Increasing temperature can also force α_T to become positive (Fig. 3.1, upper right). This could allow bottom heating to maintain a positive α_T at depth provided sufficient heat can accumulate there. Heat accumulation would be controlled in part by the magnitude of the bottom heat flux, but also by processes that can move colder waters from the ice-interface downwards, and heat away from the ocean bottom, in the absence of convection. These processes would include molecular diffusion, but could be made far more efficient within Enceladus by

mixing induced by tides and ice shell libration (periodic movement of the ice shell over the ocean; (Jansen et al. 2023)). If induced mixing is strong enough to ensure a negative α_T at all depths, Enceladus' ocean could be entirely stably stratified (Fig. 3.1, lower right). If induced mixing is weak, an inverse stratified layer would instead overlay a well-mixed convecting layer, separated by the depth at which α_T becomes negative (Fig. 3.1, lower left), henceforth referred to as the inversion depth.

The existence or extent of inverse stratification within Enceladus is currently poorly constrained. Only a handful of simulations have been conducted at salinity ≤ 20 g kg^{-1}, computing water density using a non-linear equation of state that permits a varying α_T (thus permitting an inversion depth). These include a localised (albeit unequilibrated) simulation by (Bire et al. 2023) which produced an entirely inversely stratified ocean beneath the Enceladus' south pole (akin to Fig. 3.1, lower left), along with two localised simulations by Kang et al. (2022b), one of which produced an inversion depth ~ 30 km beneath the surface (akin to Fig. 3.1, lower right). Equilibrated global simulations of Enceladus' ocean were conducted at 8.5 g kg^{-1} salinity by both Zeng and Jansen (2021) and Zeng and Jansen (2024), with an inversion depth obtained in both simulations. However, as in the aforementioned studies, (Zeng and Jansen 2021; Zeng and Jansen 2024) tested only one value of κ_z - an effective vertical diffusivity used to parameterise the vertical mixing induced by tides and libration (Jansen et al. 2023). By approximating κ_z as a function of the total energy available for ocean mixing, (Zeng and Jansen 2021) derived the range of uncertainty of κ_z within Enceladus to span five orders of magnitude, from $\sim 10^{-7}$ to 10^{-3} m^2 s^{-1}, corresponding to existing bounds in estimates of tidal and librational energy dissipation (Hay and Matsuyama 2019; Wilson and Kerswell 2018). The sensitivity of ocean stratification within Enceladus to κ_z, and implications for the transport of hydrothermally-derived particulates and dissolved substances to the ice shell, has not yet been explored.

Inferences from Cassini observations of silica nano-particles - believed to be sourced from hydrothermal alteration within Enceladus' core - suggest transport timescales through Enceladus' ocean of several months (Hsu et al. 2015). However, it is important to test how this fits within constraints provided by fluid dynamics and whether inferred transport timescales could be achieved within the plausible parameter space in ocean salinity (determined by (Hsu et al. 2015 as not exceeding ~ 40 g kg^{-1}) and κ_z. With this in

mind, the geometry of the overlying ice shell could provide additional constraints upon ocean stratification that should be accounted for (Zhu et al. 2017; Kang 2023). Enceladus' ice shell appears to be thicker at the equator than at the poles (Hemingway and Mittal 2019). To maintain a steady state ice thickness, melting would be required at the poles and freezing at the equator, to balance the expected poleward ice flow (Čadek et al. 2017; Lobo et al. 2021; Kang et al. 2022a). Stratified polar freshwater melt has previously been shown to provide a barrier to vertical particulate transport in high-resolution, localised simulations (Kang et al. 2022b), although these were not run to equilibrium.

The novelty of this manuscript is a comprehensive investigation of ocean stratification within Enceladus across the plausible parameter space in ocean salinity and κ_z, and the explicit computation of the transport timescales of entrained particulates and dissolved substances (hereafter 'tracers') from source regions at depth, to the south polar plumes. We first build upon previous work (Zeng and Jansen 2021) to develop a simple theoretical model specific to inverse stratification and corresponding tracer transport timescales. We then perform numerical simulations using an ocean general circulation model to verify the theory while accounting for ice shell melting and freezing, under the assumption of steady state. Finally, we discuss the implications of our results for interpretations of plume material and the state of Enceladus' ice shell.

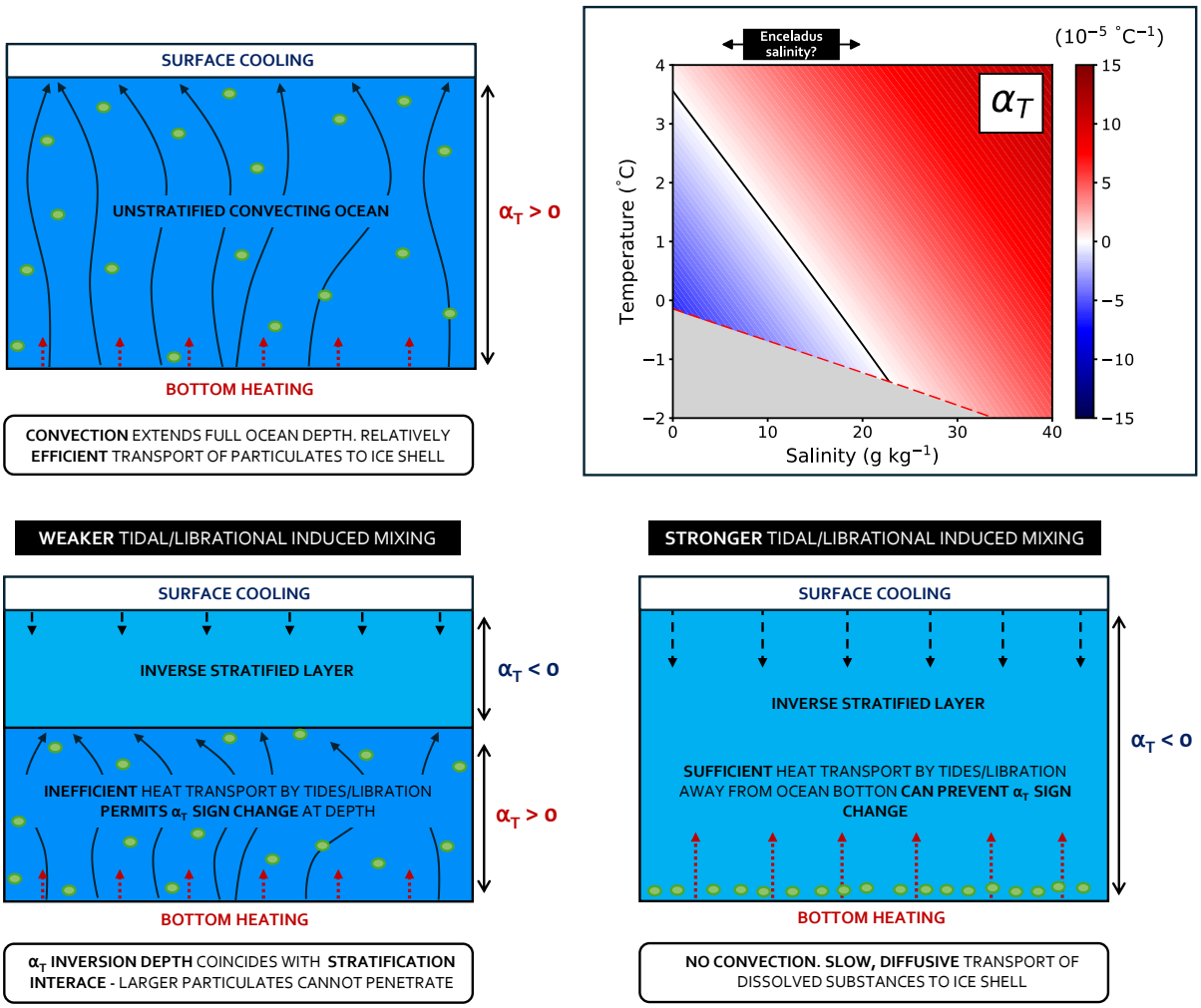

Figure 3.1: **Upper right**: Thermal expansion coefficient (α_T - $^{o}\mathrm{C}^{-1}$) plotted as a function of temperature (^{o}C) and salinity (g kg^{-1}) at constant pressure, computed under 20 km mean ice thickness for Enceladus. Black line denotes where α_T changes sign. Black box with arrows denotes the range of uncertainty for Enceladus' mean ocean salinity (5-20 g kg^{-1}) implied by Cassini E-ring ice grain observations (Postberg et al. 2009). Red dashed line denotes the water freezing temperature (corresponding to the temperature at ice-interface), using the formulation of (Losch 2008). Grey shading denotes frozen water. Water density is computed using the non-linear equation of state of (Jackett and Mcdougall 1995). **Schematics**: Illustrating an idealised ocean beneath Enceladus' south polar ice shell, either entirely unstratified (and thus convecting; **upper left**) or inversely stratified owing to negative α_T (**lower left** and **lower right**). Where $\alpha_T < 0$, cooling from the overlying ice makes water more buoyant, while warming from the underlying core makes water denser. These effects reverse where $\alpha_T > 0$, and the resultant presence of buoyant water underlying denser water induces convective overturning (indicated with solid black arrows). Dashed arrows denote the magnitude of assumed tidally and librationally induced mixing, parameterised in this work as κ_z. Red dotted lines denote heat transport by induced mixing, achieved for the same bottom heat flux. Green circles denote hypothetical particulates unable to attain neutral buoyancy where the ocean is stably stratified (light blue shading), but entrained where the ocean convects (dark blue shading). Note these schematics assume no other mechanisms for stratification of Enceladus' ocean.

3.2 Theoretical model

3.2.1 Inverse layer thickness

Following common practice in Earth ocean modelling, tidally and librationally induced mixing is parameterised using an effective vertical diffusivity κ_z. In Earth's oceans, a complex pathway links tidal energy dissipation to its mixing effects, involving the emission, transmission, and breaking of internal waves (Wunsch and Ferrari 2004). However, κ_z has proved to be a good first order representation of this pathway in ocean models (Simmons et al. 2004). As on Earth, κ_z may exhibit spatial and temporal variations within Enceladus due to stratification, topography, and profiles of tidal and librational energy dissipation, which may be concentrated within boundary layers at the ocean top and bottom (Rekier et al. 2019). Given existing uncertainties, κ_z here is assumed constant and uniform.

By assuming κ_z dominates vertical heat transport in the inverse stratified layer, a steady state heat balance requires that the vertical diffusive flux is equal to the geothermal heat flux at any depth in the inverse layer:

$$Q = c_p \rho_0 \kappa_z \frac{\partial T}{\partial z}, \tag{3.1}$$

where Q is the geothermal heat flux (W m^{-2}), c_p the specific heat capacity (J kg^{-1} K^{-1}) and ρ_0 the ocean density (kg m^{-3}).

The top of an inverse layer, in contact with the ice-ocean interface, is at freezing point T_f, while the bottom of this layer, the inversion depth, is at the critical temperature T_crit - the temperature at which α_T changes sign for a given salinity and pressure (solid black line in Fig. 3.1, upper right). Integrating across the inverse layer gives (Zeng and Jansen 2021):

$$H_\mathrm{strat} = D(T_\mathrm{crit} - T_\mathrm{f}), \tag{3.2}$$

where $D = \frac{c_p \rho_0 \kappa_z}{Q}$, and H_strat is the thickness of the inverse layer. Note that for inverse stratification, which requires $\alpha_T < 0$, to exist, T_crit must be higher than T_f (ocean temperature cannot fall below freezing point - see fig. 3.1, upper right).

T_crit varies with pressure, and is therefore not independent of H_strat. To make analytical

progress, T_{crit} is approximated as a linear function of salinity and pressure:

$$T_{\mathrm{crit}} \approx aS + bP + c, \tag{3.3}$$

where we find, a = -0.216 ^{o}C (g kg^{-1})$^{-1}$, b = -2.11 x 10^{-7} ^{o}C Pa^{-1}, and c = 4.01 ^{o}C, across the range of salinity and pressure plausible for Enceladus (see Methods, section 3.5.2).

Ocean pressure can be approximated as $P = P_{\mathrm{int}} + P_{\mathrm{ocn}}$, the pressure at the ice-ocean interface and pressure contribution from any overlying ocean respectively. $P_{\mathrm{int}} = \rho_{\mathrm{i}} g H_{\mathrm{i}}$, where g denotes gravity (m s^{-2}) and H_{i} and ρ_{i} denotes ice thickness (m) and density (kg m^{-3}). Using the hydrostatic approximation, at the inversion depth:

$$P_{\mathrm{ocn}} = \rho_0 g H_{\mathrm{strat}}. \tag{3.4}$$

Substituting Eqs. (3.3) and (3.4) into Eq. (3.2), an approximation for the inverse layer thickness can be obtained:

$$H_{\mathrm{strat}} = \frac{D(T_{\mathrm{crit}*} - T_{\mathrm{f}})}{1 - Dbg\rho_0}, \tag{3.5}$$

where $T_{\mathrm{crit}*} = aS + bP_{\mathrm{int}} + c$ is the critical temperature evaluated at the ice-ocean interface, and is independent of H_{strat}. To the first order, Eq. (3.5) has the same physical interpretation as proposed by (Zeng and Jansen 2021): Increasing bottom heat flux Q increases the thickness of the bottom convective layer, reducing the inverse layer thickness H_{strat}, while a larger vertical diffusivity κ_z is more effective at transporting the geothermal flux upward, thus reducing the penetration of convection and increasing the inverse layer thickness. Compared to (Zeng and Jansen 2021) however, Eq. (3.5) shows a non-linear dependence on Q and κ_z owing to the additional $\frac{1}{1-Dbg\rho_0}$ factor derived here. Eq. (3.5) also explicitly includes a salinity dependence through $T_{\mathrm{crit}*}$ (note that T_{f} also depends on S and P_{int}, but the behavior of $T_{\mathrm{crit}*} - T_{\mathrm{f}}$ is dominated by that of $T_{\mathrm{crit}*}$; see Methods). Further interpretation of Eq. (3.5) is discussed below.

3.2.2 Tracer age

The transport timescale of tracers sourced from the ocean bottom to the south polar plumes, gives a lower bound residence time for such tracers in Enceladus' ocean (i.e., before ejection into space) - this timescale will henceforth be referred to as the tracer age. Assuming the transport timescale through any underlying convecting layer is negligible,

the time taken to traverse diffusively through an inverse stratified layer of thickness H_{strat}, given a mixing κ_z is:

$$\tau = \frac{H_{\mathrm{strat}}^2}{2\kappa_z}. \tag{3.6}$$

Note that tracer age τ is not inversely proportional to κ_z because H_{strat} is itself a function of κ_z.

It is worth emphasizing that our timescales do not account for detrainment of matter, which could further prolong transport timescales, and even prevent sufficiently large, dense or compacted particulate matter - unable to attain neutral buoyancy - from ever being transported to the plumes (Schoenfeld et al. 2023). Because of this, and the neglect of the time in the convective layer and transit time within the ice shell, tracer ages derived here should be interpreted as lower bounds on the transport timescale from the ocean's bottom to the plumes.

3.2.3 Analytical solutions across plausible range of salinity and κ_z

Solutions for the inverse layer thickness and tracer age from Eqs. (3.5) and (3.6) are shown in Fig. 3.2 (left). These are computed across the plausible range of ocean mean salinity and κ_z for Enceladus. Bottom heating Q is set to 0.03 W m^{-2}, the approximate globally-averaged heat flux at the inversion depth, assuming a total core heat output of 20 GW, in the middle of the 10-30 GW range proposed by (Choblet et al. 2017). Interface pressure is computed assuming a mean ice thickness of 20 km, mean ice density of 925 kg m^{-3}, and gravity of 0.113 m s^{-2}.

The predicted tracer age varies by over six orders of magnitude depending upon the chosen values of mean salinity and κ_z, with an inverse layer thickness ranging from metres to the entire ocean depth.

For a given κ_z, lower salinity is predicted to yield a thicker inverse layer. This is because T_{crit} (see Eq. (3.3)) is warmer at lower salinity, and can be attained (allowing the inverse layer to extend) closer to the heat source at the bottom. A larger inverse layer thickness, in turn, results in older tracers in the plumes, owing to the greater distance that must be traversed diffusively. The dependence of H_{strat} on the mean salinity is linear through $(T_{\mathrm{crit}*} - T_{\mathrm{f}})$ (see Eq. (3.5)), except if H_{strat} reaches the full ocean depth (Fig. 3.2, top left).

For a fixed salinity, a larger κ_z results in a thicker inverse layer. The behaviour is complex due to the non-linear dependence of $H_{\rm strat}$ on κ_z (Eq. (3.5)) and saturation upon $H_{\rm strat}$ reaching the ocean depth (set to 40 km here). At high salinities, $T_{\rm crit*}$ is much nearer the freezing temperature (Fig. 3.1, upper right) (or equally, ocean pressures are more likely to force α_T to become positive at depth). As a result, above $\sim$ 20 g kg^{-1}, the inverse layer is shallow and weakly sensitive to κ_z. Conversely, at low salinities where the $T_{\rm crit*} - T_{\rm f}$ difference is large, $H_{\rm strat}$ is highly sensitive to κ_z. While $H_{\rm strat}$ increases linearly with κ_z for low κ_z, the aforementioned non-linear effect kicks in quickly and $H_{\rm strat}$ increases slowly with κ_z at higher κ_z. This is because the increase in $H_{\rm strat}$ that results from increasing κ_z causes $T_{\rm crit}$ to become cooler through its pressure dependence, counteracting the ability of the inverse layer to expand downward. At fixed salinity, the maximum value of $H_{\rm strat}$ $(=(T_{\rm crit*} - T_{\rm f})/(-bg\rho_0))$ is approached for large mixing. For our parameter choices, this maximum value ranges from $\sim$160 km at S=0 g kg^{-1} to $\sim$20 km at 20 g kg^{-1}. Importantly, above about 17 g kg^{-1}, the maximum inverse layer thickness is less than the ocean depth, i.e., limited by properties other than the ocean geometry.

Turning to the tracer age (Fig. 3.2, bottom), for low κ_z ($\leq 10^{-4}$ m^2 s^{-1}), the tracer age increases with the inverse layer thickness (thicker layers take longer to traverse). For larger κ_z, where the inverse layer saturates at either the ocean depth or its maximum $H_{\rm strat}$, further increasing κ_z makes transport through the inverse layer more efficient, decreasing tracer age. As a result, the maximum ages are obtained at $\kappa_z \approx 10^{-4}$ m^2 s^{-1}, i.e. the lowest κ_z for which the inverse layer extends the ocean depth. Despite this, an inverse layer of 50 m can still produce ages exceeding 100 years at the lowest κ_z tested, because transport is inefficient in this case.

Note that Eqs. (3.5) and (3.6) can be applied to any moon, planet or dwarf planet containing an ocean heated from below and permanently overlain by ice (see Methods, section 3.5.4 for application to Europa).

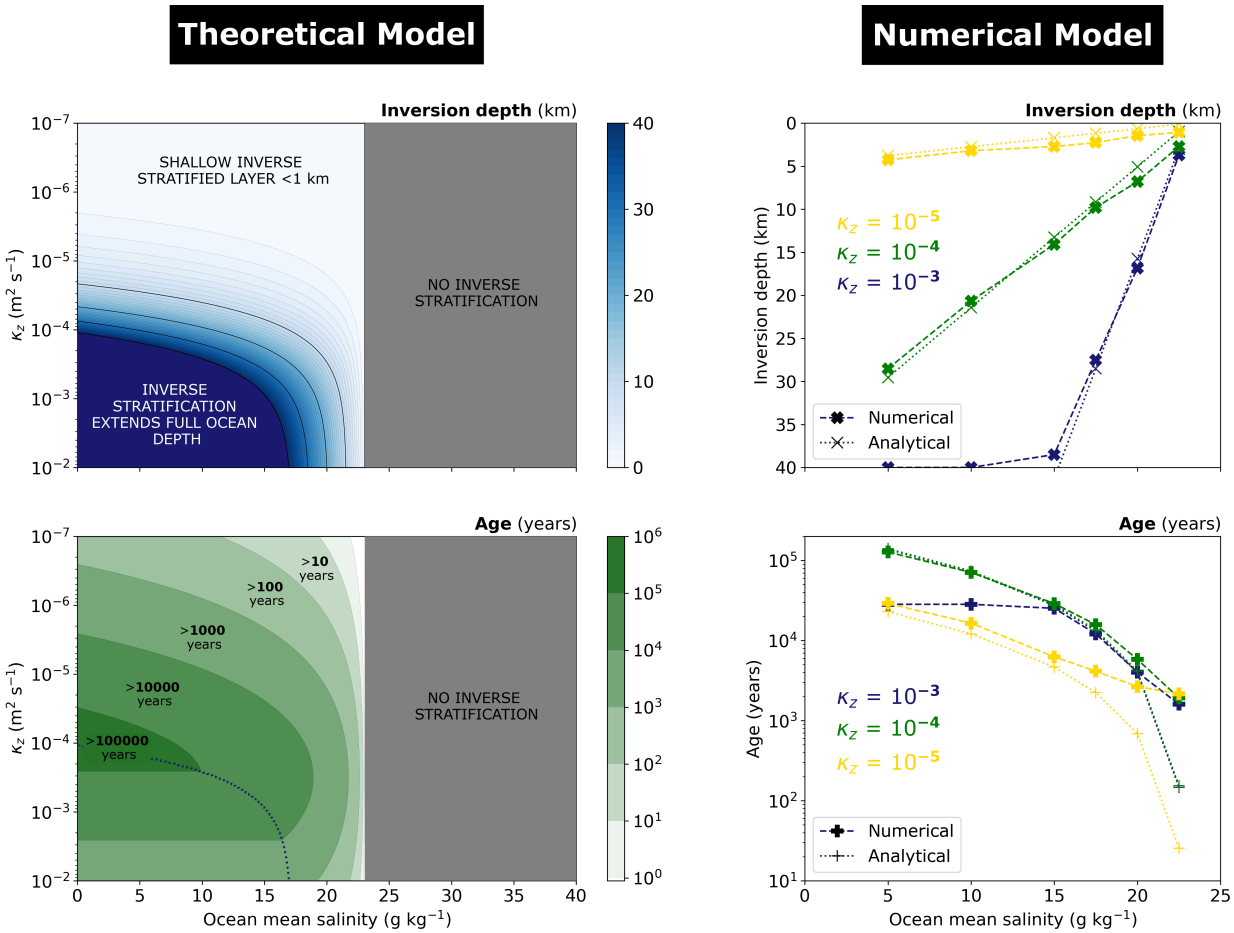

Figure 3.2: **Stratification and tracer age: results.**
Top left: Inversion depth H_{strat} (km - depth at which thermal expansion coefficient α_T becomes negative, taken here to define the inverse stratified layer thickness) computed using Eq. (3.5), plotted as a function of ocean mean salinity (g kg^{-1}) and vertical diffusivity κ_z (m^2 s^{-1}) plausible for Enceladus. Contours denote 1 km (and black contours 10 km) depth up to the assumed 40 km ocean depth for Enceladus, shaded in midnight blue. Grey shading denotes where inverse stratification cannot occur, because α_T cannot become negative at the ocean-ice interface pressure (computed under the 20 km mean ice thickness for Enceladus). **Bottom left**: Tracer age (years) at the ocean-ice interface, computed using Eq. (3.6). Note that age contours are logarithmic. Blue dotted line delineates parameter space where inverse stratification is predicted to extend the full ocean depth. Within this parameter space, age contours are horizontal, with no predicted salinity dependence. **Top right**: Numerical solution for the inversion depth (thick cross, dashed line) across a range of ocean mean salinity for three values of κ_z, denoted with different colours. This is plotted alongside the analytical solution (thin cross, dotted line) for comparison. Where the inversion depth equals the ocean depth, the whole ocean is inversely stratified. **Bottom right**: Numerical solution for the ideal age at the south polar ocean-ice interface (thick plus, dashed line), plotted alongside the analytical solution (thin plus, dotted line) for comparison. Note that age does not fall below 1000 years in any numerical simulation.

3.3 Tests with a numerical global ocean circulation model

Our 1D theoretical model neglects lateral gradients in ocean salinity (driven by ice shell melting and freezing), and in temperature (owing to the pressure dependence of freezing temperature) that could drive an overturning circulation in Enceladus' ocean. The associated heat transport could challenge the assumption of Eq. (3.5), that vertical heat transport in the inverse stratified layer is dominated by κ_z. We therefore test the robustness of our 1D theoretical model against a non-linear 2D global ocean model.

3.3.1 Model description

We use the Massachusetts Institute of Technology Ocean General Circulation Model (MITgcm; Marshall et al. 1997b) in a 2D latitude-depth setup configured for Enceladus. A fully non-linear equation of state is employed (Jackett and Mcdougall 1995), with water density computed (and α_T allowed to vary) as a function of ocean pressure, salinity and temperature. Freshwater fluxes from the ice shell are prescribed, under the assumption of steady state (Čadek et al. 2019), by computing the ice shell melting and freezing necessary to balance the ice flow induced by an idealised poleward-thinning ice shell geometry (Kang and Flierl 2020; Kang et al. 2022a). This results in freshwater input (ice melting) at the poles and freshwater output (ice freezing) at the equator, as previously proposed (Čadek et al. 2017). Temperature is restored to the pressure-dependant freezing point at the ocean top, computed using the same idealised geometry (Millero 1978), yielding polar ice-interface temperatures $\sim 0.1\ ^o$ C warmer than at the equator (see fig. 3.3). The upper boundary in the model simulation is flat for simplicity. A polar amplified geothermal heat flux is applied at the ocean bottom assuming a total core output of 20 GW (Choblet et al. 2017). Unresolved mixing by convection is parameterised via the diffusive adjustment scheme of (Klinger, Marshall and Send 1996). Ocean mesoscale eddies are parameterised using the Gent-McWilliams and Redi schemes (Gent and Mcwilliams 1990; Redi 1982) - a standard combination in Earth ocean modelling, but modified here for icy moon oceanography (see Methods).

Borrowing from studies of ocean ventilation on Earth (e.g., England 1995), solutions for tracer age are obtained by computing the ideal age. This defines the (volume-weighted) time elapsed since a water parcel lost contact with the ocean bottom. As for the theoretical age (section 3.2.2), the numerical age is a lower bound on the transport timescale of tracers from the ocean bottom to the south polar plumes.

Simulations are performed across a range of plausible ocean mean salinity (5, 10, 15, 17.5, 20, 22.5 g kg^{-1}), and κ_z (10^{-3}, 10^{-4}, 10^{-5} m^2 s^{-1}). Extended model details can be found in the Methods, section 3.5.1.

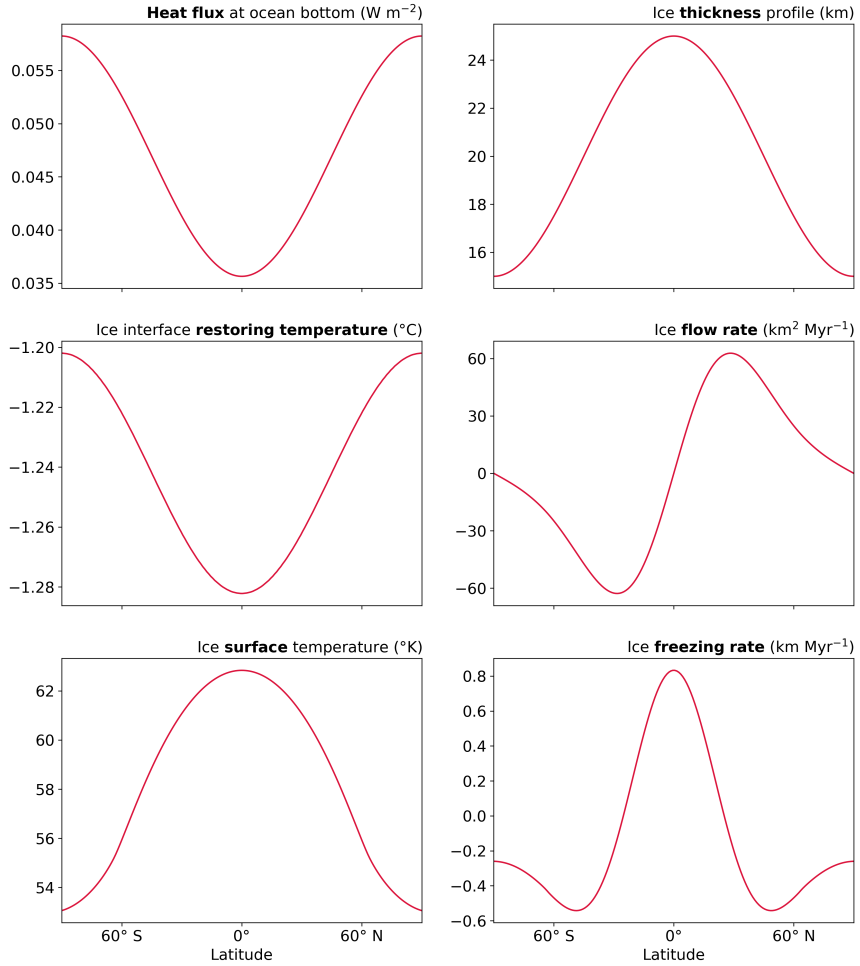

Figure 3.3: **Top left**: Bottom heating profile used in simulations (W m^{-2}), assuming a total global core heat output of 20 GW. **Middle left**: An example restoring temperature (^{o}C) profile at the ocean top (ice-interface) used in simulations at 20 g kg^{-1} - corresponding to the pressure and salinity dependant freezing temperature. **Bottom left**: Surface temperature (^{o}K) of ice used to compute ice flow rate in middle right panel. **Top right**: Idealised ice thickness profile (km) used to compute the ice-interface restoring temperature and ice flow rate (for use in computation of ice freezing rate). Note the topography itself is not used in simulations, which assume a flat ocean top. **Middle right**: Ice flow rate (km^2 per million years) used for computing the freshwater flux at the ocean top, in turn computed from the idealised geometry of the top right panel, assuming a steady state Enceladus ice shell thickness profile. **Bottom right**: Freshwater flux (km per million years) profile applied at the ocean top in simulations, computed using the ice flow rate in the middle right panel.

3.3.2 Numerical solutions

Numerical solutions for the globally-averaged inversion depth, along with the tracer age at the south polar ice interface, are plotted in the right panel of Fig. 3.2. Analytical solutions using Eqs. (3.5) and (3.6), are plotted alongside for comparison. Corresponding 2D fields of ocean temperature, salinity, stratification, and ideal age are shown in Fig. 3.4. The inversion depth is chosen as a metric for the thickness of the inverse layer. An alternative metric, the depth at which convection extending from the ocean bottom ceases, gives nearly identical results (see fig. 3.5).

Numerical and analytical solutions for the inversion depth show good agreement. Two solutions ($\kappa_z = 10^{-3}$ m^2 s^{-1} and salinity ≤ 10 g kg^{-1}) exhibit a stratified inverse layer extending through the entire ocean depth (no convection).

In all other solutions with salinity ≤ 20 g kg^{-1}, an interface develops at the inversion depth, between a cooler inverse stratified layer underlying the ice shell, and a warmer convecting layer underneath (Fig. 3.4, middle). In the convective layer, the temperature is nearly homogeneous at $\approx T_{\text{crit}}$, owing to efficient mixing there, as found previously (Zeng and Jansen 2024). A lateral temperature gradient develops at the ice-ocean interface in all solutions owing to the pressure-dependant freezing temperature there, warmer at the poles, cooler at the equator. In the 5 g kg^{-1} solution, this results in enhanced stratification at the equator relative to the poles at the highest κ_z tested (Fig. 3.4, upper). Similarly, salinity gradients develop at the ice interface in response to the imposed melting and freezing forcing pattern (see fig. 3.3). Despite these, the horizontally-averaged inversion depth follows closely the 1D theoretical model discussed in section 2.3.

Numerical and analytical solutions for the tracer age in general show good agreement, but with larger relative discrepancies where salinity $\gtrapprox 20$ g kg^{-1} (Fig. 3.2, bottom right). Discrepancies tend to be larger at the lowest κ_z tested, because the inversion depth is shallow in this case, meaning this and the corresponding age are more sensitive to the employed vertical resolution (~ 300 m at the ocean-ice interface, see Methods). However discrepancies are pronounced at 22.5 g kg^{-1}, where numerical solutions for tracer age converge to ~ 1000 years across all κ_z tested, and the inverse stratification theory appears to break down. This can be explained by the effects of ice shell melting and freezing, which are not captured by the 1D theoretical model. Freshwater melt at the pole (necessary to

maintain Enceladus' ice geometry assuming steady state) induces salinity anomalies that become the dominant control upon ocean density for salinity $\gtrapprox 10$ g kg^{-1} (owing to weaker α_T nearer the ice interface, see Fig. 1), resulting in stably stratified, buoyant, freshwater lenses at both poles. For salinity > 20 g kg^{-1}, the freshwater lens penetrates deeper than the inversion depth becoming the dominant control upon the transport timescales of tracers to the polar ice shell.

At the equator, saltier water (generated by ice freezing) can penetrate the inversion depth in solutions with 22.5 g kg^{-1} mean salinity. There, convection exists much closer to the ice-interface than at the poles. Despite this, age is still of order 100s of years at equatorial ocean top (see also numerical solution at lower κ_z in fig. 3.6). This is because a weak stratification is maintained here against convection by the eddy parameterisation scheme (see Methods). The eddy scheme is invoked because ice melting and freezing induce lateral gradients in ocean density, causing isopycnals (contours of constant density - see Fig. 3.4, middle right panel) to become 'sloped'. As in Earth's oceans, the parameterised eddies mimic the effect of baroclinic instability which extracts the potential energy stored in the sloped isopycnals and, in doing so, flattens them, re-stratifying the water column (see also Kang 2023; Zhang, Kang and Marshall 2024).

Also note the stratifying influence of eddies is likely modulated by the shape of the overlying ice shell - an effect not considered here. Because Enceladus' ice shell is expected to extend deeper into the ocean at the equator than at the poles, freezing should occur lower down in the water column than melting. Where salinity anomalies are the dominant control upon ocean density (e.g., Fig. 3, lower), a large κ_z would be necessary to mix the buoyant (fresher) water downwards to sustain the lateral density gradient at the equatorial ice interface (Jansen et al. 2023). Without this, equatorial eddy restratification would likely be weaker than obtained in our numerical solutions for this regime. Numerical solutions for the equatorial age should be interpreted with this in mind.

To quantify the potential control of freshwater melt upon tracer age at the south pole, we use the scaling proposed by (Zhang, Kang and Marshall 2024) for the thickness of a freshwater lens:

$$H_{\text{lens}} \sim R\sqrt{\frac{\kappa_z}{\kappa_{\text{GM}}}}, \tag{3.7}$$

where κ_{GM} is the eddy diffusivity and R a horizontal length scale defining the horizontal scale of salinity contours within the freshwater lens (which closely follows a region of melt-

ing - see Fig. 3.4 and fig. 3.3), taken here to equal the moons radius ($\sim \frac{1}{3}$ the length of the simulation domain). As noted by (Kang 2022) and (Zhang, Kang and Marshall 2024), this scaling is applicable only where these salinity contours do not intersect the ocean bottom.

Where H_{lens} is deeper than the inversion depth, we can substitute Eq. (3.7) into Eq. (3.6) to obtain an estimate for the tracer age at the south polar ice shell:

$$\tau \sim \frac{R^2}{2\kappa_{\text{GM}}}. \tag{3.8}$$

Note the cancellation of κ_z here: lower κ_z results in a thinner freshwater lens to be traversed, but this effect is offset because lower κ_z also yields less efficient vertical transport through this layer. Substituting in $\kappa_{\text{GM}} = 1$ m^2 s^{-1} from the numerical model setup (see Methods), Eq. (3.8) yields a tracer age $\tau \sim 1000$ years, in approximate agreement with the numerical solutions (Fig. 2, bottom right). Additional tests suggests that at very low κ_{GM} (0.01 m^2 s^{-1}) the steepening of isopycnals in a freshwater lens (owing to a deeper penetration into the ocean interior in accordance with Eq. (3.7)) allows along-isopycnal transport by eddies to become an increasingly significant contributor to the vertical tracer transport. This, combined with the saturation of H_{lens} at the ocean depth, increases discrepancies relative to Eq. (3.8). Yet, because κ_{GM} is weak in this instance, the tracer age remains larger than 10000 years (see fig. 3.7).

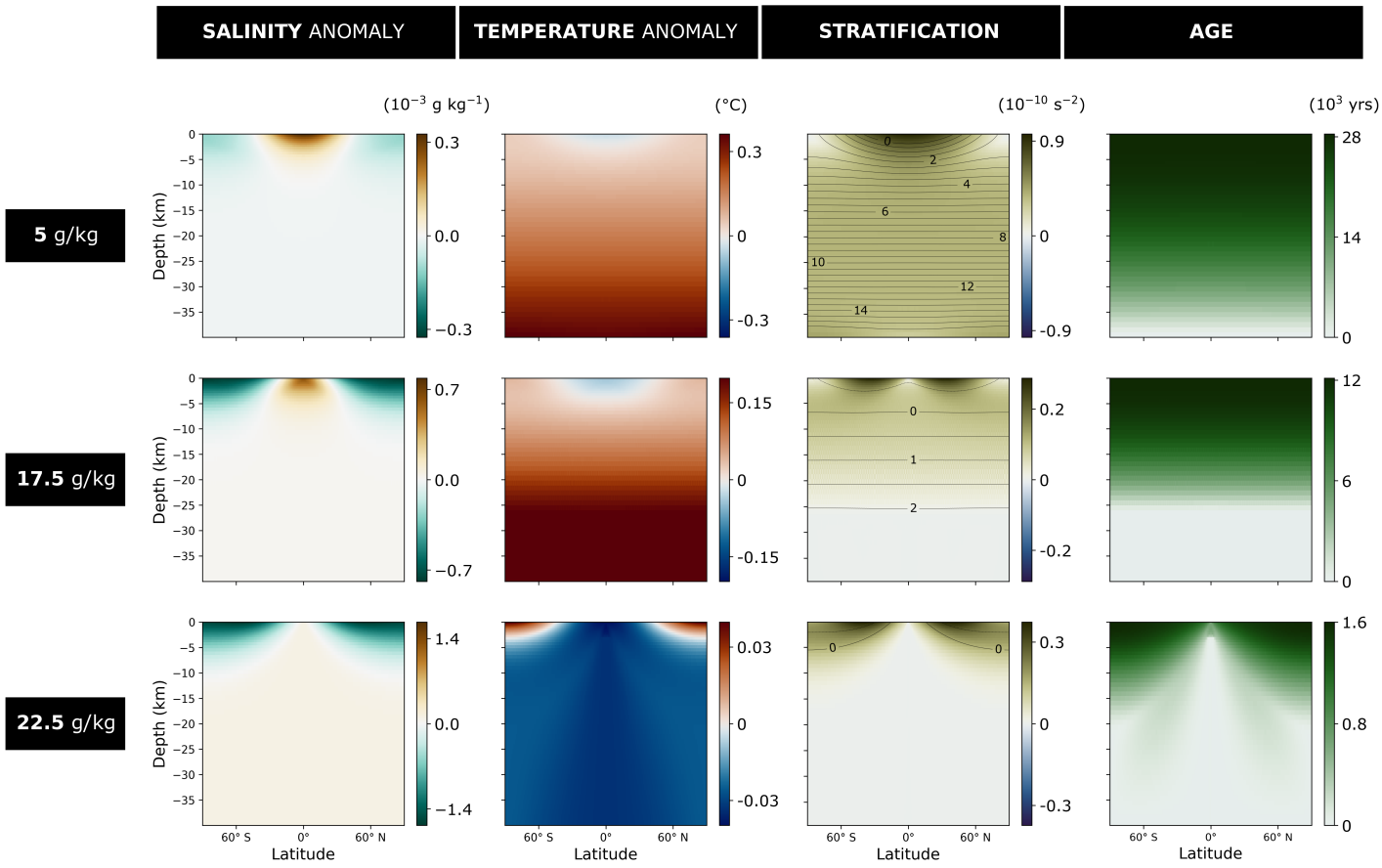

Figure 3.4: **Temperature, salinity, stratification and age: 2D fields.** Numerical solutions with effective vertical diffusivity $\kappa_z = 10^{-3}$ m^2 s^{-1}, across three different mean ocean salinities of 5 (top), 17.5 (middle), and 22.5 (bottom) g kg^{-1}, highlighting three contrasting stratification regimes. Note colour bar scales are saturated and vary throughout. **First column**: Salinity anomaly (g kg^{-1}) taken about the mean salinity. **Second column**: Potential temperature anomaly (^{o}C) taken about the simulation reference temperature T_{ref} (freezing temperature computed under 20km mean ice thickness) of -0.433 (top), -1.106 (middle) and -1.379 (bottom) ^{o}C. **Third column**: Shading shows the buoyancy frequency N^2 (s^{-2}) indicating stratification. Contours show the potential density anomaly (10^{-3} kg m^{-3}) about the ocean reference density ρ_0 of 1008.984 (top), 1015.029 (middle) and 1019.065 (bottom) kg m^{-3}. Potential density here is computed using the reference pressure P$_{ref}$ evaluated at the ocean-ice interface. **Fourth column**: Ideal age of tracers (years), sourced from the ocean bottom.

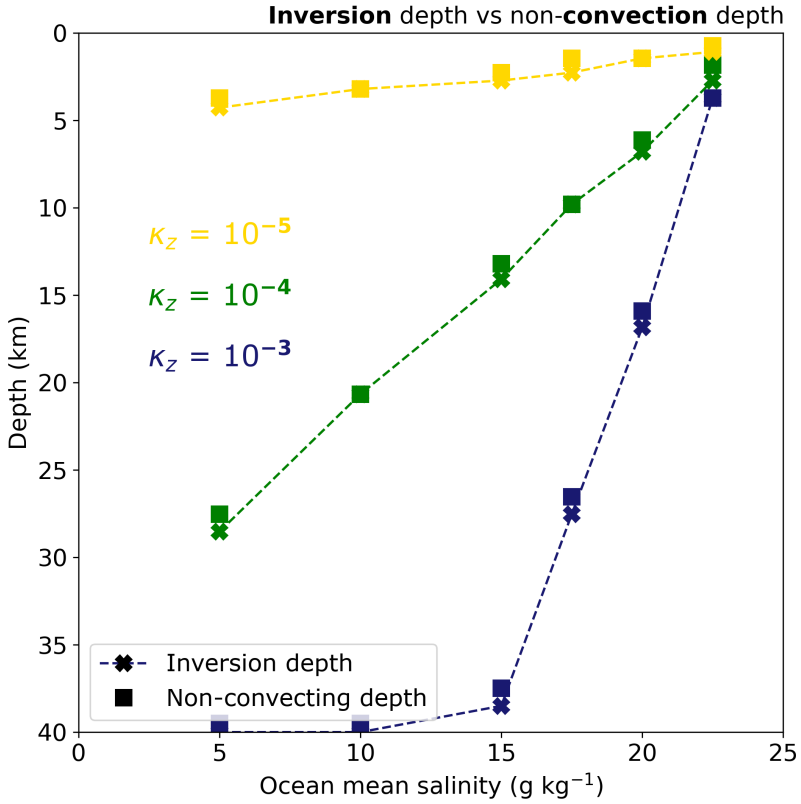

Figure 3.5: Numerical solution for the inversion depth (km - cross, dashed line - depth at which the thermal expansion coefficient α_T becomes negative) across a range of ocean mean salinity (g kg^{-1}) for three values of κ_z (m^2 s^{-1}), denoted with different colours, as in Fig. 2 of the main text. Here the inversion depth is plotted alongside the depth at which model convection extending from the ocean bottom stops (km - squares), defined as the depth at which the laterally-averaged convecting time falls below 0.01% of model time. Markers at 40 km depth denote where there is no inversion depth (meaning α_T remained negative across the whole ocean) or non-convecting depth (meaning no convection extended from the ocean bottom) respectively.

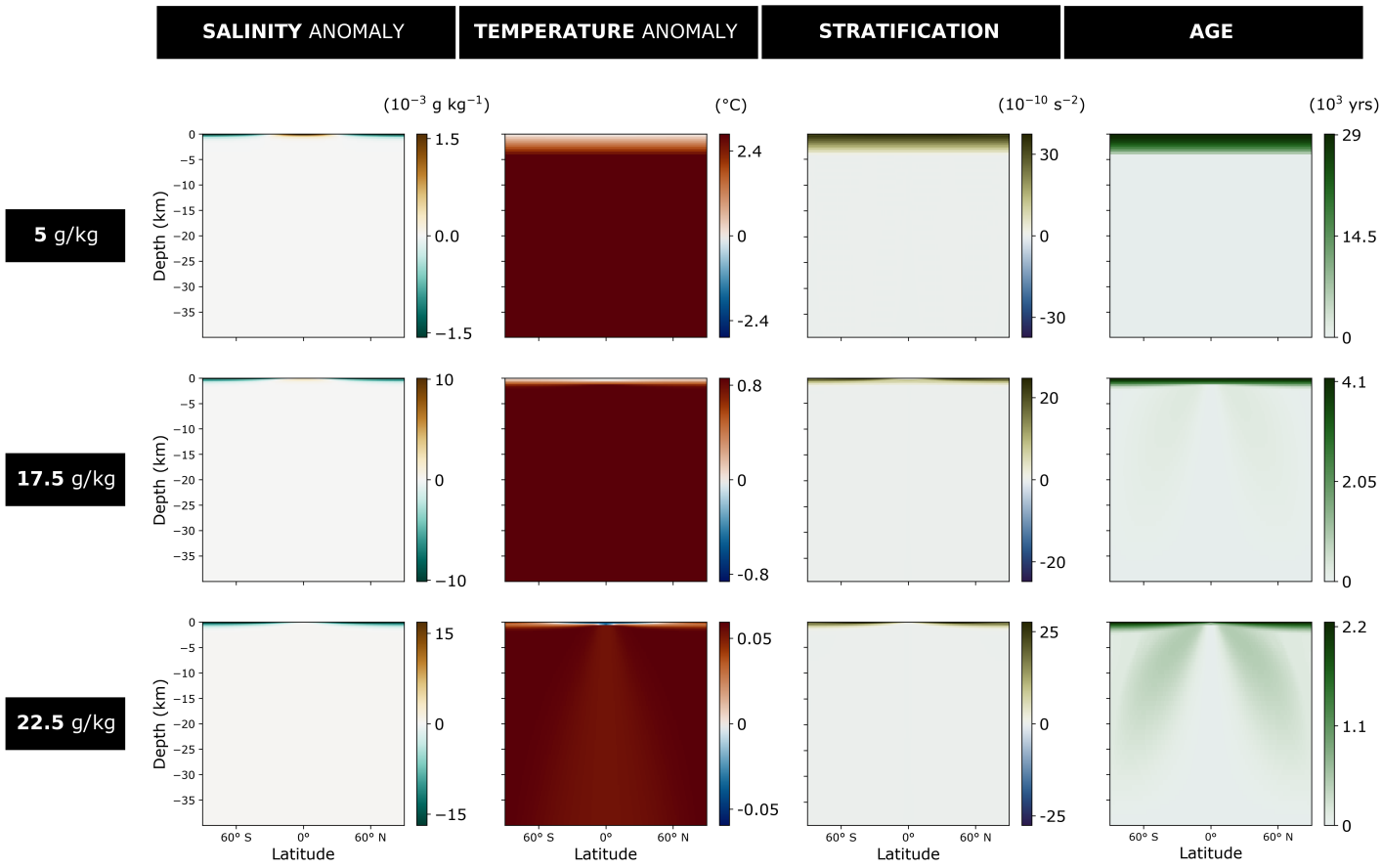

Figure 3.6: Numerical solutions with effective vertical diffusivity $\kappa_z = 10^{-5}$ m^2 s^{-1}, across three different mean ocean salinities of 5 (top), 17.5 (middle), and 22.5 (bottom) g kg^{-1}, highlighting stratification regimes at a lower κ_z than presented in the main text. Note colour bar scales are saturated and vary throughout. **First column**: Salinity anomaly (g kg^{-1}) taken about the mean salinity. **Second column**: Potential temperature anomaly (° C) taken about the simulation reference temperature T_{ref} (freezing temperature computed under 20 km mean ice thickness) of -0.433 (top), -1.106 (middle) and -1.379 (bottom) ° C. **Third column**: Buoyancy frequency N^2 (s^{-2}) indicating stratification. **Fourth column**: Ideal age of tracers (years), sourced from the ocean bottom.

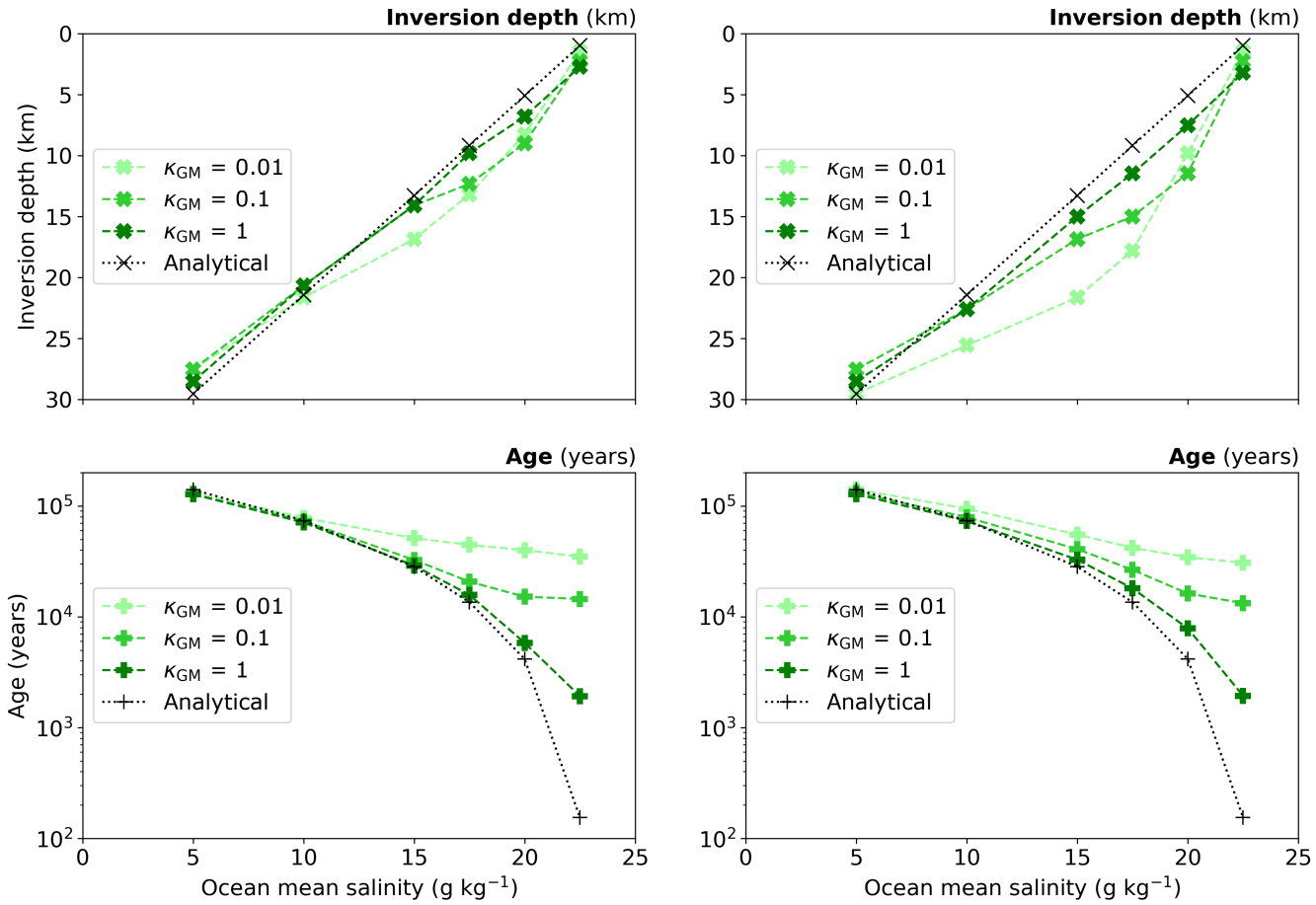

Figure 3.7: **Top**: Numerical solution for the inversion depth (km - depth at which the thermal expansion coefficient α_T becomes negative), as in Fig. 2 of the main text across a range of ocean mean salinity (g kg^{-1}), but plotted for three different values eddy diffusivity κ_{GM} (m^2 s^{-1}), indicated with varying shade of green, for constant vertical diffusivity $\kappa_z = 10^{-4}$ m^2 s^{-1}. The analytical solution (black) using Eq. (5) is plotted alongside for comparison. **Bottom**: Corresponding numerical solution for the ideal age at the south polar ocean-ice interface, plotted alongside the analytical solution (Eq. (6)). **Left**: Solutions at a melting viscosity $\eta_{\mathrm{melt}} = 10^{14}$ Pa s as used in default simulations of the main paper. **Right**: solutions with $\eta_{\mathrm{melt}} = 2\mathrm{x}10^{13}$ Pa s, which creates a 5 times larger magnitude of ice melting and freezing at the ocean top. Note increasing discrepancies relative to analytical solution at higher salinity and lower κ_{GM}, due to the formation of freshwater lenses at the ocean-ice interface at the poles.

3.4 Discussion and conclusions

In this work, we investigate ocean stratification within Enceladus' ocean and implications for the transport of hydrothermally-derived particulates and chemical species (tracers) to the south polar plumes. We develop analytical expressions for the stratification and corresponding tracer bottom-to-top transport timescales and test these successfully using a global ocean general circulation model. We explore a range of plausible salinity and tidally- and librationally-induced mixing κ_z, accounting for the non-linearities in the equation of state for water, geothermal heating and freshwater exchanges at the ocean-ice interface.

A key outcome of our study is that, regardless of the values of the salinity and mixing κ_z, there always exists ocean stratification that impedes transport to the south polar ice-interface. Ocean stratification within Enceladus is controlled to the first order by its ocean salinity, in combination with non-linearities in the equation of state for water density. Schematically, there are two limits:

- In the low salinity limit, permitting a negative α_T, cooling from the overlying ice shell stratifies the underlying ocean, as occurs in cold freshwater lakes on Earth (referred to as inverse stratification). Existing uncertainty in induced mixing yields stratification that could extend anywhere from 10s of metres to 10s of kilometres beneath the ice-interface (Fig. 3.2, upper left).

- At high salinities, enough to prevent α_T becoming negative, polar freshwater melt - required under the assumption of steady state - ensures the upper ocean remains stably stratified by freshwater lenses overlying a well-mixed ocean.

Crucially, the thinnest inverse layers and freshwater lenses are reached for low mixing rates, which are also inefficient at transporting tracers. As a result, transport timescales to the plumes do not fall below 100s of years (see Eqs. (3.1) and (3.8)). At the other end of the range, transport timescales could possibly exceed 100000 years (Fig. 3.2). In any case, such timescales provide opportunity for alteration between synthesis at depth and ejection out to space.

Our estimates are inconsistent with the inferences of several months made from Cassini observations of size-fractionated silica nanoparticles in Saturn's E-ring (Hsu et al. 2015). This discrepancy could possibly be explained by alternative particulate transport processes not considered here. For example, mechanisms associated with the opening of the plume

conduit could perhaps pull nano-particles up from underneath a stratified layer. Hydrogen gas bubbles have been suggested as an alternative nano-particle transport mechanism, but only when assuming an unstratified ocean (Zeng et al. 2022). It has also been suggested that size-fractionated silica nanoparticles could be produced by non-hydrothermal processes (Robinson et al. 2023), for example, photolytic decomposition of silica-saturated ice grains after ascent through the geyser conduit (Howell et al. 2023). If the source of observed nano-particles is not Enceladus' core, Cassini observations are not necessarily inconsistent with ocean stratification at Enceladus' south pole.

Alternatively, the discrepancy may suggest that our assumption of a steady state ice shell is incorrect. This assumption implies ice melting at the poles that maintains a stratification there and, as a result, large transport timescales, even in an otherwise predominantly convecting ocean. If Enceladus' ice shell is freezing at the poles, this could be sufficient to break down ocean stratification beneath the plumes. This would require that Enceladus' ice shell is not in a quasi-equilibrated state, which has been proposed owing to the inability of tidal heating models to reproduce the heating necessary to balance the observed heat outflow from Enceladus' south polar ice shell (Roberts and Nimmo 2008; Travis and Schubert 2015). These issues are currently being debated (see Roberts 2015; Choblet et al. 2017; Kang et al. 2022a; Kang et al. 2022b) and go beyond the scope of the present work.

Our work approaches the problem from a fluid dynamics perspective, complimentary to direct numerical simulations that can resolve much finer scale ocean dynamics (e.g., Soderlund 2019; Hartmann et al. 2024), but currently not the effects of ocean salinity and non-linearity in the equation of state for water density.

Our results emphasize that a robust evaluation of the stratification must use a non-linear equation of state that accounts for variation of the thermal expansion coefficient with temperature, salinity and pressure as well as account for the ice-ocean freshwater exchanges that create salinity gradients. We find that, under a steady state assumption and under observed constraints on geothermal heating and the shape of Enceladus' ice shell, there is no regime with bottom-to-top convection underneath the plumes. Future studies should make careful use of the assumption of a well-mixed ocean on Enceladus (and other icy moons).

We end in noting that stratification interfaces within Enceladus' ocean separate regions

with efficient and inefficient supply of hydrothermally-sourced nutrients - a dividing line for regions of ocean most favourable for life. This would also apply to other ice-covered moons, like Europa, where stratification interfaces could mark the predominant meeting point of hydrothermally-derived reductants from below with oxidants delivered from the ice shell above (Carnahan et al. 2022; Hesse et al. 2022). By constraining the extent of stratification in ice-covered oceans, further constraints upon their habitability could be obtained. In particular, improved constraints upon induced mixing within Enceladus' ocean would strongly reduce uncertainty in the transport of hydrothermally-derived tracers to the plumes.

3.5 Methods

3.5.1 Model configuration details

Numerical simulations are performed using the Massachusetts Institute of Technology Ocean General Circulation Model (MITgcm; Marshall et al. 1997b) configured for Enceladus. The MITgcm has been used previously to model the oceans of icy moons (Ashkenazy and Tziperman 2021; Zeng and Jansen 2021; Kang et al. 2022a) and the ice-covered ocean of Snowball Earth (Ferreira, Marshall and Rose 2011; Ashkenazy et al. 2014; Jansen 2016), which shares similarities with Enceladus' ocean.

The setup is fully non-hydrostatic, so that all components of the Coriolis force are considered - these were previously found to be important for icy moon ocean dynamics (Ashkenazy and Tziperman 2021; Kang et al. 2022a). The thin shell approximation is relaxed by turning on the MITgcm's deep atmosphere mode. This allows the model to more precisely represent Enceladus' ocean geometry which is of non-negligible thickness relative to its radius. Gravity is allowed to vary with depth in the model, using the formulation of (Kang and Jansen 2022):

$$g(z) = \frac{4\pi G[\rho_{\text{core}}(r_{\text{s}} - H_{\text{i}} - H_{\text{o}})^3 + \rho_{\text{oi}}((r_{\text{s}} - z)^3 - H_{\text{i}} - H_{\text{o}})^3]}{3(r_{\text{s}} - z)^2}, \tag{3.9}$$

where G = 6.67 x 10^{-11} m^3 kg^{-1} s^{-2} is the gravitational constant, ρ_{core} = 2370 kg m^{-3} and ρ_{oi} = 1000 kg m^{-3} the approximated mean densities of the core and ocean-ice (combined) layers respectively, r_{s} = 252 km the mean radius at the ice shell surface, z the ocean depth and H_{i} = 20 km and H_{o} = 40 km the mean thickness of the ice and ocean layers respectively (Hemingway and Mittal 2019).

The configuration is 2D, at a 1 degree ($\sim$ 4 km) meridional resolution with 50 layers in the vertical. The vertical resolution coarsens with depth via a hyperbolic tangent profile (Stewart et al. 2017), from $\sim$ 300 m at the ocean-ice interface, to $\sim$ 1000 m resolution at the ocean bottom. Finer resolution is used nearer the ice-interface to better resolve shallow stratified layers.

The coarse resolution employed, combined with the lack of a zonal dimension (which provide a necessary reduction in computational cost) means the effects of baroclinic eddies must be parameterised. Here we employ the GMREDI scheme, a flagship standard in

Earth ocean modelling. The parameterisation scheme consists of two components: firstly, the Gent-McWilliams (GM) component represents the adiabatic stirring effects of eddies (Gent and Mcwilliams 1990), using a bolus (i.e., eddy-induced) velocity (see Griffies 1998), parameterised as:

$$\boldsymbol{u}^* = \begin{pmatrix} u^* \\ v^* \\ w^* \end{pmatrix} = \begin{pmatrix} -\partial_z(\kappa_{\mathrm{GM}} S_x) \\ -\partial_z(\kappa_{\mathrm{GM}} S_y) \\ \partial_x(\kappa_{\mathrm{GM}} S_x) + \partial_y(\kappa_{\mathrm{GM}} S_y) \end{pmatrix}, \tag{3.10}$$

where S is the isoneutral slope (slope of locally referenced potential density) in the x or y directions (denoted by subscript), and κ_{GM} is the isopycnal diffusivity, also referred to as the GM or eddy diffusivity.

Secondly, the Redi component parameterises along-isopycnal mixing induced by meso-scale eddies using a tensor applied to the tracer field, also as a function of the isoneutral slope S (Redi 1982). In Earth ocean models, the small slope approximation is typically employed (i.e., $S << 1$). This yields the small slope Redi tensor (Griffies et al. 1998:

$$K_{\mathrm{redi}} = \begin{Bmatrix} 1 & 0 & S_x \\ 0 & 1 & S_y \\ S_x & S_y & |S|^2 \end{Bmatrix}. \tag{3.11}$$

We find this assumption to be inappropriate for icy moon oceanography where weak vertical gradients in ocean density can result in slopes orders of magnitude larger than those typically observed in Earth's oceans. Therefore, we employ the full unapproximated Redi tensor (Redi 1982, defined as:

$$K_{\mathrm{redi}} = \frac{1}{1+|S|^2} \begin{Bmatrix} 1+S_y^2 & -S_x S_y & S_x \\ -S_x S_y & 1+S_x^2 & S_y \\ S_x & S_y & |S|^2 \end{Bmatrix}. \tag{3.12}$$

A κ_{GM} of 1 $\mathrm{m}^2\ \mathrm{s}^{-1}$ is chosen, found to be near the upper bound of plausible eddy diffusivity values in the eddy resolving 3d simulations of (Zhang, Kang and Marshall 2024). This is chosen as a conservative estimate, given the referenced work did not consider freshwater fluxes from the overlying ice shell as done here, which could further enhance eddy activity. We perform sensitivity tests using lower values of κ_{GM} as described in the main text (fig. 3.7).

Due to the near infinite slopes that can develop in statically unstable regions, we

apply a slope clipping scheme which limits the magnitude of the GM streamfunction, $\psi_y = \kappa_{\mathrm{GM}} S_y$, above a slope of 5 to maintain numerical stability. While this introduces diabatic fluxes, it does so only in statically unstable regions which we find has negligible influence upon the penetration depth of a surface stratified layer. We argue this is more robust than the explicit horizontal diffusivity used in previous global simulations of icy moon ocean circulation which introduces (uncontrolled) diabatic fluxes that interfere with the effects of prescribed diapycnal mixing κ_z, rendering sensitivity experiments to mixing impractical.

For reference, numerical solutions for the vertically integrated meridional heat transport achieved by GMREDI are provided in fig. 3.8. Heat is transported equatorward, in qualitative agreement with previous work (Kang 2022; Zeng and Jansen 2024). When extrapolated to the full globe, the total meridional heat transport of $\sim$ 7-10 GW achieved by GMREDI is in approximate agreement with scalings by (Kang 2022) at $\kappa_z = 10^{-3}$ m^2 s^{-1}. Solutions at lower κ_z produce a larger meridional heat transport than predicted by existing scalings (possibly owing to the diabatic fluxes present within convecting regions, which are more extensive at low κ_z - see fig. 3.6). This is not expected to impact the conclusions presented in the main text.

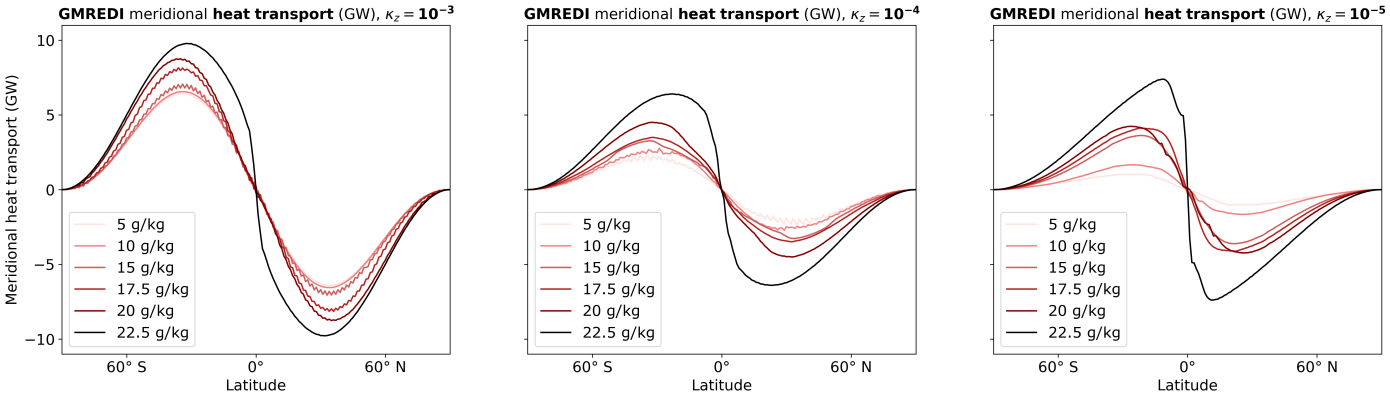

Figure 3.8: Vertically integrated global meridional heat transport (GW) achieved by parameterised eddies (GMREDI) in numerical solutions. Plotted across modelled ocean mean salinity at a modelled effective vertical diffusivity κ_z of 10^{-3} (left), 10^{-4} (middle), and 10^{-5} (right) m^2 s^{-1}. The eddy diffusivity $\kappa_{\mathrm{GM}} = 1$ m^2 s^{-1} for the presented solutions. Note the heat transports shown here are scaled up by a factor 360 to be representative of the global ocean (as the 2D simulations are based on a 1 degree wide single box in the zonal direction).

Convection is parameterised using a simple diffusive adjustment scheme, where vertical diffusivity is increased in regions of static instability to represent the vertical mixing of tracers that unresolved convection would have otherwise generated (Klinger, Marshall and Send 1996). We set this diffusivity to 1 m^2 s^{-1}, using the scaling of (Jones and Marshall 1993), assuming a buoyancy flux induced by our prescribed bottom heat flux (see below). A limitation is that this scheme inhibits slantwise convection (convection parallel to the axes of rotation) and Taylor columns that may be expected to occur on Enceladus (Goodman 2012). However, given our finding that ocean stratification extent is predominantly controlled by the vertical mixing κ_z and eddy induced mixing κ_{GM} (i.e., processes that can move heat within the stratified region of ocean), we argue this does not affect the robustness of the results and conclusions presented in the main text. Slantwise convection may alter the heat flux at the bottom of the stratified layer nearer the equator, where the rotation axis (and by extension, the direction of slantwise convection) tends towards being perpendicular to the vertical. This could enhance lateral variations in stratification extent. Future work focusing upon accurate representations of convection could determine if this is the case.

Parameters such as ocean depth, rotation rate, planetary radius and surface gravity are set to match those of Enceladus and are given in table 1. We assume a flat ocean bottom and make no attempt to include topography at the upper boundary at this stage, the former owing to lack of constraints (Hemingway and Mittal 2019), and the latter for simplicity.

A geothermal heat flux is applied at the bottom boundary. We borrow the formulation of (Zeng and Jansen 2021), which yields a bottom heating twice as large at the poles vs the equator, consistent with the tidal heating study of (Choblet et al. 2017):

$$Q_{\mathrm{core}}(\Theta) = \frac{F_{\mathrm{tot}}[0.5Y_{20}(\Theta) + K]}{4\pi K r_c^2}, \tag{3.13}$$

where $r_c = 192$ km is the core radius (radius to the ocean bottom), $K \approx 0.904$ a constant and Y_{20} a degree 2, order 0 spherical harmonic function (as a function of co-latitude Θ). A total core heat output of $F_{\mathrm{tot}} = 20$ GW is assumed. This is the mean value in the range suggested by (Choblet et al. 2017). The computed bottom heating profile is shown in fig. 3.3 (upper left).

Parameter	Value
Ice shell surface radius (r_s)	252 km
Core radius (r_c)	192 km
Ocean thickness (H_o)	40 km
Ice thickness (H_i)	20 km
Ice density (ρ_i)	925 kg m^{-3}
Gravity at ice shell surface (g)	0.113 m s^{-2}
Ocean mean salinity (S_ref)	5, 10, 15, 17.5, 20, 22.5 g kg^{-1}
Ocean reference pressure (P_ref)	$\rho_\mathrm{i} \int_{H_\mathrm{i}}^{0} g(z)\, dz$
Ocean reference temperature (T_ref)	Freezing temp at P_ref and S_ref
Ocean reference density (ρ_0)	Density at T_ref, P_ref and S_ref
Core density (ρ_core)	2370 kg m^{-3}
Rotation rate (Ω)	5.307 x 10^{-5} s^{-1}
Core total heat output (F_tot)	20 GW
Specific heat capacity (c_p)	4000 J kg^{-1} K^{-1}
Eddy diffusivity (κ_GM)	1 m^2 s^{-1}
Vertical diffusivity (κ_z)	10^{-5}, 10^{-4}, 10^{-3} m^2 s^{-1}
Prandtl number ($\frac{\nu}{\kappa}$)	10
Ice melting viscosity (η_melt)	10^{14} Pa s

Table 3.1: Key parameters used in default numerical simulations and in computation of boundary forcings in chapter 3

At the upper boundary we apply a fixed freshwater flux to simulate the effects of freezing and melting of an overlying ice shell. We follow the approach of (Kang et al. 2022a, by computing the flow rate of a prescribed ice shell geometry using the ice flow model of (Kang and Flierl 2020), then using the ice sheet divergence to compute an implied freezing rate (fig. 3.3). We use a sinusoidal curve to represent Enceladus' ice shell geometry in boundary forcing computations, with a mean thickness of 20 km, symmetrical about the equator where thickness is a maximum (10 km thicker than at the poles). While idealised, this captures the broad equator to pole variation that has been reconstructed from gravity, libration and shape data (Hemingway and Mittal 2019; Thomas et al. 2016; Iess et al. 2014) and suffices for our goal here of producing a reasonable approximation for the large-scale variations in freshwater fluxes at the ice-ocean interface. The flow of the ice shell is then computed using the following:

$$M(\phi) = -\frac{2g\frac{\rho_\mathrm{i}}{\rho_0}(\rho_0-\rho_\mathrm{i})H_\mathrm{ilat}^3}{r_\mathrm{s}\eta_\mathrm{melt} ln^3\left(\frac{T_\mathrm{s}}{T_\mathrm{f}}\right)}\frac{\mathrm{d}H_\mathrm{ilat}}{\mathrm{d}\phi}\int_{T_\mathrm{s}}^{T(z)}\int_{T_\mathrm{s}}^{T_\mathrm{f}} exp\left[\frac{-E_\mathrm{a}}{R_\mathrm{g}T_\mathrm{f}}\left(\frac{T_\mathrm{f}}{T_\mathrm{i}}-1\right)\right] ln\left(\frac{T_\mathrm{i}'}{T_\mathrm{f}}\right)\ \frac{dT_\mathrm{i}'}{T_\mathrm{i}'}\frac{dT_\mathrm{i}}{T_\mathrm{i}}, \tag{3.14}$$

where g is surface gravity, $\rho_\mathrm{i} = 925$ kg m^{-3} and ρ_0 the ice and ocean reference densities

respectively. H_{ilat} gives the thickness of the ice layer at a point latitude, r_{s} the mean radius of Enceladus, η_{melt} the ice melting viscosity (at the base of the ice shell), T_{f} and T_{s} the prescribed temperatures at the ice-ocean interface (freezing temperature) and surface respectively. T_{i}(z, ϕ) is the ice temperature (computed using Eq. (S7) from; Kang and Flierl 2020). $E_{\mathrm{a}} = 59.4$ kJ mol^{-1} is the activation energy for diffusion creep, $R_{\mathrm{g}} = 8.31$ J K^{-1} is the gas constant and $T_{\mathrm{i}}' = T_{\mathrm{i}}(z)$ is an integral variable (prime symbol used to distinguish the outer vs inner integral). The surface temperature T_{s} is computed using a radiative balance at the ice shell surface, given the solar constant at Saturn and assuming a surface bond albedo of 0.81 (Spencer et al. 2006), using the analytic approach of (Ashkenazy 2019). The profile for T_{s} is shown in fig. 3.3 (bottom left).

The implied freezing rate is then computed using the divergence of the ice shell flow:

$$q(\phi) = \frac{1}{r_{\mathrm{s}} \cos\phi} \frac{\partial}{\partial \phi}(M \cos\phi), \tag{3.15}$$

where ϕ denotes latitude. The freshwater flux profile is given in fig. 3.3 (bottom right), for an ice melting viscosity of 10^{14} Pa s. Freezing is largest at the equator where the prescribed ice geometry is thickest. Melting is largest nearer the poles where ice is thinner. Sensitivity tests, performed at a five times increased η_{melt} (corresponding to a five times stronger ice flow rate) yield similar solutions to that obtained in the main text, but with increased discrepancies relative to the theoretical model at lower κ_{GM} (fig. 3.7, right panel).

Temperature at the ocean top is restored to freezing point with a restoring timescale of 30 days. Recent studies have pointed to the importance of meridional temperature gradients at the ice shell (Kang et al. 2022a), particularly in generating baroclinic eddies which may contribute to ocean stratification (see Zhang, Kang and Marshall 2024). We therefore include this effect, by computing the salinity and pressure dependant freezing point implied by the same ice geometry used to compute our freshwater flux, using the formulation of (Millero 1978). This yields an ice-interface temperature about 0.1 °C warmer at the poles vs the equator (fig. 3.3, middle left). A linear drag coefficient of 10^{-4} m s^{-1} is applied at both the ocean top and ocean bottom. Viscosities are chosen to fix the Prandtl number at 10. Finally, we employ the fully non-linear equation of state of (Jackett and Mcdougall 1995 to capture important variations of ocean density (and α_T) with temperature, pressure and salinity.

All simulations are initiated from rest, at a uniform salinity (mean salinity) and reference temperature (freezing temperature assuming ice thickness H_{i}). Simulations are then run to equilibrium which, dependent on mean salinity and κ_z, takes anywhere between 10000-600000 model years to achieve.

3.5.2 Critical temperature computation and fitting

The following section details methods used to obtain a linear approximation for the critical temperature T_{crit} - the temperature at which the thermal expansion coefficient (α_T) changes sign for a given salinity and pressure.

T_{crit} is first obtained manually, by computing the temperature that coincides with a density maximum, across ranges in ocean salinity and pressures that permit α_T to change sign (0-25 g kg^{-1} and 0-28 MPa respectively). Water density is computed using the non-linear equation of state of (Jackett and Mcdougall 1995).

A multiple linear regression is then performed using the SciKit-Learn python package version 1.3.0 (Scikit-learn Developers 2024) to obtain coefficients for the linear approximation for the critical temperature:

$$T_{\text{crit}} \approx aS + bP + c, \tag{3.16}$$

where we find, a = -0.216 ^{o}C (g kg^{-1})$^{-1}$, b = -2.11 x 10^{-7} ^{o}C Pa^{-1}, and c = 4.01 ^{o}C (as shown in the main text). Given the dependence of T_{crit} upon pressure is slightly non-linear (Caldwell 1978), the regression is performed for pressures relevant to Enceladus, defined here to be 0-7 MPa. The upper bound is the approximate pressure under 60 km of ocean.

The linearly approximated critical temperature for Enceladus as a function of salinity and pressure is shown in fig. 3.9 (upper left). The anomaly relative to the manual computation is also shown (fig. 3.9, lower left). Mean absolute error relative to the manually computed T_{crit} is $\sim$ 0.01 ^{o}C.

A multiple linear regression is also performed for a range of larger pressures, from 12-28 MPa. The lower bound corresponds to pressures under 10 km ice on Jupiter's moon Europa - an ice-covered, ocean-bearing moon larger than Enceladus, and a target of upcoming missions (Grasset et al. 2013; Howell and Pappalardo 2020). Mean absolute error is again $\sim$ 0.01 ^{o}C. Coefficients in this case are: a = -0.221 ^{o}C (g kg^{-1})$^{-1}$, b = -2.28 x 10^{-7} ^{o}C Pa^{-1}, and c = 4.23 ^{o}C. The linearly approximated T_{crit} for Europa is shown in fig. 3.9 (right).

3.5.3 Critical temperature and freezing temperature comparison

Water freezing temperature, T_{f}, is computed in the 1D theoretical model as a linear function of ocean salinity and pressure at the ice-ocean interface:

$$T_{\mathrm{f}} = -0.055S - 0.753 \times 10^{-7} P + 0.008, \tag{3.17}$$

obtained by performing a multiple linear regression to the non-linear formulation of (Millero 1978). In doing so, Eqs. (3.3) and (3.17) take identical forms, enabling clarification of the contributions of T_{crit} and T_{f} to the inverse layer thickness (computed with Eq. (3.5) of the main text). Increasing ocean salinity and ice-interface pressure both act to cool T_{crit} and T_{f}, but the effects of doing so are three-four times stronger for T_{crit}. The constant is negligible in Eq. (3.17) compared to that in Eq. (3.3). Overall, this ensures that variations in T_{crit} dominate variations in T_{f} in influencing the inverse layer thickness. Lateral variations in T_{f} (e.g., as induced by variations in ice shell topography) are therefore expected to have little direct effect upon the inverse layer thickness, except where variations in T_{f} prevent α_T from changing sign in parts of the domain.

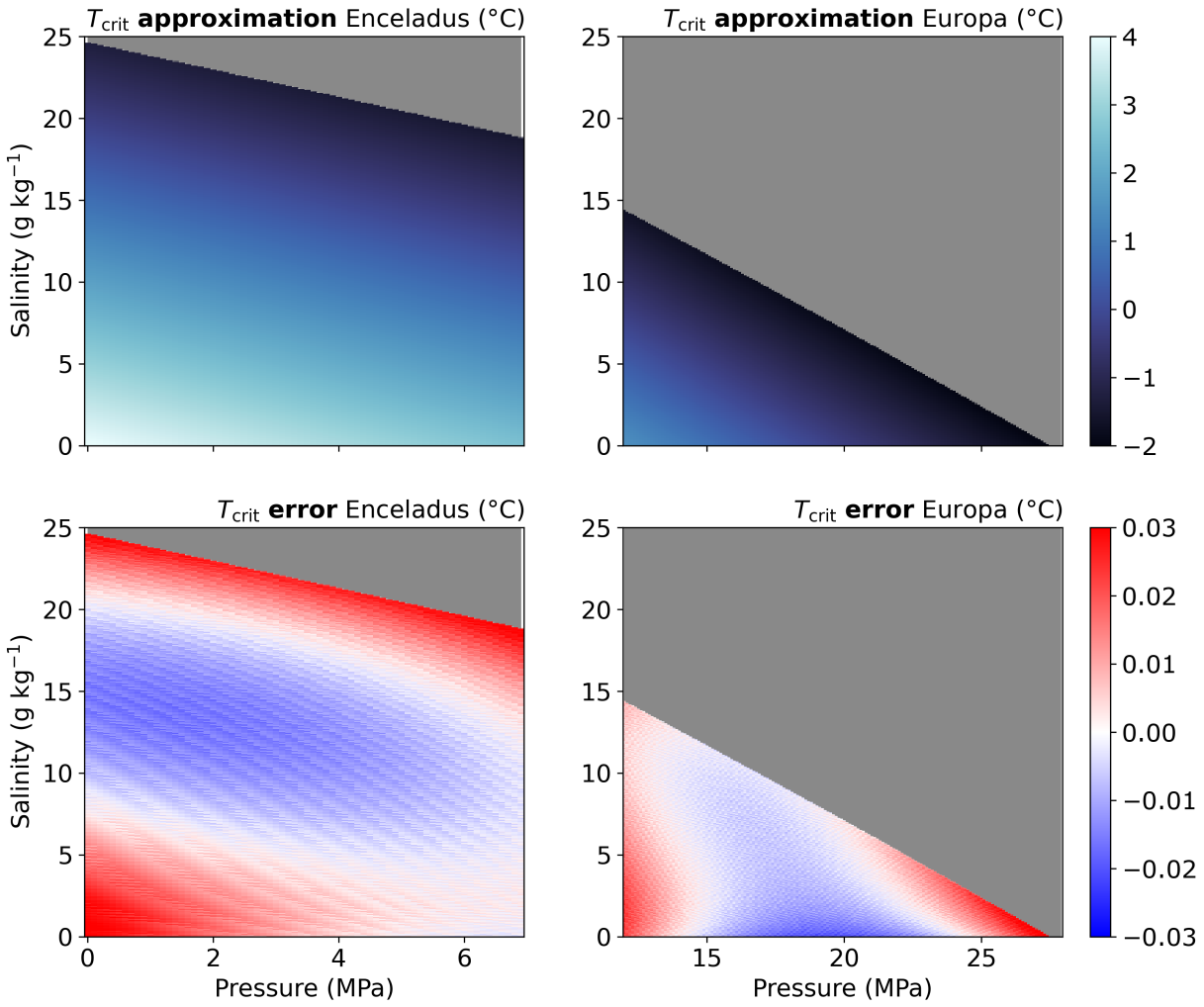

Figure 3.9: **Top:** Linearly approximated critical temperature (T_{crit} - ^{o}C) - defining the temperature at which the thermal expansion coefficient (α_T) changes sign - as a function of pressures (MPa) and salinity (g kg^{-1}) plausible for Enceladus (left) and Europa (right) respectively. Grey shading denotes where T_{crit} does not apply because α_T cannot become negative for the given salinity and pressure.
Bottom: Error of linear approximation of critical temperature (^{o}C) relative to reference computation described in the main text.

3.5.4 Application to other icy moons

The theoretical model of section 3.2 can be applied to other moons and planets permanently overlain by ice and heated from below. Fig. 3.10 shows the inversion depth and corresponding age at the ice shell for putative hydrothermally-derived tracers within Jupiter's moon Europa. For illustrative purposes, the inversion depth and age are shown for the same ranges in ocean salinity and κ_z as done for Enceladus in the main text. We assume an ice thickness of 10 km (Biersteker et al. 2023), and a bottom heat flux of 0.015 W m^{-2} (Howell 2021), nearer the lower bounds of estimates, to obtain upper bounds on the possible extent of inverse stratification in its ocean. Note that coefficients for the computation of T_{crit} are adjusted slightly as described in section 3.5.2.

For the assumed ice thickness and bottom heat flux, inverse stratification can only occur if ocean salinity is lower than $\sim$ 14 g kg^{-1}, nearer the lower bound of estimates for its ocean salinity (e.g., Hand and Chyba 2007). Using $H_{\mathrm{strat}} = (T_{\mathrm{crit}*} - T_f)/(-bg\rho_0)$, the maximum possible inverse layer thickness is approximately 8 km, regardless of the assumed bottom heating. Even so, the transport timescale through an inverse layer could still exceed 10000 years. This would also apply to materials entering Europa's ocean from above (Carnahan et al. 2022), for example oxidants delivered into Europa's ocean via ice shell brines (Hesse et al. 2022). It has been proposed that delivery of radiolytically-derived oxidants from Europa's ice surface into its ocean would improve the availability of redox gradients within Europa's ocean (compared to that in the presence of hydrothermally-derived oxidants alone), enhancing its habitability (Hand et al. 2020, and references therein). Yet, if such brines cannot penetrate the stratification, oxidant delivery into Europa's bulk ocean would be slowed. In this case, the extent to which oxidants remain concentrated within the inverse layer would depend upon the efficiency of vertical oxidant transport through the inverse layer, the frequency of brine pulses, and presence of sink mechanisms at depth.

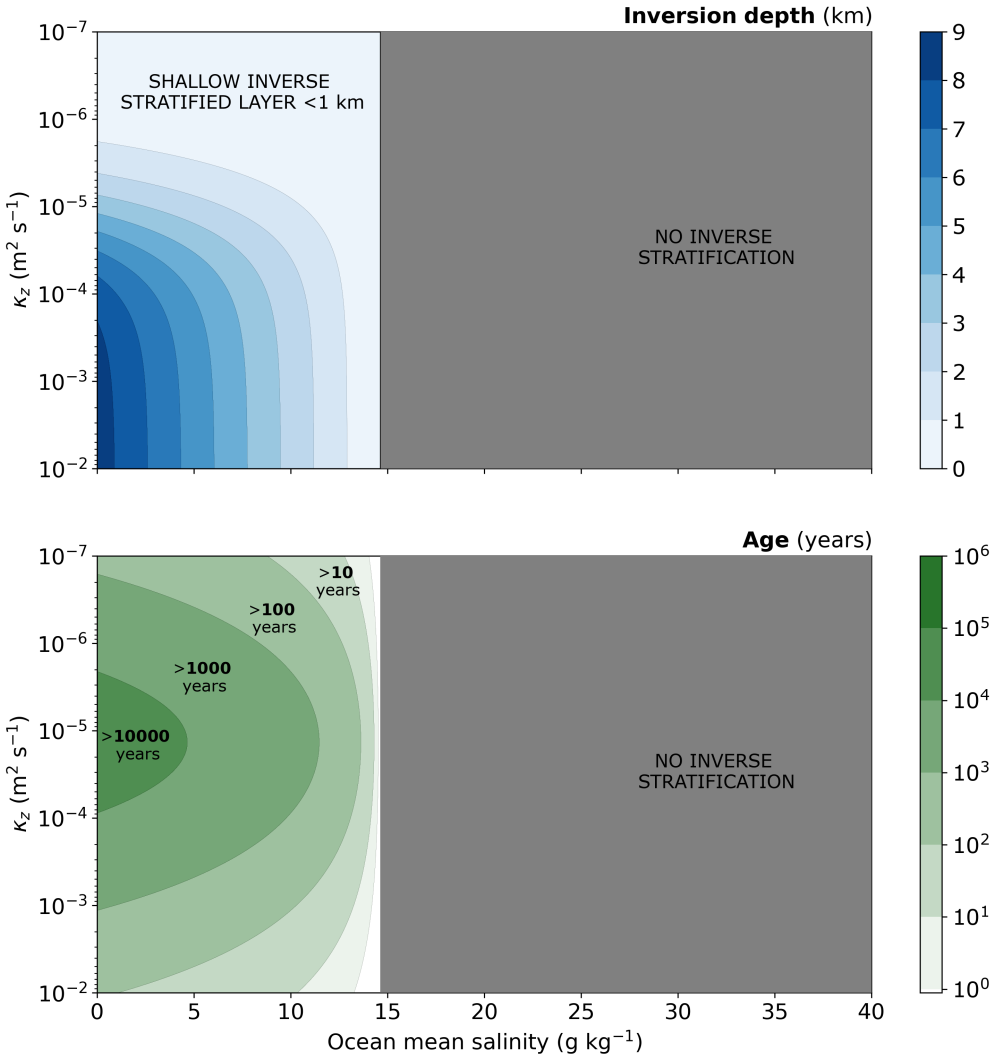

Figure 3.10: **Top**: Inversion depth H_{strat} (km - depth at which thermal expansion coefficient α_T becomes negative, taken here to define the inverse layer thickness) plotted as a function of ocean mean salinity (g kg^{-1}) and vertical diffusivity κ_z (m^2 s^{-1}), for Europa - moon of Jupiter. Grey shading denotes where inverse stratification cannot occur, because α_T cannot become negative at the ocean-ice interface pressure (computed under an assumed 10 km ice thickness). **Bottom**: Tracer age (years) at Europa's ocean-ice interface, computed using the theoretical model outlined in the main text. Note that age contours are logarithmic.

Data availability statement

The Data used during analysis and in creating the figures is openly available from the University of Reading Research Data Archive at https://researchdata.reading.ac.uk/id/eprint/1320

Code availability statement

Code and software, required to reproduce the data used in this manuscript, are openly available from the University of Reading Research Data Archive at https://researchdata.reading.ac.uk/id/eprint/1320. The MITgcm is open source and actively maintained at https://github.com/MITgcm/MITgcm/tree/master

Acknowledgements

F.A. acknowledges PhD studentship funding from the Science and Technology Facilities Council (STFC) grant ST/W507763/1. Fig. 3 uses colour-vision-deficiency-friendly and perceptually-uniform colour maps developed by (Crameri, Shephard and Heron 2020) (https://www.fabiocrameri.ch/colourmaps/). We thank W. Kang for providing constructive feedback on the manuscript.

Author contributions

F.A. derived the theoretical model; developed the numerical model configuration, designed the experiments, performed the numerical simulations, performed the data analysis and interpretation, and wrote the manuscript.

D.F. was the lead supervisor of the work. D.F. provided guidance on developing and using the model configuration; contributed ideas and provided guidance on the theory, experiment design and data analysis and interpretation. D.F. provided feedback on, edited, and made additions to the manuscript.

A.C. and A.M. were co-supervisors of the work - they contributed ideas and discussion that helped shape the concept for the manuscript. Both provided suggestions and feedback on the manuscript.

Chapter 4

Freshening of Enceladus' south polar ocean under steady state conditions

4.1 Introduction

The previous chapter explored ocean stratification within Enceladus assuming a mean ocean salinity no larger than $\sim$ 20 g kg^{-1} - the threshold above which negative thermal expansion coefficient (and thus inverse stratification) is inhibited. This assumption was made because 20 g kg^{-1} is the upper-bound estimate for Enceladus' ocean salinity obtained via Cassini observations of E-ring ice grains - believed sourced from the plumes (Postberg et al. 2009). Yet, it is plausible that Enceladus' mean ocean salinity could exceed this. Fractionation processes during plume formation could possibly act to dilute oceanic material contained within plume samples relative to the source of the plumes (Fox-Powell and Cousins 2021). The source water of the plumes could also, itself, be fresher than Enceladus' bulk ocean (Lobo et al. 2021). The latter motivates efforts to constrain ocean salinity in waters beneath plumes.

If Enceladus' ice shell is in steady state, freshening of the south polar ocean is expected because melting would be required in this instance to balance the polewards induced ice flow (Čadek et al. 2019). Estimates for the magnitude of potential freshening have been provided by studies exploring the implications of ice shell freshwater fluxes upon ocean circulation. These include Lobo et al. (2021), who suggested a relative freshening up to $\sim$ 2 g kg^{-1} is possible for Enceladus' south polar ocean, and Kang et al. (2022a), who obtained freshening no larger than 0.01 g kg^{-1} in their simulations. The large difference in these estimates likely arise from the disparate model setups and choices of uncertain mixing parameters. The freshening estimate of Lobo et al. (2021) was inferred from a 5-layer isopycnal model (where buoyancy, rather than salinity, was the prognostic variable). The Earth-like eddy diffusivity values and buoyancy fluxes (Marshall and Schott 1999) employed by Lobo et al. (2021) - likely at least three orders of magnitude too large for Enceladus' ocean (Kang et al. 2022a; Zhang, Kang and Marshall 2024) - ensured freshwater anomalies remained confined within 1 km of the ice interface across the south polar ocean. Meanwhile, Kang et al. (2022a) employed the MITgcm (with salt as a prognostic variable), prescribing an ice melting and freezing given that required to balance the poleward induced ice flow in steady state. They employed strong κ_z of 5×10^{-3} m^2 s^{-1}, at or slightly exceeding the expected upper bounds for Enceladus (Zeng and Jansen 2021; Zhang, Kang and Marshall 2024). This ensured salinity anomalies derived from the ice shell were mixed through the entire ocean depth.

The previous chapter explicitly modelled ocean salinity anomalies within Enceladus'

ocean across existing ranges of uncertainty for mixing parameters (Zeng and Jansen 2021; Zhang, Kang and Marshall 2024), but did not discuss them in detail. A maximum relative freshening of order 0.1 g kg^{-1} was obtained for the lowest κ_z tested ($\kappa_z = 10^{-5}$ m^2 s^{-1}), and relative freshening can be seen to vary approximately proportionally with κ_z, suggestive of a sensitivity to mixing parameters. However, the upper boundary of the model was assumed flat, and so its effects upon the ocean stratification, and topographic confinement of salinity anomalies, were not considered.

As far as this author is aware, the following chapter is the first dedicated effort to constrain the relative freshening of Enceladus' south polar ocean, and its sensitivity to mixing parameters and to the mean salinity of Enceladus' ocean. This chapter also extends upon the previous by exploring the effects of upper boundary height variation upon Enceladus' ocean stratification. In doing so, the inverse stratification theory is also tested in a more realistic case. Note that as in the rest of this thesis, steady state is assumed.

4.2 Scaling for the freshening of Enceladus' south polar ocean

Theoretical models for the stratification at Enceladus' poles, imparted by laterally varying buoyancy forcing, have so far focused upon constraining the penetration of stratification forced by meridional temperature gradients at Enceladus' ice-ocean interface, under the assumption of positive thermal expansion coefficient (α_T; i.e., mean ocean salinity greater than $\sim$ 20 g kg^{-1}) (Kang 2022; Kang 2023; Zhang, Kang and Marshall 2024). Where $\alpha_T > 0$, warmer ice-interface temperatures at the poles act to stratify the ocean here relative to cooler waters at the equator, owing to the pressure-dependence of water's freezing temperature. Because the freezing temperature of ice does not depend upon processes in the ocean below, the temperature (and thus buoyancy) gradient at the ocean top can be computed directly as a function of the observationally-constrained ice thickness. Yet, many previous studies have noted that salinity gradients are more likely to dominate density gradients (and thus stratification) within Enceladus' ocean where $\alpha_T > 0$ (e.g., Zeng and Jansen 2024; Ames et al. 2025). The buoyancy gradient at the ice-interface is more difficult to constrain in this case because salinity at the ocean top depends upon mixing processes within the ocean. In the following section, we explore the case where steady state is satisfied and ocean salinity gradients dominate gradients in ocean density. It will be shown later that this assumption is reasonable when assuming positive α_T, but not in cases where α_T is negative, and mixing parameters are strong.

Zhang, Kang and Marshall (2024) describe how the penetration of stratified waters, sourced from the ocean top, into the ocean interior is controlled by the slope of associated density contours (isopycnals):

$$D \sim SR \tag{4.1}$$

where S is the isopycnal slope and R the horizontal length scale (m) of the slope. Furthermore, they highlight how the isopycnal slope is, in turn, controlled by the ratio between κ_{GM} and κ_z:

$$S \sim \sqrt{\frac{\kappa_z}{\kappa_{GM}}} \tag{4.2}$$

κ_{GM} represents mixing by ocean eddies. Ocean eddies flux water along isopycnals, acting to homogenise lateral density gradients and flatten isopycnal slopes, reducing their

vertical penetration.

κ_z represents processes that can flux across isopycnals. κ_z includes molecular diffusion, but could be made far more efficient via mixing induced by tidal and librational energy dissipation (Zeng and Jansen 2021). Fluxes across isopycnals steepen their slope, increasing their penetration into the ocean interior. Using Eq. (4.1) for an ocean with a flat upper boundary (as assumed in Zhang, Kang and Marshall 2024), and molecular κ_z ($\sim 1.4\times10^{-7}$ m^2 s^{-1} for heat and $\sim 1.5\times10^{-9}$ m^2 s^{-1} for salt; Wunsch and Ferrari 2004) combined with strong κ_{GM}, would result in an increasingly thin boundary layer, as the isopycnals slope tends to zero.

The upper boundary height of Enceladus' is not expected to be flat, but instead expected to vary by as much as its mean thickness from equator to pole (Hemingway and Mittal 2019; Čadek et al. 2019). This means that any forcing of buoyancy at the ice interface would be imparted at a varying depth in the ocean. In this case, if buoyancy at the ocean top is assumed to follow the ice thickness gradient (strongest where ice is thin), isopycnal slopes of zero here would be expected to result in a stratified layer filling the south polar ocean down to the base of the ice shell, even in the case of a molecular κ_z.

Before going further, it is important to verify the pattern of freshwater forcing at the ice top expected under steady state. Fig. 4.1 illustrates Enceladus' longitudinally-averaged ice thickness profile constrained from Cassini data (Čadek et al. 2019). From this, the flow rate of the ice can be computed, and then its freezing rate. The ocean upper boundary height can also be inferred assuming Airy isostasy (that ice is floating on water). These are also plotted in fig. 4.1.

Enceladus' ice thickness profile exhibits significant meridional asymmetry, thickest slightly southward of the equator, thinnest at the south pole. Importantly, there is a varying meridional *gradient* of ice thickness, steepest in the southern hemisphere, flattening nearer the poles. This has consequence for the ice freezing rate - a function of ice flow divergence at steady state, not the ice thickness. Ice melting rates are expected to peak in the mid-latitudes, tending to zero nearer the poles. In fact, a very weak (but non-zero) freezing is predicted polewards of $\sim$ 85 degrees in the northern hemisphere, highlighting the need for care in assuming ice melting always occurs where ice is thinner. Yet despite these caveats, when using the observationally constrained Enceladus ice thickness profile under the assumption of steady state, melting is always predicted to occur higher up in the

water column than freezing in Enceladus' southern hemisphere. This suggests a freshwater stratified layer (lens) within Enceladus' south polar ocean, extending to the ice base, could be plausible under steady state. This scenario is illustrated in fig. 4.2 and explored in this chapter.

Above the ice base, flattened isopycnals would not intersect with regions of freezing below and along-isopycnal mixing via κ_{GM} may prove inefficient at mixing fresher polar waters with saltier (owing to brine rejection from freezing) equatorial waters. If this is the case, and in the absence of penetrative convection, the mixing of salt into the freshwater lens would require across-isopycnal mixing, i.e., κ_z. Where κ_z is weak, a significant relative freshening of this region of ocean could be plausible.

With knowledge of κ_z and assuming a time-steady salinity within the freshwater lens, the salinity anomaly of the lens vs the bulk ocean can be derived. For this derivation, we make two assumptions, firstly that the salt budget of the lens is controlled by 'removal' of salt via melting at the ice interface, and input of salt via processes parameterised via κ_z at the bottom of the lens. We then assume a lens that extends no deeper than the deepest point of ice within the ocean (For Enceladus, where the lens extends deeper than this, we expect an error in this approximation no larger than $\sim$ factor 2). For simplicity, we also assume the freshwater lens can be represented as a singular layer of uniform thickness across its latitudinal extent.

The rate of freshening i.e., salinity loss (S_{out}; g kg^{-1} s^{-1}) within a freshwater lens, owing to ice melting at its top, can then be approximated using the resultant salinity restoring:

$$S_{out} \approx \frac{-qS_{int}\rho_{fresh}}{\rho_0 H_{lens}} \tag{4.3}$$

where q is the ice *freezing* rate (defined as such to ensure consistency with its definition in the rest of this thesis), ρ_{fresh} the reference density of freshwater (kg m^{-3}), ρ_0 the reference ocean density, S_{int} (g kg^{-1}) the local ocean salinity at the ice interface where melting is occurring, and H_{lens} (m) the thickness of the freshwater lens, taken here as the difference in ice thickness between the south pole and latitude of maximum thickness.

The rate of salinification i.e., salinity gain in the freshwater lens (S_{in}) arising from processes encapsulated by κ_z, can be approximated assuming the salinity minima and

maxima arise at the top and bottom of the lens respectively. Here we assume a well-mixed ocean at depth where the salinity maxima does not deviate significantly from the ocean's bulk salinity S_0. We also assume a uniform κ_z within the lens for simplicity. These assumptions yield:

$$S_{in} \approx \frac{\kappa_z (S_0 - S_{int})}{H_{lens}^2} \tag{4.4}$$

Letting $S_{int} - S_0 = S_{anom}$ (where S_{anom} is the salinity anomaly of the freshwater lens vs the bulk ocean) and noting $\frac{\rho_{fresh}}{\rho_0} \approx 1$ in Eq. (4.3), we can approximate the salinity budget of the lens at steady state letting the salt output (Eq. (4.3)) equal the salt input (Eq. (4.4):

$$qS_{int} \approx \frac{\kappa_z S_{anom}}{H_{lens}} \tag{4.5}$$

Given our assumption that $S_{int} = S_{anom} + S_0$, the above can be rearranged for the salinity anomaly of the freshwater relative to the bulk ocean:

$$S_{anom} \approx \frac{S_0 q H_{lens}}{(\kappa_z - q H_{lens})} \tag{4.6}$$

In Eq. (4.6) an increased melting (negative q) increases the relative freshening of the lens, as expected. Increasing S_0 increases relative freshening, because there is greater potential for a larger salinity anomaly to arise. A greater thickness of the lens also acts to increase the salinity anomaly vs the bulk ocean, as vertical diffusion of salt upwards must occur over greater vertical scale within this stratified region. Increasing the efficiency of tidally- and librationally-induced mixing reduces the relative freshening of the lens. As κ_z tends to its molecular value, and q tends to ∞, S_{anom} tends to $-S_0$.

4.2.1 Scaling results

Fig. 4.3 illustrates the relative freshening of Enceladus' ocean as a percentage of the ocean mean salinity S_0, computed using Eq. (4.6). q is taken as the mean freezing rate southwards of Enceladus' ice thickness maxima in fig. 4.1. This is $\sim 2 \times 10^{-11}$ m s^{-1}. The freezing rate scales linearly with ice melting-point viscosity (η_{melt}) in Eq. (2.12). This parameter is poorly constrained at Enceladus, dependent upon grain sizes at the base of the ice shell (Čadek et al. 2019). Studies of tidally-heated icy moon shells suggests plausible η_{melt} of 10^{13}-10^{16} Pa s (Tobie, Choblet and Sotin 2003; Čadek et al. 2017). Relative

freshening is therefore plotted across this range in η_{melt} by scaling the default q (which assumes $\eta_{melt} = 10^{14}$ Pa s in the reference case) accordingly and uniformally. Relative freshening is also plotted across the range of uncertainty in κ_z in Enceladus' ocean suggested by Zeng and Jansen (2021).

Fig. 4.3 illustrates the strong control of κ_z upon the salinity anomaly. Where κ_z is its molecular value ($\kappa_S \approx 1.5{\times}10^{-9}$ m^2 s^{-1}; Wunsch and Ferrari 2004) - representing a case where tidal and librational energy dissipation do not significantly contribute to vertical mixing in Enceladus' ocean - Eq. (4.6) predicts a relative freshening of Enceladus' south polar ocean between $\sim$ 40% and $\sim$ 90 % across the range of η_{melt} illustrated in fig. 4.3. In the opposite case where tidal and librational energy dissipation raise κ_z in Enceladus ocean, relative freshening could fall well below 1 %.

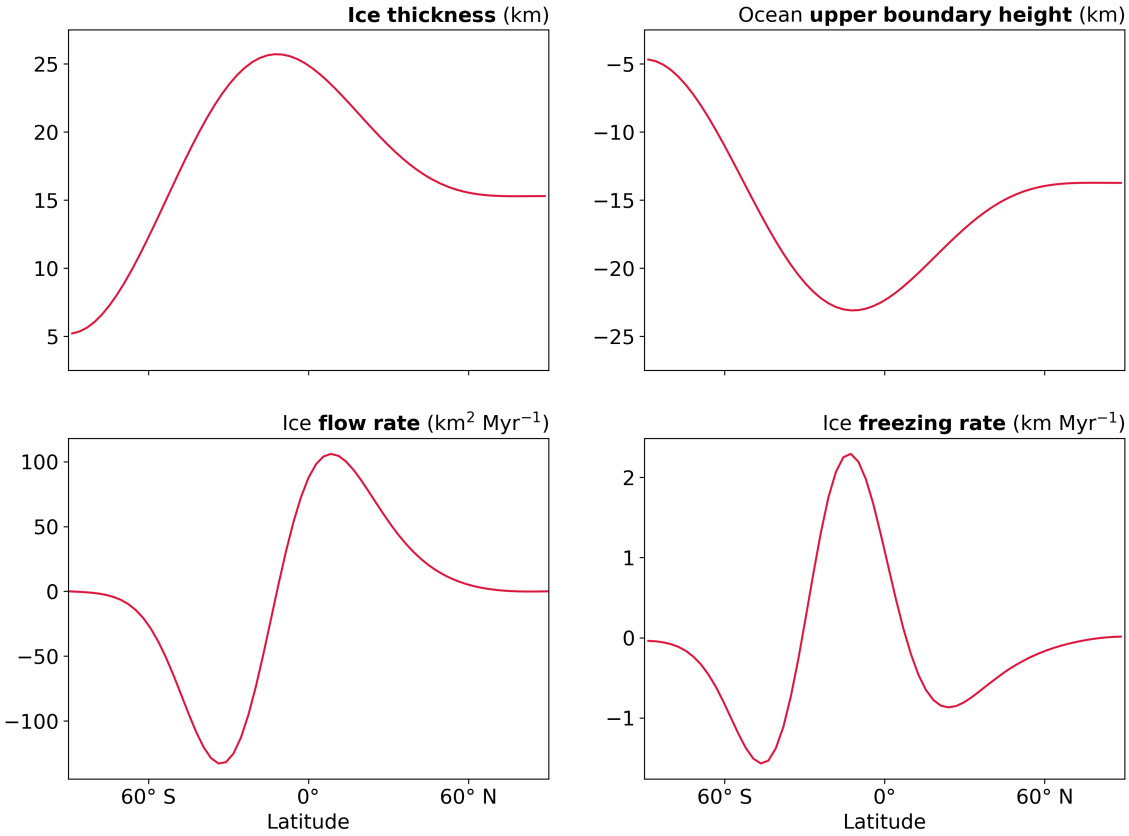

Figure 4.1: Top left: Enceladus' longitudinally-averaged ice thickness (km), reconstructed from Cassini data, using spherical harmonic coefficients from Čadek et al. (2019). Top right: Corresponding upper boundary height in the ocean (km), referenced to Enceladus' mean radius of 252 km, computed assuming Airy isostasy (i.e., the ice shell is floating on the ocean). Bottom left: Flow rate of Enceladus' ice shell (km^2 per million years), computed given the ice thickness profile in the upper right panel, using Eq. (2.12), following Kang and Flierl (2020). Bottom right: Freezing rate (km per million years) of the ice shell, computed given the divergence of the ice flow illustrated in the bottom left panel. Note that the ocean upper boundary height, ice flow, and ice freezing rates illustrated here assume an ocean salinity of 35 g kg^{-1} when computing the reference ocean density.

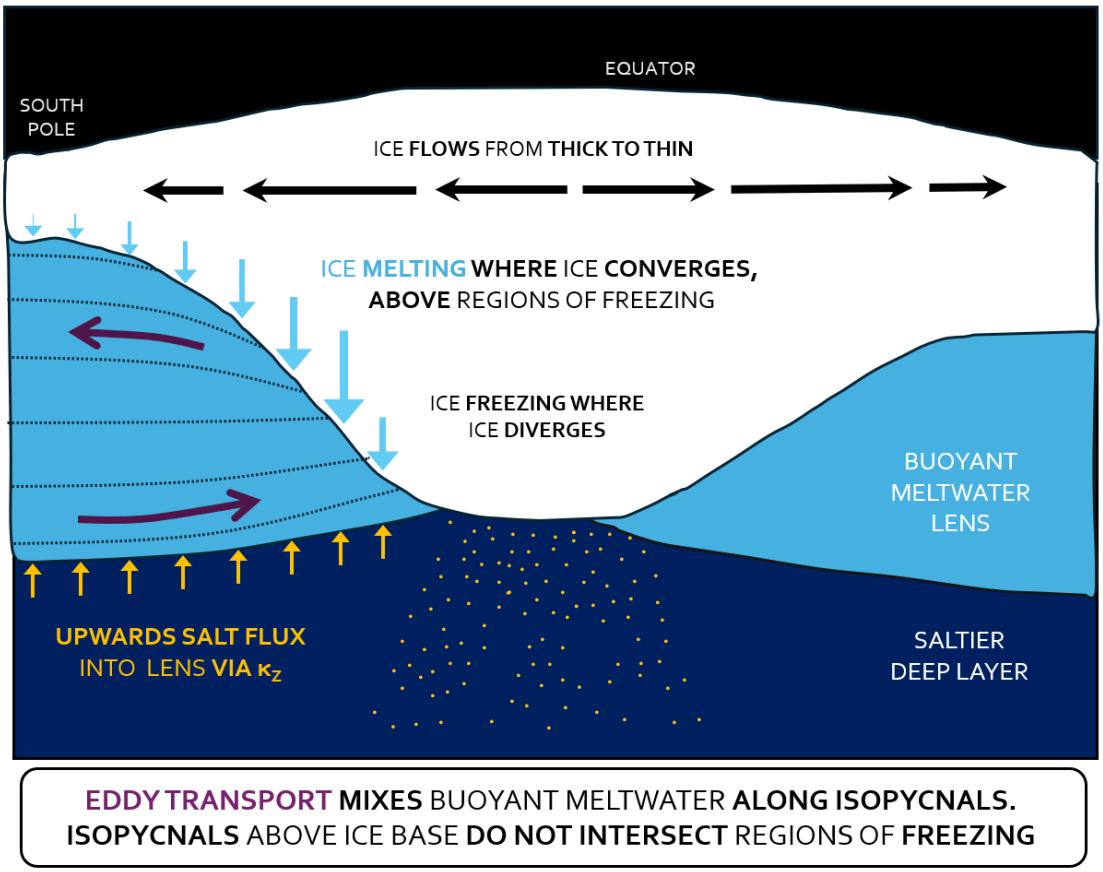

Figure 4.2: Illustrating an idealised Enceladus ocean and steady state ice shell, assuming ocean salinity gradients dominate gradients in ocean density. Enceladus' ice shell is expected to flow (black arrows) down the pressure gradient from where it is thick (near the equator) to where it is thin (e.g., at the south pole; see fig. 4.1). Under steady state, ice would need to melt (indicated with blue arrows) where its flow converges, to maintain the observed thickness profile. Ice convergence would occur in regions of thinner ice, strongest equatorwards of the south pole (see fig. 4.1). As a result, melting occurs only above regions of freezing here, enabling the development of a stratified freshwater lens (light blue shading) in the south polar region, no shallower than the depth of deepest ice melting. Within the lens, lateral gradients in freshening (and thus water density) would energise baroclinic eddies, which would then mix freshwater along the slope of isopycnals (contours of constant density). Because isopycnals would not intersect regions of freezing in this case, eddies would not efficiently mix fresher water aloft with saltier water associated with regions of freezing (yellow dots) nearer the equator. Instead, transport of salt into the freshwater lens (yellow arrows) would likely be controlled by processes encapsulated by κ_z, including molecular diffusion, along with putative mixing induced by tidal- and librational- energy dissipation. If κ_z is weak, significant freshening of the south polar ocean could plausibly arise, yielding salt concentrations within plume material (e.g., Postberg et al. 2009) fresher than the bulk ocean. The schematic here contrasts those of Zhang, Kang and Marshall (2024) and Lobo et al. (2021), where the buoyancy maximum is assumed to occur at the pole, and thus the eddy overturning circulation is not predicted to reverse orientation in the freshwater lens as predicted here.

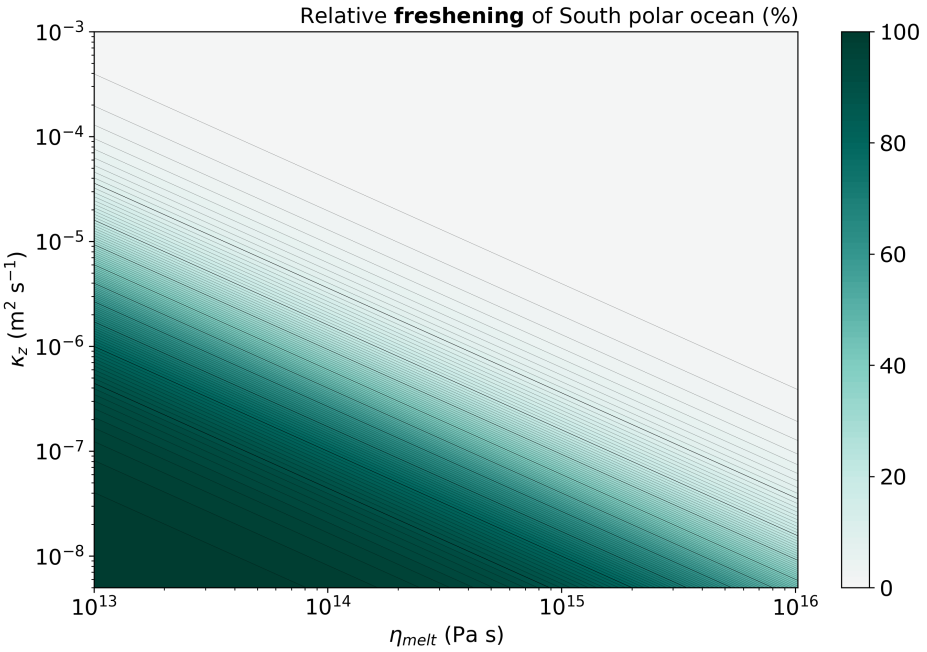

Figure 4.3: The relative freshening of Enceladus' south polar ocean as a percentage of its bulk-mean ocean salinity, computed using Eq. (4.6). Plotted across ranges of uncertainty in effective vertical ocean diffusivity κ_z (m^2 s^{-1}; Zeng and Jansen 2021; Zhang, Kang and Marshall 2024) and ice melting viscosity η_{melt} (Pa s; defining the viscosity at the bottom of the ice shell; Tobie, Choblet and Sotin 2003; Čadek et al. 2017). The thickness for the freshwater layer is assumed 20 km, corresponding to the approximate variation in ocean upper boundary height within Enceladus' southern hemisphere. Thinner and thicker contours denote increments of 1 and 10 % respectively. Note that both axis are logarithmic.

4.3 Numerical simulations

The previous section assumed ocean stratification dominated by salinity gradients. Yet, previous work has noted that temperature gradients can dominate stratification where $\alpha_T < 0$ (Zeng and Jansen 2021; Ames et al. 2025). The following section details numerical simulations performed to determine the validity of Eq. (4.6), as well as to explore competing mechanisms for ocean stratification, in oceans of positive and negative α_T near an ice interface of varying height.

4.3.1 Methods: model configuration

Numerical simulations are performed using the MITgcm in a 2D latitude-depth configuration. The model is identical to that used in the previous chapter except for the differences outlined below.

The ice flow rate (in turn used to compute the ice freezing rate) is computed using Enceladus' realistic longitudinally-averaged ice thickness profile, derived from Cassini gravity, shape and libration data. The degree three spherical harmonic model of Čadek et al. (2019) is employed (fig. 4.1). The freezing rate is then converted to a salinity restoring as a function of the local salinity at the ice interface. This is to permit a more precise estimation of the polar freshening by permitting a negative feedback mechanism between freshening of the ocean and its ability to be freshened further for constant ice melting.

The upper boundary height of the ocean is allowed to vary assuming Airy isostasy and defined relative to sea level - taken here as Enceladus' mean radius (fig. 4.1). This permits a variation in height of the imposed freshwater and temperature forcings at the ocean top. Note that because of the relaxation of the thin shell approximation in our ocean model, a small adjustment to the imposed freezing rate is necessary to maintain a balance in the freshwater budget at the ocean top and avoid a drift in mean salinity. This has negligible effects upon the solution.

Ice-interface restoring temperature is computed interactively within the model as a function of in-situ salinity and pressure at the top of the ocean, using the non-linear formulation of Millero (1978). This differs to the previous chapter in which idealised experiments used a constant reference salinity to compute the salinity restoring. Using the formula of Millero (1978), a 1 g kg^{-1} freshening of salinity yields a ~ 0.05 °C warming

of the interface temperature, providing a negative feedback mechanism for the control of salinity upon ocean density (strong freshening of the ocean nearer the poles raises the polar ice interface temperature, enhancing the equator-to-pole temperature gradient). The ice-interface restoring temperature at equilibrium is plotted at 35 g kg^{-1} across three solutions in fig. 4.4 to illustrate this.

The lateral resolution of the model is 2.8125 degrees - coarse but necessary to enable equilibration of solutions at lower κ_z. The vertical resolution in the ocean is 550 m down to the ice base, thickening via a hyperbolic tangent profile to $\sim$ 2000 m at the ocean bottom (Stewart et al. 2017). Finer vertical resolution is used nearer the ice shell to better resolve the freshwater lens here. Ice is allowed to occupy increments of 20 % of the grid cell height, to permit a more precise representation of the topography.

Experiments are performed for two mean salinity values: 5 and 35 g kg^{-1}. The former represents a lower bound estimate for Enceladus' salinity inferred from Cassini observations of E-ring ice grains (Postberg et al. 2009). The latter represents an Earth-like salinity, which Eq. (4.6) predicts could plausibly be reconciled with observations if Enceladus' south polar ocean is significantly freshened relative to the bulk ocean (see fig. 4.3). Experiments are performed across vertical diffusivity $\kappa_z = 10^{-3}$, 10^{-4}, and 10^{-5} m^2 s^{-1}. Modelling lower κ_z is computationally prohibitive owing to long diffusive adjustment timescales within the freshwater lens. κ_z is assumed uniform in the ocean and potential double-diffusive effects (Schmitt 1994) are therefore excluded at this stage.

Eddy diffusivity likely varies spatially in Enceladus' ocean, as a function of κ_z and local buoyancy gradients. Given these are poorly constrained in Enceladus' ocean, we assume a uniform κ_{GM} and perform experiments at $\kappa_{GM} = 0.01$, 0.1 and 1 m^2 s^{-1} - within a range found plausible for Enceladus in the eddy resolving simulations of Zhang, Kang and Marshall (2024).

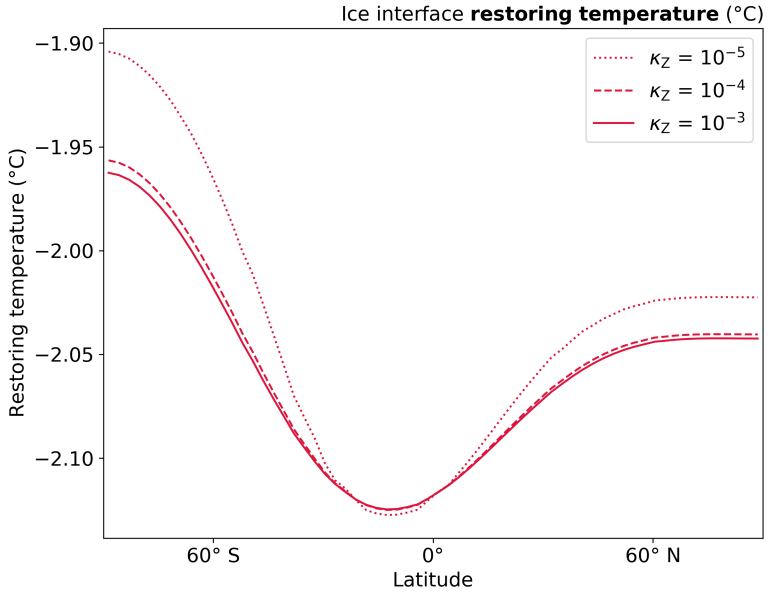

Figure 4.4: The restoring temperature at the ice-interface at equilibrium for three solutions at 35 g kg^{-1} mean salinity, and vertical diffusivity $\kappa_z = 10^{-3}$, 10^{-4} and 10^{-5} m^2 s^{-1}. The restoring temperature is the water freezing temperature, computed interactively as a function of the local salinity and pressure (Losch 2008).

4.3.2 Results: high salinity

Fig. 4.5 illustrates the volume-weighted salinity anomaly at the ice interface of the south polar region for numerical solutions at 35 g kg^{-1}. Here, the south polar region is defined as the ocean polewards of 60°S, corresponding to the source region of the plumes (Porco, DiNino and Nimmo 2014). Also shown is the penetration depth of the freshwater lens into the ocean interior at the south pole. This is defined as the depth at which the vertical salinity gradient $\frac{dS}{dz}$ falls below $\frac{1}{e}$ times its maximum value (which, excluding cases where the lens extends the full ocean depth, arises at the depth of maximum melting).

Numerical solutions for freshening of the south polar ocean show good agreement with Eq. (4.6). Freshening scales approximately inversely with κ_z, with salinity anomalies of order 0.01, 0.1 and 1 g kg^{-1} for κ_z of 10^{-3}, 10^{-4}, and 10^{-5} m^2 s^{-1} respectively. The freshening also scales approximately proportionately with the ice melting viscosity, with salinity anomalies of order 0.01, 0.1, and 1 g kg^{-1} for η_{melt} of 10^{15}, 10^{14} and 10^{13} Pa s, at the tested κ_z. In contrast, there is only a minor role for κ_{GM} in controlling the magnitude of salinity anomaly in the presented numerical solutions.

The penetration depth of the freshwater lens at the south pole increases with increasing κ_z, and decreasing κ_{GM}, as previously suggested (Zhang, Kang and Marshall 2024) and predicted by Eq. (4.1). For the weakest κ_{GM} tested, penetration depth scales approximately proportionately with κ_z. This relationship is not obtained at larger κ_{GM}, where the penetration depth tends towards the ice shell base as κ_z is reduced. The penetration depth does not exhibit significant variation with ice melting viscosity, despite significant variation in freshening magnitude. This contrasts with the results of Zhang, Kang and Marshall (2024), who found that strengthening the lateral buoyancy gradient at the ocean top reduces its penetration into the ocean interior. The reason is likely because κ_{GM} is prescribed in simulations here, and not allowed to vary in response to the isopycnal slope, unlike the eddy resolving simulations of Zhang, Kang and Marshall (2024), where κ_{GM} is shown to strengthen with a stronger prescribed buoyancy gradient.

Fields of salinity, temperature, and potential density anomalies are illustrated in figures 4.7 and 4.6. These show solutions across tested ranges of κ_{GM} and κ_z respectively at $\kappa_z = 10^{-4}$ and $\kappa_{GM} = 0.01$ respectively. Anomalies are taken about the mean salinity and reference temperature and density (see table 3.1)

Across all solutions in figures 4.5, 4.6 and 4.7, salinity anomalies control ocean density gradients. As a result, isopycnals tend to follow salinity contours. Isopycnals are steepest for weaker κ_{GM}, and stronger κ_z, as predicted by Eq. (4.2).

Where $\kappa_{GM} = 0.01$ m^2 s^{-1} *and* $\kappa_z \leq 10^{-4}$ m^2 s^{-1} (fig. 4.6, upper panel), freshening is strongest equatorwards of the south pole. Above the depth of maximum prescribed melting ($H_{maxmelt}$; ~ 17 km), denser waters are located polewards and isopycnals slope downwards towards (and in places, along) the ice interface. Beneath $H_{maxmelt}$, the meridional density gradient reverses and isopycnals slope upwards towards the ice shell. Because of this, the freshwater lens penetrates deepest at the south pole.

At $\kappa_{GM} > 0.01$ (fig. 4.6, bottom panel), freshening is instead strongest at the south pole. This difference may arise from stronger mixing by parameterised eddies. Eddies tend to flux water 'up' the isopycnal slope. Above $H_{maxmelt}$, this results in a net polewards and upwards transport of freshwater by the parameterised eddies so long as the ocean at the polar ice interface is denser than that at $H_{maxmelt}$ (because in this case, isopycnals would always slope downwards towards the ice interface). As κ_{GM} is increased, the parameterised

eddies become more effective at fluxing freshwater polewards, flattening the isopycnals. The combination of this, and prescribed (albeit weaker) melting at the south pole permits a freshening (and thus buoyancy) strongest at the pole, displaced from the maxima in the buoyancy forcing.

Turning attention to the North pole, it is worth highlighting that at the lowest κ_{GM} tested, stratification is broken here for $\kappa_z \geq 10^{-4}$ m^2 s^{-1}. This is permitted because of a weak (but non-zero) prescribed freezing in the northernmost latitudes (see fig. 4.1). The weak freezing occurs higher up in the water column than melting, and therefore acts to destabilise the stratification here in all solutions. Yet despite this, a freshwater lens is maintained in most solutions because of the aforementioned eddy mixing: where ocean density increases polewards, parameterised eddies flux freshwater polewards. Where the polewards eddy freshwater flux exceeds freshwater fluxes owing to ice freezing, a relative freshening (and thus stratification) can be maintained at the north pole. In solutions with $\kappa_{GM} = 0.01$ m^2 s^{-1} and $\kappa_z \geq 10^{-4}$ m^2 s^{-1}, a tipping point appears to have been reached where isopycnals outcropping from the north pole intersect the ocean bottom, rather than regions of melting further polewards. The polewards eddy freshwater flux is then cut off, and the ocean becomes unstably stratified here, convecting from top to bottom.

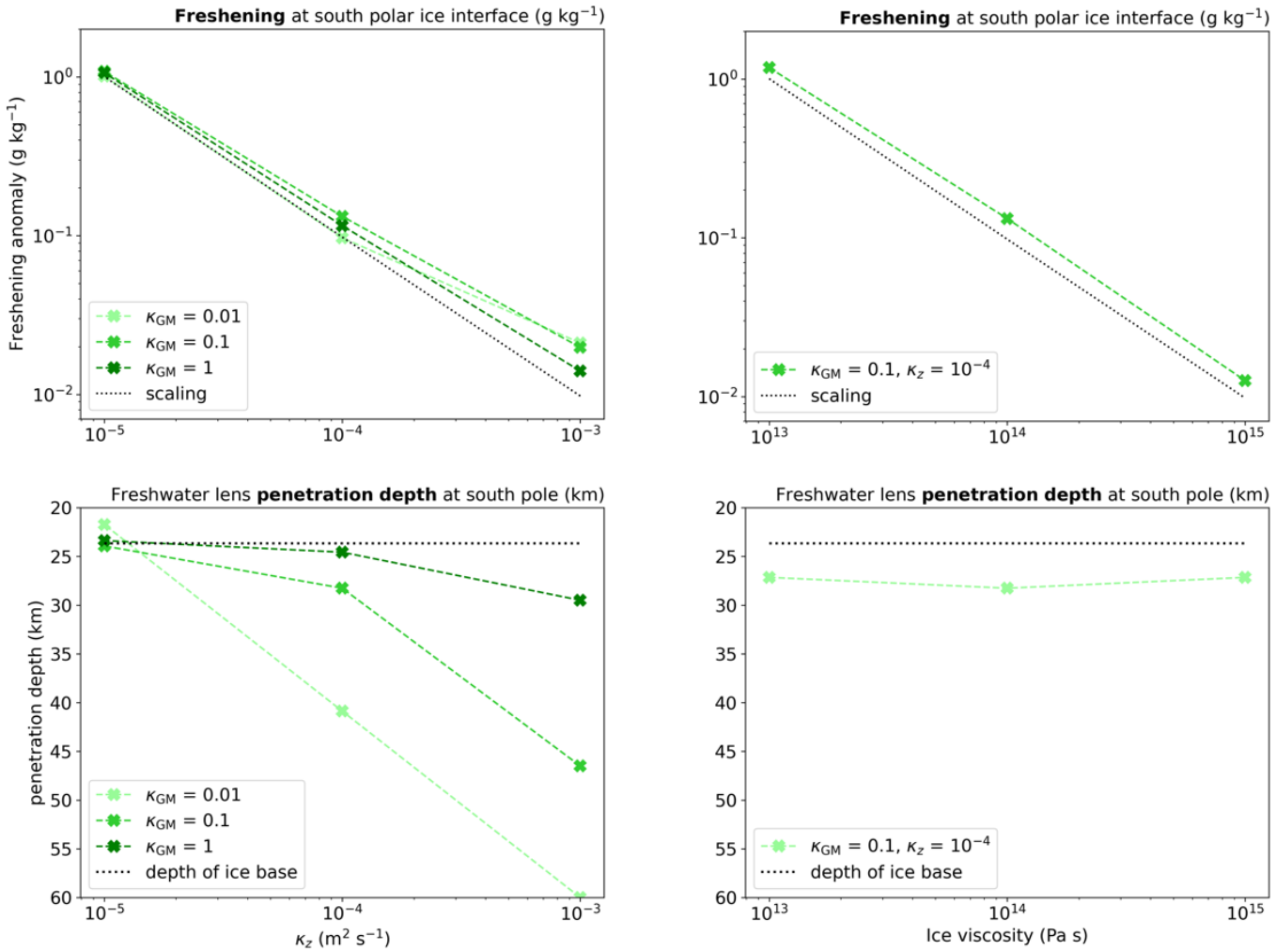

Figure 4.5: Numerical solutions at 35 g kg^{-1}. Top: The volume-weighted mean salinity anomaly (g kg^{-1}) at the ocean top within south polar region, defined here as polewards of 60 ° S (Porco, DiNino and Nimmo 2014). Left shows solutions across effective vertical diffusivity κ_z and eddy diffusivity κ_{GM} (indicated with varying green shading; m^2 s^{-1}). Right shows tests across ice melting viscosity η_{melt} (Pa s; corresponding to proportionate changes in the magnitude of freezing rate) for constant κ_{GM} = 0.1 m^2 s^{-1} and κ_z = 10^{-4} m^2 s^{-1}. The black dotted line shows the salinity anomaly predicted by Eq. (4.6). Note all axis in the upper panel are logarithmic. Bottom: As in the top panel, except showing the penetration depth (km) of the freshwater lens beneath Enceladus' surface, computed at the south pole, defined as the depth at which the vertical salinity gradient falls to factor 1/e its maximum value. Black dotted line denotes the depth of the ice shell base in the model.

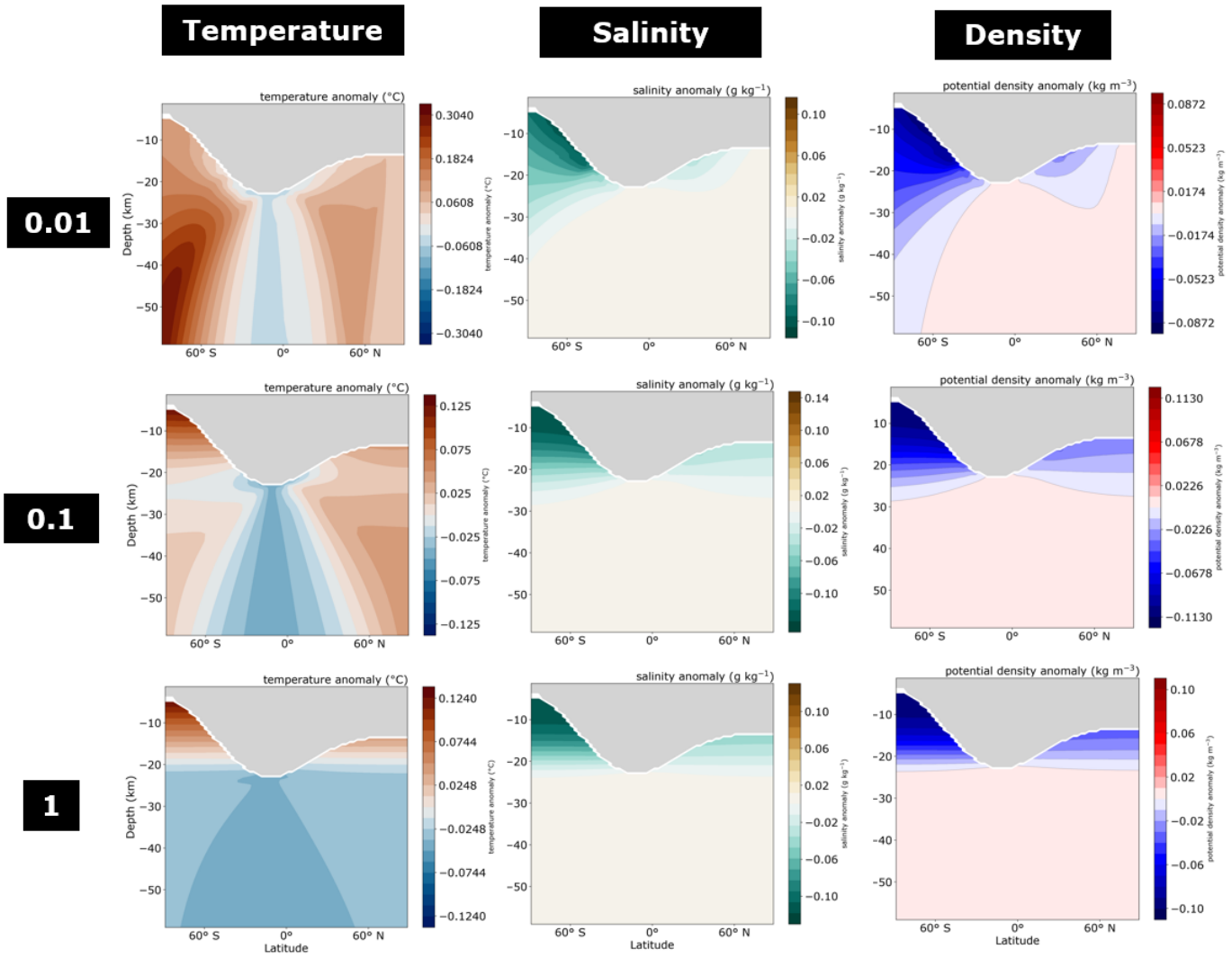

Figure 4.6: Numerical solutions at 35 g kg^{-1}, at constant effective vertical diffusivity $\kappa_z = 10^{-4}$ m^2 s^{-1}, across κ_{GM} of 0.01, 0.1 and 1 m^2 s^{-1} (top, middle, and bottom rows respectively). Shown are the temperature (left), salinity (middle) and potential density (right) anomalies computed about the reference temperature (T_{ref}), salinity (S_{ref}) and potential density (ρ_0) respectively. S_{ref} is the mean salinity of the ocean. T_{ref} is the freezing temperature computed at the reference salinity and reference pressure (P_{ref}), computed under Enceladus' mean ice thickness. ρ_0 is the density computed at the reference temperature, salinity and pressure. Note all colourbars are saturated and vary throughout.

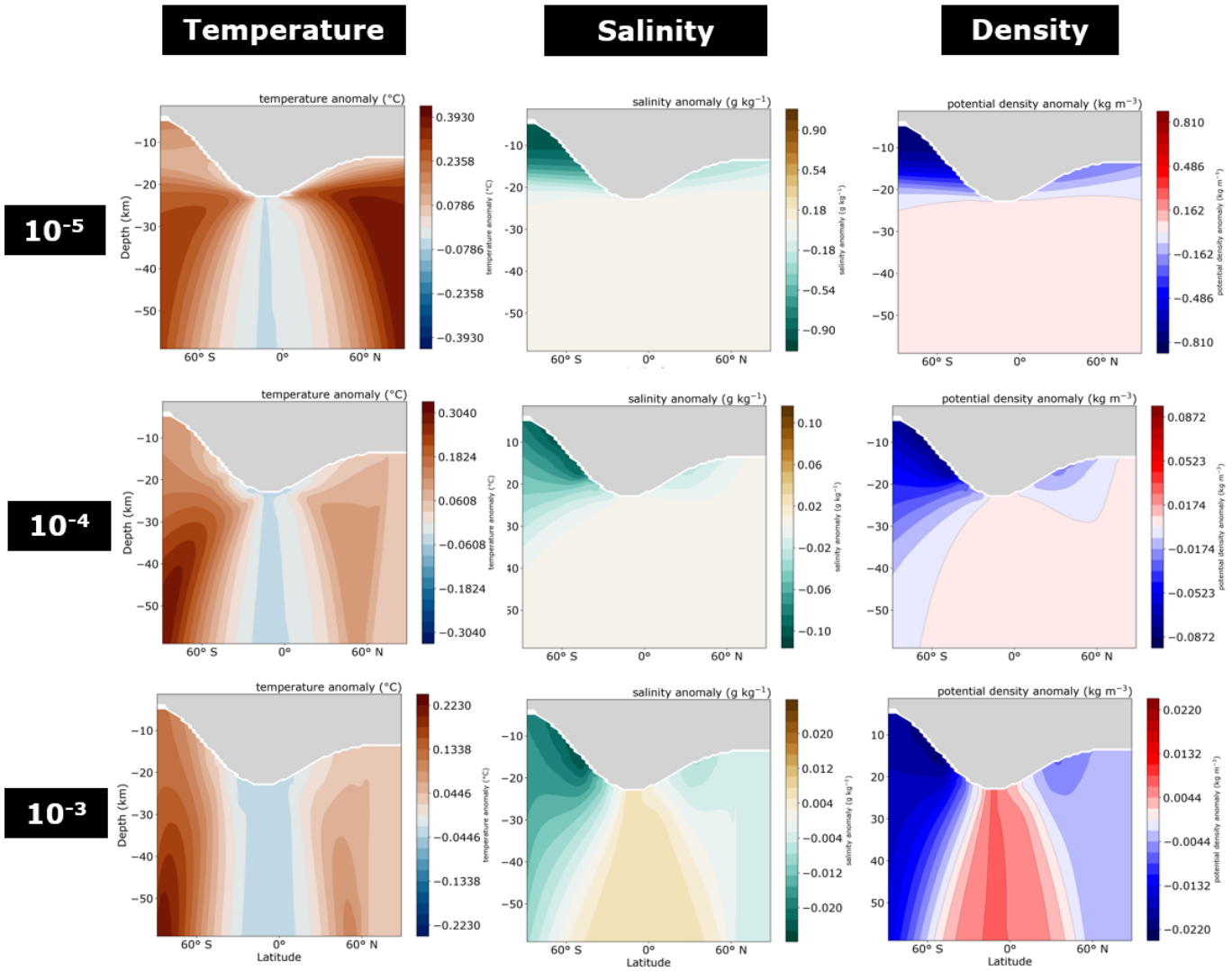

Figure 4.7: Numerical solutions at 35 g kg^{-1}, at eddy diffusivity $\kappa_{GM} = 0.01$, across effective vertical diffusivity κ_z of 10^{-5}, 10^{-4}, and 10^{-3} m^2 s^{-1} (top, middle, and bottom rows respectively). Shown are the temperature (left), salinity (middle) and potential density (right) anomalies computed about the reference temperature (T_{ref}), salinity (S_{ref}) and potential density (ρ_0) respectively. S_{ref} is the mean salinity of the ocean. T_{ref} is the freezing temperature computed at the reference salinity and reference pressure (P_{ref}), computed under Enceladus' mean ice thickness. ρ_0 is the density computed at the reference temperature, salinity and pressure. Note all colourbars are saturated and vary throughout.

4.3.3 Results: low salinity

Fig. 4.8 show numerical solutions for the volume-weighted mean salinity anomaly at the south polar ice interface at 5 g kg^{-1} mean ocean salinity.

At 5 g kg^{-1}, south polar freshening exhibits a strong dependence upon κ_{GM}, contrasting solutions presented in the previous section. Freshening weakens by up to three orders of magnitude as κ_{GM} is increased from 0.01 to 1. Sensitivity of freshening to vertical diffusivity κ_z depends upon the prescribed κ_{GM}. At stronger $\kappa_{GM} = 1$ m^2 s^{-1}, freshening exhibits little sensitivity to κ_z, and order-of-magnitude discrepancies are obtained relative to predictions using Eq. (4.6). Discrepancies relative to Eq. (4.6) are smaller for weaker $\kappa_{GM} = 0.01$ m^2 s^{-1}, where freshening decreases with increasing κ_z as predicted.

Corresponding fields of salinity, temperature, and potential density anomalies are illustrated in figures 4.10 and 4.9, showing solutions across tested ranges of κ_{GM} and κ_z respectively at $\kappa_z = 10^{-4}$ m^2 s^{-1} and $\kappa_{GM} = 0.01$ m^2 s^{-1} respectively.

Figures 4.9 and4.10 show that, in contrast to 35 g kg^{-1} solutions, temperature anomalies dominate gradients in ocean density near the ice interface in most solutions at 5 g kg^{-1}. Owing to the negative α_T in the upper ocean, warmer waters aloft at south polar ice interface are denser than the cooler waters at the ice shell base nearer the equator. The presence of denser water polewards *and* aloft in the south polar region confines isopycnals to follow the slope of the ice interface. Importantly, these isopycnals cross the equatorial ocean, and by extension, latitudes where ice freezing is occurring. This allows along-isopycnal mixing to mix fresher polar waters with saltier equatorial waters. In numerical solutions at $\kappa_{GM} = 1$ m^2 s^{-1}, eddy mixing is efficient enough to entirely inhibit development of a freshwater lens at the poles. The assumption of Eq. (4.6) - that the salt flux into the south polar ocean is dominated by κ_z - is therefore violated. As κ_{GM} is weakened, the mixing of lateral salinity gradients imparted by κ_{GM} is reduced, and salinity anomalies at the ice interface can grow larger, permitting formation of a freshwater lens.

At $\kappa_z = 10^{-5}$ m^2 s^{-1} *and* $\kappa_{GM} = 0.01$ m^2 s^{-1}, salinity anomalies appear to grow large enough to dominate stratification at the ice interface, with isopycnals following salinity contours in the south polar region. The reason is likely because at low κ_z and κ_{GM}, processes moving salinity anomalies away from the ice interface are weaker, permitting greater freshening of the south polar ocean. If freshening exceeds the threshold at which salinity anomalies dominate stratification, a tipping point can then occur: Once isopycnals no

longer intersect regions of freezing, κ_{GM} becomes less efficient in homogenising the lateral salinity gradient at the ice interface, permitting freshening to become stronger still. As a result, a salinity dominated stratification regime can arise nearer the ice interface at 5 g kg^{-1} mean salinity. A scaling law for this tipping point is provided in section 4.4.

Note that below the ice shell base, the ocean is inversely stratified. Here, the ocean is heated from below (owing to the prescribed bottom heating) and cooled globally from above, where eddy mixing efficiently homogenises lateral temperature gradients at the ice base (preventing temperature anomalies - forced by meridional temperature gradients at the ice interface - penetrating much below this region). The setup beneath the ice base is therefore analogous to the flat-top solutions presented in the previous chapter.

Fig. 4.11 shows numerical solutions for the meridionally averaged inversion depth (depth of reversal in sign of α_T, corresponding to the thickness of the inverse stratified layer) for experiments at 5 g kg^{-1} mean salinity. This is compared to predictions using Eq. (3.5) from the previous chapter, using the freezing temperature computed at the ice base as the upper boundary temperature of the theoretical model. Also plotted in fig. 4.11 is the volume-weighted tracer age averaged over the south polar ice interface. This is plotted alongside theoretical predictions using Eq. (3.6), computed assuming an inverse stratified extending from the south polar ice interface to the computed inversion depth.

Numerical solutions for the inversion depth show broad agreement with theoretical predictions across tested parameter space in κ_{GM} and κ_z, suggesting the inversion depth theory of Ames et al. (2025) holds in the case of a varying upper boundary height. There is less agreement between analytical and theoretical predictions in the case of tracer age. This is simply because efficient mixing above the ice shell base (where stratification here dominated by temperature) improves the efficiency of vertical transport here. Discrepancies increase at larger κ_{GM}, where more efficient eddy mixing can more efficiently flux tracers from the ice base to the south polar interface. Discrepancies also increase at weaker κ_z, because the thickness of the stratified layer experiences a greater relative reduction in this case. However, note that age is still of order 100,000 years. This is because the inversion depth always occurs beneath the ice base. This means the ocean is always inversely stratified between the inversion depth and the ice base in solutions here, providing a barrier to the vertical transit of tracers sourced from depth.

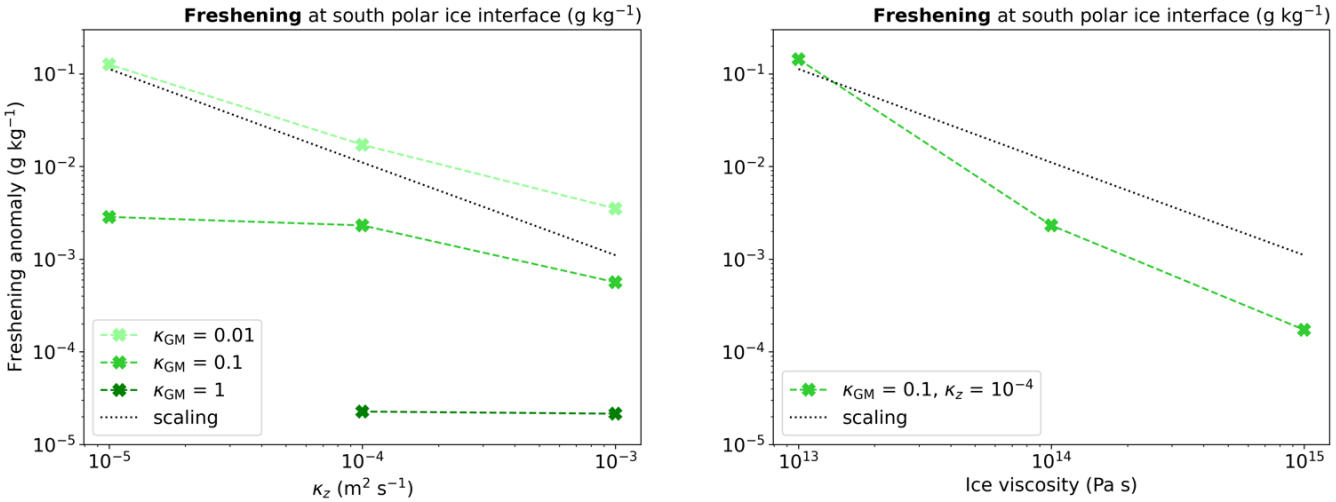

Figure 4.8: As in fig. 4.5, but showing numerical solutions at 5 g kg^{-1} of the volume-weighted mean salinity anomaly (g kg^{-1}) at the ocean top within south polar region, defined here as polewards of 60 ° S (Porco, DiNino and Nimmo 2014). Left shows solutions across effective vertical diffusivity κ_z and eddy diffusivity κ_{GM} (latter indicated with varying green shading; m^2 s^{-1}). Right shows tests across ice melting viscosity η_{melt} (Pa s; corresponding to proportionate changes in the magnitude of freezing rate) for constant $\kappa_{GM} = 0.1$ m^2 s^{-1} and $\kappa_z = 10^{-4}$ m^2 s^{-1}. The black dotted line shows the salinity anomaly predicted by Eq. (4.6). Note all axis are logarithmic.

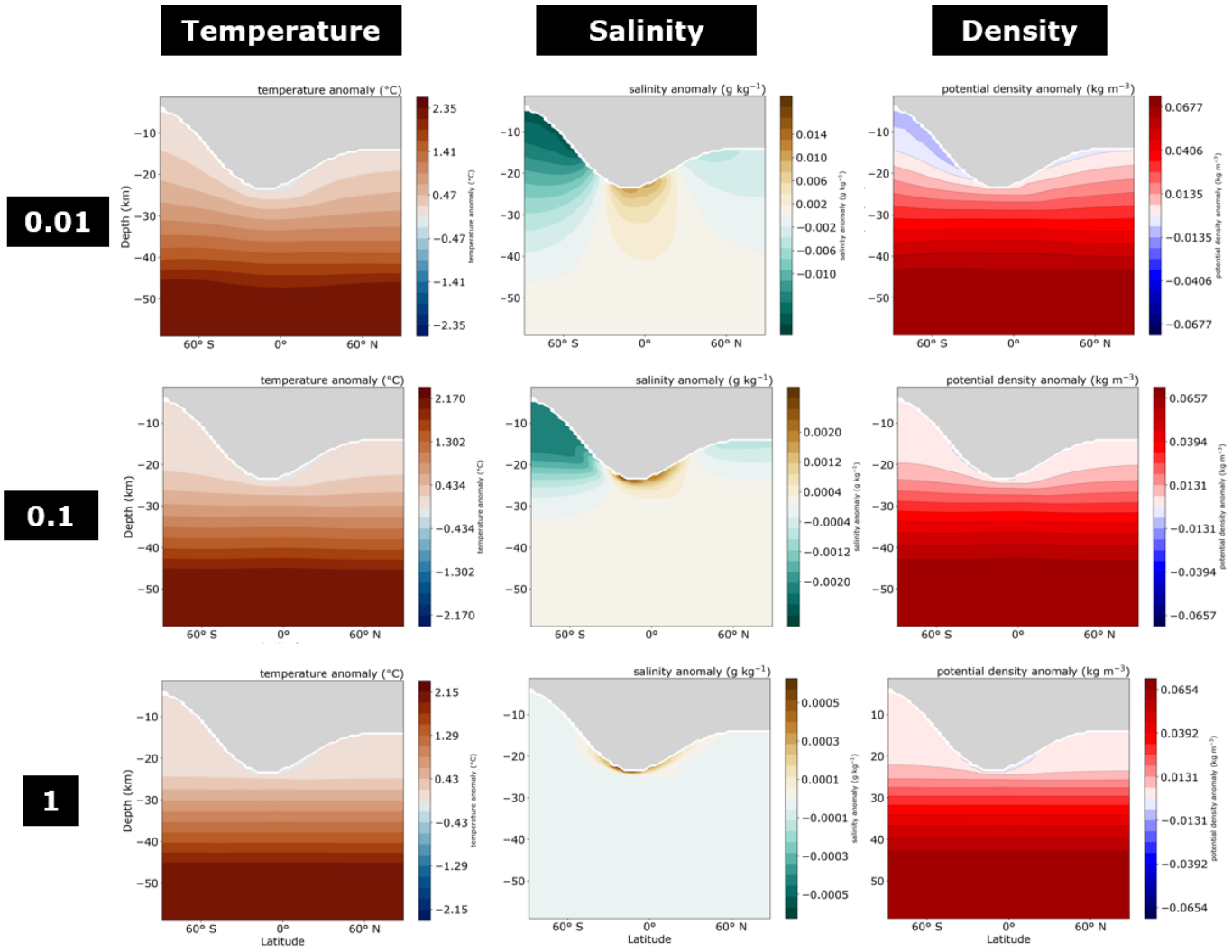

Figure 4.9: Numerical solutions at 5 g kg^{-1}, at constant effective vertical diffusivity $\kappa_z = 10^{-4}$ m^2 s^{-1}, across κ_{GM} of 0.01, 0.1 and 1 m^2 s^{-1} (top, middle, and bottom rows respectively). Shown are the temperature (left), salinity (middle) and potential density (right) anomalies computed about the reference temperature (T_{ref}), salinity (S_{ref}) and potential density (ρ_0) respectively. S_{ref} is the mean salinity of the ocean. T_{ref} is the freezing temperature computed at the reference salinity and reference pressure (P_{ref}), computed under Enceladus' mean ice thickness. ρ_0 is the density computed at the reference temperature, salinity and pressure. Note all colourbars are saturated and vary throughout.

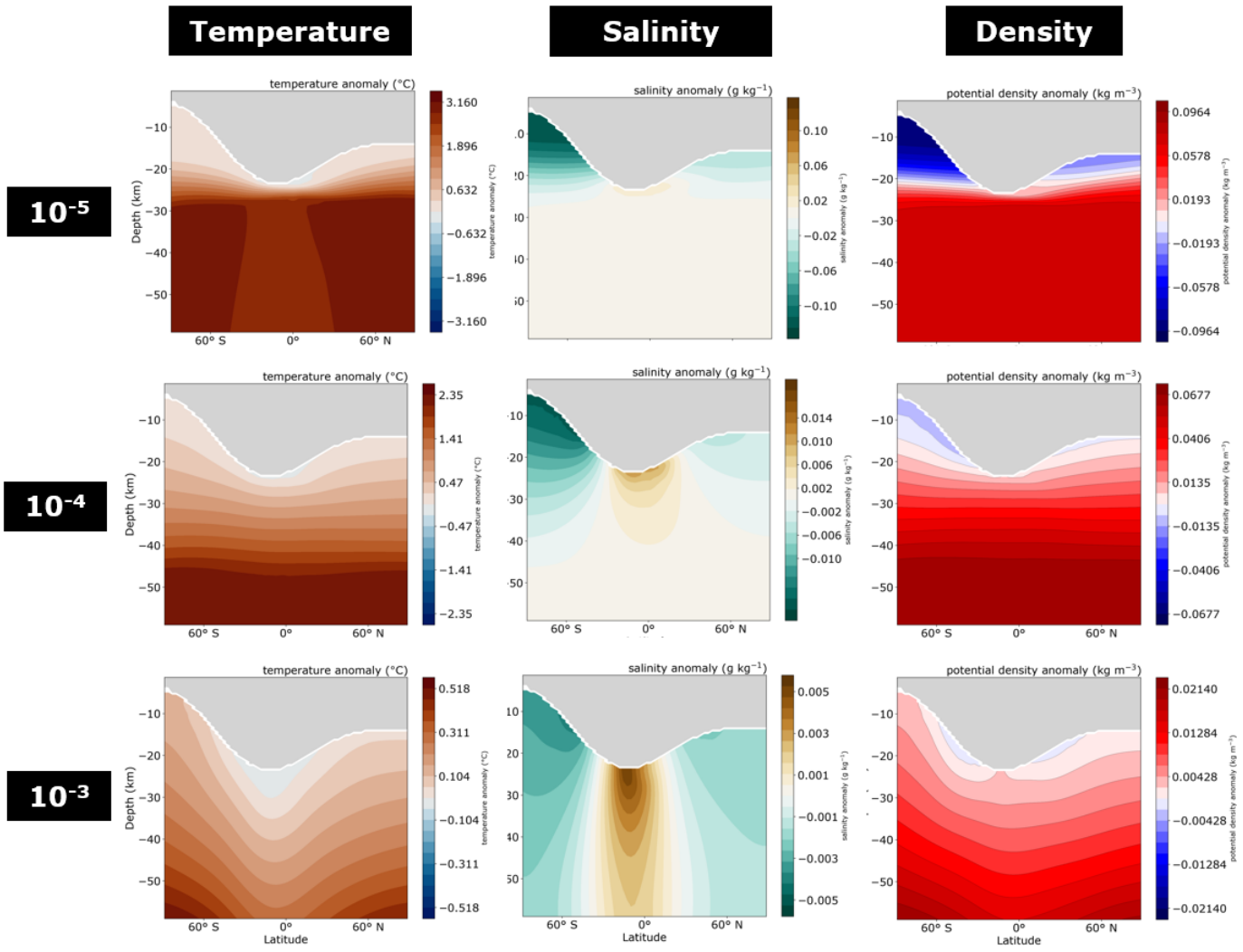

Figure 4.10: Numerical solutions at 5 g kg^{-1}, at eddy diffusivity $\kappa_{GM} = 0.01$, across effective vertical diffusivity κ_z of 10^{-5}, 10^{-4}, and 10^{-3} m^2 s^{-1} (top, middle, and bottom rows respectively). Shown are the temperature (left), salinity (middle) and potential density (right) anomalies computed about the reference temperature (T_{ref}), salinity (S_{ref}) and potential density (ρ_0) respectively. S_{ref} is the mean salinity of the ocean. T_{ref} is the freezing temperature computed at the reference salinity and reference pressure (P_{ref}), computed under Enceladus' mean ice thickness. ρ_0 is the density computed at the reference temperature, salinity and pressure. Note all colourbars are saturated and vary throughout.

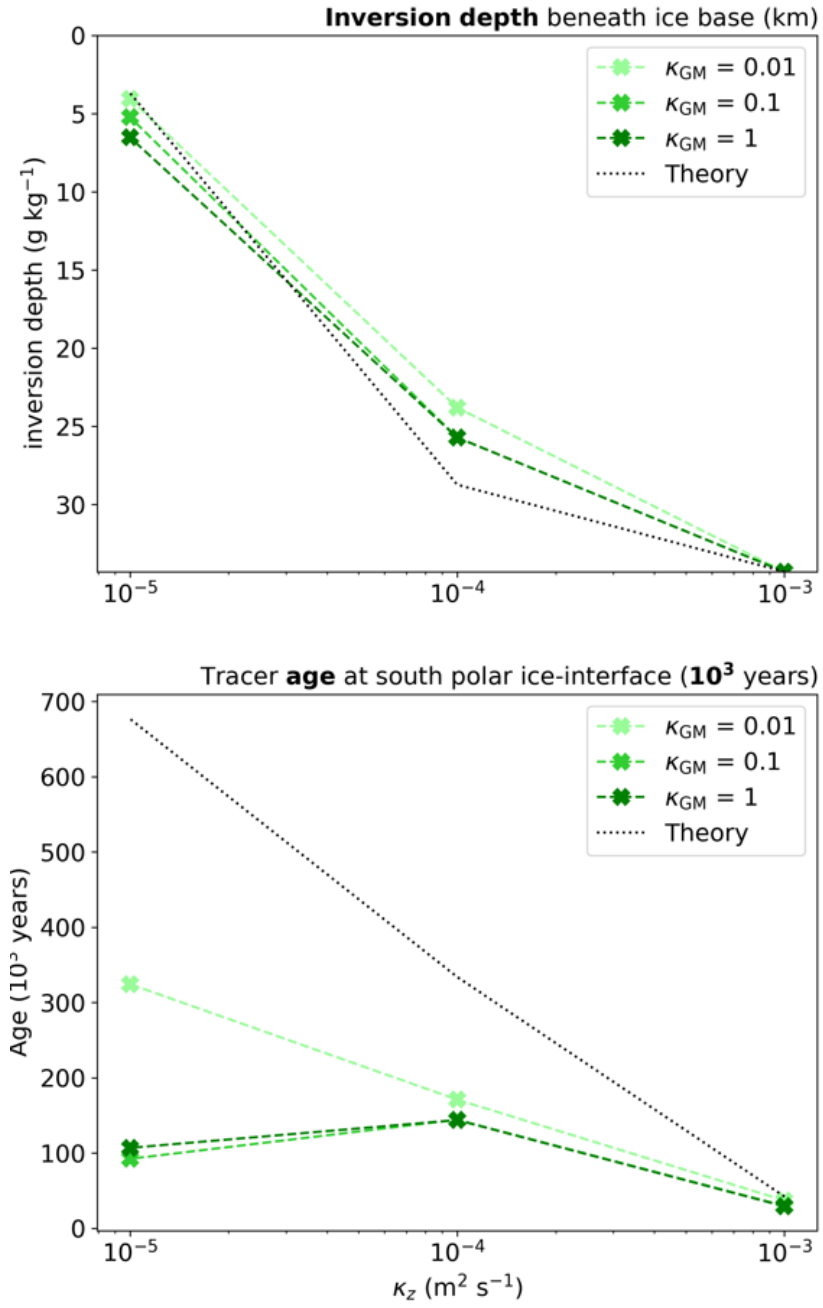

Figure 4.11: Numerical solutions at 5 g kg^{-1} mean ocean salinity, across effective vertical diffusivity κ_z and eddy diffusivity κ_{GM} (indicated with varying green shading; m^2 s^{-1}). Top: The meridionally averaged inversion depth (km; depth at which the thermal expansion coefficient changes sign, corresponding to the thickness of the inverse stratified layer), referenced to the depth of the ice shell base. This is compared to theoretical predictions using Eq. (3.5) (black dotted line), which assumes an upper boundary temperature equivalent to the freezing temperature of water computed at the ice base. Bottom: The volume-weighted mean tracer age (years) at the ice interface across the south polar region (polewards of 60°S), indicating the lower bound transit timescale of hydrothermally-derived particulates from ocean bottom-to-top. This is compared to theoretical predictions from Eq. (3.6), assuming an inverse stratified layer at the south pole extending from the inversion depth to the ice interface.

4.4 Tipping point for meltwater-dominated stratification: scaling

In numerical solutions presented in the previous section, it is found that where the thermal expansion coefficient $\alpha_T < 0$, a tipping point appears to exist above the ice base between ocean stratification controlled by freshwater melt, and that controlled by meridional temperature gradients at the ice interface. For local salinity gradients to dominate stratification in Enceladus' south polar ocean, the buoyancy gradient along the ice-interface arising from salinity gradients must exceed that owing to temperature gradients. Neglecting the effects of pressure upon ocean density, this implies:

$$-\beta_S(\Delta S) \gtrapprox \alpha_T(\Delta T) \tag{4.7}$$

Here ΔS and ΔT are the difference in salinity and temperature at the ice interface, in regions of thinner ice vs regions of thicker ice (note that the scaling here assumes that salinity minima and maxima are co-located with regions of thinnest and thickest ice respectively)

The temperature at the ice interface is the freezing temperature T_f, which can be approximated linearly (Ames et al. 2025):

$$T_f = aS + bP + c, \tag{4.8}$$

where P is pressure (pascals), $a = -0.055^\circ$ C $(\text{g kg}^{-1})^{-1}$, $b = -0.753 \times 10^{-7}$ $^\circ$ C Pa^{-1} and $c = 0.008^\circ$ C. The difference in temperature between two points along the ice interface is then:

$$\Delta T = a\Delta S + b\Delta P, \tag{4.9}$$

where ΔP represents the difference in pressure in regions of thinner ice vs regions of thicker ice. Making the hydrostatic approximation, $\Delta P = \rho_0 g \Delta z$, where Δz is the difference in height between regions of thinner ice and thicker ice at the ocean top, Eq. (4.7) then becomes:

$$-\beta_S \Delta S \gtrapprox \alpha_T(a\Delta S + bg\rho_0\Delta z) \tag{4.10}$$

rearranging for ΔS yields:

$$\Delta S \gtrapprox \frac{b\alpha_T g \rho_0 \Delta z}{\beta_S - a\alpha_T} \tag{4.11}$$

In icy moon oceans, $a\alpha_T \ll \beta_S$. The relative freshening of the south polar region needed to permit meltwater dominated stratification above the ice base can therefore be approximated as:

$$\Delta S \gtrapprox \frac{b\alpha_T g \rho_0 \Delta z}{\beta_S} \tag{4.12}$$

In the 5 g kg^{-1} ocean simulations modelled here, $\alpha_T \approx$ -5 $\times 10^{-5}$ °K^{-1}. $\beta_S \approx 10^{-3}$ (g kg^{-1})$^{-1}$, $\Delta z \approx -20000$ m, $g \approx 10^{-1}$ m s^{-2} and $\rho_0 \approx 10^3$ kg m^{-3}. Eq. (4.12) then yields $\Delta S \approx 0.01$ g kg^{-1} for freshening to dominate the stratification in the south polar ocean. This agrees fairly well with numerical solutions from simulations. Solutions at the lowest eddy diffusivity $\kappa_{GM} = 0.01$ m^2 s^{-1}, and $\kappa_z = 10^{-4}$ and 10^{-5} m^2 s^{-1}, exhibit south polar freshening that exceeds this threshold. In the latter, south polar freshening is clearly the dominant control upon stratification above the ice base, with isopycnals following salinity contours (see fig. 4.9). The former solution, with freshening very near ΔS, appears to exhibit a more-transitionary regime, with isopycnals an increasing function of salinity nearer the depth of maximum melting.

Given that the magnitude of α_T is expected to tend to zero at the ice interface as ocean salinity tends towards $\sim$ 20 g kg^{-1} (Ames et al. 2025), Eq. (4.12) suggests that for a given ice melting rate, the resultant freshening would be increasingly likely to dominate ocean stratification as Enceladus' mean ocean salinity tends towards $\sim$ 20 g kg^{-1}.

4.5 Discussion

4.5.1 Stratification breaking at high salinity

In numerical simulations at 35 g kg^{-1}, stratification breaking occurred at the north pole at the weakest κ_{GM} tested (and $\kappa_z \geq 10^{-4}$ $m^{2\ -1}$), owing to weak (but non-zero) prescribed freezing aloft here. In light of this result, it is important to note that κ_{GM} is prescribed in simulations whereas in reality, κ_{GM} would be expected to increase in the presence of a stronger buoyancy gradient, such as that which may arise in regions of localised freezing. We are therefore hesitant to speculate further about the possibility that weak freezing could break stratification in the south polar ocean, before investigating the problem with a κ_{GM} that can respond appropriately to local buoyancy gradients. If the ice shell in Enceladus' south polar region exhibits a stronger flattening towards the pole than currently constrained (Čadek et al. 2019), weak time-mean freezing could be permitted. Transient freezing can also be permitted in quasi-equilibrium, even in the case of time mean-melting. The implications of these for ocean freshening and stratification should be investigated in future work.

The possibility of stratification breaking via heating from below has been investigated previously (Kang 2023), albeit assuming meridional buoyancy gradients forced only by temperature, and $\alpha_T > 0$. Kang (2023) derived a critical bottom heat flux of 2 W m^{-2} required to break south polar stratification, assuming a $\alpha_T = 10^{-4}$ K^{-1} (a larger value, employed to account for density gradients induced by salinity anomalies). For comparison, the bottom heat flux prescribed in simulations here does not exceed ~ 0.03 W m^{-2}, taken as the global mean bottom heat flux given a total core heat output 20 GW (Choblet et al. 2017). While Choblet et al. (2017) argue that heat fluxes of order W m^{-2} could occur be present in localised regions at the ocean bottom, it has been suggested that baroclinic eddies would homogenise lateral variations in vertical heat flux (Kang et al. 2022b; Zhang et al. 2025), rendering it less likely that strong localised bottom heating could break the stratification of the freshwater lens, particularly where relative freshening is strong.

4.5.2 Expected stratification regimes at alternate mean salinity

In numerical solutions at 5 g kg^{-1}, where an inversion depth forms, it always resides below the ice base, ensuring maintenance of stratification within the inverse layer up to this point. At intermediate salinity near $\sim$ 20 g kg^{-1}, pressure effects alone could be sufficient to force an inversion depth at or above the ice base (Ames et al. 2025). In this case, meridional gradients in ice interface temperature would act to destabilise stratification within the entire inverse layer. Yet, if the inversion depth occurs above the ice base, a stably stratified region would still likely form in the region between the inversion depth and ice base. This is because, in the presence of a positive thermal expansion coefficient (α_T), warmer waters aloft in this region would act to stably stratify the ocean here. Moreover and as stated in the previous section, α_T would tend to zero near the inversion depth for ocean mean salinity near $\sim$ 20 g kg^{-1}. As a result, freshwater melt would be increasingly likely to control ocean density here and maintain stable stratification above the ice base near $\sim$ 20 g kg^{-1}.

4.5.3 Comparison with E-ring ice grain salinity observations

If ocean salinity could be constrained via an alternative means to plume material, Eq. (4.6) could be used alongside E-ring ice grain observations (Postberg et al. 2009) to constrain possible values of ice melting viscosity and κ_z within the south polar region.

Saur et al. (2024) argued that an ocean conductivity greater than that implied by E-ring ice grain observations would be necessary to permit an induction response of Enceladus' ocean (in response to time-variation in Enceladus' magnetic field environment owing to its orbital eccentricity) consistent with perturbations in Cassini magnetometer data. A moderate Earth-like conductivity of 5 S m^{-1} would require a larger ocean salinity of 70 g kg^{-1} at Enceladus' owing to its lower ocean temperatures vs Earth (Saur et al. 2024). If one assumes that the salt concentrations within ice grains are representative of waters sourcing the plumes (i.e., not significantly altered during generation of ice grains and their transmission to space via the geyser conduit), a relative freshening of at least $\sim$ 70% would be necessary in the south polar ocean for compatibility with E-ring ice grain observations. At steady state, this would require $\kappa_z \lessapprox 10^{-6}$ m^2 s^{-1} according to equation 4.6. For comparison, an Earth-like bulk ocean salinity of 35 g kg^{-1} - simulated here - would require $\kappa_z \lessapprox 10^{-5}$ m^2 s^{-1} for compatibility with E-ring ice grain observations.

4.5.4 Implications for tracer transport

Where a freshwater lens develops in Enceladus' south polar region, any vertical transport of tracers from ocean bottom-to-top must traverse a stratified layer at least ~ 15 km thick at the south pole. As discussed in the previous chapter, vertical transport through stratified layers scale inversely with κ_z (Eq. (3.6)). Assuming value of $\kappa_z = 1.3 \times 10^{-7}$ m^2 s^{-1} (as employed in previous work exploring transit timescales to the ocean top, but neglecting ocean stratification (Bouffard et al. 2025)) yields a transit timescale through a 15 km thick freshwater lens of millions to tens of millions of years. This is notable in exceeding lower bound (and in the case of threonine and aspartic acid, upper bound) decomposition timescales for many amino acids at freezing point (Truong et al. 2019). It also exceeds the timescale over which, in the absence of a present-day source (argued to likely be of hydrothermal origin - Waite et al. (2017)), Enceladus' hydrogen inventory would be expected to be depleted given its current outgassing rate via the plumes (Waite et al. 2017). Here, we are unable to simulate such low κ_z owing to computational cost. It is currently unclear if other pathways of transport within the ocean would provide a more efficient means of moving hydrothermally derived tracers to the ice shell in the case of a thick stratified layer and molecular κ_z. While we consider a molecular κ_z a less likely scenario, it further highlights the role that tidally- and librationally- induced mixing may play in improving the efficiency of vertical transport within stratified regions of Enceladus' ocean. Constraining both the magnitude and distribution of κ_z within Enceladus is an important path for future research.

4.6 Conclusions

In this chapter, the freshening of Enceladus' south polar ocean is explored assuming steady state of its overlying ice shell. A scaling law is derived and numerical simulations conducted, to explore the sensitivity of freshening to varying ocean mean salinity, eddy mixing κ_{GM}, and tidal and librationally induced mixing κ_z. In doing so, the implications of varying upper boundary height upon ocean stratification are also explored. The central findings are as follows:

- Where salinity gradients dominate ocean stratification at the ice interface, a freshwater lens develops in the south polar region, always extending at least to the base of the ice shell, regardless of employed κ_{GM} and κ_z. In this case, the relative freshening of the south polar ocean (vs the bulk mean salinity) can be approximated reliably as a function of κ_z - the dominant means of fluxing salt into the lens in this case.

- Eq. (4.6) predicts that relative freshening of the south polar ocean could be anywhere from $\ll 1\%$ to $\sim 90\%$, given existing ranges of uncertainty for κ_z and ice melting viscosity in Enceladus' ocean. It is therefore possible that salt concentrations within plume material (Postberg et al. 2009) underestimate the mean salinity of Enceladus' bulk ocean. Until alternative constraints upon salinity can be obtained that do not rely upon measuring salt concentrations of plume material (e.g., a magnetic signature), future work should consider the possibility that Enceladus' ocean is saltier than inferred from E-ring ice grains.

- At steady state, an alternative, temperature-dominated stratification regime can arise at the ice-interface in the presence of a negative thermal expansion coefficient (α_T). Here the south polar ocean is destabilised by warmer polar ice-interface temperatures aloft, expected due to the pressure dependence of waters' freezing temperature. In contrast to the salinity-dominated regime, freshening of the south polar ocean exhibits a strong sensitivity to eddy mixing in this case, which can homogenise lateral salinity gradients by fluxing saltier waters towards the poles. Relative freshening does not exceed ~ 0.01 g kg^{-1} in this regime, which is increasingly favoured at lower mean salinity (stronger magnitude α_T) and stronger κ_{GM} and κ_z.

- Efficient mixing above the ice base in the temperature-dominated regime can significantly improve the vertical transport of hydrothermally-derived particulates and chemical species (tracers) to the ice shell above the inversion depth. However, the

inversion depth always resides beneath the ice base in parameter space tested here, meaning tracers are still required to travel via κ_z though stratified regions of ocean. Inverse stratification is therefore still expected to provide a barrier to vertical transport in the case that Enceladus' mean salinity permits a negative α_T. The inversion depth can be predicted using theory found in Ames et al. (2025), which is found here to hold in the presence of a varying ocean upper boundary height.

Chapter 5

Modelling the magnetic signature of 3D time-mean ocean flows within Enceladus

5.1 Introduction

In the previous chapter, it was argued that the source reservoir of Enceladus' plumes could be significantly freshened relative to the bulk ocean if steady state is assumed. Along with the findings of chapter 3, this motivates efforts to constrain Enceladus' ocean salinity that do not rely upon plume material. The next chapter explores whether an additional consequence of salt - that it makes water electrically conductive - could provide a means to do this.

5.2 Equations

The following section briefly describes the fundamental equations of magnetohydrodynamics referred to in this chapter.

5.2.1 Theory: Ohms law

In its macroscopic form, Ohms Law states that the electrical current I (amperes; quantifying the rate of flow of charged particles) between two points is directly proportional to the voltage V (volts; quantifying the work required per unit charge to move a test charge between the two points - proportional to the difference in electrical potential between them):

$$V = IR \tag{5.1}$$

where R is the resistance (ohms; measuring opposition of a medium to the flow of electrical charge through it).

In magnetohydrodynamics it is customary to use the microscopic form of Ohms law:

$$\vec{J} = \sigma \vec{E} \tag{5.2}$$

where V is replaced with the electric field vector $\vec{E}$ (V m^{-1}; quantifying the physical field present around any given point charge that either attracts or repels other point charges present therein), I with the current density vector $\vec{J}$ (A m^{-2}; quantifying the electrical current per unit area; A m^{-2}) and R with conductivity σ (S m^{-1}; quantifying the ability of a material to conduct electricity).

5.2.2 Theory: Maxwells equations

The foundations of magnetohydrodynamics are Maxwells equations of electromagnetism. There are four of these: Ampere's Law, Faraday's law, Gauss's law and Gauss's continuity equation defined (respectively) as follows:

$$\frac{\nabla \times \vec{B}}{\mu_0} = \vec{J} \tag{5.3}$$

$$\nabla \times \vec{E} = -\frac{\partial \vec{B}}{\partial t} \tag{5.4}$$

$$\nabla.\vec{E} = \frac{\rho_t}{\epsilon_0} \tag{5.5}$$

$$\nabla.\vec{B} = 0 \tag{5.6}$$

Amperes' Law (Eq. (5.3)) states that an electric current (or more precisely a non-zero electric current density $\vec{J}$) is equivalent to a non-zero curl of the ambient magnetic field vector $\vec{B}$ (where $\mu_0 = 4\ \pi \times 10^{-7}$ H m^{-1} is the magnetic permeability of free space). Electrical currents are therefore associated with magnetic fields, the direction of which can be obtained using the right hand-corkscrew rule.

Faradays law (Eq. (5.4)) states that a time varying magnetic field vector $\vec{B}$ is equivalent to a non-zero curl of the electric field vector $\vec{E}$.

Gauss' law (Eq. (5.5)) states that a non-zero charge is equivalently a source or sink of an electric field (where $\epsilon_0 = 8.85 \times 10^{-12}$ F m^{-1} is the magnetic permittivity of free space). Gauss's magnetic monopole law (Eq. (5.6)) states that there can be no source or sink of a magnetic field.

5.2.3 Theory: Lorentz force law

The force exerted upon a point charge within an ambient electromagnetic field is referred to as the Lorentz force (derived from Coulombs law), defined as:

$$\vec{F} = q(\vec{E} + \vec{U} \times \vec{B}) \tag{5.7}$$

where $\vec{U}$ the velocity vector (m s^{-1}) of the point charge, of magnitude q (Coulombs).

A point charge within an electric field experiences a force either parallel or antiparallel to the direction of the electric field where the charge is positive or negative respectively. A moving point charge within a magnetic field experiences a force perpendicular to both its direction of motion and to the direction of the magnetic field (direction obtainable via the right hand rule), again proportional to the point charge. If a point charge is stationary, no Lorentz force arises.

5.3 Motional induction

Motional induction refers to the generation of secondary magnetic fields arising from the movement of a conductor through a primary magnetic field. In the context of an ocean, the mechanism is as follows:

- Salt ions within flowing seawater represents moving charges
- Any point charge moving within an ambient magnetic field is acted upon by the Lorentz force $\vec{F}$, directed perpendicular to that of the ambient magnetic field and direction of travel, in accordance with Eq. (5.7)
- The proportionality of the Lorentz force to charge in Eq. (5.7) mandates that positively and negatively charged salt ions are deflected in opposing directions for a given flow velocity and ambient magnetic field vector. This charge separation enables charge accumulation in the ocean and, in accordance with Eq. (5.5), the generation of an electric field (and thus a spatial gradient in electrical potential i.e., voltage).
- In accordance with ohms law (Eq. (5.2)), the induced electric fields (arising from charge accumulation) are shorted via electrical currents within the ocean and surrounding conducting sediment.
- Electrical currents give rise to secondary magnetic fields, as described by Amperes law (Eq. (5.3) - these are the motionally-induced *magnetic* fields, which are the focus of this chapter (see also fig. 5.1).

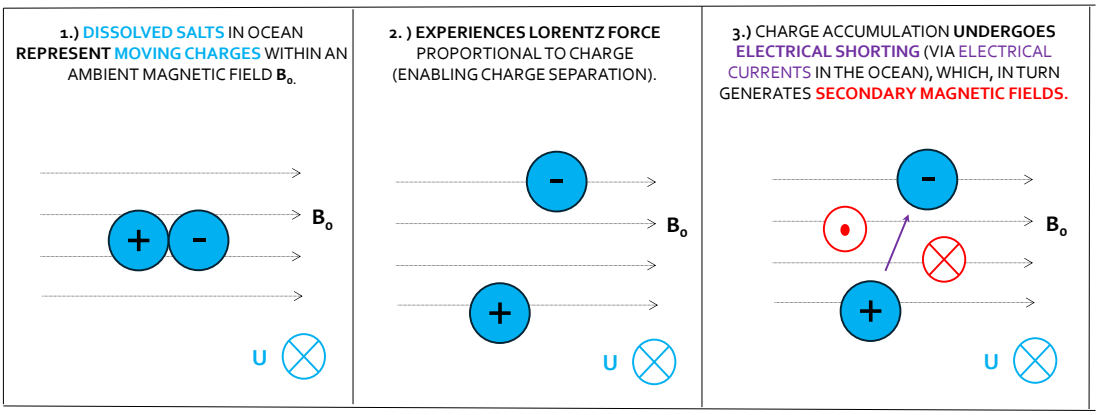

Figure 5.1: Illustrating the mechanism of motional induction. A salt-bearing ocean contains ions of opposing charge (indicated with blue circles) (1). Where an ocean (and thus ions therein) flows within an ambient magnetic field across magnetic field lines (indicated with arrows), the ions within will experience a Lorentz force, proportional to the charge and perpendicular to the directions of motion and the ambient magnetic field). Because of the proportionality to charge, oppositely charged ions are displaced in opposing directions (2). This sets up an accumulation of charge and electric field, which is eventually neutralised via electrical shorting (i.e., electrical currents - indicated with purple arrow) in the surrounding ocean and sediment. The electrical currents then give rise to a secondary magnetic field (indicated in red). This is the motionally induced magnetic field.

5.3.1 Motional induction at Earth

Since initial investigations by Faraday (1832), a large body of work has explored the possibility of inferring ocean flow features from motionally induced electromagnetic fields, encompassing theory (e.g., Larsen 1968; Sanford 1971; Chave 1983; Chave and Luther 1990), observation (e.g., Larsen 1968; Larsen and Sanford 1985; FEM et al. 1993; Lilley, White and Heinson 2001; Toh et al. 2011) and numerical modelling (e.g., Stephenson and Bryan 1992; Tyler, Mysak and Oberhuber 1997; Flosadottir, Larsen and Smith 1997; Tyler, Maus and Luhr 2003; Vivier, Maier-Reimer and Tyler 2004; Maus and Kuvshinov 2004; Manoj et al. 2006; Dostal, Martinec and Thomas 2012; Šachl et al. 2019; Petereit et al. 2019).

At Earth's surface, the use of ocean induced electric fields (OIEF) to infer ocean flows is a matured technique (Szuts 2012). Vertically integrated ocean flows can be inferred via seafloor electrometers (e.g., Luther, Filloux and Chave 1991), and vertical variation in horizontal flows via Lagrangian vertical profilers (e.g., Sanford, Price and Girton 2011), using measurements of electric field. OIEF has also been used to infer bulk ocean properties. Variations in volume transport across the Florida straights has been monitored using the

motionally induced voltage difference across submarine telecommunication cables (Larsen and Sanford 1985). This has in turn, been used to estimate associated ocean heat transport (Larsen 1992).

While OIEF are preferred in observational oceanography at Earth's surface (owing to a much larger signal to noise ratio), ocean induced magnetic fields (OIMF) have been detected at satellite altitude (e.g., Tyler, Maus and Luhr 2003) and therefore offer a means for remote observation of ocean flows (e.g., Petereit et al. 2019). So far, only tidal magnetic signatures have been observed by satellites (Sabaka, Tyler and Olsen 2016). Despite the signal being weak (order 1 nT; Tyler, Maus and Luhr 2003) compared to other contributions to magnetic field (Kuvshinov 2008), the regular periodicity of tides facilitate their extraction from magnetometer data. Observation of an OIMF arising from the time-mean ocean circulation is an objective of the ongoing SWARM satellite mission (Friis-Christensen, Lühr and Hulot 2006). However, as at Earth's surface (Luther, Filloux and Chave 1991; Lilley, White and Heinson 2001), its definitive detection has been precluded given the lack of a periodicity.

The search for OIMF at satellite altitude has been facilitated by numerical modelling of motional induction, which has provided a baseline to which observations can be compared. These have either used GCM output (e.g., Vivier, Maier-Reimer and Tyler 2004; Manoj et al. 2006) or observations (e.g., Petereit et al. 2019) of ocean flows, temperature, and salinity, to compute the resultant electrical currents and ocean conductivity for insertion into solvers employing varying approximations to Maxwells equations (e.g., Šachl et al. 2019). From these, expected characteristics of OIMF owing to Earth's long-period ocean flows have been inferred. For example, there is agreement (across varying modelling approaches) that the OIMF is strongest near the Antarctic Circumpolar Current, and secondarily near western boundary currents, namely owing to larger ocean transport in these regions (Stephenson and Bryan 1992; Vivier, Maier-Reimer and Tyler 2004; Manoj et al. 2006; Velímskỳ, Šachl and Martinec 2019; Šachl et al. 2019). Here, the OIMF may reach $\sim$ 2 nT at Swarm satellite altitude (430 km), small relative to the magnitude of Earth's geomagnetic field ($\sim$ 50000 nT; Alken et al. 2021), but comparable to the tidal signature (Grayver et al. 2016; Velímskỳ et al. 2018). At satellite altitude, the OIMF typically represents domain integrated transports because higher order components of the signal are increasingly attenuated with distance above the ocean surface (where signals may reach $\sim$ 10 nT (Manoj et al. 2006). As a result, it has been shown that using higher

resolution velocity data (from an eddy resolving GCM vs a non-eddy resolving GCM) has little influence upon the OIMF at satellite altitude, but can increase the magnitude of OIMF in localised regions at sea level by $\sim$ factor 2 (Manoj et al. 2006).

5.3.2 Motional induction at ice-covered moons

The majority of ice-covered ocean worlds in the solar system orbit permanently within the magnetosphere of their host planet. If these oceans contain salt (e.g., Hand and Chyba 2007), motional induction would be expected. Despite this, motional induction at ice-covered moons has received very little attention and until the past year, had not been numerically modelled (see the very recent study of Šachl et al. (2024)).

Two studies have derived scalings for an OIMF within an ice-covered moon, arising from tidal (Tyler 2011) and time-mean (Vance et al. 2021) ocean flows. The scaling of the latter is as follows:

$$b \sim \mu_0 \sigma H_{ocn} U B_0 \tag{5.8}$$

Where b (Tesla) is the motionally induced field, $\mu_0 = 4\pi \times 10^{-7}$ H m^{-1} is a constant representing the permeability of free space, σ the ocean conductivity (S m^{-1}), H_{ocn} the ocean depth (m) and B_0 the magnitude of the ambient magnetic field.

Inserting characteristic velocity scales into Eq. (5.8) derived from the DNS experiments of Soderlund (2019), Vance et al. (2021) obtain OIMF magnitudes up to 20 nT for Europa, and 300 nT for Ganymede. Such magnitudes of OIMF are stronger than observed at Earth and would be large enough to permit detection by the Europa Clipper magnetometer (Kivelson et al. 2023). Eq. (5.8) was not applied to Enceladus in Vance et al. (2021), and so the possible motional induction of Enceladus' ocean has not yet been explored.

Inserting characteristic scales for Enceladus:

$\mu_0 = 4\pi \times 10^{-7}$ H m^{-1}
$\sigma \sim 1$ S m^{-1} (using the Gibbs seawater toolbox; McDougall and Barker 2011)
$H_{ocn} \sim 40$ km (Hemingway and Mittal 2019)
$U \leq 10^{-3} - 10^{-2}$ m s^{-1} (Jansen et al. 2023; Zhang, Kang and Marshall 2024)

$B_0 = 325$ nT (Dougherty et al. 2006),

into Eq. (5.8), one obtains $b \approx 0.01 - 0.1$ nT within Enceladus' ocean. This signal is near the limit of detectability of the Cassini magnetometer (Dougherty et al. 2006). The weaker signal compared to that predicted by Vance et al. (2021) for the Jovian moons is owing to a 2-3 orders of magnitude weaker assumed ocean velocity for Enceladus here.

Given the prediction of an OIMF at Enceladus near the limit of detectability, the remainder of this chapter aims to verify this prediction, exploring motional induction at Enceladus following the 3D electromagnetic modelling approach used and verified at Earth (e.g., Šachl et al. 2019). In doing so, this chapter aims to determine if Enceladus' motionally induced magnetic signature could be detectable, and whether different salinity oceans leave a distinguishable signature. If the case, the OIMF could plausibly provide a constraint upon ocean salinity independent of plume material.

The structure of this chapter is as follows: First, the ocean and electromagnetic modelling approaches are outlined. Then, some physical intuition is provided and highly idealised tests performed to clarify how patterns of electrical currents (arising from ocean flows) translate to patterns of OIMF. Numerical solutions for ocean velocity, resultant electrical currents and OIMF are then shown and described. In the latter, OIMF is first obtained within the ocean, then extrapolated to satellite altitude. The chapter is rounded out with a discussion and a statement of the key findings.

5.4 Methods

5.4.1 Ocean modelling approach

Ocean simulations are performed using the MITgcm. The configuration is identical to that described chapter 2, except for the key differences outlined below.

Firstly, the configuration is 3D and fully global, extending pole-to-pole and spanning the full 360 degrees longitude. Global simulations are necessary to obtain a global solution for the OIMF, while avoiding the need for artificial lateral boundaries in electromagnetic simulations that could introduce artifacts (Stephenson and Bryan 1992). To achieve this, a cubed sphere topology is employed (Adcroft et al. 2004). This splits the model domain laterally into six 'faces', here containing 96×96 points for each vertical layer of the model, yielding a resolution of 0.9375 degrees at the equator. In doing so, CFL numerical stability constraints associated with the convergence of the meridians at the poles are relaxed, preventing the need to mask these with land, as commonly done in 3D icy moon ocean simulations using GCMs (e.g., Ashkenazy and Tziperman 2021; Zeng and Jansen 2024).

Next, the ocean upper boundary is assumed flat. This is chosen to simplify electromagnetic simulations and interpretation thereof at this stage. The effects of upper boundary height variation upon the OIMF should be explored in future work. Freshwater fluxes from the overlying ice shell are also neglected at this stage, the effects of which upon the OIMF are also left for future work.

At the upper boundary, temperature is restored to the salinity and pressure-dependant freezing temperature (Millero 1978) that Enceladus' realistic ice topography would otherwise induce. To compute this, the thickness profile of Čadek et al. (2019) is employed and truncated at degree 3, as in the reference configuration. Unlike the reference configuration, the 3D model here permits longitudinal variation in the restoring temperature, allowing the effects of these upon ocean flow to be explored (as far as this author is aware, for the first time). The restoring temperature profile is shown in fig. 5.2. Longitudinal variation is strongest at the equator, with the coldest restoring temperature residing at the sub- and anti- Saturn points.

An idealised 2D heat flux is imposed at the ocean bottom, following the pattern of vertically integrated core heating obtained by Choblet et al. (2017). For this, we borrow equation B2 from Zeng and Jansen (2021):

$$Q_{\mathrm{core}}(\Theta) = \frac{F_{\mathrm{tot}}[0.5Y_{20}(\Theta) - 0.25Y_{22}(\Theta,\lambda) + K]}{4\pi K r_c^2}, \tag{5.9}$$

where $r_c = 192$ km is the core radius (radius to the ocean bottom), $K \approx 0.904$ a constant, Y_{20} a degree 2, order 0 spherical harmonic function and Y_{22} a degree 2, order 2 spherical harmonic function (as a function of co-latitude Θ and longitude λ). A total core heat output of $F_{\mathrm{tot}} = 20$ GW is assumed. The bottom heating profile is shown in fig. 5.2. Heating is strongest nearer the poles, weakest at the sub- and anti-Saturn points. Note that the manifestation of vertically integrated core heating at Enceladus' core-ocean boundary is likely to be far more heterogenous than employed here (exhibiting a complex web-like pattern, with strong localised variation; Choblet et al. 2017). Studies employing heterogenous bottom heating have come to differing conclusions about its influence upon ocean circulation (Zhang et al. 2025; Bouffard et al. 2025), likely owing to differing model assumptions. Given that here, the goal is to conduct an initial exploration into the modulation of OIMF by zonal variations in ocean flows, an idealised pattern of bottom heating is adopted and effects of strong, localised variations in heating left for future work.

Simulations are performed at 5 and 35 g kg^{-1}, representing 'low' and 'high' salinity regimes, within the expected range of uncertainty for Enceladus' ocean (Zolotov 2007; Postberg et al. 2009; Hsu et al. 2015; Ingersoll and Nakajima 2016; Glein and Truong 2025). The eddy diffusivity κ_{GM} is set to 1 m^2 s^{-1}. The background effective vertical diffusivity κ_z is set to 10^{-3} m^2 s^{-1}. Before input into the magnetic model, Eulerian velocity fields are interpolated from a cubed-sphere grid to a regular latitude-longitude grid.

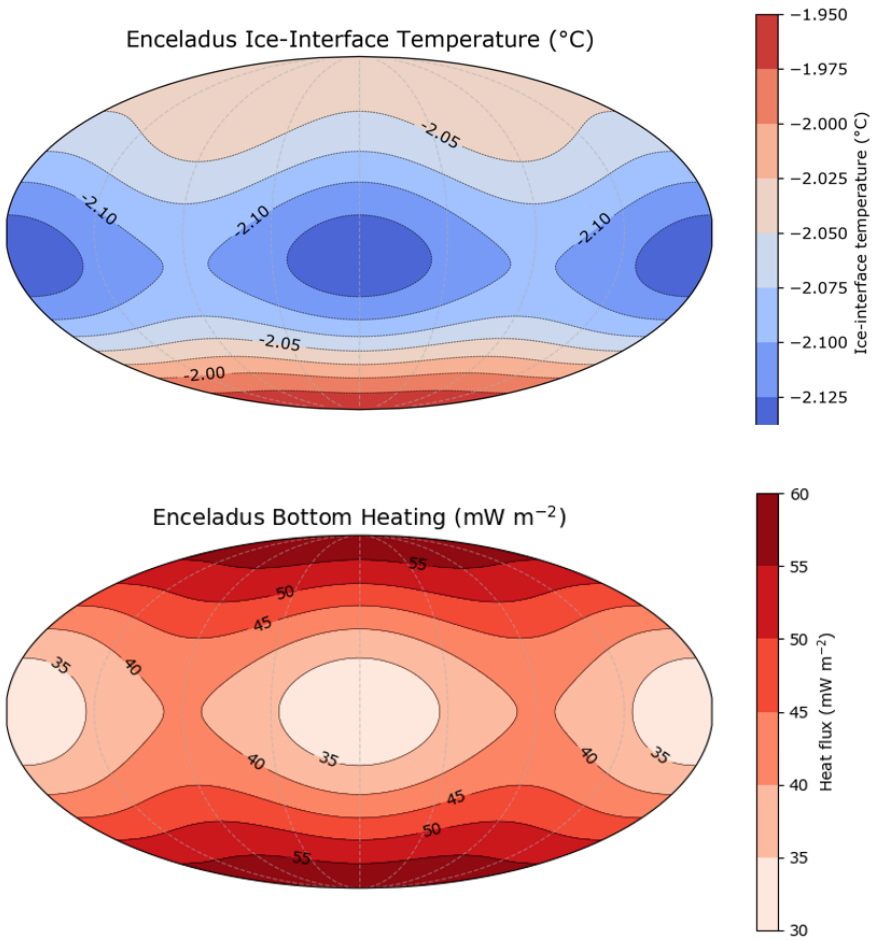

Figure 5.2: Boundary forcings for 3D global simulations of Enceladus' ocean. Top shows the ice-interface restoring temperature (°C) - the water freezing point - computed under the degree 3 ice thickness patterned derived by Čadek et al. (2019), using the formulation of Millero (1978), here shown for a 35 g kg^{-1} reference salinity. Bottom shows the bottom heating profile assuming a total core heat output of 20 GW - the pattern corresponds to the expected pattern of vertically integrated tidal heating within Enceladus' core (Choblet et al. 2017), used here to create an idealised profile of heating at the core-ocean interface.

5.4.2 Electromagnetic modelling approach

Here the OIMF is obtained using the 3D electromagnetic solver GEMMIE (Global EM modelling code based on Integral Equation (IE) approach). GEMMIE is a successor to the X3DG solver used in previous studies simulating the motional induction of Earth's oceans (e.g., Irrgang, Saynisch-Wagner and Thomas 2018; Petereit et al. 2019; Šachl et al. 2019), in turn benchmarked against other solvers (Kelbert et al. 2014). The algorithm solves Maxwell equations in the frequency domain via an integral equation method using a Greens functions technique (see Kuvshinov (2008) and Kuvshinov and Semenov (2012)).

In simulations here, the model is configured with three distinct layers, representing Enceladus' ice shell, ocean, and silicate rocky core. The radius of the model surface is set to 252 km (Enceladus' surface radius - Porco et al. 2006). The thickness of the ice, ocean and core layers are set to 20, 40, and 192 km respectively to match that assumed in the ocean model. The configuration is fully global, deploying a regularly spaced grid of 0.9375 degrees resolution in spherical coordinates, extending pole-to-pole. A singular layer is employed for the ice and core while 40 layers of 1 km thickness are deployed in the ocean, again to match the GCM simulations.

GEMMIE is run in its 'distributed currents' mode. In this mode, longitudinal (λ), colatitudinal (Θ) and radial (r) components of the in-situ electrical current density $\vec{J}$ (A m^{-2}) must be prescribed. The resultant OIMF is then obtained iteratively at specified vertical levels within the model (compute time is proportional to the number of 'receivers' requested). Electrical currents are prescribed within the ocean layer, to represent those arising from oceanic motion through an ambient magnetic field.

Saturn's ambient magnetic field is assumed to be time constant and a uniform 325 nT, pointing due southward at Enceladus (i.e., antiparallel to Enceladus' axis of rotation) (Dougherty et al. 2006). This is done to isolate (and thus clarify) the influence of Enceladus' ocean flows upon the OIMF. We argue the approach is justified because Saturn's magnetic dipole axis is near perfectly aligned to its rotation axis (Burton, Dougherty and Russell 2009). This means the rotation of Saturn does not, itself, produce significant time variation of the magnetic field at Enceladus (unlike other planets such as Jupiter, Uranus, and Neptune, whose magnetic and rotation axis exhibit misalignment - Connerney 1993). A small periodicity in the ambient magnetic field vector may be expected owing to Enceladus' orbital eccentricity, which causes its distance from Saturn to vary. In addition, periodicity may be expected as Enceladus moves between the day and night side of Saturn's magnetosphere, owing to compression of the magnetosphere imparted by the solar wind (Souček et al. 2019). Periodicity in Enceladus' plume activity associated with plume activity could also alter the magnetic environment (Hedman et al. 2013). The effects of these upon the OIMF go beyond the scope of this chapter and are left for future work. Components of the ambient magnetic field assumed here are shown in fig. 5.3.

Given knowledge of the ambient magnetic field vector $\vec{B}_0$ and the time-mean ocean velocity vector $\vec{u}$, the ocean induced electrical current density $\vec{J_{imp}}$ is computed as (Šachl et al. 2019):

$$\vec{J_{imp}} = \sigma(\vec{u} \times \vec{B}_0) \tag{5.10}$$

where σ is the ocean conductivity. Remembering that $\vec{B}_0$ is assumed here uniform and antiparallel to Enceladus' rotation axis, the individual components of the imposed ocean induced electrical current are computed as follows:

$$\vec{J_\lambda} = \sigma(B_\Theta u_r - B_r u_\Theta) \tag{5.11}$$

$$\vec{J_\Theta} = \sigma B_r u_\lambda \tag{5.12}$$

$$\vec{J_r} = -\sigma B_\theta u_\lambda \tag{5.13}$$

where subscripts of λ, Θ, and r represent longitudinal, colatitudinal and radial components respectively. Note that the electrical current density prescribed here is time constant. Thus in accordance with Faraday's Law, (Eq. (5.4)), self-induction effects - where the OIMF itself feed back onto the electrical currents (Šachl et al. 2019) - are excluded. Also note that owing to the simplified treatment of Saturn's magnetic field here, meridional and vertical velocities control only the longitudinal component of the resultant electric current (Eq. (5.11)).

A uniform conductivity is assumed for each model layer. Ocean conductivity is set to 0.5 and 2.7 S m^{-1} for the 'low' and 'high' salinity configurations. These are (rounded) mean values of conductivity obtained from the ocean simulations performed at 5 and 35 g kg^{-1} mean salinity respectively (see fig. 5.12). In section 5.6.1, it will be shown that conductivity gradients in ocean simulations performed here, arising from ocean stratification, do not exceed $\sim$ 0.01 S m^{-1}. The possibility of larger variations in ocean conductivity within Enceladus' ocean is discussed in section 5.9.1.

The conductivity of the silicate core layer is set to 10^{-4} S m^{-1} to match typical values for Earth's lithosphere (Grayver et al. 2016). The overlying ice is also expected to much more resistive than the ocean and is set to 10^{-5} S m^{-1}. Note that if Enceladus' core is

porous, then core conductivity could be larger, particularly if the temperature and salinity of water contained within are large (Saur et al. 2024). Given the lack of time variation in the OIMF simulated here, significant coupling between the induction responses of the ocean and the core are not expected. The effects of core and ice conductivity are not considered further in this chapter.

All OIMF shown in the following section are extracted in the ocean's uppermost layer. Extrapolation of OIMF to satellite altitude is performed offline in section 5.8.

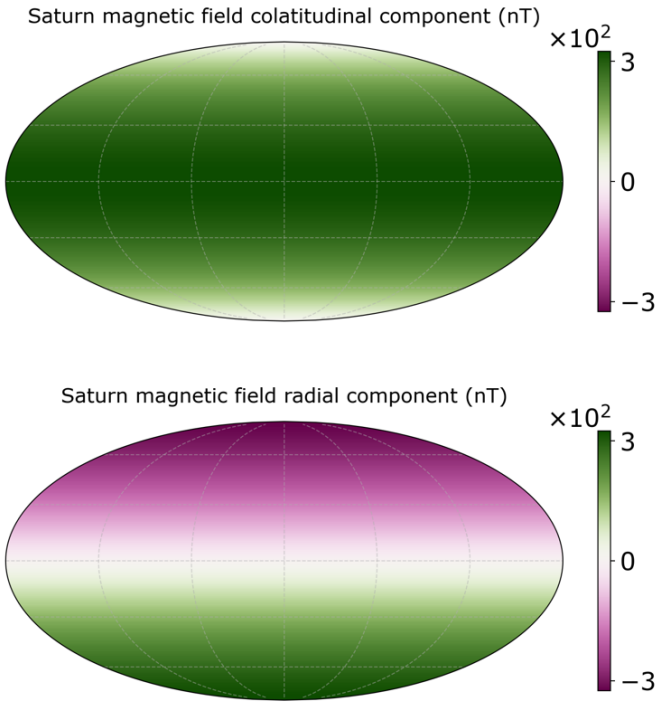

Figure 5.3: Colatitudinal and radial components of the ambient magnetic field vector (nT; corresponding to Saturn's magnetic field at Enceladus) assumed in computation of electrical currents induced by simulated ocean flows. Note that no radial variation (relative to Enceladus) in the ambient magnetic field vector is assumed here.

5.5 Physical intuition and idealised tests

In the following section, some intuition is provided to highlight how patterns of electrical current translate to patterns of OIMF.

5.5.1 The induction equation and importance of the curl

Maxwells equations, combined with the Ohms law, can be rearranged to obtain the induction equation (Šachl et al. 2019):

$$\nabla \times (\frac{1}{\sigma}\nabla \times \vec{B}) + \frac{\partial \vec{B}}{\partial t} = \mu_0 \nabla \times (\sigma \vec{J}) \tag{5.14}$$

Here $\vec{B}$ is the OIMF and $\vec{J}$ the imposed electrical current density computed using Eq. (5.10). For all electromagnetic simulations presented in this chapter, a time-mean electrical current is imposed and there is no time variation in the OIMF solution. The induction equation then simplifies to:

$$\nabla \times (\frac{1}{\sigma}\nabla \times \vec{B}) = \mu_0 \nabla \times (\sigma \vec{J}) \tag{5.15}$$

Furthermore, a uniform ocean conductivity is assumed. In the context of this work, the induction equation then becomes:

$$\nabla \times (\nabla \times \vec{B}) = (\mu_0 \sigma^2) \nabla \times \vec{J} \tag{5.16}$$

Which relates the OIMF to an imposed time-mean electrical current assuming uniform ocean conductivity.

The OIMF in Eq. (5.16) depends upon the curl of the imposed electrical current. Where this curl is zero:

$$\nabla \times (\nabla \times \vec{B}) = 0.$$

Using the vector identity

$$\nabla \times (\nabla \times \vec{B}) = \nabla(\nabla . \vec{B}) - \nabla^2 \vec{B},$$

and the magnetic monopole law (Eq. (5.6)), this yields:

$$-\nabla^2 \vec{B} = 0.$$

Given the boundary conditions imposed in GEMMIE (where Greens functions tend to zero as r $\rightarrow$ 0 and r $\rightarrow \infty$) the OIMF is expected to be zero where $\vec{J} = 0$, and $\nabla \times \vec{J} = 0$, provided these conditions also hold in the modelled ice and silicate core layers.

The formula for the curl of the electrical current, in spherical coordinates, is:

$$\nabla \times \vec{J} = \frac{1}{r \sin\Theta}\left(\frac{\partial}{\partial\Theta}(J_\lambda \sin\Theta) - \frac{\partial J_\Theta}{\partial\lambda}\right)\,\hat{r}$$

$$+ \frac{1}{r}\left(\frac{1}{\sin\Theta}\frac{\partial J_r}{\partial\lambda} - \frac{\partial}{\partial r}(rJ_\lambda)\right)\,\hat{\Theta} \tag{5.17}$$

$$+ \frac{1}{r}\left(\frac{\partial}{\partial r}(rJ_\Theta) - \frac{\partial J_r}{\partial\Theta}\right)\,\hat{\lambda}$$

where $\hat{r}$, $\hat{\Theta}$, $\hat{\lambda}$ are unit vectors in the radial, colatitudinal, and longitudinal directions respectively.

Note that where J_λ, J_Θ and J_r are uniform relative to the sphere, the curl of the electrical current density simplifies to:

$$\nabla \times \vec{J} = \frac{J_\lambda}{r}(\cot\Theta)\,\hat{r}$$

$$- \frac{J_\lambda}{r}\,\hat{\Theta} \tag{5.18}$$

$$+ \frac{J_\theta}{r}\,\hat{\lambda}$$

i.e., non-zero curl of the electrical current (and thus non-zero OIMF) can arise even in the case where J_λ and J_Θ are uniform relative to the planetary body, owing to the spherical geometry upon which the electrical current flows. The OIMF can therefore be thought of as containing two components: that arising due to local variation in the electrical currents (in this chapter arising solely due to local variation in ocean flow velocity), and that arising due to spherical geometry effects (permitting larger scale, uniform, electrical current features to generate OIMF provided they are orientated in the Θ and λ directions).

5.5.2 Idealised tests: uniform electrical current case

To illustrate the control of spherical geometry effects upon the OIMF, tests are performed inserting highly idealised profiles of electrical current into GEMMIE. These consist of electrical current directed in one component - either longitudinal or radial - either uniform, or with a sign reversal in the λ or Θ directions. The magnitude of imposed electrical current in these tests is assumed 10^{-10} A m^{-2} unless specified otherwise. This magnitude corresponds to that expected given an ocean velocity of order 10^{-3} m s^{-1}, background magnetic field of order 100 nT, and ocean conductivity of order 1 S m^{-1} (e.g., Eq. (5.11)). This is comparable to the magnitude of electrical currents used in the 'realistic' 3D simulations presented in section 5.6.3. The resolution employed in these tests is a coarser 5 degrees. Aside from this, the employed configuration of GEMMIE is identical to that described in section 5.4.2.

In the first test, a uniform eastwards electrical current is prescribed: $\vec{J} = J_\lambda = 10^{-10}$ A m^{-2}. While the imposed current is uniform relative to the sphere, it possesses a non-zero curl owing to the effects of spherical geometry (5.18). The curl is orientated in the radial and colatitudinal directions (parallel to the axis of rotation). Upon visual inspection using the right hand corkscrew rule, taking the inverse curl twice, one would expect a pole-to-pole OIMF loop, directed southwards at the ocean top, northwards at the ocean bottom, and upwards and downwards at the north and south pole respectively (fig. 5.4). Fig. 5.5 illustrates the numerical solutions for this test (using GEMMIE) extracted at the ocean top and bottom, which confirm the prediction. An OIMF of order $\sim 10^{-3}$ nT is obtained, exhibiting slight variation in magnitude depending upon component and location. In fig. 5.6, solutions for the radial OIMF are also shown with the magnitude of the imposed current raised and lowered by two orders of magnitude. The OIMF magnitude scales proportionately with electrical current, and an OIMF of ~ 0.5 nT is achieved with $\vec{J} = J_\lambda = 10^{-8}$ A m^{-2} at the ocean top.

In the second test, a uniform upwards (i.e., radially outwards) electrical current is imposed. This results in no OIMF (solution not shown), because there is zero curl in the imposed electrical current (Eq. (5.18)).

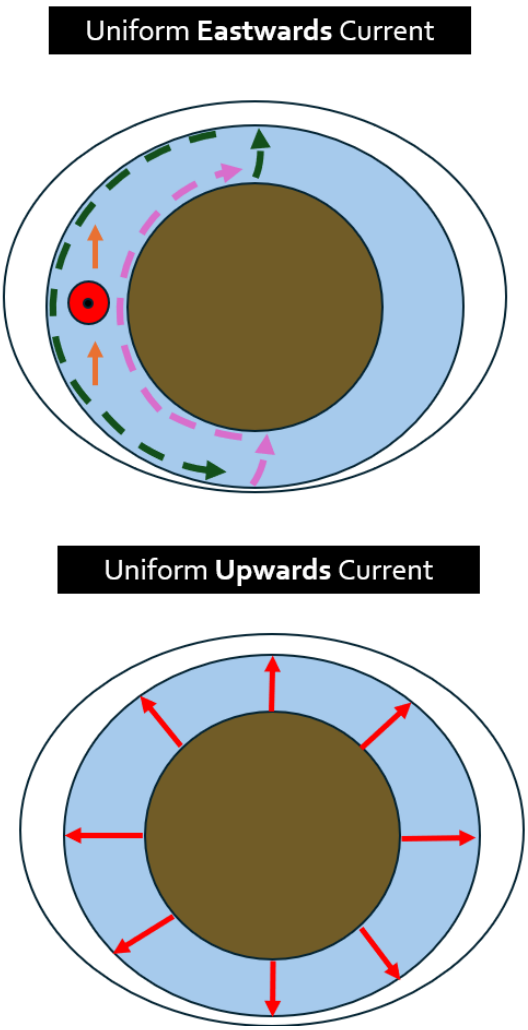

Figure 5.4: Schematic illustrating two idealised configurations imposing a uniform eastwards (top) and upwards (bottom) electrical current (indicated with red) in the ocean. Showing the direction of the curl of the electrical current (orange), and resultant ocean induced magnetic field (OIMF; indicated with green and pink, to colour-match plots of the OIMF outputted from GEMMIE, shown in fig. 5.5). Patterns of OIMF can be obtained visually via a two-fold inverse curl of the electric current curl, using the right hand corkscrew rule. Note that the uniform upwards current has zero curl and therefore does not produce an OIMF.

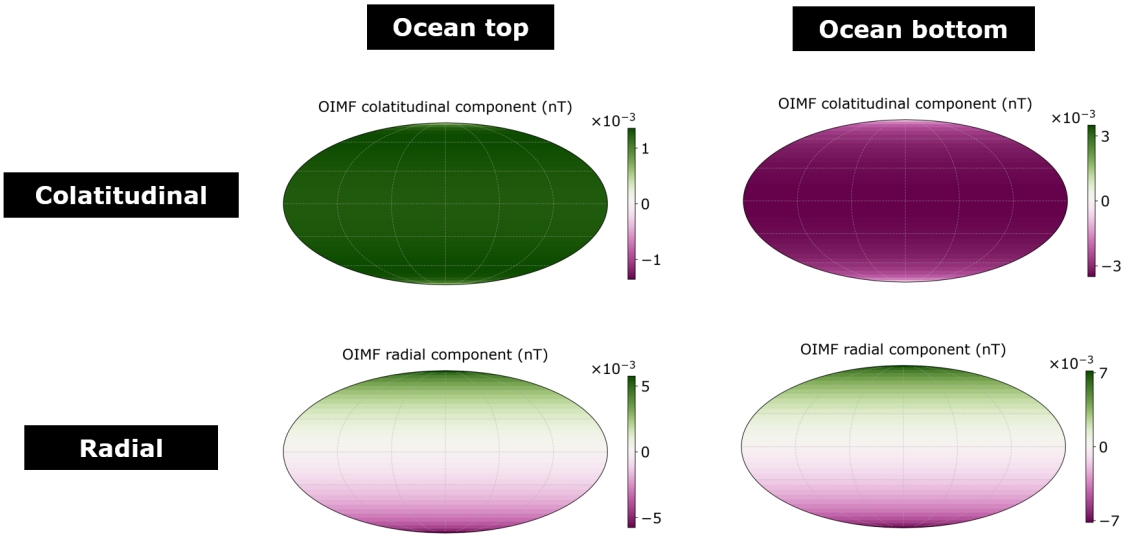

Figure 5.5: Ocean induced magnetic field (OIMF; nT) at the ocean top (left) and bottom (right) given an idealised imposed electrical current, uniform in the eastward direction, of magnitude 10^{-10} A m^{-2}. In this case a non-zero OIMF arises in the colatitudinal (top) and radial (bottom) directions. Note colourbars are saturated and vary throughout.

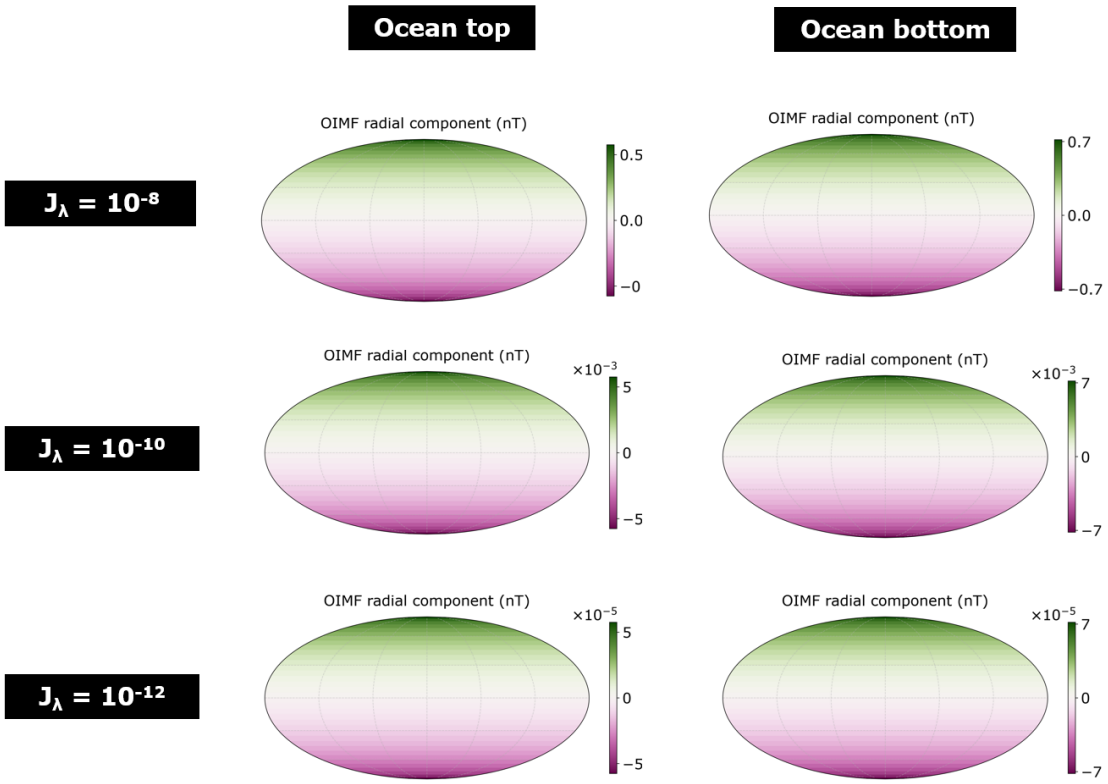

Figure 5.6: Radial component of the ocean induced magnetic field (OIMF; nT) at the ocean top (left) and bottom (right) given an idealised imposed electrical current (J_λ), uniform in the eastward direction. Showing solutions for $J_\lambda = 10^{-8}$ (top), 10^{-10} (default; middle) and 10^{-12} (bottom) A m^{-2}. Note colourbars are saturated and vary throughout.

5.5.3 Idealised tests: latitudinal current variation

Using the same model configuration described in the previous section, tests are performed reversing the sign of the inputted electrical current across the equator, thus introducing local variation (and by extension, curl) into the imposed electrical current.

The first test imposes an eastwards electrical current: $\vec{J} = J_\lambda = 10^{-10}$ A m^{-2} in the northern hemisphere and westwards electrical current: $\vec{J} = J_\lambda = -10^{-10}$ A m^{-2} in the southern hemisphere. From Eq. (5.17), the change in sign of electrical current across the equator yields a downwards (radially inwards) orientated curl. From visual inspection using the right hand corkscrew rule, this is expected to yield an OIMF consisting of two meridional hemispheric loops, directed polewards at depth, equatorwards aloft, downwards at the equator and upwards at the poles (5.7). Numerical solutions obtained using GEMMIE confirm this pattern (fig. 5.8). Note that an OIMF is still expected to arise from spherical geometry effects in this case, however the outputted OIMF is dominated by that arising from the reversal in sign of the electrical current across the equator.

The second test imposes an upwards electrical current: $\vec{J} = J_r = 10^{-10}$ A m^{-2} in the northern hemisphere and downwards electrical current: $\vec{J} = J_r = -10^{-10}$ A m^{-2} in the southern hemisphere. The introduction of meridional variation in J_r introduces an eastwards curl into the radially orientated electrical current. This results in an eastwards OIMF at the equator, as shown in fig. 5.9. The OIMF in this case is orders of magnitude weaker than that induced by meridional variation in the longitudinal electric current, despite the imposed current having the same magnitude.

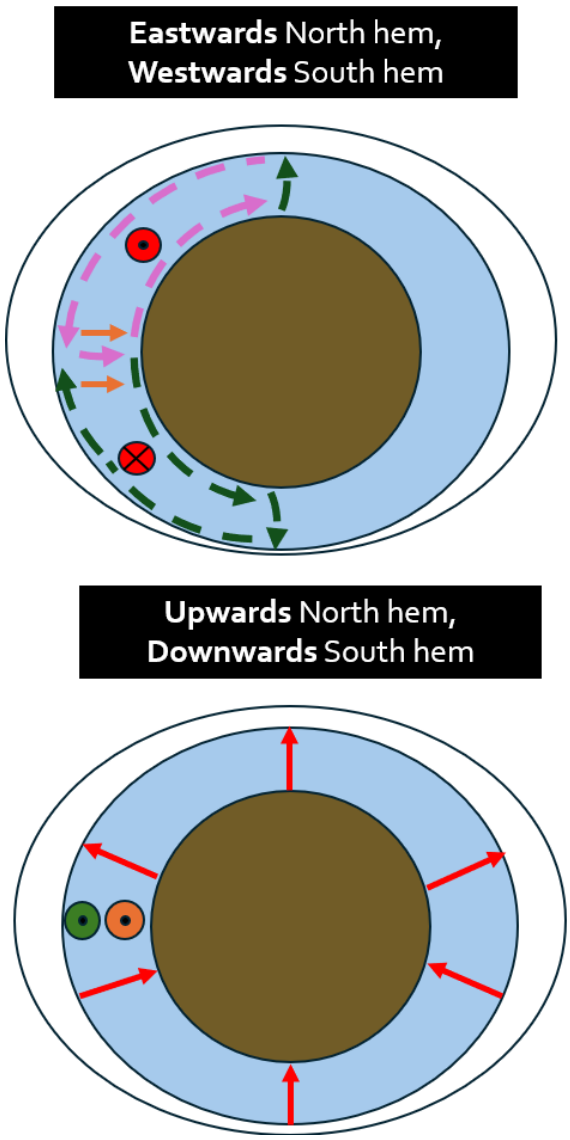

Figure 5.7: Schematic illustrating two idealised configurations, with the sign of the imposed electrical current reversed across the equator. Top shows configuration with uniform eastwards and westwards imposed current in northern and southern hemisphere respectively. Bottom shows configuration with uniform upwards and downwards imposed current in northern and southern hemisphere respectively. Direction of the curl of the electrical current is indicated with orange, and resultant ocean induced magnetic field (OIMF) indicated with green and pink, to colour-match plots of the OIMF outputted from GEMMIE, shown in fig. 5.8). Patterns of OIMF can be obtained visually via a two-fold inverse curl of the electric current curl, using the right hand corkscrew rule.

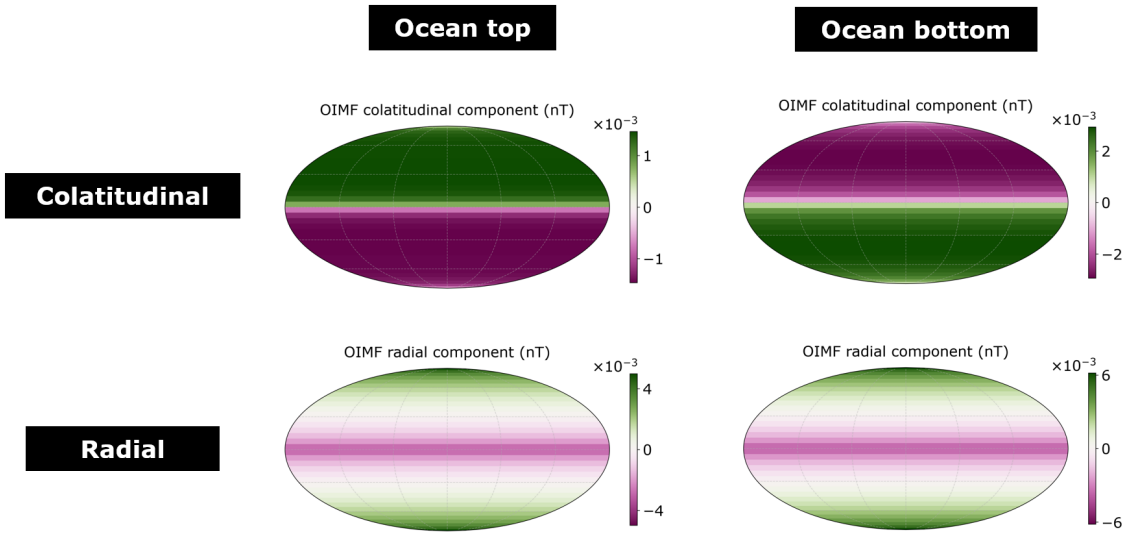

Figure 5.8: Ocean induced magnetic field (OIMF; nT) at the ocean top (left) and bottom (right) given an idealised imposed electrical current, of uniform magnitude in the longitudinal direction, eastwards in the northern hemisphere, southwards in the southern hemisphere. In this case, only the colatitudinal and radial components of the OIMF are non-zero. Note colourbars are saturated and vary throughout.

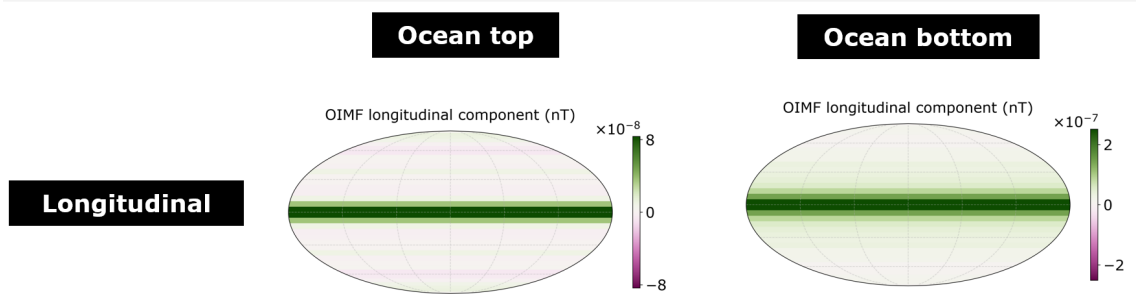

Figure 5.9: Ocean induced magnetic field (OIMF; nT) at the ocean top (left) and bottom (right) given an idealised imposed electrical current, of uniform magnitude in the radial direction, upwards in the northern hemisphere, downwards in the southern hemisphere. In this case, only the longitudinal component of the OIMF is non-zero. Note colourbars are saturated and vary throughout.

5.5.4 Idealised tests: longitudinal current variation

A final test is performed reversing the sign of the imposed electrical current in longitude. In this test, an eastwards electrical current: $\vec{J} = J_\lambda = 10^{-10}$ A m^{-2} is imposed in the western half of the ocean, and a westwards electrical current: $\vec{J} = J_\lambda = -10^{-10}$ A m^{-2} in the eastern half of the ocean.

Given that longitudinal variation in the longitudinally-orientated electric current does not introduce curl (see Eq. (5.17)), an OIMF is expected to arise here solely due to spherical geometry effects. Despite this, the pattern of OIMF outputted by GEMMIE (fig. 5.11) is more complex than previous tests. An OIMF is obtained in all three components, contrasting previous tests where an OIMF is typically not produced in the same component as the imposed current.

A possible explanation for this is illustrated in fig. 5.10. The more complex curl pattern in this case (orientated along the axis of rotation, reversing sign between western and eastern hemispheres) results in an OIMF that is a superposition of multiple magnetic field loops, arising in turn from a superposition of curls. Given this, relating patterns of OIMF to the imposed electrical current by visual means may become more challenging for a complex imposed current not dominated by any particular feature.

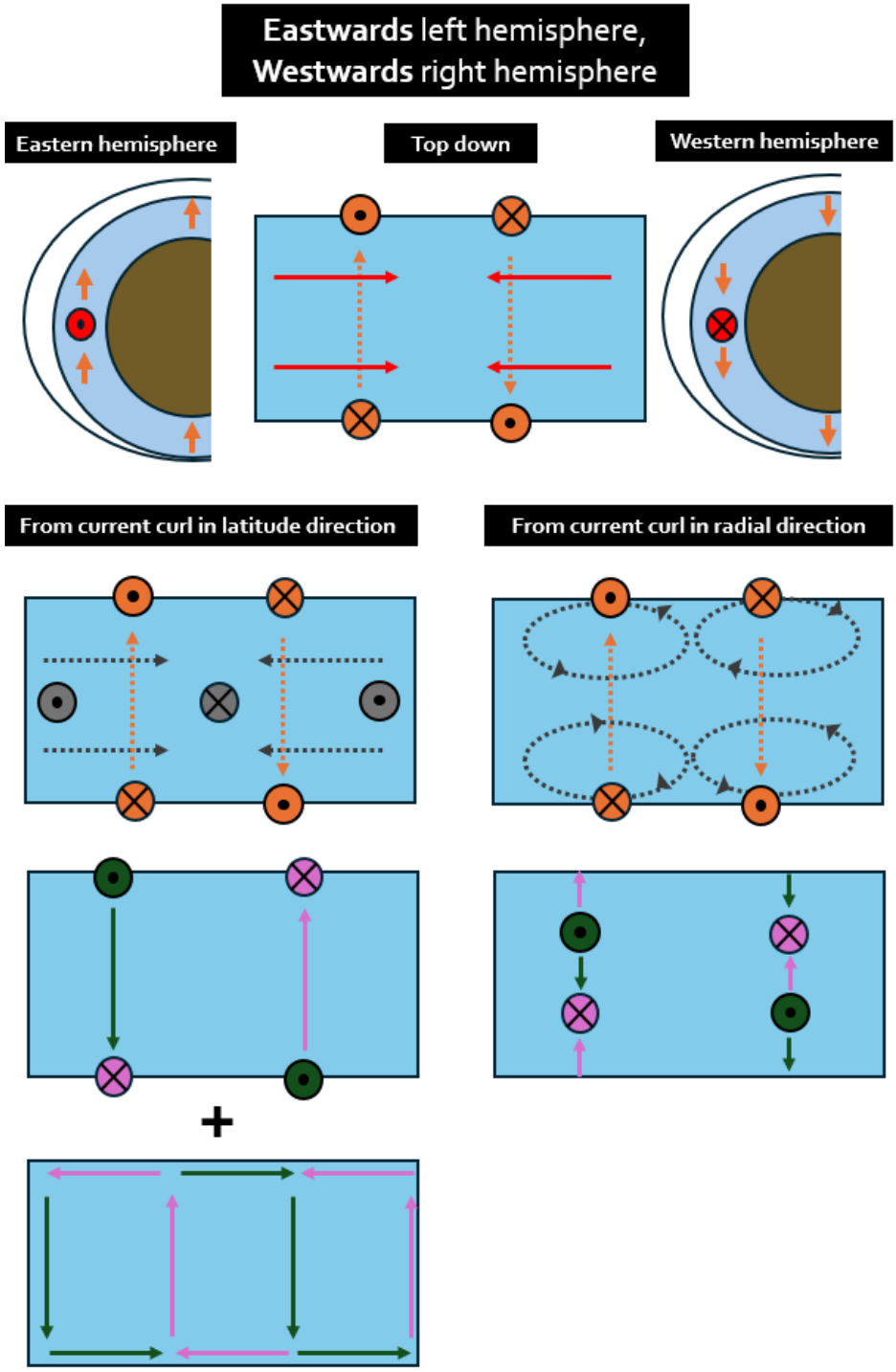

Figure 5.10: Schematic illustrating an idealised configuration, with the sign of the imposed longitudinal electrical current reversed across the middle longitude of the ocean. Direction of the curl of the electrical current is indicated with orange. The inverse curl of this is indicated with dark grey. The ocean induced magnetic field at the ocean top (OIMF; obtained via the inverse curl of dark grey features) is indicated with green and pink, to colour-match with numerical solutions of the OIMF shown in fig. 5.11. Note that the OIMF in this case is more complex, resembling a superposition of magnetic field loops, separated here to aid visualisation. Patterns of OIMF can be obtained visually using the right hand corkscrew rule.

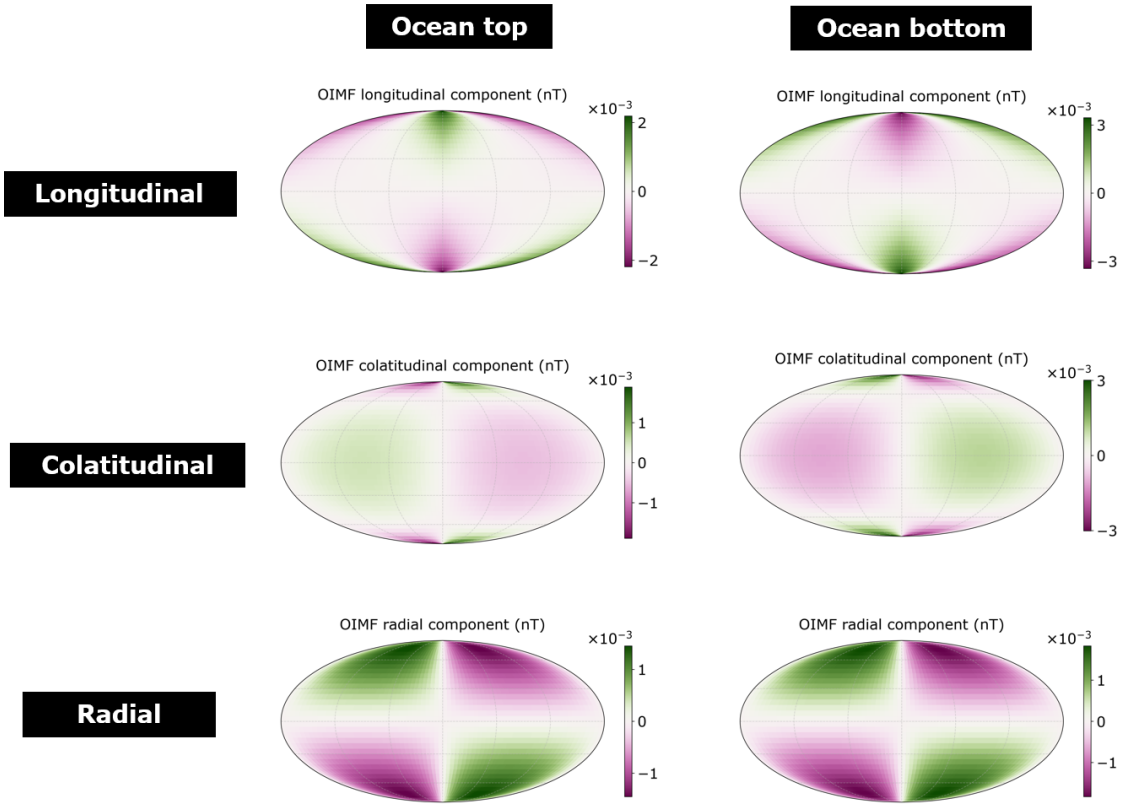

Figure 5.11: Ocean induced magnetic field (OIMF; nT) at the ocean top (left) and bottom (right) given an idealised imposed electrical current, eastwards in the western hemisphere and westwards in the eastern hemisphere. In this case, a non-zero OIMF is obtained in the longitudinal, colatitudinal and radial directions.

5.6 Ocean simulation results

The following section illustrates numerical solutions from the global 3D ocean simulations used to compute electrical currents for input into the electromagnetic solver.

5.6.1 Temperature and conductivity

Numerical solutions of the zonally averaged ocean temperature and conductivity at 5 and 35 g kg^{-1} mean salinity are shown in fig. 5.12.

At 5 g kg^{-1}, the solution is poorly mixed, with a diffuse, vertical gradient in temperature, $\sim$ 0.4 °C warmer at the ocean bottom vs the ice interface. The whole ocean in inversely stratified owing to the large effective vertical diffusivity κ_z employed, which ensures the thermal expansion coefficient remains negative across the whole ocean.

At 35 g kg^{-1}, warmest waters are found at the polar ice interface, co-located with regions of warmest temperature restoring. Here the ocean is approximately $\sim$ 0.1 °C warmer than the well-mixed waters at depth. Owing to the larger employed ocean salinity, the thermal expansion coefficient is positive. Relatively warmer temperatures aloft stratify the ocean at the poles while bottom heating destabilises the ocean at depth, ensuring efficient mixing here by the convection parameterisation scheme.

The ocean conductivity structure follows that of temperature. Conductivity gradients are largest in the 35 g kg^{-1} solution, despite weaker temperature gradients than the 5 g kg^{-1} solution. This is owing to the non-linear dependence of conductivity upon salinity, (where equivalent increases in temperature yield larger gains in conductivity at high mean ocean salinity, see section 5.9.1 for further discussion). Variation in conductivity in the 35 g kg^{-1} solution barely exceeds 0.01 S m^{-1} owing to the weak temperature gradients. This is two orders of magnitude weaker than conductivity variations observed in Earth's oceans (Tyler et al. 2017).

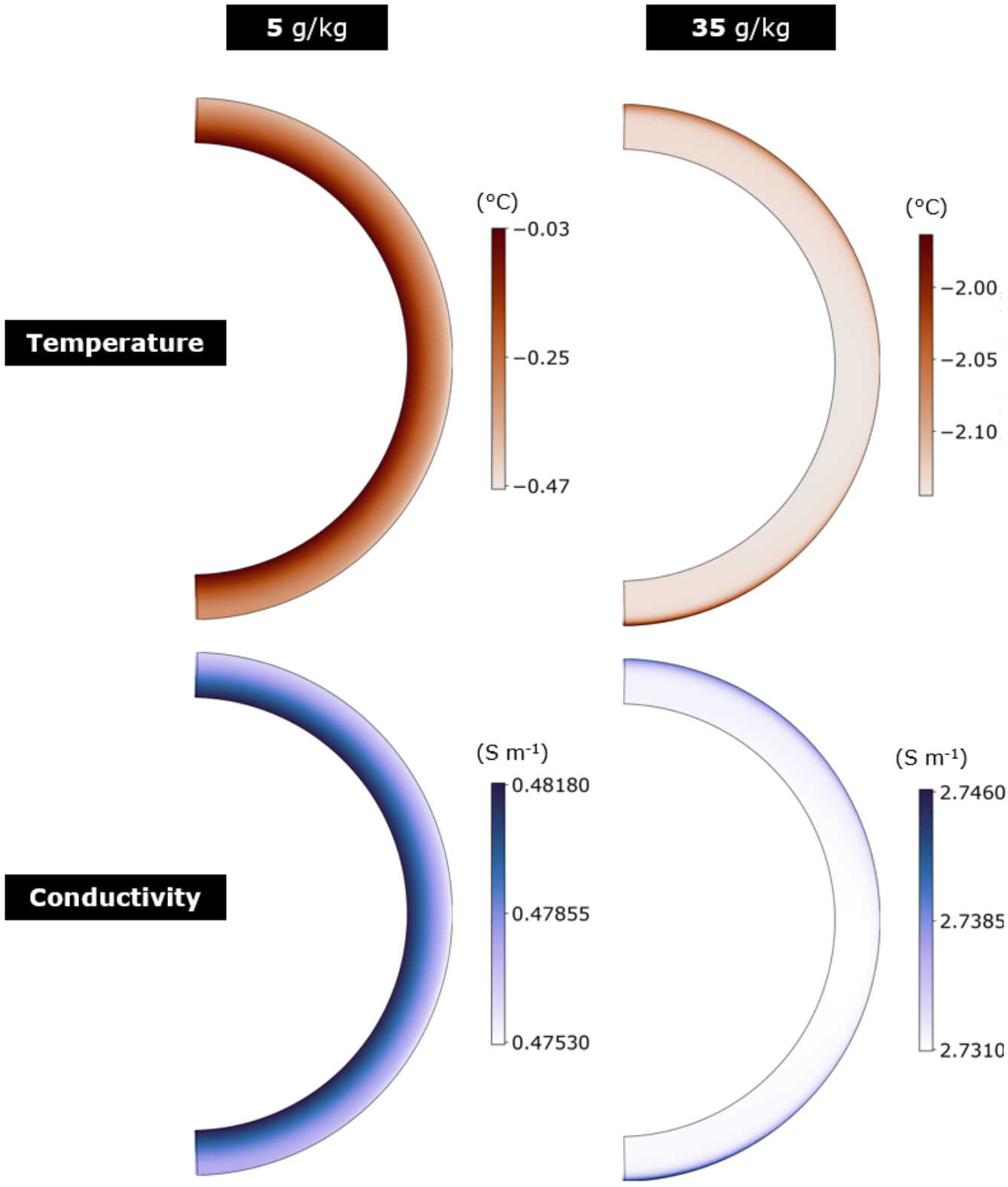

Figure 5.12: Zonally averaged solutions of ocean temperature (°C; top) and conductivity (S m^{-1}; bottom) from 3D simulations at 5 and 35 g kg^{-1} mean ocean salinity (left and right respectively). Conductivity is computed offline using the Gibbs Seawater Toolbox (McDougall and Barker 2011). Note that colourbars are saturated and vary throughout.

5.6.2 Ocean velocity

Solutions for longitudinal, colatitudinal and radial ocean velocity components are shown in figures 5.13 (zonally averaged) and 5.14 (extracted at the ocean top).

In both solutions, ocean velocity is strongest nearer the equator, where four cell-like structures develop near the ocean top in the longitudinal direction, of alternating sign. This follows from the longitudinal variation in upper boundary restoring temperature, in turn strongest slightly southward of the equator (fig. 5.2).

At 5 g kg^{-1}, zonal flows diverge at $\sim$ -160 and 20 degrees longitude, slightly eastwards of longitudes corresponding to the sub- and anti-Saturn points, where upper boundary temperatures are coldest (corresponding to longitudes of thicker ice on Enceladus). At these longitudes, the colatitudinal and radial ocean flows converge at the equatorial ocean top to maintain continuity (i.e., conserve mass). The situation is reversed in the 35 g kg^{-1} solution, where zonal flows tend to converge nearer the sub- and anti- Saturn points, with colatitudinal and radial flows diverging here. This can be explained by the reversal of the longitudinal density gradient at the ocean top between the 5 and 35 g kg^{-1} solutions, owing to the negative thermal expansion coefficient in the former, and positive in the latter. This also causes the latitudinal density gradient to reverse between the solutions. As a result, the zonal velocity at depth is of opposing sign between the two solutions, in accordance with thermal wind balance.

Ocean velocities are strongest in the zonal direction, of order 10^{-3} m s^{-1}, consistent with predictions made using energetic constraints (Jansen et al. 2023). Colatitudinal velocities are weaker and of order 10^{-5} m s^{-1} in both solutions, except in narrow cells straddling the equator in the high salinity solution, located at the region of zonal flow convergence. Here the colatitudinal velocity reaches 10^{-4} m s^{-1}. This is weaker than derived from energetic constraints, perhaps owing to numerical viscosity employed here for numerical stability, and the use of an eddy parameterisation scheme that accomplishes mixing leaving the Eulerian flow with less to do. Radial velocities are weaker still, of order 10^{-6} m s^{-1}, except again in narrow regions of downwelling in the high salinity solution. Weak vertical velocities arise because the resolution of the configuration is too coarse to resolve convection. Plotting a longitude depth-projection of ocean velocity at the equator shows that velocity features at the ocean top persist $\sim$ 5 km into the ocean, but with velocity contours tilted westward with increasing depth in the low salinity solution (fig. 5.16).

In both solutions, the zonally averaged radial and latitudinal flows are dominated by boundary circulations at the ocean top and bottom, their orientation reversed between the two solutions. The bottom boundary flow feature aligns with the axis of rotation in both solutions, in accordance with Taylor Proudman theorem, following the tangent cylinder. This alignment is not observed in the zonally averaged zonal velocity.

The zonal average masks some of the complexity in the flow field, and to illustrate this, fig. 5.15 shows velocity fields at the sub-Saturnian longitude. Alignment with the axis of rotation is much more apparent here in the 35 g kg^{-1} solution, occurring also in the zonal flows. The strongest colatitudinal and radial flows are notably confined outside the tangent cylinder, with transport directed towards the equatorial ocean top. In contrast, boundary circulations in the low salinity solutions are confined to the uppermost few grid points of the ocean and do not exhibit strong alignment to the axis of rotation. The greater radial extent of velocity features at high salinity may arise because eddies are less efficient here in redistributing cooler waters laterally vs the low salinity case, enabling meridional gradients in ocean temperature to be fluxed deeper into the ocean interior which, in turn, give rise to an Eulerian meridional flow.

Finally, fig. 5.17 shows the vertically integrated ocean transport (m^2 s^{-1}). Transport is strongest in the longitudinal direction in both simulations, reversing sign dependant upon the mean salinity. Transport in the radial direction is weakest. Note that colatitudinal and radial transport is 2-3 orders of magnitude weaker at 5 g kg^{-1} mean salinity. This is because a much larger share of transport in the ocean interior is achieved by the employed eddy parameterisation scheme at low salinity vs the high salinity solution. Also note that the largest zonal transport simulated here (~ 10 m^2 s^{-1}) is ~ 4 orders of magnitude weaker than used in OIMF studies of Earth's ocean (e.g., Šachl et al. 2019). This is owing to more sluggish flows here compared to those typically observed in Earth's oceans.

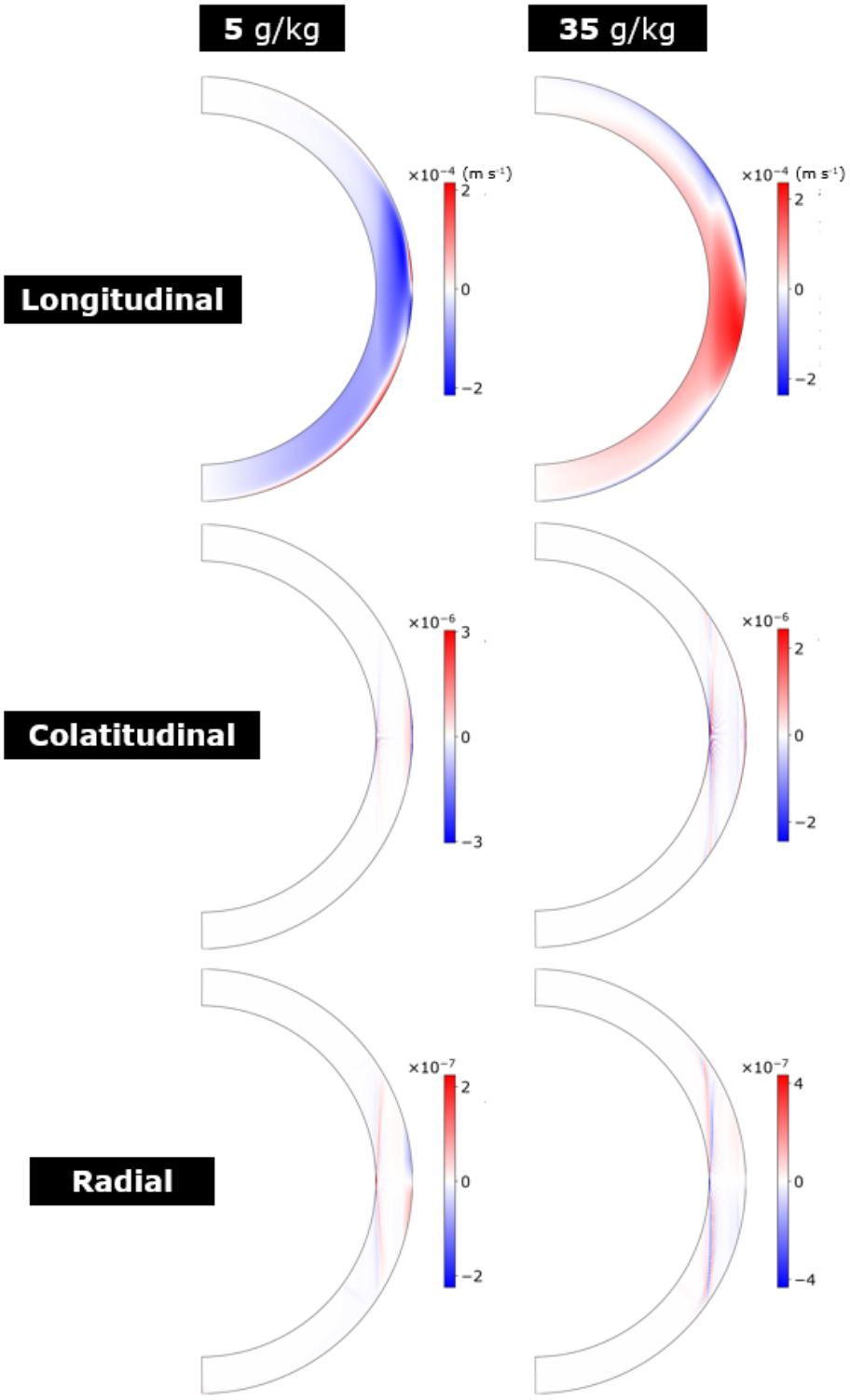

Figure 5.13: Zonally averaged ocean velocity (m s^{-1}) in the longitudinal (top), colatitudinal (middle) and radial directions (bottom) for solutions at 5 and 35 g kg^{-1} mean salinity (left and right respectively).

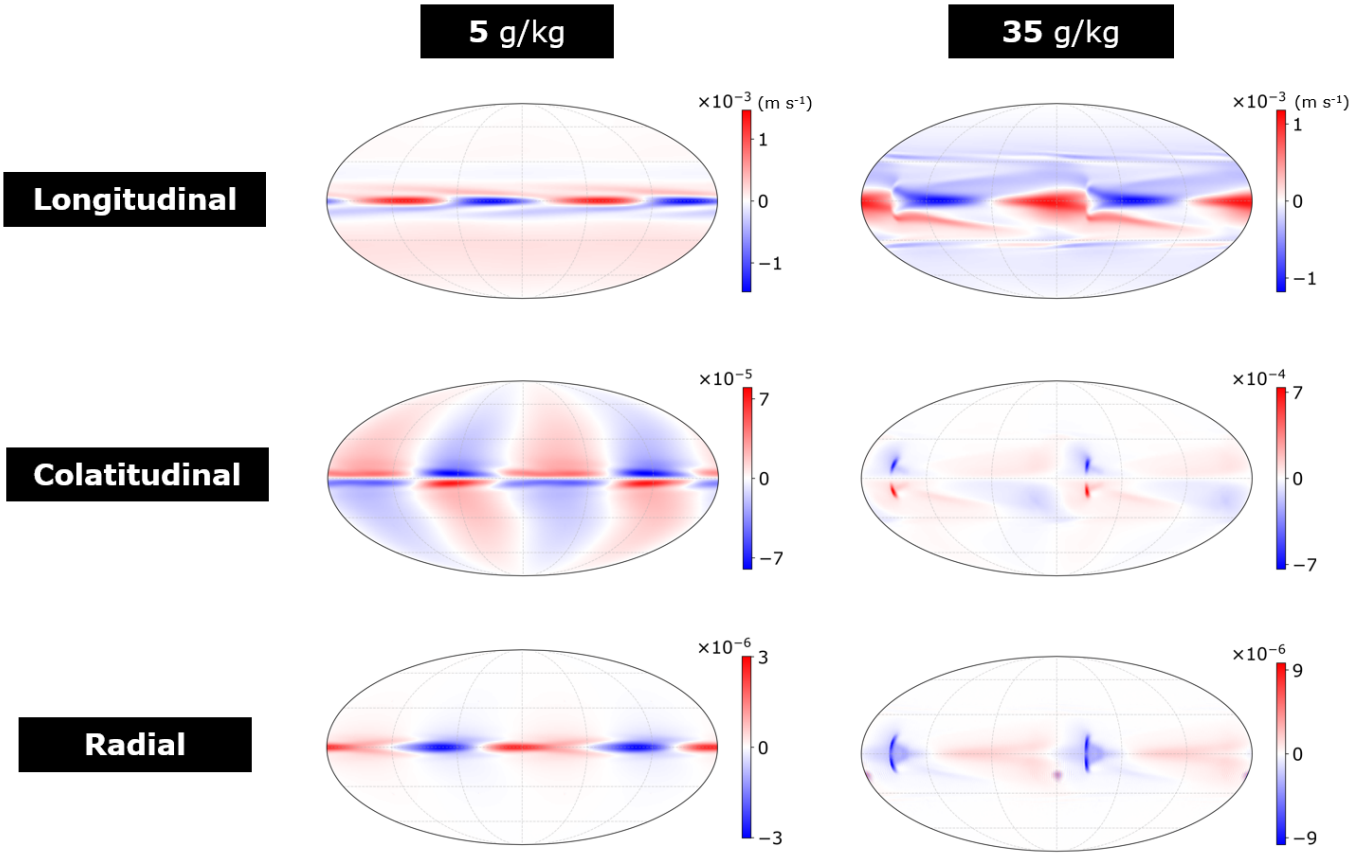

Figure 5.14: Ocean velocity (m s^{-1}) in the longitudinal (top), colatitudinal (middle) and radial (bottom) directions for solutions at 5 and 35 g kg^{-1} mean salinity (left and right respectively), here shown at the top of the ocean.

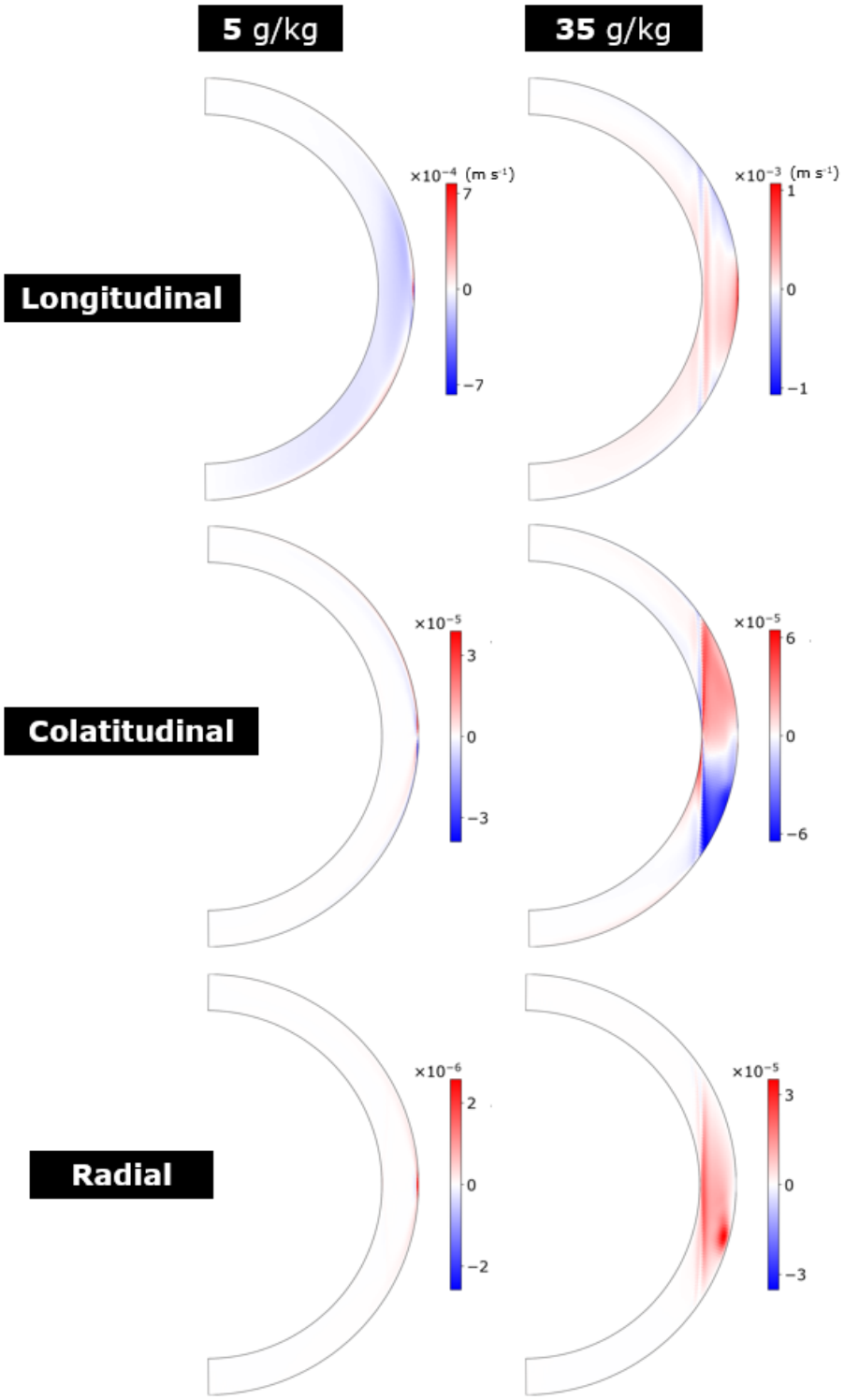

Figure 5.15: Ocean velocity (m s^{-1}) in the longitudinal (top), colatitudinal (middle) and radial (bottom) directions for solutions at 5 and 35 g kg^{-1} mean salinity (left and right respectively), here shown at the Sub-Saturnian longitude.

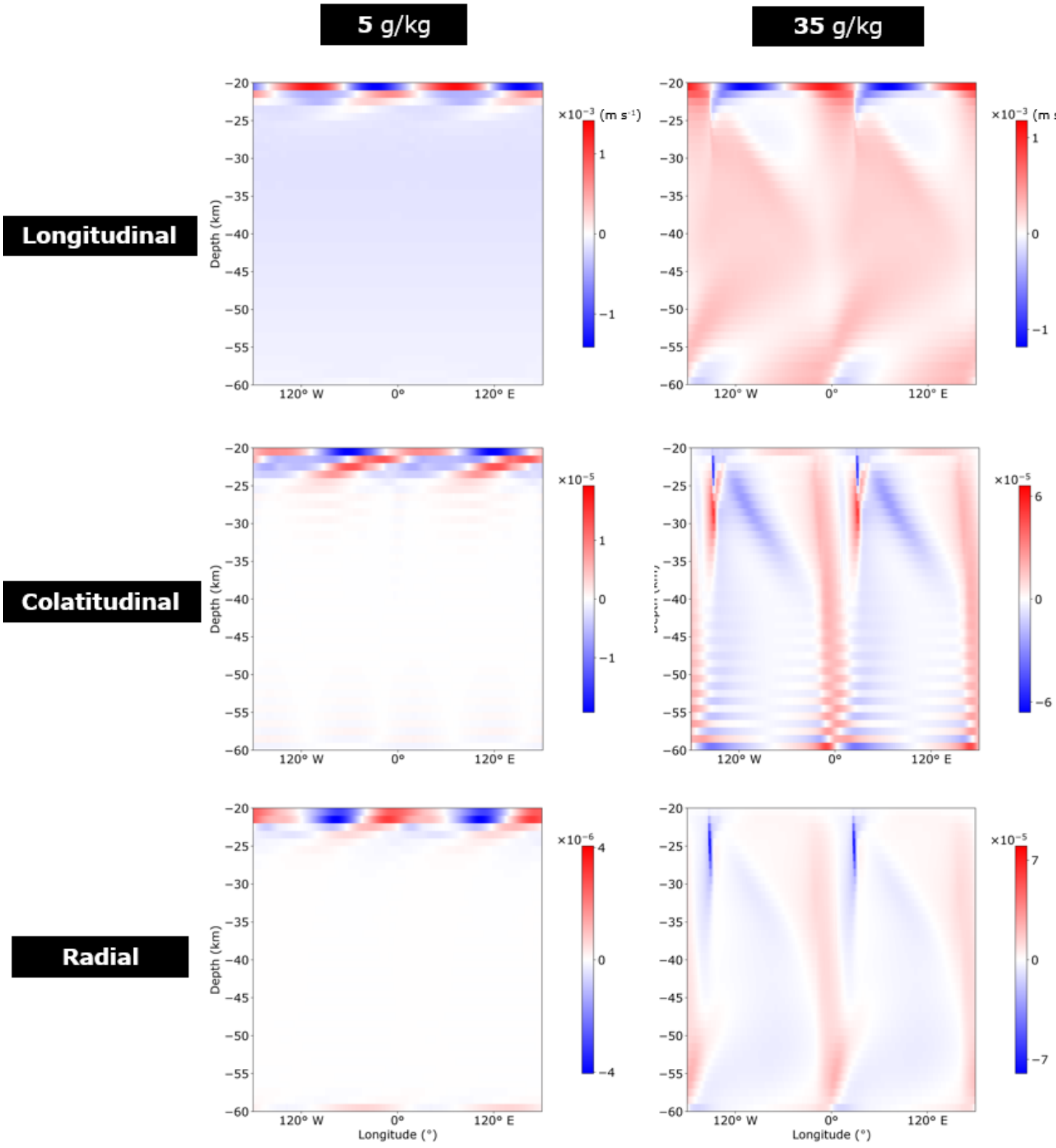

Figure 5.16: Ocean velocity (m s^{-1}) in the longitudinal (top), colatitudinal (middle) and radial (bottom) directions for solutions at 5 and 35 g kg^{-1} mean salinity (left and right respectively), here shown at the equator.

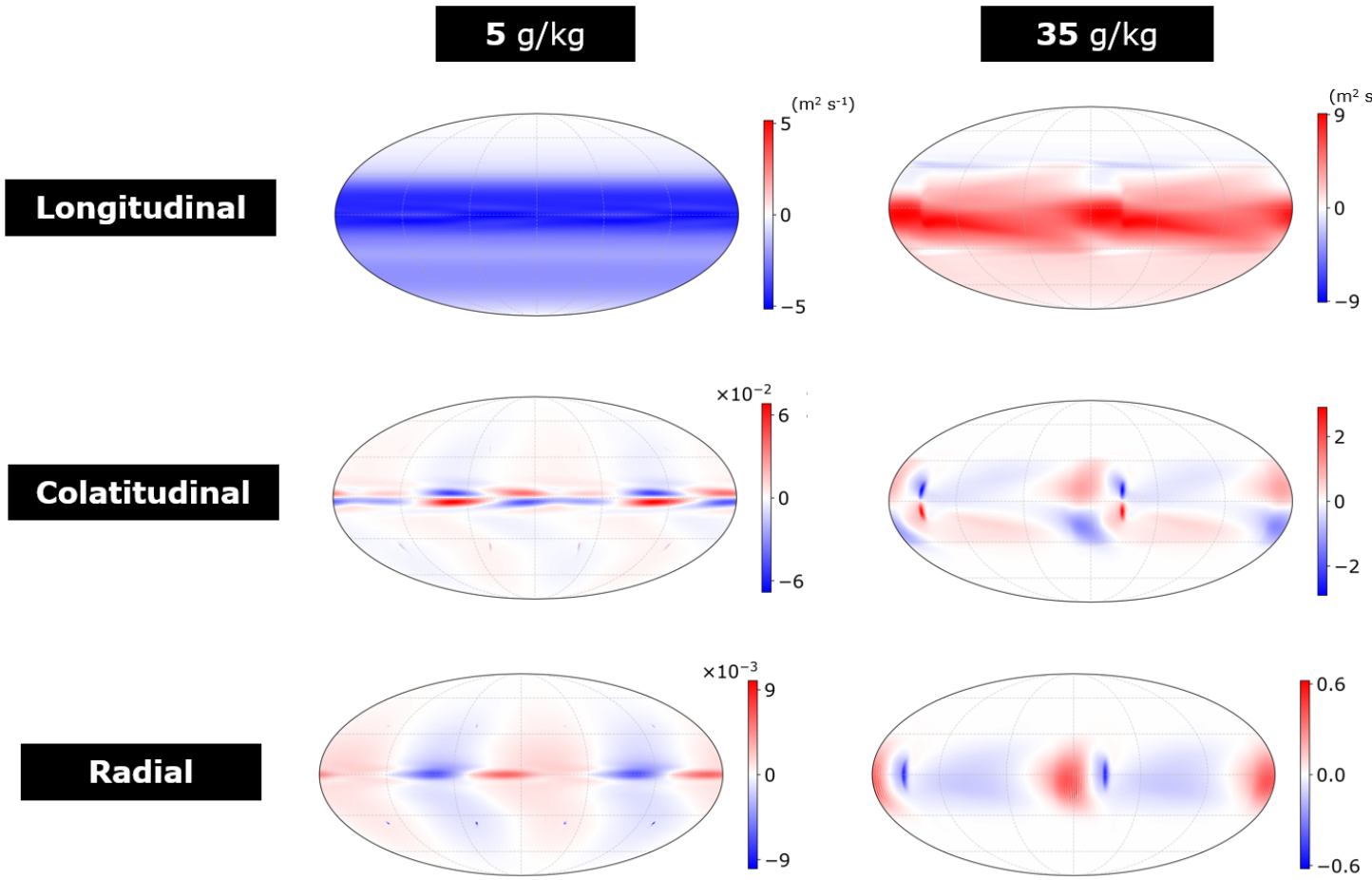

Figure 5.17: Vertically integrated ocean transport (m^2 s^{-1}) in the longitudinal (top), colatitudinal (middle) and radial (bottom) directions for solutions at 5 and 35 g kg^{-1} mean salinity (left and right respectively).

5.6.3 Electrical currents

Solutions for the zonally averaged electrical current density (A m^{-2}; computed using Eq. (5.10) and velocity fields illustrated in the previous section) are shown in fig. 5.18.

Patterns of electrical current follow those of ocean velocity, modulated by variation in the ambient magnetic field vector. J_r follows the zonal ocean velocity in accordance with Eq. (5.13), but tends to zero near the poles, where the Θ component of the ambient magnetic field vector tends to zero. J_Θ instead tends to zero and reverses sign at the equator, where the r component of ambient magnetic field tends to zero (in accordance with Eq. (5.12)). J_λ is controlled by both the radial and colatitudinal ocean flows (Eq. (5.11)), and is strongest at the boundaries, where these flows are strongest. The zonally averaged J_λ is two and three orders of magnitude weaker than the other current components in the 5 and 35 g kg^{-1} solutions respectively, following from the weaker radial and meridional vs zonal flows.

Fig. 5.19 show the imposed electrical current at the ocean top and fig. 5.20 the vertically integrated electrical current (A m^{-1}). From fig. 5.19 one can see that electrical currents are weaker in 5 g kg^{-1} solution, even where ocean velocities are of comparable magnitude to those at 35 g kg^{-1} (e.g., compare with fig. 5.14). This is owing to the $\sim$ 5-6 times weaker electrical conductivity at 5 vs 35 g kg^{-1}. Overall, the vertical integral of the electrical current exhibits much stronger longitudinal variation in its longitudinal component. This corresponds to the increased longitudinal variation in the vertically integrated radial and colatitudinal transports in these two solutions, unlike the longitudinal transport, where longitudinal variation is confined closer to the ocean boundary (e.g., see fig. 5.14).

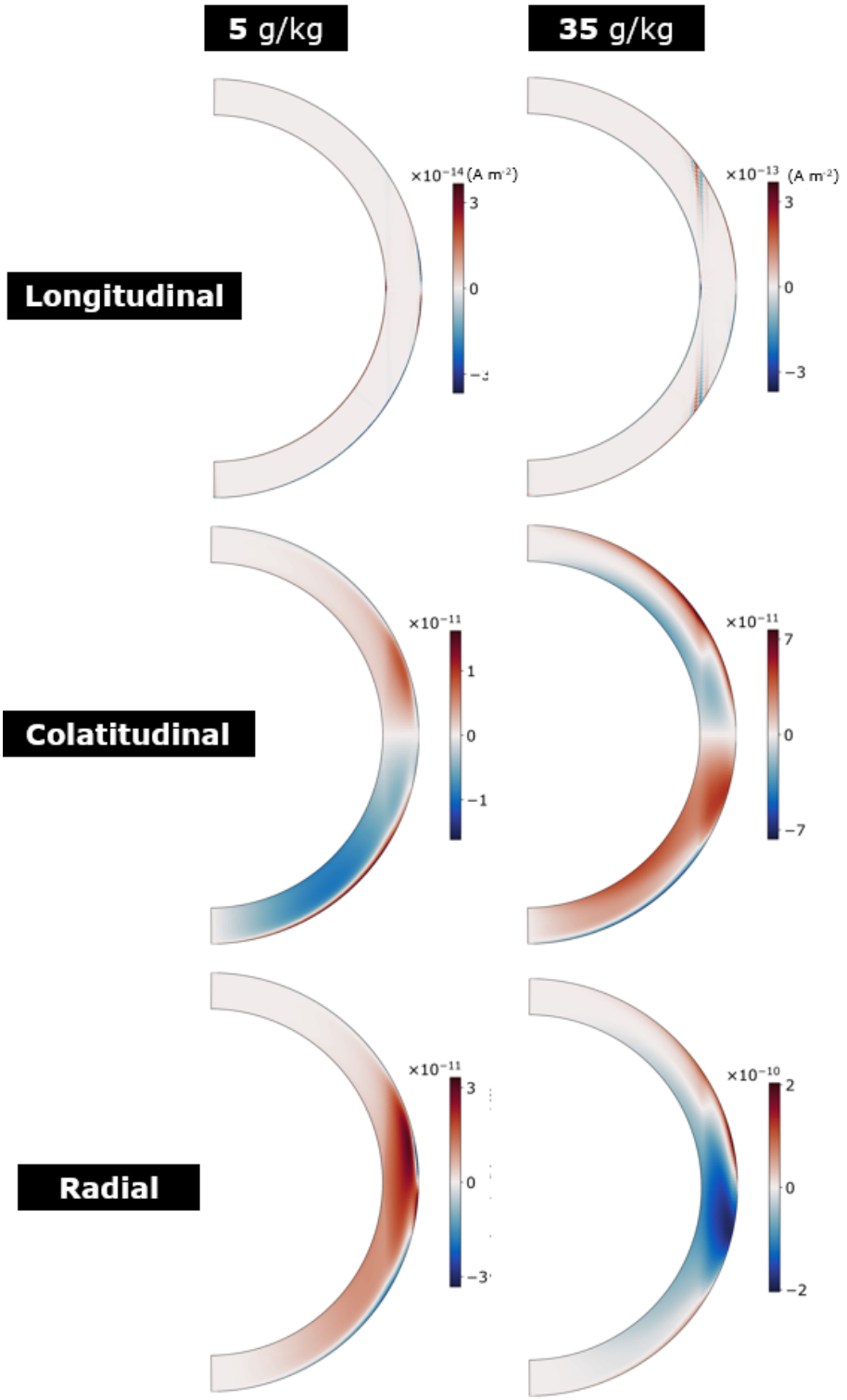

Figure 5.18: Zonally averaged electrical current density (A m^{-2}) imposed in electromagnetic simulations in the longitudinal (top), colatitudinal (middle) and radial (bottom) directions, computed using Eq. (5.10) and ocean velocity solutions at 5 and 35 g kg^{-1} mean salinity (left and right respectively)

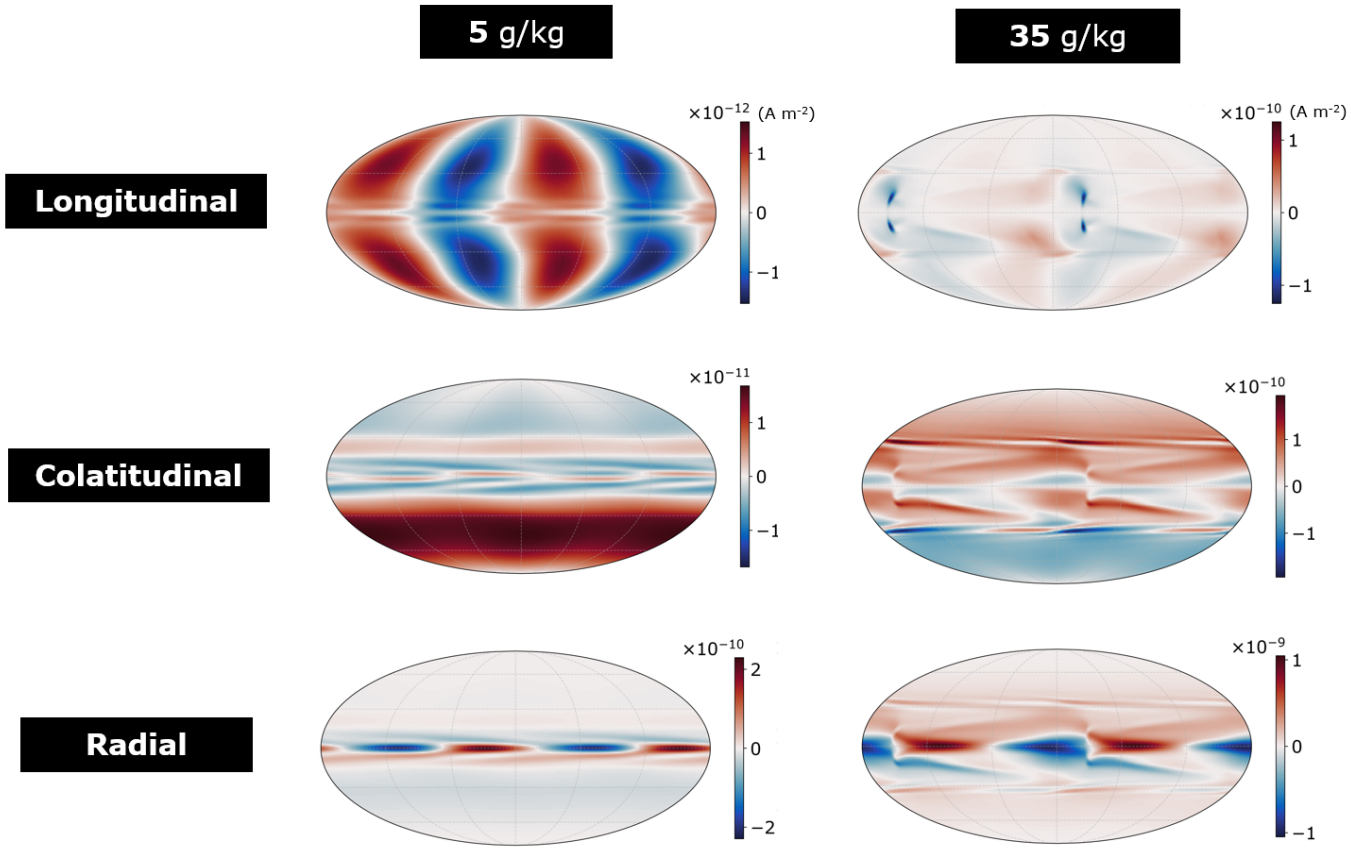

Figure 5.19: Electrical current density (A m^{-2}) imposed in electromagnetic simulations, here shown at the ocean top. The longitudinal (top), colatitudinal (middle) and radial directions (bottom) are computed using Eq. (5.10) and ocean velocity solutions at 5 and 35 g kg^{-1} mean salinity (left and right respectively).

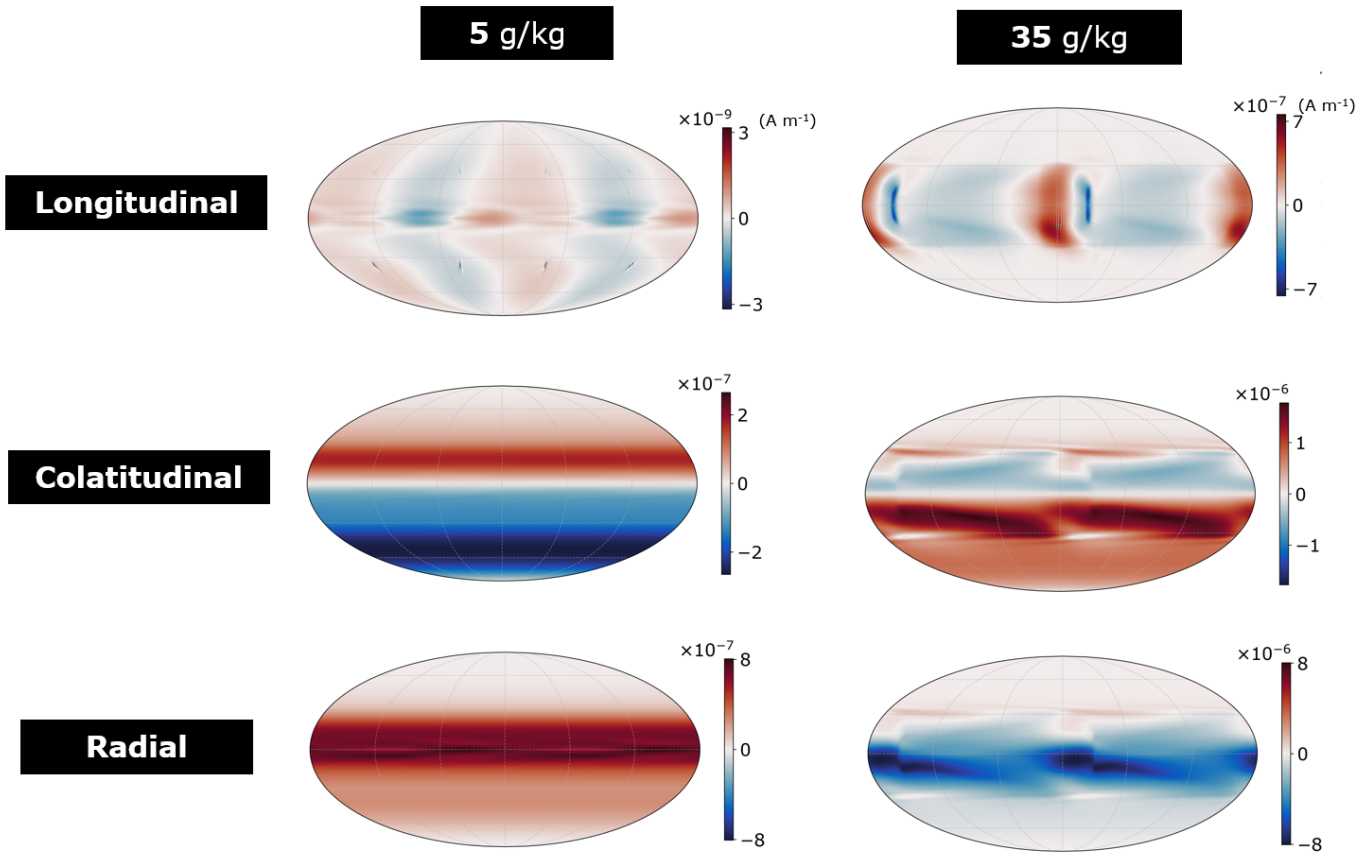

Figure 5.20: Vertical integral of electrical current density (A m^{-1}) imposed in the longitudinal (top), colatitudinal (middle) and radial directions (bottom), computed using Eq. (5.10) and ocean velocity solutions at 5 and 35 g kg^{-1} mean salinity (left and right respectively).

5.7 Results: electromagnetic modelling

5.7.1 OIMF

Fig. 5.23 shows solutions for the OIMF (nT) extracted at the ocean's uppermost layer, in the longitudinal (B_λ), colatitudinal (B_Θ) and radial (B_r) directions.

The OIMF in the ocean is dominated by B_λ in both solutions. B_λ exhibits a hemispheric dipole, reversing sign across the equator. Importantly, the orientation of the hemispheric dipole is reversed at 5 vs 35 g kg^{-1}, corresponding to the reversal of sign in zonal velocity between these solutions. B_λ appears to follow the vertically integrated zonal transport illustrated in fig. 5.17. The reversal in sign of B_λ across the equator occurs because of the reversal in sign of the radial component of Saturn's magnetic field here (with which the zonal ocean flows interact; see bottom panel in fig. 5.3 and Eq. (5.12)). B_λ is ~ 5 times weaker at 5 g kg^{-1} vs 35 g kg^{-1}, owing to the weaker ocean conductivity.

B_Θ is the second strongest OIMF component in both solutions. Unlike B_λ, B_Θ appears to be dominated by local ocean flows (near the ocean top), rather than following the vertically integrated transport. The reason for this is not clear. In the high salinity case, it may be because the strong narrow circulation features introduce a strong local curl in the imposed electrical currents, allowing these to dominate over the larger scale transports at depth (as discussed in section 5.5.2). At 5 g kg^{-1} salinity, the dominance of boundary circulations in the ocean flow could possibly explain why these dominate the OIMF.

As with B_λ, B_Θ tends to zero at the equator, where the radial component of Saturn's magnetic field (with which the colatitudinal flows interact - see Eq. (5.11)) tends to zero. Yet, a reversal in sign of B_Θ does not occur at the equator because the ocean flows themselves also reverse sign here.

B_r is the weakest OIMF component and exhibits differing behaviour between the high and low salinity solutions. At 5 g kg^{-1}, B_r is dominated by the local flows, strongest at the equator (where the colatitudinal component of Saturn's magnetic field is strongest), weaker nearer the poles. At 35 g kg^{-1}, B_r notably does not appear to follow either the vertically integrated or local ocean flows. Instead, B_r is strongest in a band (of what at first appears noise-like in nature) straddling $\sim 30^\circ$ latitude, peaking at the sub- and anti-Saturnian longitudes. This latitude corresponds to that of the tangent cylinder, to which a boundary circulation remains confined in the simulation here (e.g., see fig. 5.13).

It is not clear why this feature produces a noise-like pattern that dominates the OIMF at the ocean top.

Overall, the OIMF does not exceed 10^{-4} nT, approximately two orders of magnitude weaker than predicted using the scaling of Vance et al. (2021) (Eq. (5.8)) and 1-2 orders of magnitude weaker than idealised tests performed in section 5.5.2. While the electrical currents employed here reach comparable magnitude to the idealised tests, this is not achieved globally (e.g., see fig. 5.19). Variations of ocean flows with depth permits cancellation in the overall depth-integrated transport. This may explain why the OIMF found here is weaker than predicted using the scaling of Vance et al. (2021).

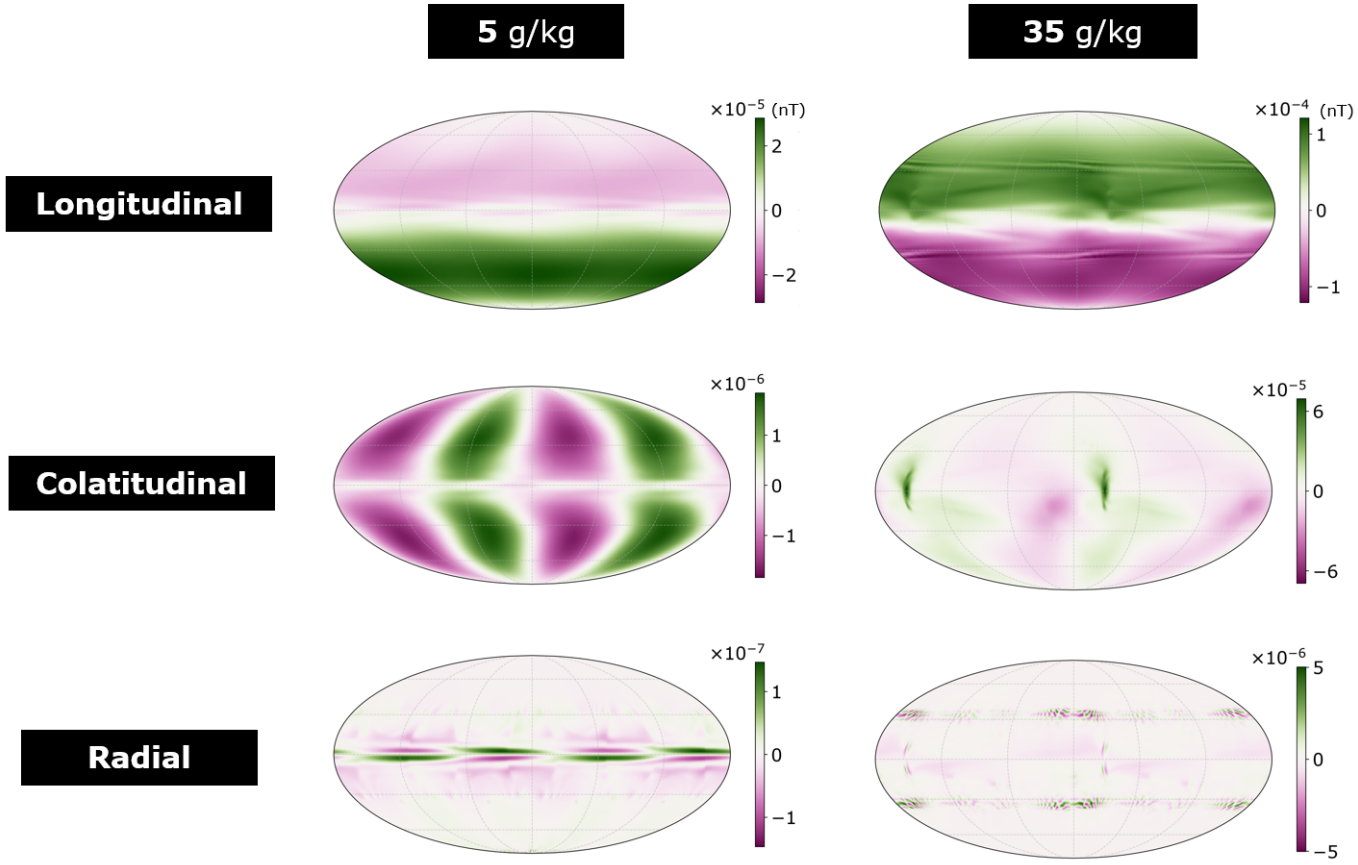

Figure 5.21: Ocean induced magnetic field (OIMF; nT) extracted at the oceans' uppermost layer, in the longitudinal (top), colatitudinal (middle) and radial (bottom) directions, at 5 and 35 g kg^{-1} mean salinity (left and right respectively). Solutions here are obtained imposing a 3D varying electrical current (illustrated in fig. 5.19, in-turn computed given a 3D ocean velocity field outputted from an ocean general circulation model, and described in section 5.6.2)

.

5.7.2 OIMF in the absence of longitudinal variation

To clarify the role of longitudinal variation in the ocean flow in shaping the OIMF, tests are performed using the zonally averaged ocean velocity fields illustrated in fig. 5.13. The imposed electrical currents in this case are therefore uniform in the longitudinal direction. Simulations are otherwise identical to those performed in the previous section. The vertically integrated ocean transports (m^2 s^{-1}) for this test are shown in fig. 5.17 and corresponding OIMF shown in fig. 5.23.

A key consequence of using a zonally averaged flow is a $\sim$ 1-2 orders of magnitude reduction in the strength of the OIMF. This occurs in B_λ despite the vertically integrated zonal ocean transport (which controls B_λ in simulations here, see previous section) being similar to the reference case (compare upper panels of figures 5.17 and 5.22). This suggests the magnitude of local flows near the ocean top - an order weaker in this zonally averaged case - also has a role in controlling the OIMF magnitude. Despite this discrepancy, the dipole structure of B_λ from the reference case is well reproduced.

Because there is no longitudinal variation in the imposed current, the outputted OIMF is zonally uniform. This results in patterns of B_Θ and B_r that differ significantly from the reference case. Namely, B_Θ and B_r appear to more closely follow the vertically integrated ocean transport, contrasting the solutions presented in the previous section, which were instead dominated by local flows. As a result, the structure of B_Θ and B_r are more similar to one other than in the reference case, exhibiting alternating bands that straddle the tangent cylinder at 35 g kg^{-1}, and the equatorial region at 5 g kg^{-1}.

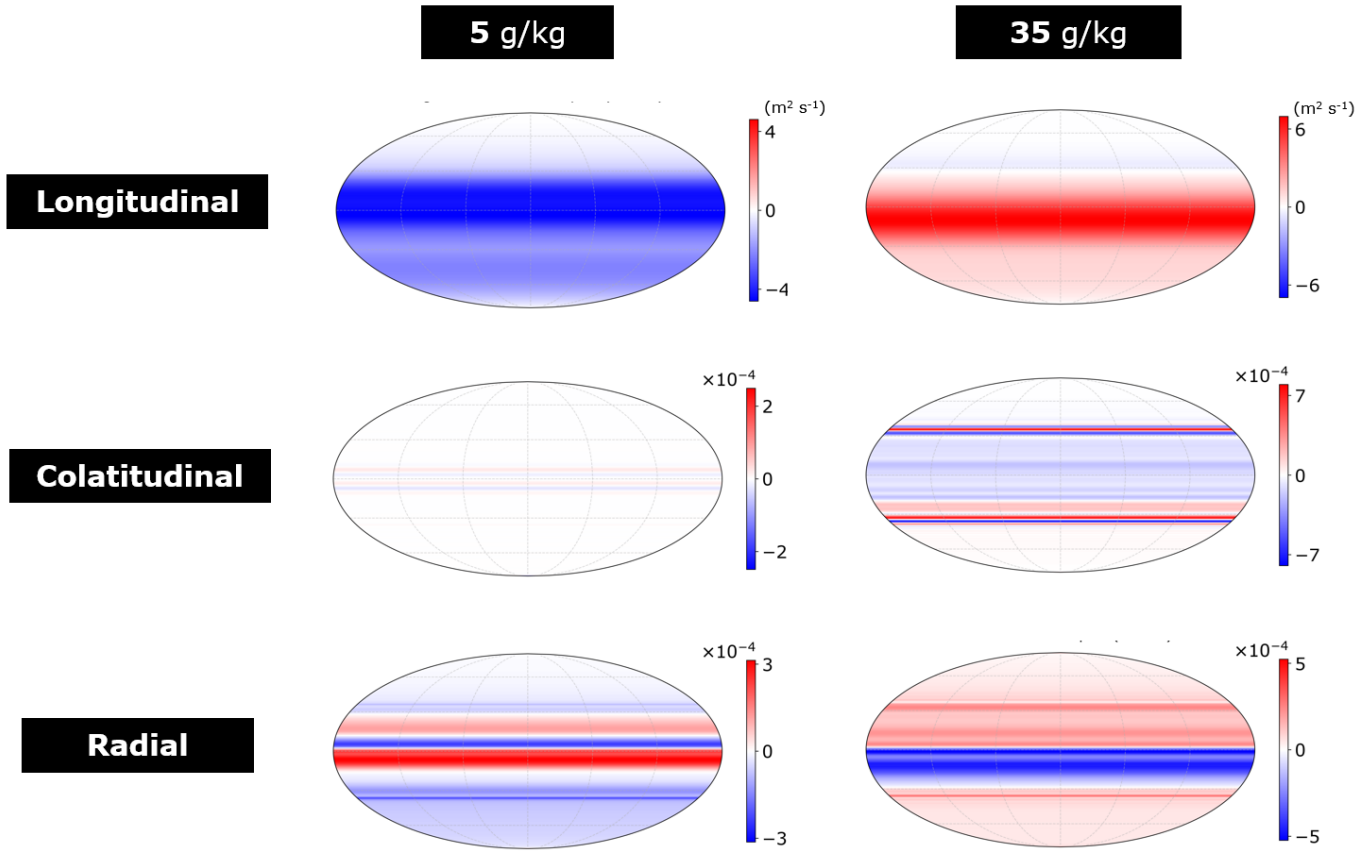

Figure 5.22: Vertically integrated ocean transport ($m^2\ s^{-1}$) assuming a zonally averaged velocity field as illustrated in fig. 5.13. The longitudinal (top), colatitudinal (middle) and radial (bottom) directions, are shown at 5 and 35 g kg^{-1} mean salinity (left and right respectively).

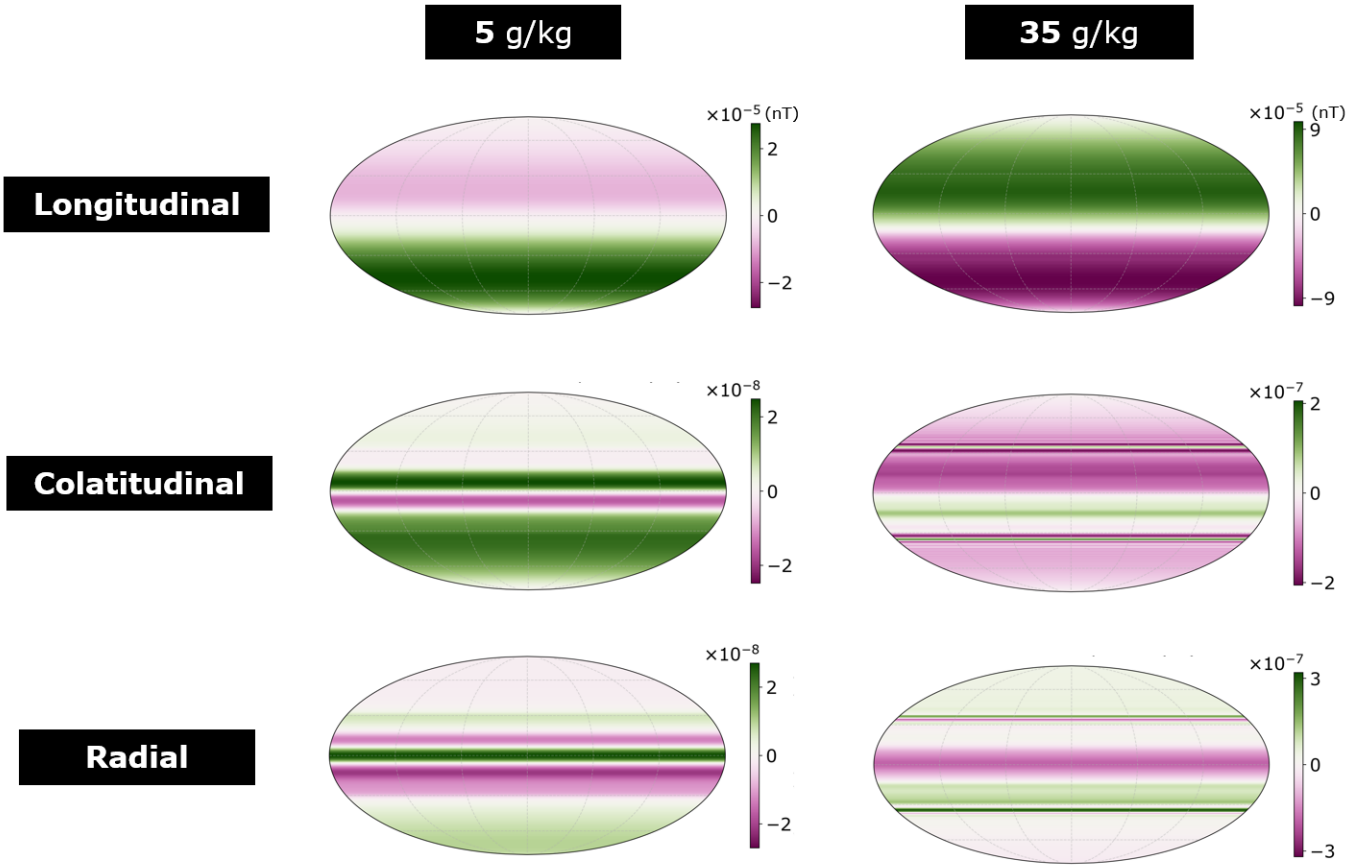

Figure 5.23: Ocean induced magnetic field (OIMF; nT) assuming a zonally averaged ocean velocity field as illustrated in fig. 5.13. Shown is the OIMF extracted from the ocean's uppermost layer in the longitudinal (top), colatitudinal (middle) and radial (bottom) directions, at 5 and 35 g kg^{-1} mean salinity (left and right respectively).

5.8 Extrapolation of OIMF to satellite altitude

While a lander component of a future Enceladus mission could probe the magnetic environment at the ice surface, detection of any time-mean OIMF would very likely need information about its spatial structure, possibly attainable via an orbiting probe (e.g., MacKenzie et al. 2021). The following section investigates how the OIMF modelled here would manifest above the ice surface at orbit.

5.8.1 Approach

Assuming the absence of local electrical currents above Enceladus' ice surface (i.e, $\nabla \times \vec{B} = 0$), the magnetic field can be expressed as the gradient of a scalar potential $B = -\nabla\Psi$. The scalar potential can then, in turn, be expanded into spherical harmonics (Connerney 1993):

$$\psi = r_s \sum_{n=1}^{\infty} ((\frac{r}{r_s})^n C_n^e + (\frac{r_s}{r})^{n+1} C_n^i) \tag{5.19}$$

where r is the radial distance from the centre of the body, r_s the equatorial radius of the body (taken here as Enceladus' mean radius of 252 km) and C^e and C^i series representing contributions from external and internal sources. In this chapter, contributions from external sources are not considered. C_n^i is defined as (Connerney 1993):

$$\sum_{m=0}^{n} (P_n^m(\cos(\Theta)(g_n^m \cos(m\lambda) + h_n^m \sin(m\lambda))) \tag{5.20}$$

where $P_n^m(\cos(\Theta))$ are Schmidt quasi-normalised associated Legendre functions of degree n and order m, and g_n^m and h_n^m the internal Schmidt coefficients.

From Eq. (5.19), it can be determined that the control of internal sources (e.g., an OIMF) upon the magnetic field at a given point in space diminishes with increasing radial distance from its source. The control of internal sources is also smaller for a body of smaller radius (and vice versa). Furthermore, it is expected that higher degree terms (larger n) exhibit a much stronger attenuation with increasing radial distance from the source.

It is typical to express r and r_s in units of the radius of the source (i.e., Enceladus' radius). In doing so, r_s can be set to 1 (Connerney 1993). Equations for the three components of the magnetic field at given radial distance can be obtained by taking the

gradient of Eq. (5.19) (Connerney 1993; Burton, Dougherty and Russell 2009):

$$B_\lambda = -\frac{1}{r\sin\Theta}\frac{\partial\psi}{\partial\lambda} = \sum_{n=1}^{\infty}\sum_{m=0}^{n}((\frac{1}{r})^{(n+2)}[g_n^m\cos(m\lambda) + h_n^m\sin(m\lambda)]P_n^m(\cos\Theta)) \tag{5.21}$$

$$B_\Theta = -\frac{\partial\psi}{r\partial\Theta} = -\sum_{n=1}^{\infty}\sum_{m=0}^{n}((\frac{1}{r})^{(n+2)}[g_n^m\cos(m\lambda) + h_n^m\sin(m\lambda)]\frac{dP_n^m(\cos\Theta)}{d\Theta}) \tag{5.22}$$

$$B_r = -\frac{\partial\psi}{\partial r} = \sum_{n=1}^{\infty}\sum_{m=0}^{n}((n+1)(\frac{1}{r})^{(n+2)}[g_n^m\cos(m\lambda) + h_n^m\sin(m\lambda)]P_n^m(\cos\Theta)) \tag{5.23}$$

where r is the radial distance from Enceladus' in units of Enceladus radii (R_E).

The OIMF, extracted in the oceans' uppermost layer, is expanded into spherical harmonics using PyShtools (Wieczorek and Meschede 2018), enabling the OIMF to be computed at a specified distance from Enceladus' surface. Flybys of Enceladus performed by the Cassini probe came no closer than $\sim 1\ R_E$. The Enceladus Orbilander mission is proposed to orbit at a much lower 20-70 km altitude (MacKenzie et al. 2021). In the following section, the OIMF is therefore illustrated at 20, 70 and 252 km altitude. Note that focus is paid to B_r only. B_λ, while stronger in the ocean, would be undetectable at satellite altitude because it forms part of the 'toroidal' field - in turn defining magnetic loops tangential to the sphere which cannot extend above the ocean surface (Chave 1983).

5.8.2 Results

The radial OIMF at 20, 70, and 252 km satellite altitude is shown in the top three rows of fig. 5.24 respectively.

The OIMF magnitude weakens significantly with altitude. At 1 R_E (252 km), the OIMF is two orders of magnitude weaker than at the ocean top. For comparison, the weakening of OIMF at Earth from ocean top-to-satellite (430 km) altitude is $\sim$ factor 5 (Manoj et al. 2006). The greater attenuation observed here is owing to Enceladus' small size, in accordance with Eq. (5.19). From this, it appears that any orbiting mission aiming to detect a magnetic signature of Enceladus' ocean would greatly benefit from close proximity to the ice surface.

Higher order components are attenuated preferentially with altitude (according to Eq. (5.19)) and as a result, the pattern of OIMF is smoothed with greater distance from Enceladus, tending towards a dipole. To illustrate this tendency, the OIMF at 10 R_E is also shown in fig. 5.24 (bottom row). In the case of the radial OIMF modelled here, the dipole orientation is similar in both solutions at this altitude.

By extrapolating the zonally uniform OIMF solutions to satellite altitude (illustrated in fig. 5.23), it can be seen that this solution converges with the reference case (fig. 5.24) at 10 R_E. This suggests that if an OIMF were detectable, a 2D ocean model could suffice for identifying the dipole orientation at satellite altitude, providing it reproduces the direction of the domain-integrated flows.

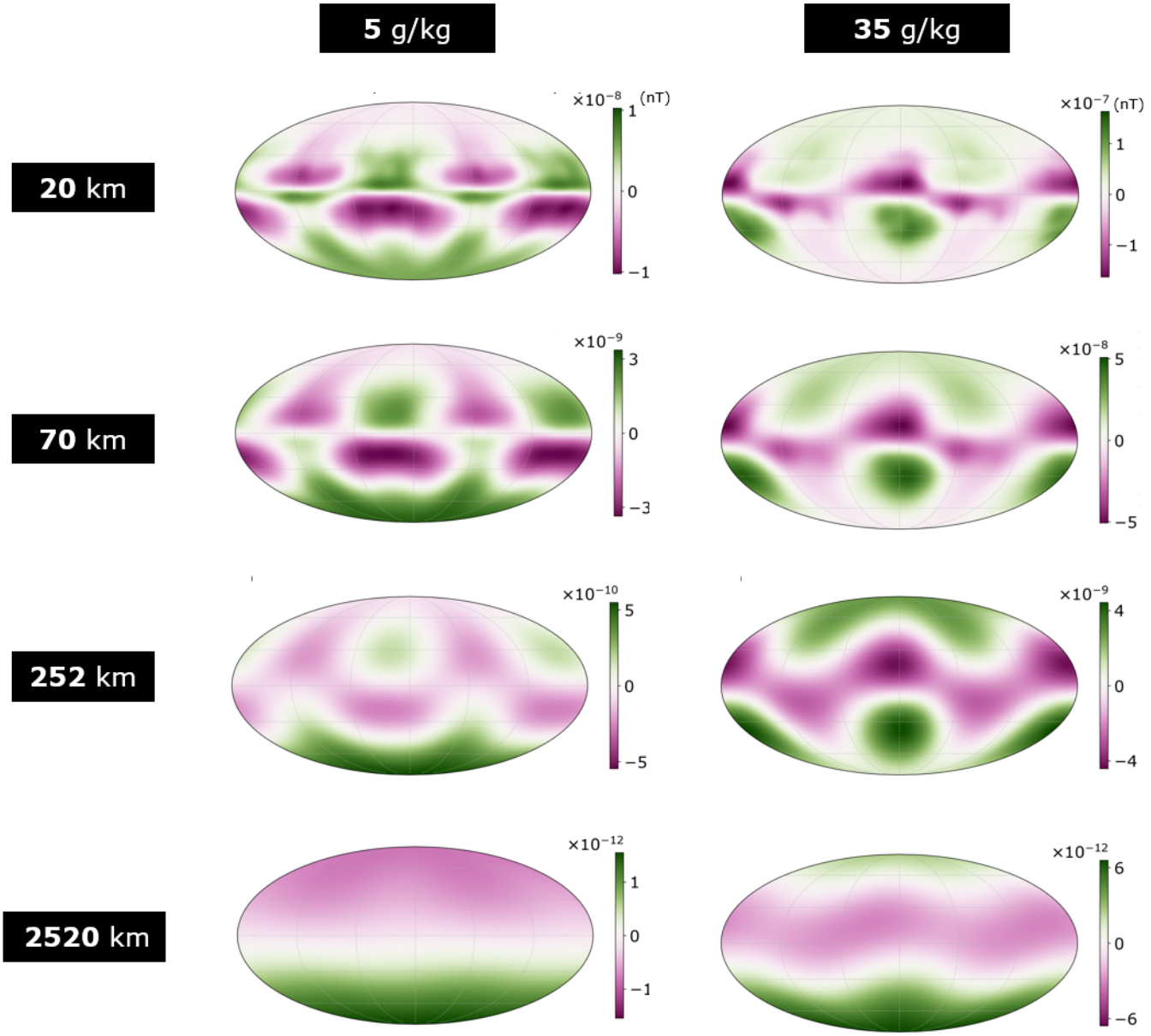

Figure 5.24: Radial component of the ocean induced magnetic field (OIMF; nT) at 20 (top), 70 (2nd from top), 252 (2nd from bottom) and 2520 (bottom) km altitude above Enceladus' ice surface, at 5 and 35 g kg^{-1} mean salinity (left and right respectively). Solutions here are obtained via spherical harmonic expansion of the OIMF extracted at the ocean's uppermost layer. Note that colourbars are saturated and vary throughout.

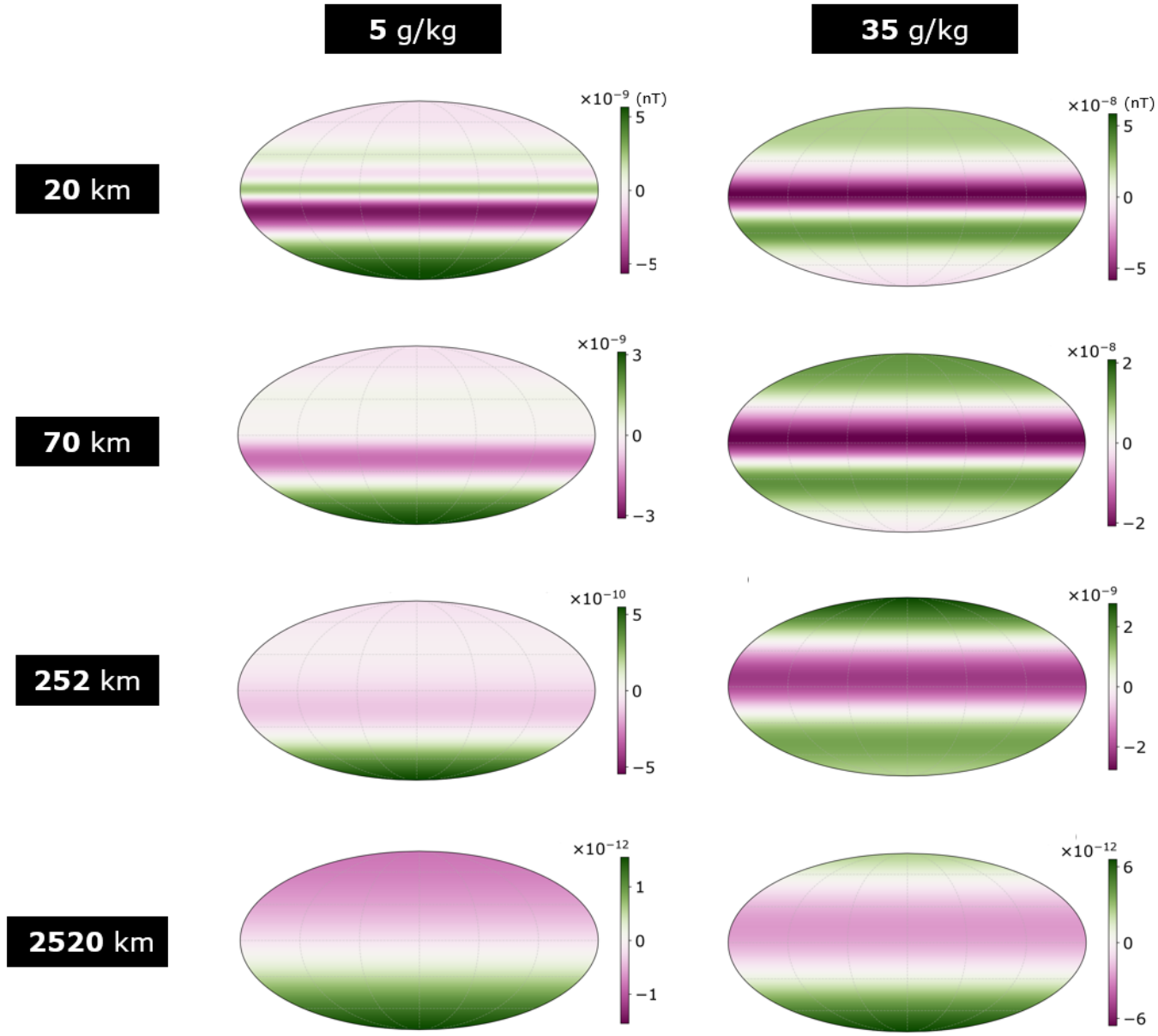

Figure 5.25: Radial component of the ocean induced magnetic field (OIMF; nT) at 20 (top), 70 (2nd from top), 252 (2nd from bottom) and 2520 (bottom) km altitude above Enceladus' ice surface, where a zonally averaged velocity field is employed. Shown at 5 and 35 g kg^{-1} mean salinity (left and right respectively). Solutions here are obtained via spherical harmonic expansion of OIMF extracted at the ocean's uppermost layer. Note that colourbars are saturated and vary throughout.

5.9 Discussion

The magnitude of OIMF simulated here is too weak to be detectable via modern fluxgate magnetometers at or above Enceladus' surface. For comparison, the resolution of the Cassini magnetometer was 0.0488 nT (Dougherty et al. 2004), while the resolution of Europa Clipper's magnetometer is expected to be 0.008 nT (Kivelson et al. 2023). Note that this resolution does not equate to what is detectable: A magnetic signature must be separable from background noise and other sources of magnetic disturbance, for example, that associated with Enceladus' erupting south polar plumes, the signature of which may dwarf that of an OIMF (Saur et al. 2024). Separating the OIMF from other disturbances within Enceladus' magnetic environment would prove a major challenge even if the OIMF is stronger than simulated here.

It is worth highlighting that the ocean model used here does not resolve all expected ocean motion, namely eddies and convection which are parameterised and their influence upon the OIMF therefore not accounted for. If eddies only contribute higher order components to the OIMF as suggested for Earth (Manoj et al. 2006), their effect upon the OIMF at satellite altitude may be limited according to Eq. (5.19). However, ocean eddies may, themselves, shape the mean ocean circulation. For example, Zhang, Kang and Marshall (2024) find baroclinic eddies sustain alternating zonal jets stiffened along the axis of rotation, with velocities an order of magnitude larger than obtained here. In this case, forcing GEMMIE with output from an eddy resolving model could yield a stronger and structurally different OIMF to that obtained here.

Existing convection-resolving GCM simulations have obtained vertical ocean flows 2-3 orders larger than simulations here (Zhang, Kang and Marshall 2024; Bire et al. 2023) and given that the OIMF scales proportionately to the magnitude of electrical current (and by extension ocean velocity) in time-mean electromagnetic simulations (e.g., see fig. 5.6), resolving convection may be expected to increase the magnitude of the radial OIMF by an equivalent order. Scaling up the colatitudinal OIMF by three orders yields ~ 0.01 nT within the ocean, albeit still likely beyond detectability. As in the case of eddies, a convection resolving model would likely produce a structurally different OIMF to that obtained here.

It is worth mentioning that because ocean flows induce magnetic fields only when flowing *across* magnetic field lines, any convection-induced OIMF would likely be stronger

nearer Enceladus' equator and weakest nearer the poles, owing to the orientation of Saturn's magnetic field, approximately aligned with Enceladus' rotation axis. This may further dampen the prospects of using OIMF to constrain convection underneath Enceladus' south polar plumes.

5.9.1 On the possibility of ocean conductivity gradients

Electromagnetic simulations in this chapter assume a uniform ocean conductivity and in this subsection, the possibility of significant conductivity gradients within Enceladus' ocean is discussed. To aid this discussion, fig. 5.26 shows the conductivity of seawater computed using the Gibbs seawater toolbox (McDougall and Barker 2011) as a function of salinity and temperature, at uniform pressure computed under 20 km mean ice thickness for Enceladus (Hemingway and Mittal 2019).

Conductivity is larger where water is saltier (owing to a greater abundance of ions). Enceladus' ocean has been constrained between 5 and 20 g kg^{-1} from Cassini observations of E-ring ice grains (Postberg et al. 2009). It is possible that these observations underestimate the bulk salinity owing to fractionation processes in the plume conduit (Fox-Powell and Cousins 2021), or relative freshening of the south polar ocean from ice melting (see chapter 4).

Conductivity is larger where water is warmer (owing to greater ion mobility). Enceladus' ocean temperature at the ice-interface is freezing point. Conductivity here is therefore not expected to exceed ~ 4 S m^{-1} unless Enceladus' ocean salinity substantially exceeds estimates obtained from plume material.

Assuming steady state, temperatures at Enceladus' ocean depths are unlikely to exceed 4 °C, owing to inverse stratification theory (Ames et al. 2025; see chapter 3). This is because at temperatures exceeding 4 °C, warmer waters at depth will convect and mix with cooler waters aloft regardless of the ocean salinity and pressure. It is worth highlighting that such large temperature gradients (and the inverse stratified regime) require an ocean salinity less than $\sim$ 22 g kg^{-1} (Ames et al. 2025). It can be seen from fig. 5.26 that conductivity gains for a given temperature increase are diminished where salinity is lower (less mobile ions). As a result, in a 5 g kg^{-1} salinity ocean, a 4 °C temperature gradient fails to produce a conductivity gradient exceeding 0.1 S m^{-1}. In an ocean of (Earth-like)

35 g kg^{-1} salinity, a conductivity gradient exceeding 0.1 S m^{-1} requires a temperature gradient exceeding 1 ° C. This is an order of magnitude larger than that induced by the pressure dependence of freezing temperature at the ocean top that, in turn, is typically found to control the temperature gradient in GCM simulations of Enceladus' ocean at high salinity (Kang 2023; Zeng and Jansen 2024; e.g., see chapter 2). Conductivity gradients arising from temperature gradients within Enceladus are therefore expected to be smaller than 0.1 S m^{-1} (Tyler et al. 2017).

Significant gradients in ocean conductivity could plausibly arise from salinity gradients. Ice melting is expected to produce a relative freshening of Enceladus' south polar waters assuming steady state (see chapter 4). A 0.1 S m^{-1} gradient in ocean conductivity requires a 2 g kg^{-1} gradient in ocean salinity. In chapter 4, gradients of this order are obtained in numerical simulations assuming an effective vertical diffusivity κ_z in Enceladus' ocean of 10^{-5} m^2 s^{-1} (chapter 4). A conductivity gradient of order 1 - as observed in Earth's oceans - would require a relative freshening of the south polar ocean exceeding 13 g kg^{-1}. The scaling from chapter 4 suggests that such freshening could occur within Enceladus (see fig. 4.3), e.g., for an Earth-like bulk salinity of 35 g kg^{-1}, where κ_z does not exceed 10^{-5} m^2 s^{-1} and ice melting viscosity is sufficiently low. If the freshwater lens extends to the ice base as found in chapter 4, it would represent a significant portion of Enceladus' ocean ($\sim$ 15 km thickness at the south pole) with weakened ocean conductivity. The impact of such a conductivity gradient upon an OIMF, as well as other means of sounding this conductivity gradient, should be explored in future work.

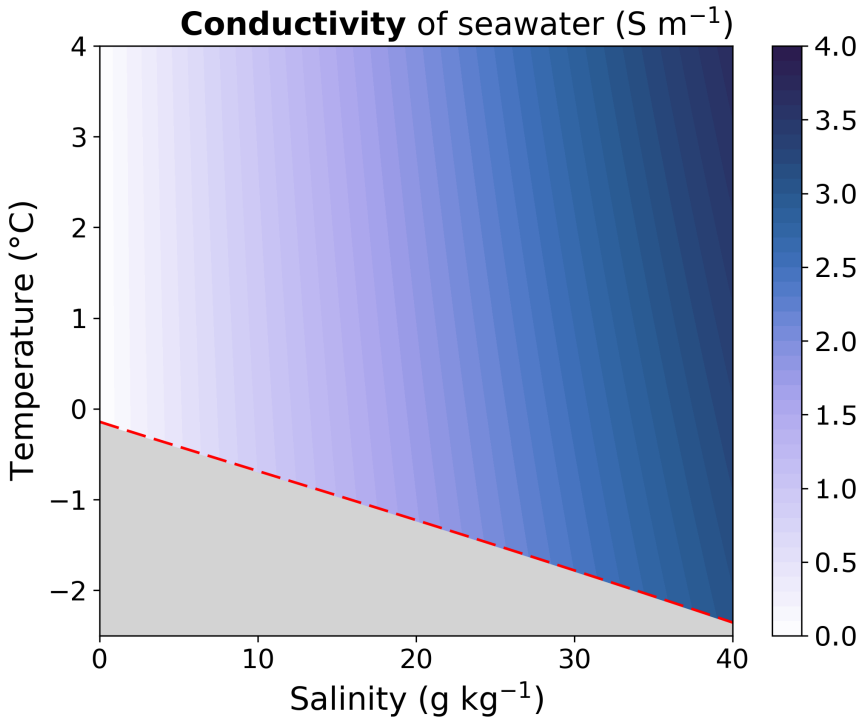

Figure 5.26: Conductivity of water (S m^{-1}) as a function of salinity (g kg^{-1}) and temperature (°C) at constant pressure computed under 20 km mean ice thickness for Enceladus. Computed using the Gibbs Seawater Toolbox (McDougall and Barker 2011), thus assuming an Earth-like ocean composition. Grey shading denotes parameter space where water is frozen, and the red dashed line the expected temperature at the ice-ocean interface (water freezing temperature). Contour spacing is 0.1 S m^{-1}.

5.10 Conclusions

In this chapter fully global, 3D simulations of Enceladus' ocean are performed at high (35 g kg^{-1}) and low (5 g kg^{-1}) salinity, and the motionally induced magnetic signature of outputted ocean flows investigated. The central findings are as follows:

- **Different salinity oceans can induce different patterns of ocean induced magnetic signature** (OIMF), owing to the reversal in lateral density gradients, which reverses the orientation of ocean flows. Reversal in ocean density gradients arise here because of a reversal in the sign of the thermal expansion coefficient at high vs low salinity.

- **Longitudinal variation in ocean flow velocity can raise the magnitude of the OIMF**, and alter its structure within the ocean. Effects are diminished at increasing distance from Enceladus, because longitudinal variation is found to introduce higher order components to the OIMF that are preferentially attenuated with increasing altitude, according to Eq. (5.19).

- T**he simulated OIMF is likely far too weak to be detectable above Enceladus' surface** using modern fluxgate magnetometers, particularly where its ocean salinity (and by extension, conductivity) is low. The presence of a two orders weaker ambient field at Enceladus (and other ice-covered moons) vs Earth, combined with a smaller size, and more sluggish ocean flows, are expected to make Enceladus a challenging location in the search for a time-mean OIMF beyond Earth.

Chapter 6

Conclusions and Future work

In this thesis, the effects of salinity upon Enceladus' ocean stratification, circulation and, by extension, potential observables have been investigated via modelling approaches adopted from terrestrial oceanography. In the following, the work of each chapter is summarised, followed by discussion of how they link together to identify paths for future work. Concluding remarks are then provided.

6.1 Chapters summary

In chapter 2, the ocean model used in this thesis is described. To the end of being usable to explore uncertain parameter space, a two-dimensional (latitude-depth) configuration is employed. This means it must parameterise processes that cannot be resolved as consequence, namely eddies and convection. Parameterisation schemes are adopted from terrestrial oceanography and the modular nature (along with computational cheapness) of the model permits the sensitivity of outputted solutions to these parameterisation schemes (as well as other model components) to be explored. Sensitivities to the choices of currently available parameterisation schemes are found to predominantly manifest in quasi-permanent unstably- or neutrally-stratified regions of ocean (not present at Earth). The choice of parameterisation scheme is not found to significantly affect the strength and extent of stable stratification nearer the ice interface.

Instead, stratification extent is found to be highly sensitive to two other model components. The first of these is lateral variation in the upper boundary temperature forcing. Its inclusion permits stable stratification nearer the polar ice-ocean interface, while its exclusion results in a globally unstratified ocean. This occurs because lateral temperature

variation gives rise to sloping isopycnals, energising baroclinic eddies (here parameterised) that act to flatten the isopycnals and restratify the ocean, as occurs in Earth's oceans. The second component is non-linearity in the equation of state. At salinity lower than $\sim$ 20 g kg^{-1}, its inclusion results in global, stable stratification at the ice interface. This is owing to a reversal in sign of the thermal expansion coefficient (α_T) near freezing point (and by extension, the ice-ocean interface) at low salinity (requiring a non-linear equation of state to be resolved), which allows cooling from the overlying ice to stratify the adjacent waters, as occurs in lakes and ponds during winter on Earth.

Following from the finding of stable stratification near the south polar ice interface (the source of Enceladus' plumes) in chapter 2, chapter 3 explores the sensitivity of Enceladus's ocean stratification to uncertain ocean salinity and κ_z - an effective vertical diffusivity parameterising mixing induced by tidal- and librational- energy dissipation. It is found that when assuming a steady state ice shell, Enceladus' south polar ocean is always stratified, regardless of assumed salinity and κ_z. This occurs owing to ocean salinity effects, via two mechanisms.

At salinity lower than $\sim$ 20 g kg^{-1}, the reversal in sign of α_T near freezing point ensures a global, stratified layer adjacent to the ice interface as mentioned above (dubbed the 'inverse layer'). The vertical extent of this layer could be anywhere from metres to the entire ocean depth, dependent upon κ_z. A stronger κ_z is able to more efficiently flux cooler waters from the ice interface into the ocean interior. This ensures a negative α_T at greater depth in the ocean, deepening the inverse layer.

At salinity larger than $\sim$ 20 g kg^{-1} where α_T cannot become negative, ice melting freshens the ocean from aloft at the poles, ensuring stable stratification here. The melting here is prescribed assuming steady state of the ice shell, given that necessary to balance the freshwater budget given the polewards induced ice flow.

From tracer age simulations, this stable stratification is found to delay the transit of hydrothermally derived tracers to the plumes by at least 1000 years, three orders of magnitude larger than timescales inferred from Cassini observations of silica nanoparticles believed sourced from Enceladus' core (Hsu et al. 2015). Given this, we conclude that in the absence of alternative transport mechanisms, a hydrothermal origin for silica nanoparticles is inconsistent with stable stratification underlying the plumes.

Following its identification in chapter 3, chapter 4 attempts to provide constraints upon

the relative freshening of Enceladus' south polar ocean, given ice melting expected here under the assumption of a steady state ice shell. A scaling for this freshening is derived and verified via numerical simulations, which account for Enceladus' expected upper boundary height variation (the effects of which are excluded in chapter 3). Two freshening regimes are identified.

At salinity lower than $\sim$ 20 g kg^{-1}, the meridional temperature gradient at the ice interface (warmer aloft at the poles, cooler deeper at the equator) acts to destabilises the ocean here. If this temperature gradient is the dominant control upon ocean density, cross-equatorial, along-isopycnal mixing by parameterised eddies ensures that salinity anomalies are efficiently redistributed between equator and pole, resulting in little freshening of the south polar ocean.

An alternate regime arises where salinity gradients, arising from ice melting and freezing, become the dominant control upon ocean density. In this case, a freshwater lens forms and fills the south polar ocean down to the depth of deepest melting. Along-isopycnal eddy mixing then becomes an inefficient means to mix fresher polar waters with saltier equatorial waters. When this happens, the predominant salt balance in the lens is between the rate of melting (controlled by uncertain ice melting viscosity) and uncertain κ_z. A significant relative freshening of Enceladus' ocean is predicted if κ_z is nearer its molecular value, i.e., where tides and libration do not significantly contribute to vertical mixing within the ocean interior. If the case, concentrations of salt within E-ring ice grains (sourced from the south polar ocean and the only existing observational constraint upon Enceladus' ocean salinity) may represent an underestimate of the Enceladus' bulk ocean salinity.

Finally, in chapter 5 it is shown that Enceladus' salt-bearing ocean circulation - flowing within Saturn's magnetosphere - should produce motionally induced magnetic fields as occurs at Earth. The ocean induced magnetic field (OIMF) is shown to differ at differing mean ocean salinity, where meridional and zonal flows can reverse orientation if the latitudinal density gradient at the ocean top also reverses (occurring in simulations here owing to the reversal in sign of the thermal expansion coefficient at the ice interface for salinities below 20 g kg^{-1}). However, the OIMF is found too weak to detect, at least four orders of magnitude weaker than at Earth, owing to more sluggish ocean transport and a weaker ambient field with which the ocean flows interact. We conclude that a time-mean OIMF is unlikely to provide an alternative constraint upon Enceladus' ocean salinity at present.

6.2 Limitations and paths for future work

The 2D and 3D GCM configurations employed in this thesis rely upon the parameterisation of eddies and convection using schemes designed for terrestrial oceanography. While expected to be valid for stratified regions of ocean, it is not fully clear if they are valid within quasi-permanently convecting regions as may be present within Enceladus and other ice-covered moons (but not presently at Earth). Convection may more predominantly be directed along the axis of rotation within Enceladus (e.g., as shown in figure 2.25). Because patterns of heating, cooling, and ice freezing are very likely to be heterogeneous within Enceladus, this convection likely interacts with ocean eddies (as they do during transient deep convection events at Earth). This interaction would govern stratification and thus transport within convecting regions of ocean.

Future work should therefore attempt to clarify how eddies and convection interact within the ocean of Enceladus and other ice-covered moons, in the presence of ice shell freshwater fluxes as well as non-linearities in the equation of state. This will require eddy and convection resolving simulations, possibly supplemented by lab experiments. Using these, the applicability of existing eddy and convection parameterisation schemes could be verified and, if necessary, modified or an alternative parameterisation scheme developed. This would significantly reduce the computational burden of robust GCM simulations of convecting regions within ice-covered oceans.

The freshwater forcings employed in this work are computed under the assumption of steady state and assumed time constant. Yet, the melting and freezing of Enceladus' ice shell could be undergoing temporal variability, still permitted under the assumption of quasi-equilibrium. Future work should investigate the effects of temporal variability in melting and freezing upon stratification and freshening near the ice interface. For example, whether a transient freezing episode could be sufficient to break ocean stratification nearer the poles (provided a physical basis for this occurring can be established).

Vertical particulate transport within Enceladus' ocean was shown here to be delayed by stratification, but alternative transport mechanisms were not considered. For example, flows imparted by the opening of the geyser conduit (and resultant pressure gradient) may mix the adjacent ocean with implications for stratification here. Moreover, frazil ice - where water can become supercooled if raised to a height where it is cooler than freezing temperature (owing to the pressure dependence of freezing temperature) - may

form within Enceladus' ocean as on Earth. In addition to having implications for the ocean heat budget (via latent heat release upon freezing), frazil ice formation could offer a means to improve vertical transport to the ice shell in stratified oceans: If particulate and chemical species become trapped within ice crystals, they could plausibly rise buoyantly to the ice-interface, provided the frazil ice does not re-melt before getting there. Future work should explore these possibilities, to identify plausible, alternative paths for particulate transport within Enceladus' ocean.

The work here found κ_z to control stratification extent within Enceladus, assuming κ_z to be uniform in the ocean. In Earth's oceans, κ_z is largest near topography at the ocean bottom. At Enceladus, κ_z may be larger near the ocean top, in the presence of librating (i.e., periodically moving) ice topography. While future work should investigate the effects of a spatially varying κ_z within Enceladus, such work would be most informative if coupled to a models of tides and libration. This is because tidal and librational energy dissipation is, itself, dependent upon ocean stratification, because a stratified ocean can support internal gravity waves. Work coupling models of ocean stratification, tides and libration, would permit investigation into the dependence of tidal and librational energy dissipation upon ocean salinity, as well as patterns of melting and freezing at the ocean top.

The above work could then feed into a study of the motional induction of tidally- and librationally- driven flows at Enceladus. Given tidal and librationally-driven flows are likely to be periodic, this would facilitate their detection. Rovira-Navarro, Matsuyama and Hay (2023) found that if Enceladus' tides are in a resonant state, they could produce flow velocities as large as 1 m s^{-1}. Such flows may be strong enough to produce a detectable magnetic signature. If tidally- and librationally- driven flows produce distinguishable OIMF under different stratification regimes, the OIMF could optimistically be used as a constraint upon ocean salinity, and possibly offer a means to probe the presence of a freshwater layer at Enceladus' south pole.

6.3 Closing remarks

Constraining Enceladus' ocean transport is a challenging problem owing to a lack of observations. While numerical simulations can yield insights, one must approach these with caution. Unlike at Earth, numerical solutions for Enceladus' ocean transport cannot be verified via observation, only benchmarked by theory. Further and as demonstrated here, ocean transport is sensitive to a myriad of parameters that, at Enceladus, are poorly constrained.

In this thesis, we emphasise that at present, the greatest utility of numerical modelling is not in obtaining a precise constraint upon Enceladus' ocean transport, but rather in exploring sensitivity to uncertain parameter space. In adopting this approach, the work here has identified possible regimes of ocean stratification, freshening, and transport within Enceladus, and obtained order-of-magnitude bounds upon these. It is hoped that this will provide observational scientists with a better gauge of uncertainty in these ocean properties at Enceladus, informative for efforts to infer ocean environments from plume material that are, in turn, expected to be sensitive to them.

Bibliography

Adcroft, Alistair et al. (1997). Representation of topography by shaved cells in a height coordinate ocean model. *Monthly Weather Review*. **125** (9), pp. 2293–2315.

Adcroft, Alistair et al. (2001). Impact of geothermal heating on the global ocean circulation. *Geophysical Research Letters*. **28** (9), pp. 1735–1738.

Adcroft, Alistair et al. (2004). Implementation of an atmosphere–ocean general circulation model on the expanded spherical cube. *Monthly Weather Review*. **132** (12), pp. 2845–2863.

Alken, Patrick et al. (2021). International geomagnetic reference field: The thirteenth generation. *Earth, Planets and Space*. **73** (1), p. 49.

Ames, Flynn et al. (2025). Ocean stratification impedes particulate transport to the plumes of Enceladus. *Communications Earth & Environment*. **6** (1), pp. 1–11.

Ashkenazy, Yosef (2019). The surface temperature of Europa. *Heliyon*. **5** (6), e01908.

Ashkenazy, Yosef and Tziperman, Eli (2021). Dynamic Europa ocean shows transient Taylor columns and convection driven by ice melting and salinity. *Nature communications*. **12** (1), pp. 1–12.

Ashkenazy, Yosef et al. (2014). Ocean circulation under globally glaciated Snowball Earth conditions: Steady-state solutions. *Journal of physical oceanography*. **44** (1), pp. 24–43.

Ashkenazy, Yosef et al. (2018). Dynamics of the global meridional ice flow of Europa's icy shell. *Nature Astronomy*. **2** (1), pp. 43–49.

Béghin, Christian et al. (2012). Analytic theory of Titan's Schumann resonance: Constraints on ionospheric conductivity and buried water ocean. *Icarus*. **218** (2), pp. 1028–1042.

Beuthe, Mikael (2016). Crustal control of dissipative ocean tides in Enceladus and other icy moons. *Icarus*. **280**, pp. 278–299.

Biersteker, John B et al. (2023). Revealing the interior structure of icy moons with a Bayesian approach to magnetic induction measurements. *The Planetary Science Journal*. **4** (4), p. 62.

Bire, Suyash et al. (2022). Exploring ocean circulation on icy moons heated from below. *Journal of Geophysical Research: Planets*. **127** (3), e2021JE007025.

Bire, Suyash et al. (2023). Divergent behavior of hydrothermal plumes in fresh versus salty icy ocean worlds. *Journal of Geophysical Research: Planets*. **128** (11), e2023JE007740.

Bouffard, Mathieu et al. (2025). Seafloor hydrothermal control over ocean dynamics in Enceladus. *Nature Astronomy*. Pp. 1–8.

Burton, ME et al. (2009). Model of Saturn's internal planetary magnetic field based on Cassini observations. *Planetary and Space Science*. **57** (14-15), pp. 1706–1713.

Čadek, Ondřej et al. (2017). Viscoelastic relaxation of Enceladus's ice shell. *Icarus*. **291**, pp. 31–35.

Čadek, Ondřej et al. (2019). Long-term stability of Enceladus' uneven ice shell. *Icarus*. **319**, pp. 476–484.

Caldwell, Douglas R (1978). The maximum density points of pure and saline water. *Deep Sea Research*. **25** (2), pp. 175–181.

Carnahan, Evan et al. (2022). Surface-to-ocean exchange by the sinking of impact generated melt chambers on Europa. *Geophysical Research Letters*. e2022GL100287.

Chave, Alan D (1983). On the theory of electromagnetic induction in the earth by ocean currents. *Journal of Geophysical Research: Solid Earth*. **88** (B4), pp. 3531–3542.

Chave, Alan D and Luther, Douglas S (1990). Low-frequency, motionally induced electromagnetic fields in the ocean: 1. Theory. *Journal of Geophysical Research: Oceans*. **95** (C5), pp. 7185–7200.

Chelton, Dudley B et al. (1998). Geographical variability of the first baroclinic Rossby radius of deformation. *Journal of Physical Oceanography*. **28** (3), pp. 433–460.

Choblet, Gaël et al. (2017). Powering prolonged hydrothermal activity inside Enceladus. *Nature Astronomy*. **1** (12), pp. 841–847.

Choblet, Gaël et al. (2021). Enceladus as a potential oasis for life: Science goals and investigations for future explorations. *Experimental Astronomy*. Pp. 1–39.

Cochrane, Corey J et al. (2021). In search of subsurface oceans within the Uranian moons. *Journal of Geophysical Research: Planets*. **126** (12), e2021JE006956.

Cochrane, Corey J et al. (2025). Stronger evidence of a subsurface ocean within Callisto from a multifrequency investigation of Its induced magnetic field. *AGU Advances*. **6** (1), e2024AV001237.

Connerney, JEP (1993). Magnetic fields of the outer planets. *Journal of Geophysical Research: Planets*. **98** (E10), pp. 18659–18679.

Crameri, Fabio et al. (2020). The misuse of colour in science communication. *Nature communications*. **11** (1), p. 5444.

Crane, Kathleen et al. (1991). Hydrothermal vents in Lake Baikal. *Nature*. **350** (6316), pp. 281–281.

Dachwald, Bernd et al. (2014). IceMole: a maneuverable probe for clean in situ analysis and sampling of subsurface ice and subglacial aquatic ecosystems. *Annals of Glaciology*. **55** (65), pp. 14–22.

Danabasoglu, Gokhan et al. (1996). Approach to equilibrium in accelerated global oceanic models. *Journal of Climate*. Pp. 1092–1110.

Dostal, Jan et al. (2012). The modelling of the toroidal magnetic field induced by tidal ocean circulation. *Geophysical Journal International*. **189** (2), pp. 782–798.

Dougherty, MK et al. (2004). The Cassini magnetic field investigation. *Space Science Reviews*. **114** (1), pp. 331–383.

Dougherty, MK et al. (2006). Identification of a dynamic atmosphere at Enceladus with the Cassini magnetometer. *Science*. **311** (5766), pp. 1406–1409.

Durack, Paul J (2015). Ocean salinity and the global water cycle. *Oceanography*. **28** (1), pp. 20–31.

England, Matthew H (1995). The age of water and ventilation timescales in a global ocean model. *Journal of Physical Oceanography*. **25** (11), pp. 2756–2777.

Faraday, Michael (1832). VI. The Bakerian lecture.-Experimental researches in electricity.-Second series. *Philosophical transactions of the royal society of London*. (122), pp. 163–194.

FEM, Lilley et al. (1993). Magnetic signals from an ocean eddy. *Journal of geomagnetism and geoelectricity*. **45** (5), pp. 403–422.

Ferrari, Raffaele and Wunsch, Carl (2009). Ocean circulation kinetic energy: Reservoirs, sources, and sinks. *Annual Review of Fluid Mechanics*. **41** (1), pp. 253–282.

Ferreira, David et al. (2011). Climate determinism revisited: Multiple equilibria in a complex climate model. *Journal of Climate*. **24** (4), pp. 992–1012.

Fifer, Lucas M et al. (2022). Chemical fractionation modeling of plumes indicates a gas-rich, moderately alkaline Enceladus ocean. *The Planetary Science Journal*. **3** (8), p. 191.

Flosadottir, AH et al. (1997). Motional induction in North Atlantic circulation models. *Journal of Geophysical Research: Oceans*. **102** (C5), pp. 10353–10372.

Forel, François Alphonse (1892). *Le Léman: monographie limnologique*. Vol. 1. F. Rouge.

Fox-Kemper, Baylor et al. (2019). Challenges and prospects in ocean circulation models. *Frontiers in Marine Science*. **6**, p. 65.

Fox-Powell, Mark G and Cousins, Claire R (2021). Partitioning of crystalline and amorphous phases during freezing of simulated Enceladus ocean fluids. *Journal of Geophysical Research: Planets*. **126** (1), e2020JE006628.

Friis-Christensen, Eigil et al. (2006). Swarm: A constellation to study the Earth's magnetic field. *Earth, planets and space*. **58** (4), pp. 351–358.

Gent, Peter R and Mcwilliams, James C (1990). Isopycnal mixing in ocean circulation models. *Journal of Physical Oceanography*. **20** (1), pp. 150–155.

Gill, AE et al. (1974). Energy partition in the large-scale ocean circulation and the production of mid-ocean eddies. *Deep sea research and oceanographic abstracts*. Vol. 21. 7. Elsevier, pp. 499–528.

Gissinger, Christophe and Petitdemange, Ludovic (2019). A magnetically driven equatorial jet in Europa's ocean. *Nature Astronomy*. **3** (5), pp. 401–407.

Glein, Christopher R and Truong, Ngoc (2025). Phosphates reveal high pH ocean water on Enceladus. *Icarus*. P. 116717.

Goodman, Jason C (2012). Tilted geostrophic convection in icy world oceans caused by the horizontal component of the planetary rotation vector. *AGU Fall Meeting Abstracts*. Vol. 2012, P51A–2017.

Goodman, Jason C and Lenferink, Erik (2012). Numerical simulations of marine hydrothermal plumes for Europa and other icy worlds. *Icarus*. **221** (2), pp. 970–983.

Grasset, Olivier et al. (2013). JUpiter ICy moons Explorer (JUICE): An ESA mission to orbit Ganymede and to characterise the Jupiter system. *Planetary and Space Science*. **78**, pp. 1–21.

Grayver, Alexander V et al. (2016). Satellite tidal magnetic signals constrain oceanic lithosphere-asthenosphere boundary. *Science advances*. **2** (9), e1600798.

Griffies, SM et al. (2005). Formulation of an ocean model for global climate simulations. *Ocean Science*. **1** (1), pp. 45–79.

Griffies, Stephen M (1998). The Gent–Mcwilliams skew flux. *Journal of Physical Oceanography*. **28** (5), pp. 831–841.

Griffies, Stephen M et al. (1998). Isoneutral diffusion in a z-coordinate ocean model. *Journal of Physical Oceanography*. **28** (5), pp. 805–830.

Griggs, Jennifer A and Bamber, JL (2011). Antarctic ice-shelf thickness from satellite radar altimetry. *Journal of Glaciology*. **57** (203), pp. 485–498.

Hand, Kevin P and Chyba, Christopher F (2007). Empirical constraints on the salinity of the Europan ocean and implications for a thin ice shell. *Icarus*. **189** (2), pp. 424–438.

Hand, Kevin P et al. (2020). On the habitability and future exploration of ocean worlds. *Space science reviews*. **216** (5), pp. 1–24.

Hartmann, Robert et al. (2024). Toward understanding polar heat transport enhancement in subglacial oceans on icy moons. *Geophysical Research Letters*. **51** (3), e2023GL105401.

Hay, Hamish CFC and Matsuyama, Isamu (2019). Nonlinear tidal dissipation in the subsurface oceans of Enceladus and other icy satellites. *Icarus*. **319**, pp. 68–85.

Hay, Hamish CFC et al. (2024). Tidal forcing in icy-satellite oceans drives mean circulation and ice-shell torques. *Journal of Geophysical Research: Planets*. **129** (6), e2024JE008408.

Hedman, MM et al. (2013). An observed correlation between plume activity and tidal stresses on Enceladus. *Nature*. **500** (7461), pp. 182–184.

Hemingway, Douglas J and Mittal, Tushar (2019). Enceladus's ice shell structure as a window on internal heat production. *Icarus*. **332**, pp. 111–131.

Hendrix, Amanda R et al. (2019). The NASA roadmap to ocean worlds. *Astrobiology*. **19** (1), pp. 1–27.

Hesse, Marc A et al. (2022). Downward Oxidant Transport Through Europa's Ice Shell by Density-Driven Brine Percolation. *Geophysical Research Letters*. **49** (5), e2021GL095416.

Hofmann, M and Morales Maqueda, MA (2009). Geothermal heat flux and its influence on the oceanic abyssal circulation and radiocarbon distribution. *Geophysical Research Letters*. **36** (3).

Holland, David M and Jenkins, Adrian (1999). Modeling thermodynamic ice–ocean interactions at the base of an ice shelf. *Journal of physical oceanography*. **29** (8), pp. 1787–1800.

Holland, Paul R and Feltham, Daniel L (2005). Frazil dynamics and precipitation in a water column with depth-dependent supercooling. *Journal of Fluid Mechanics*. **530**, pp. 101–124.

Howell, Samuel et al. (2023). Enceladus: An Enthalpic Jet Propulsion Laboratory. *AGU Fall Meeting Abstracts*. Vol. 2023, P43E–3321.

Howell, Samuel M (2021). The likely thickness of Europa's icy shell. *The Planetary Science Journal*. **2** (4), p. 129.

Howell, Samuel M and Pappalardo, Robert T (2020). NASA's Europa Clipper—a mission to a potentially habitable ocean world. *Nature Communications*. **11** (1), pp. 1–4.

Howett, Carly JA et al. (2025). Constraining the Mass and Energy of Enceladus' Dissipation Systems. *Space Science Reviews*. **221** (5), pp. 1–36.

Hsu, Hsiang-Wen et al. (2015). Ongoing hydrothermal activities within Enceladus. *Nature*. **519** (7542), pp. 207–210.

Hussmann, Hauke et al. (2006). Subsurface oceans and deep interiors of medium-sized outer planet satellites and large trans-neptunian objects. *Icarus*. **185** (1), pp. 258–273.

Iess, Luciano et al. (2012). The tides of Titan. *Science*. **337** (6093), pp. 457–459.

Iess, Luciano et al. (2014). The gravity field and interior structure of Enceladus. *Science*. **344** (6179), pp. 78–80.

Ingersoll, Andrew P and Nakajima, Miki (2016). Controlled boiling on Enceladus. 2. Model of the liquid-filled cracks. *Icarus*. **272**, pp. 319–326.

Irrgang, Christopher et al. (2018). Depth of origin of ocean-circulation-induced magnetic signals. *Annales Geophysicae*. Vol. 36. 1. Copernicus GmbH, pp. 167–180.

Iversen, Morten H and Lampitt, Richard S (2020). Size does not matter after all: no evidence for a size-sinking relationship for marine snow. *Progress in Oceanography*. **189**, p. 102445.

Jackett, David R and Mcdougall, Trevor J (1995). Minimal adjustment of hydrographic profiles to achieve static stability. *Journal of Atmospheric and Oceanic Technology*. **12** (2), pp. 381–389.

Jansen, Malte F (2016). The turbulent circulation of a Snowball Earth ocean. *Journal of Physical Oceanography*. **46** (6), pp. 1917–1933.

Jansen, Malte F et al. (2023). Energetic Constraints on Ocean Circulations of Icy Ocean Worlds. *The Planetary Science Journal*. **4** (6), p. 117.

Jones, Helen and Marshall, John (1993). Convection with rotation in a neutral ocean: A study of open-ocean deep convection. *Journal of Physical Oceanography*. **23** (6), pp. 1009–1039.

Kang, Wanying (2022). Different Ice-shell Geometries on Europa and Enceladus due to Their Different Sizes: Impacts of Ocean Heat Transport. *The Astrophysical Journal*. **934** (2), p. 116.

Kang, Wanying (2023). The modulation effect of ice thickness variations on convection in icy ocean worlds. *Monthly Notices of the Royal Astronomical Society*. **525** (4), pp. 5251–5261.

Kang, Wanying and Flierl, Glenn (2020). Spontaneous formation of geysers at only one pole on Enceladus's ice shell. *Proceedings of the National Academy of Sciences*. **117** (26), pp. 14764–14768.

Kang, Wanying and Jansen, Malte (2022). On Icy Ocean Worlds, Size Controls Ice Shell Geometry. *The Astrophysical Journal*. **935** (2), p. 103.

Kang, Wanying et al. (2022a). How does salinity shape ocean circulation and ice geometry on Enceladus and other icy satellites? *Science Advances*. **8** (29), eabm4665.

Kang, Wanying et al. (2022b). Ocean dynamics and tracer transport over the south pole geysers of Enceladus. *Monthly Notices of the Royal Astronomical Society*. **517** (3), pp. 3485–3494.

Kang, Wanying et al. (2022). The role of ocean circulation in driving hemispheric symmetry breaking of the ice shell of Enceladus. *Earth and Planetary Science Letters*. **599**, p. 117845.

Kelbert, Anna et al. (2014). Global 3-D electromagnetic forward modelling: a benchmark study. *Geophysical Journal International*. **197** (2), pp. 785–814.

Kelley, Deborah S et al. (2005). A serpentinite-hosted ecosystem: the Lost City hydrothermal field. *Science*. **307** (5714), pp. 1428–1434.

Khurana, KK et al. (1998). Induced magnetic fields as evidence for subsurface oceans in Europa and Callisto. *Nature*. **395** (6704), pp. 777–780.

Kite, Edwin S and Rubin, Allan M (2016). Sustained eruptions on Enceladus explained by turbulent dissipation in tiger stripes. *Proceedings of the National Academy of Sciences*. **113** (15), pp. 3972–3975.

Kivelson, Margaret G et al. (2000). Galileo magnetometer measurements: A stronger case for a subsurface ocean at Europa. *Science*. **289** (5483), pp. 1340–1343.

Kivelson, Margaret G et al. (2023). The Europa clipper magnetometer. *Space Science Reviews*. **219** (6), p. 48.

Klinger, Barry A et al. (1996). Representation of convective plumes by vertical adjustment. *Journal of Geophysical Research: Oceans*. **101** (C8), pp. 18175–18182.

Konstantinidis, Konstantinos et al. (2015). A lander mission to probe subglacial water on Saturn' s moon Enceladus for life. *Acta astronautica*. **106**, pp. 63–89.

Kotelnikova, Svetlana (2002). Microbial production and oxidation of methane in deep subsurface. *Earth-Science Reviews*. **58** (3-4), pp. 367–395.

Kuvshinov, Alexey and Semenov, Alexey (2012). Global 3-D imaging of mantle electrical conductivity based on inversion of observatory C-responses—I. An approach and its verification. *Geophysical Journal International*. **189** (3), pp. 1335–1352.

Kuvshinov, AV (2008). 3-D global induction in the oceans and solid Earth: recent progress in modeling magnetic and electric fields from sources of magnetospheric, ionospheric and oceanic origin. *Surveys in Geophysics*. **29** (2), pp. 139–186.

Lainey, V et al. (2024). A recently formed ocean inside Saturn's moon Mimas. *Nature*. **626** (7998), pp. 280–282.

Large, WoG and Yeager, SG (2009). The global climatology of an interannually varying air–sea flux data set. *Climate dynamics*. **33** (2), pp. 341–364.

Larsen, JC (1968). Electric and magnetic fields induced by deep sea tides. *Geophysical Journal International*. **16** (1), pp. 47–70.

Larsen, JC (1992). Transport and heat flux of the Florida Current at 27 N derived from cross-stream voltages and profiling data: Theory and observations. *Philosophical Transactions of the Royal Society of London. Series A: Physical and Engineering Sciences*. **338** (1650), pp. 169–236.

Larsen, Jimmy C and Sanford, Thomas B (1985). Florida Current volume transports from voltage measurements. *Science*. **227** (4684), pp. 302–304.

Lemasquerier, Daphné G et al. (2023). Europa's Ocean Translates Interior Tidal Heating Patterns to the Ice-Ocean Boundary. *AGU Advances*. **4** (6), e2023AV000994.

Lewis, EL and Perkin, RG (1986). Ice pumps and their rates. *Journal of Geophysical Research: Oceans*. **91** (C10), pp. 11756–11762.

Li, Guancheng et al. (2020). Increasing ocean stratification over the past half-century. *Nature Climate Change*. **10** (12), pp. 1116–1123.

Lilley, FEM et al. (2001). Earth's magnetic field: ocean current contributions to vertical profiles in deep oceans. *Geophysical Journal International*. **147** (1), pp. 163–175.

Lobo, Ana H et al. (2021). A pole-to-equator ocean overturning circulation on Enceladus. *Nature Geoscience*. **14** (4), pp. 185–189.

Losch, Martin (2008). Modeling ice shelf cavities in az coordinate ocean general circulation model. *Journal of Geophysical Research: Oceans*. **113** (C8).

Luther, Douglas S et al. (1991). Low-frequency, motionally induced electromagnetic fields in the ocean: 2. Electric field and Eulerian current comparison. *Journal of Geophysical Research: Oceans*. **96** (C7), pp. 12797–12814.

MacKenzie, Shannon M et al. (2021). The Enceladus Orbilander mission concept: Balancing return and resources in the search for life. *The Planetary Science Journal*. **2** (2), p. 77.

Manoj, Chandrasekharan et al. (2006). Ocean circulation generated magnetic signals. *Earth, Planets and Space*. **58** (4), pp. 429–437.

Marshall, John and Schott, Friedrich (1999). Open-ocean convection: Observations, theory, and models. *Reviews of geophysics*. **37** (1), pp. 1–64.

Marshall, John et al. (1997a). A finite-volume, incompressible Navier Stokes model for studies of the ocean on parallel computers. *Journal of Geophysical Research: Oceans*. **102** (C3), pp. 5753–5766.

Marshall, John et al. (1997b). Hydrostatic, quasi-hydrostatic, and nonhydrostatic ocean modeling. *Journal of Geophysical Research: Oceans*. **102** (C3), pp. 5733–5752.

Martins, Z et al. (2024). Report of the Expert Committee for the Large-class mission in ESA's Voyage 2050 plan covering the science theme "Moons of the Giant Planets". *Moons Giant Planets*. Pp. 1–45.

Maus, S and Kuvshinov, A (2004). Ocean tidal signals in observatory and satellite magnetic measurements. *Geophysical Research Letters*. **31** (15).

McDougall, Trevor J and Barker, Paul M (2011). Getting started with TEOS-10 and the Gibbs Seawater (GSW) oceanographic toolbox. *Scor/iapso WG*. **127** (532), pp. 1–28.

Measures, Chris et al. (2015). Dissolved Al in the zonal N Atlantic section of the US GEOTRACES 2010/2011 cruises and the importance of hydrothermal inputs. *Deep Sea Research Part II: Topical Studies in Oceanography*. **116**, pp. 176–186.

Melosh, HJ et al. (2004). The temperature of Europa's subsurface water ocean. *Icarus*. **168** (2), pp. 498–502.

Miles, Georgina et al. (2025). Endogenic heat at Enceladus' north pole. *Science Advances*. **11** (45), eadx4338.

Millero, FJ (1978). Freezing point of sea water. *Eighth report of the Joint Panel of Oceanographic Tables and Standards, appendix*. **6**, pp. 29–31.

Munk, Walter H (1950). On the wind-driven ocean circulation. *Journal of Atmospheric Sciences*. **7** (2), pp. 80–93.

Nishioka, Jun et al. (2013). Evidence of an extensive spread of hydrothermal dissolved iron in the Indian Ocean. *Earth and Planetary Science Letters*. **361**, pp. 26–33.

Olbers, Dirk et al. (2004). The dynamical balance, transport and circulation of the Antarctic Circumpolar Current. *Antarctic science*. **16** (4), pp. 439–470.

Osborn, TR (1980). Estimates of the local rate of vertical diffusion from dissipation measurements. *Journal of physical oceanography*. **10** (1), pp. 83–89.

Pappalardo, Robert T et al. (1999). Does Europa have a subsurface ocean? Evaluation of the geological evidence. *Journal of Geophysical Research: Planets*. **104** (E10), pp. 24015–24055.

Paranicas, C et al. (2009). Europa's radiation environment and its effects on the surface. *Europa*. Pp. 529–544.

Park, RS et al. (2024). The global shape, gravity field, and libration of Enceladus. *Journal of Geophysical Research: Planets*. **129** (1), e2023JE008054.

Petereit, Johannes et al. (2019). Analysis of Ocean Tide-Induced Magnetic Fields Derived From Oceanic In Situ Observations: Climate Trends and the Remarkable Sensitivity of Shelf Regions. *Journal of Geophysical Research: Oceans*. **124** (11), pp. 8257–8270.

Pollack, Henry N et al. (1993). Heat flow from the Earth's interior: analysis of the global data set. *Reviews of Geophysics*. **31** (3), pp. 267–280.

Porco, Carolyn et al. (2006). Cassini observes the active south pole of Enceladus. *science*. **311** (5766), pp. 1393–1401.

Porco, Carolyn et al. (2014). How the geysers, tidal stresses, and thermal emission across the south polar terrain of Enceladus are related. *The Astronomical Journal*. **148** (3), p. 45.

Postberg, F et al. (2011). A salt-water reservoir as the source of a compositionally stratified plume on Enceladus. *Nature*. **474** (7353), pp. 620–622.

Postberg, Frank et al. (2009). Sodium salts in E-ring ice grains from an ocean below the surface of Enceladus. *Nature*. **459** (7250), pp. 1098–1101.

Postberg, Frank et al. (2018). Macromolecular organic compounds from the depths of Enceladus. *Nature*. **558** (7711), pp. 564–568.

Postberg, Frank et al. (2023). Detection of phosphates originating from Enceladus's ocean. *Nature*. **618** (7965), pp. 489–493.

Redi, Martha H (1982). Oceanic isopycnal mixing by coordinate rotation. *Journal of Physical Oceanography*. **12** (10), pp. 1154–1158.

Rekier, Jeremy et al. (2019). Internal energy dissipation in Enceladus's subsurface ocean from tides and libration and the role of inertial waves. *Journal of Geophysical Research: Planets*. **124** (8), pp. 2198–2212.

Resing, Joseph A et al. (2015). Basin-scale transport of hydrothermal dissolved metals across the South Pacific Ocean. *Nature*. **523** (7559), pp. 200–203.

Roberts, James H (2015). The fluffy core of Enceladus. *Icarus*. **258**, pp. 54–66.

Roberts, James H and Nimmo, Francis (2008). Tidal heating and the long-term stability of a subsurface ocean on Enceladus. *Icarus*. **194** (2), pp. 675–689.

Robinson, Kirtland J et al. (2023). Ethene-ethanol ratios as potential indicators of hydrothermal activity at Enceladus, Europa, and other icy ocean worlds. *Icarus*. **406**, p. 115765.

Roquet, Fabien et al. (2015a). Accurate polynomial expressions for the density and specific volume of seawater using the TEOS-10 standard. *Ocean Modelling*. **90**, pp. 29–43.

Roquet, Fabien et al. (2015b). Defining a simplified yet "realistic" equation of state for seawater. *Journal of Physical Oceanography*. **45** (10), pp. 2564–2579.

Roquet, Fabien et al. (2022). Unique thermal expansion properties of water key to the formation of sea ice on Earth. *Science Advances*. **8** (46), eabq0793.

Roshan, Saeed et al. (2020). Reversible scavenging traps hydrothermal iron in the deep ocean. *Earth and Planetary Science Letters*. **542**, p. 116297.

Rovira-Navarro, Marc et al. (2023). Thin-shell Tidal Dynamics of Ocean Worlds. *The Planetary Science Journal*. **4** (2), p. 23.

Sabaka, Terence J et al. (2016). Extracting ocean-generated tidal magnetic signals from Swarm data through satellite gradiometry. *Geophysical Research Letters*. **43** (7), pp. 3237–3245.

Šachl, L et al. (2024). Magnetic field induced by convective flow in Europa's subsurface ocean. *Icarus*. P. 116375.

Šachl, Libor et al. (2019). Modelling of electromagnetic signatures of global ocean circulation: physical approximations and numerical issues. *Earth, Planets and Space*. **71** (1), pp. 1–13.

Saito, Mak A et al. (2013). Slow-spreading submarine ridges in the South Atlantic as a significant oceanic iron source. *Nature Geoscience*. **6** (9), pp. 775–779.

Sanford, Thomas B (1971). Motionally induced electric and magnetic fields in the sea. *Journal of Geophysical research*. **76** (15), pp. 3476–3492.

Sanford, Thomas B et al. (2011). Upper-ocean response to Hurricane Frances (2004) observed by profiling EM-APEX floats. *Journal of Physical Oceanography*. **41** (6), pp. 1041–1056.

Saur, Joachim et al. (2015). The search for a subsurface ocean in Ganymede with Hubble Space Telescope observations of its auroral ovals. *Journal of Geophysical Research: Space Physics*. **120** (3), pp. 1715–1737.

Saur, Joachim et al. (2024). Analysis of Enceladus's Time-variable Space Environment to Magnetically Sound its Interior. *The Planetary Science Journal*. **5** (11), p. 245.

Schmitt, Raymond W (1994). Double diffusion in oceanography. *Annual Review of Fluid Mechanics*. **26** (1), pp. 255–285.

Schoenfeld, Ashley M et al. (2023). Particle entrainment and rotating convection in Enceladus' ocean. *Communications Earth & Environment*. **4** (1), p. 28.

Scikit-learn Developers (2024). *LinearRegression*. URL: https://scikit-learn.org/stable/modules/generated/sklearn.linear_model.LinearRegression.html.

Scott, Jeffery R et al. (2001). Geothermal heating and its influence on the meridional overturning circulation. *Journal of Geophysical Research: Oceans*. **106** (C12), pp. 31141–31154.

Simmons, Harper L et al. (2004). Tidally driven mixing in a numerical model of the ocean general circulation. *Ocean Modelling*. **6** (3-4), pp. 245–263.

Soderlund, Krista M (2019). Ocean dynamics of outer solar system satellites. *Geophysical Research Letters*. **46** (15), pp. 8700–8710.

Soderlund, Krista M et al. (2014). Ocean-driven heating of Europa's icy shell at low latitudes. *Nature Geoscience*. **7** (1), pp. 16–19.

Soderlund, Krista M et al. (2024). The physical oceanography of ice-covered moons. *Annual Review of Marine Science*. **16**, pp. 25–53.

Souček, Ondřej et al. (2019). Tidal dissipation in Enceladus' uneven, fractured ice shell. *Icarus*. **328**, pp. 218–231.

Spencer, JR et al. (2006). Cassini encounters Enceladus: Background and the discovery of a south polar hot spot. *science*. **311** (5766), pp. 1401–1405.

Stephenson, David and Bryan, Kirk (1992). Large-scale electric and magnetic fields generated by the oceans. *Journal of Geophysical Research: Oceans*. **97** (C10), pp. 15467–15480.

Stewart, KD et al. (2017). Vertical resolution of baroclinic modes in global ocean models. *Ocean Modelling*. **113**, pp. 50–65.

Stommel, Henry (1948). The westward intensification of wind-driven ocean currents. *Eos, Transactions American Geophysical Union*. **29** (2), pp. 202–206.

Szuts, Zoltan B (2012). Using motionally-induced electric signals to indirectly measure ocean velocity: Instrumental and theoretical developments. *Progress in Oceanography*. **96** (1), pp. 108–127.

Thomas, PC et al. (2016). Enceladus's measured physical libration requires a global subsurface ocean. *Icarus*. **264**, pp. 37–47.

Tobie, Gabriel et al. (2003). Tidally heated convection: Constraints on Europa's ice shell thickness. *Journal of Geophysical Research: Planets*. **108** (E11).

Toh, Hiroaki et al. (2011). Tsunami signals from the 2006 and 2007 Kuril earthquakes detected at a seafloor geomagnetic observatory. *Journal of Geophysical Research: Solid Earth*. **116** (B2).

Travis, BJ and Schubert, G (2015). Keeping Enceladus warm. *Icarus*. **250**, pp. 32–42.

Truong, Ngoc et al. (2019). Decomposition of amino acids in water with application to in-situ measurements of Enceladus, Europa and other hydrothermally active icy ocean worlds. *Icarus*. **329**, pp. 140–147.

Turner, Jefferson T (2015). Zooplankton fecal pellets, marine snow, phytodetritus and the ocean's biological pump. *Progress in Oceanography*. **130**, pp. 205–248.

Tyler, Robert H (2011). Magnetic remote sensing of Europa's ocean tides. *Icarus*. **211** (1), pp. 906–908.

Tyler, Robert H et al. (1997). Electromagnetic fields generated by a three dimensional global ocean circulation. *Journal of Geophysical Research: Oceans*. **102** (C3), pp. 5531–5551.

Tyler, Robert H et al. (2003). Satellite observations of magnetic fields due to ocean tidal flow. *Science*. **299** (5604), pp. 239–241.

Tyler, Robert H et al. (2017). Electrical conductivity of the global ocean. *Earth, Planets and Space*. **69** (1), pp. 1–10.

Vallis, Geoffrey K (2017). *Atmospheric and oceanic fluid dynamics*. Cambridge University Press.

Vance, Steven D et al. (2018). Geophysical investigations of habitability in ice-covered ocean worlds. *Journal of Geophysical Research: Planets*. **123** (1), pp. 180–205.

Vance, Steven Douglas et al. (2021). Magnetic induction responses of Jupiter's ocean moons including effects from adiabatic convection. *Journal of Geophysical Research: Planets*. **126** (2), e2020JE006418.

Velímskỳ, Jakub et al. (2018). On the modelling of M2 tidal magnetic signatures: effects of physical approximations and numerical resolution. *Earth, Planets and Space*. **70** (1), p. 192.

Velímskỳ, Jakub et al. (2019). The global toroidal magnetic field generated in the Earth's oceans. *Earth and Planetary Science Letters*. **509**, pp. 47–54.

Vivier, Frédéric et al. (2004). Simulations of magnetic fields generated by the Antarctic Circumpolar Current at satellite altitude: Can geomagnetic measurements be used to monitor the flow? *Geophysical Research Letters*. **31** (10).

Waite, Anya et al. (1997). Sinking rate versus cell volume relationships illuminate sinking rate control mechanisms in marine diatoms. *Marine Ecology Progress Series*. **157**, pp. 97–108.

Waite, J Hunter et al. (2009). Liquid water on Enceladus from observations of ammonia and 40Ar in the plume. *Nature*. **460** (7254), pp. 487–490.

Waite, J Hunter et al. (2017). Cassini finds molecular hydrogen in the Enceladus plume: evidence for hydrothermal processes. *Science*. **356** (6334), pp. 155–159.

Wieczorek, Mark A and Meschede, Matthias (2018). SHTools: Tools for working with spherical harmonics. *Geochemistry, Geophysics, Geosystems*. **19** (8), pp. 2574–2592.

Wilson, Alec and Kerswell, Rich R (2018). Can libration maintain Enceladus's ocean? *Earth and Planetary Science Letters*. **500**, pp. 41–46.

Woolway, R Iestyn et al. (2022). Winter inverse lake stratification under historic and future climate change. *Limnology and Oceanography Letters*. **7** (4), pp. 302–311.

Wunsch, Carl and Ferrari, Raffaele (2004). Vertical mixing, energy, and the general circulation of the oceans. *Annu. Rev. Fluid Mech.*. **36**, pp. 281–314.

Zeng, Yaoxuan and Jansen, Malte F (2021). Ocean circulation on enceladus with a high- versus low-salinity ocean. *The Planetary Science Journal*. **2** (4), p. 151.

Zeng, Yaoxuan and Jansen, Malte F (2024). The Effect of Salinity on Ocean Circulation and Ice–Ocean Interaction on Enceladus. *The Planetary Science Journal*. **5** (1), p. 13.

Zeng, Yaoxuan and Jansen, Malte F (2025). Slantwise convection and heat transport in the icy moon oceans. *arXiv preprint arXiv:2508.06480*.

Zeng, Yaoxuan et al. (2022). The effect of gas bubbles on nanoparticle transport and ocean circulation on Enceladus. *AGU Fall Meeting Abstracts*. Vol. 2022, P35D–1908.

Zhang, Yixiao et al. (2024). Ocean weather systems on icy moons, with application to Enceladus. *Science Advances*. **10** (45), eadn6857.

Zhang, Yixiao et al. (2025). Long Transit Time from the Seafloor to the Ice Shell on Enceladus.

Zhu, Peiyun et al. (2017). The influence of meridional ice transport on Europa's ocean stratification and heat content. *Geophysical Research Letters*. **44** (12), pp. 5969–5977.

Zolotov, Mikhail Y (2007). An oceanic composition on early and today's Enceladus. *Geophysical Research Letters*. **34** (23).

Zolotov, Mikhail Y and Shock, Everett L (2001). Composition and stability of salts on the surface of Europa and their oceanic origin. *Journal of Geophysical Research: Planets*. **106** (E12), pp. 32815–32827.